UNIVERSIDAD COMPLUTENSE DE MADRID
FACULTAD DE CIENCIAS FÍSICAS

TESIS DOCTORAL

Verificación del rango de los protones en el ámbito de la protonterapia y la física nuclear

Proton range verification in the fields of proton therapy and nuclear physics

MEMORIA PARA OPTAR AL GRADO DE DOCTOR

PRESENTADA POR

Víctor Valladolid Onecha

Directores

Luis Mario Fraile Prieto
Samuel España Palomares
Harald Paganetti

Madrid

Universidad Complutense de Madrid
Facultad de Ciencias Físicas

UNIVERSIDAD
COMPLUTENSE
MADRID

VERIFICACIÓN DEL RANGO DE LOS PROTONES EN EL ÁMBITO DE LA PROTONTERAPIA Y LA FÍSICA NUCLEAR

PROTON RANGE VERIFICATION IN THE FIELD OF PROTON THERAPY AND NUCLEAR PHYSICS

MEMORIA PARA OPTAR AL GRADO DE DOCTOR PRESENTADA POR

Victor Valladolid Onecha

Directores:
Luis Mario Fraile Prieto
Samuel España Palomares
Harald Paganetti

Madrid, 2023

Universidad Complutense de Madrid
Facultad de Ciencias Físicas

Programa: D9AD - Doctorado en Física

UNIVERSIDAD
COMPLUTENSE
MADRID

VERIFICACIÓN DE RANGO EN EL ÁMBITO DE LA PROTONTERAPIA Y LA FÍSICA NUCLEAR

PROTON RANGE VERIFICATION IN THE FIELD OF PROTON THERAPY AND NUCLEAR PHYSICS

MEMORIA PARA OPTAR AL GRADO DE DOCTOR PRESENTADA POR

Victor Valladolid Onecha

Directores:
Luis Mario Fraile Prieto
Samuel España Palomares
Harald Paganetti

Madrid, 2023

Contents

Motivation and objectives of this thesis

Proton radiotherapy, or proton therapy for short, uses protons instead of photons or electrons to treat tumors, as in conventional radiotherapy. It was first proposed in the 1940s by Wilson [1946], the need for proper advances in accelerator technology and treatment planning, delayed its clinically implementation until the 1990s [Mohan and Grosshans, 2017]. Since then, proton therapy has rapidly evolved, and there are currently over 100 proton therapy centers in operation worldwide (two in Spain), and many more under construction plans, including 11 of them in Spain.

The main reason why proton therapy has had a fast development, is related to how protons deposit their energy, which is the fundamental advantage of proton therapy over traditional radiation therapy. Unlike photons or electrons, which deposit energy along their entire path through tissue, proton beams deposit most of their energy at a specific depth, the Bragg peak [Paganetti, 2011; Knopf and Lomax, 2013; Knoll, 2010]. This allows for a highly conformal dose distribution to the tumor while sparing nearby healthy tissues from unnecessary radiation exposure. In addition, the sharp dose fall-off beyond the Bragg peak would allow for dose delivery plans without irradiating organs at risk (OARs) [Moteabbed et al., 2011; Knopf and Lomax, 2013]. This reduces the potential long-term side effects of radiation therapy in comparison with traditional techniques. Overall, the unique characteristics of the Bragg peak make proton therapy an attractive option for a wide range of tumors, especially for pediatric purposes due to the reduction of secondary effects.

However, the full potential of proton therapy will not be reached until several issues that complicate treatment planning are dealt with. A proton therapy treatment plan

details how protons will be delivered to a specific patient's tumor. It includes information on the target volume, dose to the target and normal/healthy tissues, beam angles, beam energy, and number of treatment fractions. Ideally, the treatment plan should cover only with the prescribed dose the clinical target volume (CTV), which comprises the area of the visible tumor, along with surrounding regions where microscopic spreads of the tumor are likely to occur. Due to the inherent uncertainties in any raditherapy plan [Moteabbed et al., 2011; Paganetti, 2012; Knopf and Lomax, 2013], additional safety margins are added to the CTV, to account for these technological uncertainties in dose delivery and planning. The resulting area to be irradiated is the Planning Target Volume (PTV). When OARs are close to the tumor, plans are designed considering possible failures due to range uncertainties. Thus, proton plans are often composed by several lateral beams (fields) arranged in parallel-opposed directions. By arranging the beams in this way, the OARs will be out of the trajectory of the individual beams in case of gross under/over-estimation of the proton range.

If proton range uncertainties could be largely reduced, and the possibility of proton range miss-estimation (due for instance to a problem with the machine) could be removed out from the picture, less conservative PTVs and less complex plans would be possible, involving the use of fewer fields and number of beam irradiation, with considerable resulting benefits for the patients and costs and time reduction. This will be possible by means of **proton range verification techniques** Paganetti [2011]; Knopf and Lomax [2013]; Krimmer et al. [2018]. These techniques aim to measure the actual range of protons inside the patient and compare it to the predicted range assumed during treatment planning. The implementation of these techniques would enable even real-time identification during irradiations of any deviations with respect to the plan [Knopf and Lomax, 2013; Krimmer et al., 2018], making unnecessary to generate a larger PTV with larger safety margins. Instead, a plan covering only the CTV could be generated, and any deviations detected through verification techniques could be corrected in real-time. In addition, the use of proton range verification techniques would not only allow for the identification of possible range deviations but also make it possible to implement more ambitious and efficient treatment plans. For instance, single-field plan facing OARs could be employed [Knopf and Lomax, 2013]. This would significantly reduce the amount of healthy tissue exposed to radiation and ultimately decrease the risk of side effects and complications for the patient, and largely speed up

the procedures. Therefore, the implementation of proton range verification techniques will have a significant impact on the effectiveness, and safety of proton therapy.

Two of the most promising techniques for proton range verifications are Positron Emission Tomography (PET) and Prompt-Gamma (PG). Both techniques use secondary radiation emitted from the patient as a consequence of the nuclear reactions induced by protons to verify their range.

- **PET** uses the 511 kev photons from the positron annihilation to estimate where these emissions have been produced. Protons generate in biological tissues β^+ isotopes which emit a positron when decayed. The annihilation photons can be detected by a PET scanner, and the resulting data can be used to verify the position and shape of the dose distribution within the patient [Zhu et al., 2011; Zhu and Fakhri, 2013; Paganetti and Fakhri, 2015; Onecha et al., 2020; España et al., 2021, 2022].

- **PG** is based on the detection of gamma rays that are emitted in those nuclear reactions in which the nucleus ends in an excited level and further decays rapidly to the ground level. The measurement of the energy or the spatial distribution of these photons is used to verify the proton range and therefore the dose distribution [Verburg and Seco, 2014; Hueso-González et al., 2018; Richter et al., 2016].

However, none of these techniques have been fully implemented successfully in a clinical case because they have several limitations that constrain their use. These limitations, in the case of PET, are related to the low positron production rate, time delays between the proton irradiation and PET data acquisition, which introduces biological wash-out and shifting of the activity produced, and the incomplete correlation between the produced activity and the dose, as protons usually do not produce significant activation in biological tissues close to the Bragg peak, which complicates the estimation of dose (or range) from PET images [Moteabbed et al., 2011]. In the case of PG, the limitations are related to the large energy of the emitted photons and the demands on the PG detection system in terms of the rates needed, and that they must run during irradiations. Furthermore, this technique was introduced more recently than PET, and it has been somewhat less developed, thus a mature and accepted solution based on it is still on the works Knopf and Lomax [2013]; Krimmer et al. [2018]. There is a need

of new tools to facilitate its implementation in clinical environments, such as fast PG Monte Carlo simulators.

This thesis has been developed in the Nuclear Physics Group (GFN) of the Universidad Complutense de Madrid, in the context of the activities related to project PROton therapy and nuclear Techniques for ONcology (PRONTO) project, funded by the Government of Madrid, in which the GFN coordinates another 5 groups in the area of Madrid. The objective of this project was to develop, from the nuclear perspective, the implementation of new ideas and tools to improve the accuracy of the proton therapy. Among several ideas proposed in the project, much attention is devoted to range verification techniques with the aim of reducing the uncertainties that exist in proton therapy. This thesis has focused mainly on the development of this part of the PRONTO project, proposing and implementing new ideas to improve PET and PG proton range verification techniques [Onecha et al., 2020; Rodriguez et al., 2021; Onecha et al., 2022; España et al., 2022].

The goals of this thesis related to PRONTO project can be summarized as follows:

- The use of **contrast agents** in proton therapy. Contrast agents are common in every modality of medical imaging to improve image quality by introducing in the patient a certain substance. These substances induce an increase in image contrast or a better response of the organs or tissues to the physical agent used to obtain the image. However, it has not been (or at all, or ever) satisfactorily applied to proton therapy so far.[España et al., 2021; Onecha et al., 2022; España et al., 2022].

  In **chapter 2**, we propose the use of contrast agents to improve the accuracy of proton range verification techniques. Suitable contrast agents will solve both the low number of useful counts in imaging devices and the imperfect correlation between activity and dose by generating $\beta+$ isotopes under the PG, where there is no activity induced by biological tissues [España et al., 2021, 2022; Rodriguez et al., 2021]. In the case of PGs, they will add low-energy γ-ray emissions (1-2 MeV), which are much easier to detect than PGs emitted by biological tissues[Verburg et al., 2012; Verburg and Seco, 2014].

- Contrast agents **cross-sections** have been measured in **chapter 3** because their knowledge is essential for studying its impact on proton range verification. For this

reason, we have performed experiments to measure and analyze the cross-sections channels of our proposed contrast agents which have never been measured before, or those that have not been measured across the entire proton therapy energy spectrum.

- In **chapter 4**, a new **PET to dose program (DAD-MSA)** is proposed and validated over simulated realistic clinical scenarios. The motivation of this chapter comes from one of the limitations in both PET and PG verification techniques, which is the lack of a reliable and validated program that transforms the medical image, or the detected secondary radiation, into deposited dose or proton range [Parodi and Bortfeld, 2006; Masuda et al., 2020; Liu et al., 2019]. The most outstanding properties of the developed code are: 1) its computational speed, which would allow it to be implemented in real time. 2) Its millimetric precision and accuracy. 3) Its capacity to adapt to verification system other than PET.

- The last objective is the combination of the three previous points. In **chapter 5**, we make use of the DAD-MSA to identify deviations in a proton therapy treatment with and without the use of one of the proposed contrast agents (water-18). Furthermore, we have implemented the cross-section measurements carried out in chapter 3 to make the case as realistic as possible. The results of this chapter show the huge potential of contrast agents, make it possible the identification of range deviations which would be completely unidentifiable with activation of biological tissues only.

As part of a collaboration with the Massachusetts General Hospital and Harvard Medical School, a specific tool for their own PG prototype detection system has been developed. This PG verification system is one of only two in the world that have been used successfully under real clinical conditions [Hueso-González et al., 2018; Verburg and Seco, 2014].

The main objective in this collaboration is the development of a fast Monte Carlo simulator for Prompt Gamma transportation. The motivation of this tool is given by the necessity of simulating around 10^{11} photons in less than a few minutes to generate the PG detection model to estimate the range. Until now, this was not achievable by any other Monte Carlo code.

In **chapter 6**, we show our Hybrid Prompt gamma Transportation Monte Carlo (HPT-MC) code designed for the transportation of high energy photons (1-10 MeV). The HPT-MC is fully implemented in GPU to thousand-fold increase in the speed of the simulation. This new proposed code can simulate up to 500M photons per second for a realistic scenario in the PG system at the MGH. The whole PG detection model is computed in less than 4 minutes, which is almost 100 times faster than in the previous version of the code.

The last chapter contains the conclusions of this thesis, highlighting the most promising results and possible further investigations.

Summary

Introduction and motivation

In this chapter, we will introduce all the necessary physics for understanding proton therapy and range verification. Apart from this, certain concepts that will be used throughout the thesis will be detailed. One of them is the detection of ionizing radiation that will be used to measure cross sections in Chapter 3. We will also introduce Monte Carlo simulators for particle transport since they will be used throughout the thesis. Finally, we will briefly introduce what GPUs (Graphics Processing Units) are and how they can be used to considerably accelerate almost any code. In this thesis, both the proposed reconstructor in Chapter 4 and the MC simulator in Chapter 6 are fully implemented on a GPU.

Contrast Agents in proton therapy

Contrast agents in medicine are substances or isotopes that are introduced into the patient before certain medical imaging procedures to improve their quality. Their use is well established in computed tomography (CT) with the use of iodine to increase image resolution.

In this chapter, the use of contrast agents in proton therapy is proposed to improve the quality of verification techniques that use both PET and PGs to estimate the deposited dose and proton range. First, the limitations of each technique are detailed, and subsequently, the characteristics that contrast agents must have to overcome them are described. In addition, a series of possible candidates for both techniques are proposed. The chapter ends with the first proof of concept that was carried out to test the application and expectations of contrast agents.

Cross-Section Measurements

The only way to test the true applications of contrast agents is by knowing their effective cross-sections. In this chapter, we review the literature to gather all the effective cross-sections that have already been measured for the contrast agents proposed in the previous chapter.

Three different experiments have been conducted in this thesis: 1) Measurement of effective cross-sections of PET contrast agents at high clinical energies (50-250 MeV). 2) Measurement of effective cross-sections of PET contrast agents at low energies (<10 MeV). 3) Measurement of effective cross-sections of prompt gamma emission from ^{18}O contrast agents at low energies (<10 MeV). For each experiment, the entire experimental set-up and analysis carried out to calculate the effective cross-sections and angular distribution in the case of prompt gammas are detailed.

Dictionary-based software for proton range verification

One of the most important and delicate phases of range verification techniques is the conversion of measured data (PET or PG) into deposited dose and proton range. Over the past few years, several methods have been proposed, and although they work correctly, they have some disadvantages such as high execution time or noisy generated doses.

In this chapter, a new method is proposed to obtain deposited dose and proton range from secondary radiation data of a patient (DAD-MSA). The program proposed has been implemented in range verification using PET, but it could be extrapolated to any other verification system such as PGs. This program works on a database, which we call the Dictionary, consisting of the activation and dose that each beam of the plan would produce separately. The code uses two reconstruction algorithms, maximum-likelihood expectation-maximization (MLEM) Maxim et al. [2016]; Ma et al. [2013] and simulated annealing (SA) [Rutenbar, 1989], which find the linear combination of activations from the database that best represents the PET image measured from the patient. The same solution on activation is applied to dose to obtain the final result. Throughout this chapter, the operation of this program is explained in detail, and a series of tests have been performed to verify its validity for clinical scenarios.

Clinical implementation of PET contrast agents (water-18)

One of the main objectives of this thesis is to validate contrast agents as a real solution to the limitations that exist in range verification techniques. In this chapter, we use the effective cross-sections measured in Chapter 3 and the reconstructor from Chapter 4 to test the impact of using ^{18}O in range verification in a patient using PET images.

The usefulness of this contrast has been tested in a realistic clinical scenario, in which a series of range deviations due to anatomical changes were assumed. These deviations were attempted to be identified with and without contrast using the DAD-MSA as a reconstruction tool. The results show how deviations in the last millimeters of the proton range are only identifiable with the use of contrast agents.

Ultra-fast GPU MC for Promtp-Gamma transportation

This chapter describes the development and validation of a Monte Carlo simulator, HPTC-MC, implemented on GPU for high-energy photon propagation. The simulator was developed in collaboration with the Massachusetts General Hospital, which houses one of the few existing PG verification systems in the world. The chapter provides details on the characteristics of this Monte Carlo simulator and the acceleration techniques that have been implemented. The validation of the simulator was carried out through comparisons with other Monte Carlo simulators, as well as reproducing the proton range estimations that had been obtained previously. The results demonstrate that the program reproduces simulations from other Monte Carlos almost exactly, while using 1000 times less time. Additionally, the verification tool generates results with higher accuracy and in just 5 minutes, compared to the 3-4 hours it took previously.

Resumen

Introducción y motivación

La protonterapia es una técnica de radioterapia que usa protones como partícula ionizante para irradiar tumores [Paganetti, 2011]. La principal ventaja de esta técnica con respecto a la radioterapia tradicional viene dada por la forma en que los protones depositan energía, caracterizada por concentrar la mayor parte de la dosis en la zona más distal del rango del protón, generando un pico de dosis conocido como pico de Bragg [Paganetti, 2011; Knoll, 2010].

El uso de protones en general presenta varias ventajas con respecto al resto de técnicas de radioterapia [Paganetti, 2011]. A pesar de esto, todavía existen una serie de limitaciones que no permiten aplicar todo su potencial. Estas limitaciones tienen relación con la precisión del rango del protón, que no se puede calcular dentro de un paciente con un error inferior al 3% del valor del rango del protón [Paganetti, 2012]. Estas incertidumbres hacen que se tengan que buscar escenarios más conservadores para asegurar la irradiación de toda la zona tumoral a expensas de irradiar más tejido sano Paganetti [2011, 2012]. La solución a este problema es uno de los temas más importantes de la protonterapia, y de entre todas las técnicas que lo intentan solucionar, en esta tesis nos centraremos en el uso de técnicas de verificación de rango, que facilitan información sobre la dosis se ha depositado en el paciente a partir de la radiación secundaria.

En este capítulo introduciremos toda la física necesaria para la comprensión de la protonterapia y la verificación del rango. Aparte de esto, se detallarán ciertos conceptos que se usarán a lo largo de la tesis. Uno de ellos, la detección de radiación ionizante que se usará para medir secciones eficaces en el capítulo 3. Introduciremos también los simuladores Monte Carlo para el transporte de partículas ya que se usarán a lo largo de toda la tesis. Por último, se introducirá brevemente que son las GPUs (Graphics

Processing Units) y como se pueden usar para acelerar considerablemente casi cualquier código. En esta tesis, tanto el reconstructor propuesto en el capítulo 4 como el simulador MC en el capitulo 6 están totalmente implementados en GPU.

Agentes de contraste en protonterapia

Los agentes de contrastes en medicina son sustancias o isótopos que se introducen en el paciente antes de realizar ciertas imágenes médicas para mejorar su calidad. Su uso está totalmente asentado en tomografía computarizada (TC) con el uso de Iodo para aumentar la resolución de la imagen.

En el capítulo 2 se propone el uso de contrastes en protonterapia para mejorar la calidad de las técnicas de verificación que usan tanto PET como PGs para estimar la dosis depositada y el rango del protón. Primero se detallan las limitaciones de cada una de las técnicas, y a posteriori, las características que tienen que poseer los agentes de contrastes para solventarlas. Además, se proponen una serie de posibles candidatos para ambas técnicas. El capítulo acaba con la primera prueba de concepto que se realizó para probar la aplicación y las expectativas que había en los contrastes.

Medidas de secciones eficaces de agentes de contrastes

La única forma de testear las verdaderas aplicaciones de los agentes de contraste es conociendo sus secciones eficaces. En este capítulo hacemos una revisión de la bibliografía para recabar todas las secciones eficaces que ya se han medido de los contrastes propuestos en el capítulo anterior.

Tres diferentes experimentos se han llevado a cabo en esta tesis: 1) Medida de secciones eficaces de contrastes PET a altas energías clínicas (50-250 MeV). 2) Medidas de secciones eficaces de contrastes PET a bajas energías ($<$10 MeV). 3) Medidas de secciones eficaces de emisión de PGs de ^{18}O de contrastes a bajas energías ($<$10 MeV). En el capítulo 3 se detalla, para cada uno de los experimentos, todo el set-up experimental y el análisis que se ha llevado a cabo para calcular las secciones eficaces y la distribución angular en el caso de los Prompt-gammas.

Software de reconstrucción para la verificación del rango del protón (DAD-MSA)

Una de las fases más importantes y a la vez delicadas de las técnicas de verificación de rango es el pasar de los datos medidos (PET o PG) a dosis depositada y rango del protón. A lo largo de los últimos años se han propuesto varias ideas, y aunque funcionan correctamente, tienen algunas desventajas como el alto tiempo de ejecución o que las dosis que generan son ruidosas.

En el capítulo 4 se propone un nuevo método para obtener la dosis depositada y el rango del protón a partir de datos de radiación secundaria de un paciente (DAD-MSA). El programa que se propone se ha implementado en la verificación del rango usando PET, pero podría ser extrapolado a cualquier otro sistema de verificación como los PGs. Este programa funciona sobre una base de datos, a la que llamamos Diccionario, que está formada por la activación y la dosis que producirían cada uno de los haces del plan por separado. El código usa dos algoritmos de reconstrucción, maximum-likelihood expectation-maximization (MLEM) Maxim et al. [2016]; Ma et al. [2013] y simulated annealing (SA) [Rutenbar, 1989], que encuentran la combinación lineal de activaciones de la base de datos que mejor representa la imagen PET que se ha medido del paciente. La misma solución sobre la activación se aplica sobre la dosis para obtener el resultado final. A lo largo de este capítulo se explica en detalle el funcionamiento de este programa y se muestran una serie de pruebas que se han realizado para comprobar su validez en escenarios clínicos.

Implementación clínica de los agentes de contrastes PET usando agua-18

Uno de los principales objetivos de esta tesis es la validación de los contrastes cómo una solución real a las limitaciones que existen en las técnicas de verificación de rango. En el capítulo 5 se hace uso de las secciones eficaces medidas en el capítulo 3 y del reconstructor del capítulo 4, para testear el impacto de usar ^{18}O en la verificación del rango en un paciente usando imágenes PET.

La comprobación de la utilidad de este contraste se ha llevado a cabo en un escenario clínico realista, en el que se han supuesto una serie de desviaciones del rango debido a

cambios anatómicos. Estas desviaciones se han intentado identificar con y sin contraste usando como el DAD-MSA como herramienta de reconstrucción. Los resultados muestran como desviaciones en los últimos milímetros del rango del protón son únicamente identificables con el uso de contrastes.

GPU Monte Carlo para el transporte de Prompt-Gammas

En colaboración con el Hospital General de Massachusetts, donde se encuentra uno de los pocos sistemas de verificación de PG que existen en el mundo [Hueso-González et al., 2018], se ha desarrollado un simulador Monte Carlo implementado en GPU para la propagación de fotones de alta energía (HPTC-MC). Este código ha sido implementado en la herramienta de verificación y ha sido testeado con datos experimentales.

En este capítulo se detallan las características de este Monte Carlo junto con todas las técnicas de aceleración que se han implementado. La validación de este código se ha llevado a cabo mediante comparaciones con otros Monte Carlos y reproduciendo las estimaciones en el rango del protón que ya se habían obtenido anteriormente. Los resultados muestran que el programa reproduce las simulaciones de otros MC de forma casi exacta usando un tiempo 1000 veces menor. Además, los resultados que genera la herramienta de verificación con este código tienen una mayor precisión y se generan en apenas 5 minutos, en comparación con las 3-4 horas que tardaba antes.

Chapter 1

Introduction

Cancer is one of the leading causes of death in the world. In 2018, there were 18.1 million new cases and 9.5 million cancer deaths worldwide [Sudhakar, 2009; Baskar et al., 2012]. There are several techniques to treat this disease depending on where the tumor is located, but none of them are 100 % effective. Between all of them, the three most widely used are surgery, chemotherapy and radiotherapy [Sudhakar, 2009]. Each one is used in different scenarios but almost 70 % of oncology patients receive radiotherapy treatment at least once. Leveraging external ionizing beams, radiotherapy administers high doses to targeted tumor areas, aiming to eradicate malignant cells. Conventionally, photon or electron beams have dominated the field, yet in recent years, proton beams have gained prominence due to their inherent advantages [Paganetti, 2011; Tian et al., 2018]. Proton therapy, which employs protons for cancer treatment, constitutes the primary focus of this thesis.

This chapter will introduce photon and proton physics, focusing on how they interact with matter and how they deposit energy. By gaining a comprehensive understanding of these fundamental principles, we will proceed to elucidate the intricacies of proton therapy, shedding light on its key advantages. A meticulous comparison will be drawn between the depth dose profiles of proton therapy and those of traditional techniques, allowing for a reasoned evaluation. Furthermore, this thesis aims to introduce novel techniques for proton range verification, accompanied by innovative ideas and tools to enhance these methods. Among the proposed advancements are Monte Carlo methods for particle transport and the utilization of Graphics Processing Units (GPUs), which hold immense potential for this purpose.

1.1 Physics behind radiotherapy

Radiotherapy is a medical treatment that uses ionizing beams to selectively irradiate tumor sites, effectively delivering substantial energy doses to eradicate cancer cells while minimizing harm to healthy tissues. The extent of cellular damage inflicted corresponds to the amount of energy deposited in a specific area, potentially resulting in cell death [Mehta et al., 2010]. This energy deposition per unit volume is quantified by the physical measure known as the Gray (Gy), denoted in international units as joules per kilogram (J/kg). In a standard radiotherapy regimen, the cumulative dose administered to the tumor region typically reaches approximately 60 Gy, a level deemed sufficient for tumor cell elimination.

The ideal goal of radiotherapy is to precisely target the tumor region while entirely sparing healthy tissues from any dose deposition. However, given the intrinsic nature of tumors being located within the human body, it becomes inevitable that healthy tissues are affected in the process of reaching the tumor. Radiotherapy strives to optimize irradiation plans with meticulous precision, aiming to deliver the necessary therapeutic dose to the tumor while simultaneously minimizing radiation exposure to healthy tissues and organs at risk (OAR) [Mehta et al., 2010].

In order to properly optimize radiotherapy plans, it is necessary to understand the physics of the particles used for this purpose. Photons, electrons and protons have different properties and consequently, they interact with matter differently. The following portion of this work will topic on explaining the physics of these particles, how they interact with matter and how they can be used for radiotherapy.

1.1.1 Physics of Photon Interactions in Matter

Photons are elementary particles which exhibit wave-particle duality behavior. They are massless and chargeless and because of that they always travel at the speed of light in vacuum despite its energy [Knoll, 2010]. We are used to relate energy with speed but in case of photons is different. In photons, energy describes the wave behavior as the frequency (ν) and it is proportional to energy, in other words, inverse to wavelength (λ).

$$E = \hbar\omega = h\nu = \frac{hc}{\lambda} \tag{1.1}$$

Photon radiation encompasses low-energy photons commonly referred to as radio waves. Only photons with a wavelength of up to 10 nm (equivalent to 125 eV) are considered non-ionizing radiation because above this energy photons interact with electrons. In these interactions, photons transfer energy to electrons, which subsequently deposit the energy within the medium. This measure of deposited energy per unit mass is commonly known as dose. In the subsequent sections, we will explore and elucidate the various conceivable interactions of photons with matter.

- **Photoelectric effect**

  Photoelectric effect happens when a photon of a certain energy interacts with electrons in the atomic structure and the whole energy is transferred to the electron [Knoll, 2010]. As a result of this interaction, the electron is ejected from the atom with a certain energy which is given by the following expression,

  $$E_{e^-} = h\nu - E_b \tag{1.2}$$

  where E_{e^-} is the kinetic energy of the ejected electron, $h\nu$ is the photon energy and E_b is the binding energy. For this effect to occur, the photon energy must be higher than the binding energy, which is around 10-1000 keV. Therefore, this effect has a well-defined lower limit given by the binding energy, but there is not an upper limit.

  This effect is more likely at low photon energies (< 1 MeV) and in materials with high atomic number (Z). We can approximate the probability of interaction using the following expression which relate the probability (τ) with the atomic number (Z) and the photon energy (E_γ). The n value is 4 or 5 depending on the atomic number.

  $$\tau \approx C\frac{Z^n}{E_\gamma^{3.5}} \tag{1.3}$$

- **Compton Scattering**

  Compton or inelastic scattering [Compton, 1923] takes place when a photon interact with a free [Cherry et al., 2012] or a binding electron [Motz and Missoni, 1961] , transferring part of its energy to the electron. As a result, an electron of a certain energy and a secondary photon with less energy than the initial one

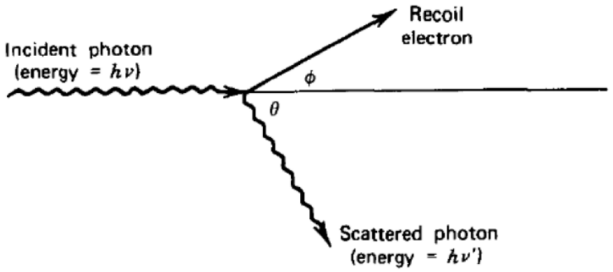

Figure 1.1: Compton scatter diagram [Knoll, 2010]. An incident photon with an energy $h\nu$ interacts with a free electron. As a consequence, the electron is scattered with an angle ϕ along with a secondary photon, which is emitted with a new energy $h\nu'$ and with an angle θ with respect to the initial photon direction.

are emitted. Assuming a free electron at rest and the momentum and energy conservation laws, we can deduce the expression

$$h\nu' = \frac{h\nu}{1 + \frac{h\nu}{m_e c^2}(1 - \cos\theta)}, \tag{1.4}$$

where $h\nu'$ is the energy of the scattered photon, $h\nu$ is the energy of the initial photon, m_e is the electron mass and θ is the photon scattered angle. The energy of the recoil electron is given by the difference of the incident and scattered photons.

The scattered angle θ can take any value from 0^{o} to 180^{o} but the emission is not isotropic. Assuming again a free electron at rest, the angular scattering distribution is given by Klein-Nishina equation [Knoll, 2010; Klein and Nishina, 1929]. In more complex scenarios, where the electron is not at rest or bound to an atom, these expressions are more complex. Further information can be found in [Motz and Missoni, 1961; Knoll, 2010].

- **Rayleigh**

  Rayleigh effect [Knoll, 2010], also known as elastic scattering, occurs when a photon interacts with an electron, but unlike Compton, there is no energy transfer. As a result, the incident photon modifies its trajectory but remains with the same energy.

- **Pair production**

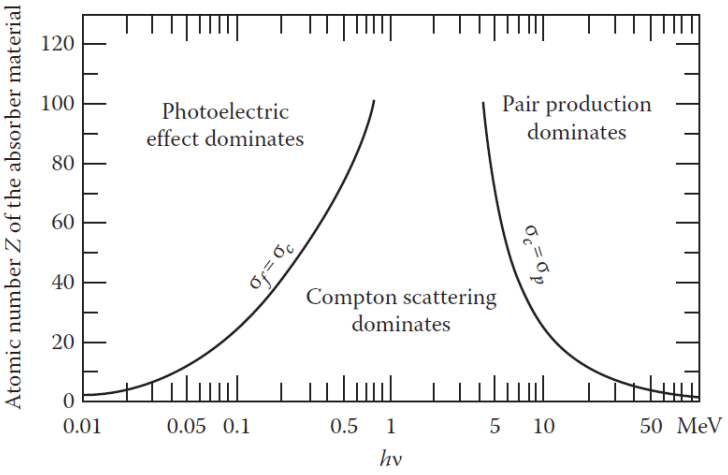

Figure 1.2: Schematic representation of the dominance of photon interactions in function of its energy and the atomic number (Z) of the medium [Knoll, 2010]. At lower energies the most important process is the photoelectric effect and its dominance remain up to 1 MeV for high Z materials. At higher energies over 4 MeV the pair production is the interaction which dominates. In the energy range between these two cases, the most dominant interaction is the Compton scattering.

Pair production is an effect that happens when a photon annihilates itself in the medium, producing an electron and a positron [Knoll, 2010]. The lower energy limit of this reaction is 1.022 MeV, which is the sum of the masses of the two generated particles. However, the reaction probability is very low up to 3-4 MeV in high atomic number materials. In low Z materials the contribution of this effect is almost negligible up to 10 MeV.

These are all the possible interactions of photons with matter. We have mentioned that some interactions are more likely at low energies or in materials with a high Z. Figure 1.2 presents a scheme that shows the dominant reactions in function of the photon energy and the Z of the material. At low energies, photoelectric absorption is the dominant process, while at high energies, pair production takes over, and in between these energy ranges, Compton scattering dominates. This knowledge is crucial for selecting appropriate materials for various applications, including radiation detection, shielding, and more.

In the previous discussion about the interaction between photons and matter, we presented an overview of the process, but we omitted any information regarding the spe-

cific timing of such interactions. It's worth noting that the interaction between photons and matter is a probabilistic phenomenon, meaning that the likelihood of interaction occurring is not guaranteed. The probability of such interactions increases exponentially as the photon travels through matter over a certain distance, which is commonly referred to as the path length or "d".

$$W(x) = 1 - e^{-\mu d} \tag{1.5}$$

where μ is the linear attenuation coefficient which indicates how likely is that a photon interacts in a specific material [Knoll, 2010]. Furthermore, this coefficient can be expressed as the sum of the contributions of the four interactions described above.

$$\mu_{tot} = \mu_{Ph} + \mu_{Ray} + \mu_{Cmpn} + \mu_{Pair} \tag{1.6}$$

In nuclear physics, we usually talk about cross-section (σ) instead of linear attenuation coefficients, but in the case of photons, this terminology is widely used. These two magnitudes are very similar and they are correlated with the next formula, where N is the atomic density of the material.

$$\mu(E) = \sigma(E)N \tag{1.7}$$

1.1.2 Physics of Proton Interactions in Matter

Protons are subatomic particles with a mass of 938.27 MeV/c^2 and a positive charge equivalent to an electron [Knoll, 2010; Paganetti, 2011]. A single proton is a hydrogen nucleus and it combines with an electron to form an atom. In terms of radiation interaction with matter, any nucleus without electrons is considered a hadron. They are *heavy* charged particles, in the sense that they interact mostly with electrons, which are 2000 times less massive. Hadrons travels through matter ionizing the medium and loosing energy until they completely slow down. Protons, unlike photons, continuously interact with the electrons in the medium due to Coulomb force [Knoll, 2010], but they also can interact directly with other nucleus because they have mass [Paganetti, 2011]. For all the mentioned reasons, we will separate proton interaction in four different types.

- **Stopping**

Proton stopping power (dE/dx) is an essential concept in radiation physics that characterizes the energy loss of protons as they travel through matter. When high-energy protons interact with a material, they transfer energy to the electrons in the medium, causing ionization and excitation processes. As a result, the protons gradually lose their energy and come to a stop, leading to the deposition of their energy in the material. Proton stopping power describes the rate of this energy loss per unit distance, and it is a crucial parameter for various applications in radiation therapy, dosimetry, and material science.

The Bethe formula describes the stopping power (dE/dx) of a charged particle with energy E, charge z, and velocity β as it travels a distance x through a target with mean excitation energy I and electron density n. The formula includes various factors that influence the energy loss of the particle, such as the ionization of atomic electrons and the atomic structure of the target material. The expression involves fundamental physical constants such as the speed of light (c), the vacuum permittivity (ϵ_0), the electron mass (m_e), and the electron charge (e). Overall, the Bethe formula provides a theoretical framework for calculating the stopping power of charged particles in a given medium, and it is widely used in radiation physics and material science.[Bethe, 1930; Knoll, 2010; Paganetti, 2011]

$$-\frac{dE}{dx} = \frac{4\pi}{m_e c^2}\frac{nz^2}{\beta^2}\left(\frac{e^2}{4\pi\epsilon_0}\right)^2\left[ln\left(\frac{2m_e c^2\beta^2}{I(1-\beta^2)}\right) - \beta^2\right] \tag{1.8}$$

The electron density of the material depends on the density ρ, the atomic number Z and the atomic mass A density as follows

$$n = \frac{N_A Z \rho}{A M_u} \tag{1.9}$$

where N_A is the Avogadro number and M_u the molar mass constant.

The Bethe formula is a complex equation that takes into account various factors affecting the stopping power of charged particles. However, a general trend can be observed across different scenarios: the stopping power is inversely proportional to the square of the velocity of the particle. This implies that as the velocity of the charged particle decreases, the amount of energy transferred to the medium per unit distance increases. This relationship is essential in radiation physics, where

the energy deposition of particles in matter is a crucial parameter for a wide range of applications.

- **Scattering**

  Protons experience scattering when they interact with the nuclei of a medium due to Coulomb interactions. Although the energy loss and deflection of a proton after a single interaction with a nucleus is typically small, the angular spread of a proton beam passing through a medium arises from multiple such interactions with different nuclei. This phenomenon is known as Multiple Coulomb Scattering (MCS). The angular spread of a proton beam passing through a material is Gaussian in nature, and by measuring this spread, the width of the Gaussian distribution can be predicted accurately using the MCS theory [Paganetti, 2011]. The theory can be applied to beams of any energy travelling through any type of material, making it a valuable tool for modeling and predicting proton scattering in various applications.

- **Nuclear Reactions**

  As mentioned before, protons mainly interacts with nucleus by Coulombs interactions. However, in rare cases, protons directly interacts with the nucleus of an atom. Protons with enough energy to overcome the Coulomb repulsion of the nucleus, enter into them knocking out one or more protons, neutrons or light nucleus clusters. These ejected particles usually have much less energy than the initial proton and are scattered at larger angles. Along the proton beam path, up to 20% of the protons are lost due to this interaction [Paganetti, 2011]. In some cases, the resulting nucleus clusters are β^+ unstable isotopes, which emit radiation when they decay. Furthermore, in some reactions the nucleus ends in an excited level, which decays with a half-life of fs to the ground level (g.l.), emitting a photon named Prompt-Gamma (PG). All this emitted radiation is known as secondary radiation, as it is produced as a consequence of proton interaction with matter.

- **Inelastic collisions**

  We have previously mentioned the main types of proton interactions: the soft scattering due to Coulomb interactions and the nuclear reactions where the primary proton is lost in the interaction. However, there is a third type of interaction that

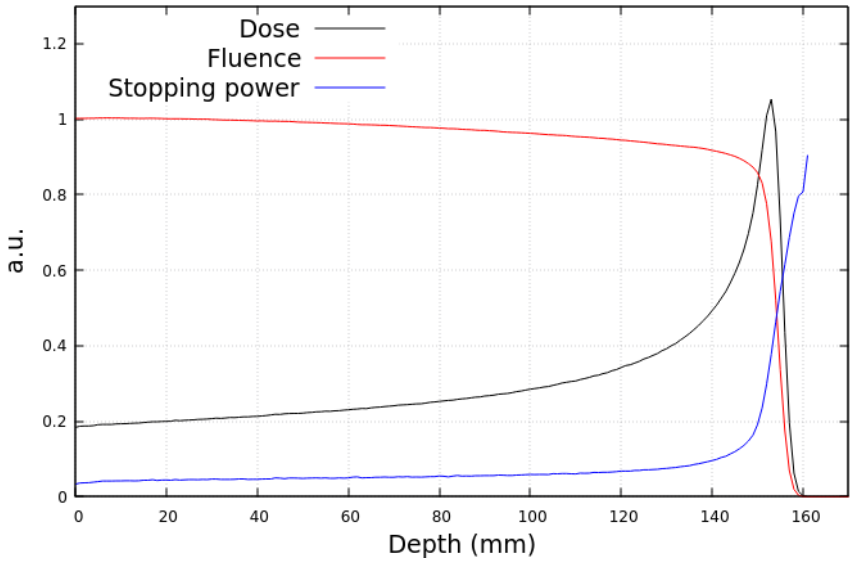

Figure 1.3: Dose (red), fluence (blue) and stopping power (green) profiles of a 150 MeV proton beam in water. Dose is the energy deposited per unit of volume, therefore, it depends on the deposited energy (ST) and the number of protons (fluence). Dose is the result of the convolution of these two magnitudes.

falls in between the other two, known as inelastic scattering. In this process, the primary proton interacts directly with a nucleus, transferring part of its energy to it. As a result, the nucleus ends up in an excited state, and the primary proton is ejected with less energy and at a larger angle. This excited nucleus then decays to the ground level, emitting prompt gamma rays.

Figure 1.3 shows the resulting dose as a combination of all of these interactions in function of the proton depth in a material. Fluence is plotted in red and it shows how the number of protons decreases with depth due to more protons have produced a nuclear reaction. The stopping power is plotted in blue and it shows how the transmission of energy to the medium remains almost constant during most part of the proton path, but just in the end of the proton range it increases exponentially due to speed reduction, among other things (Bethe formula 1.8). The combination of these two effects produces a deposited dose characterized by a flat region at the entrance of the protons, and a high dose peak at the end of the proton range known as Bragg peak (BP). This BP is the main property which makes protons a more suitable option for tumor irradiation in some scenarios.

1.1.3 Physics of decay

When high-energy protons pass through a material, they can induce the production of secondary radiation. This secondary radiation can be composed of various particles such as neutrons, photons, electrons, and positrons. The production of secondary radiation is due to the interaction of primary protons with the atomic nuclei of the material, resulting in the emission of particles. Understanding the production and decay of secondary radiation induced by protons is crucial in radiation therapy and other applications that require accurate prediction and control of deposited dose and its effects.

One of these applications is the verification of the proton range. Throughout this thesis, we will come back again and again to secondary radiation as the proton range verification is the main topic of this work. This topic will be explained in detail in section 1.3, but first, it is necessary to consider how and when the secondary radiation induced by the protons is emitted.

An isotope is considered radioactive when it is not stable and it transforms into a different isotope through a process of disintegration, in which ionizing particles are emitted [Knoll, 2011]. This process is stochastic at the level of single atoms and it is impossible to predict when a specific atom will decay. However, for a significant number of identical unstable atoms, the decay follows an exponential decay (equation 1.10) ruled by a decay constant λ.

$$A(t) = A_0 exp(-\lambda t) \tag{1.10}$$

This decay constant is specific of each decay and it is defined as $\lambda = log(2)/t_{1/2}$. The $t_{1/2}$ parameter is known as half-life and it indicates the required time for half of the isotopes of a set of identical unstable atoms to decay [Knoll, 2010]. This decay constant describes how quickly the decay process undergoes, or consequiently, how long the unstable atoms survive. There is a wide variation in the half-lives of radioactive atoms, from almost instantaneous with $t_{1/2}$ in the order of fento and picoseconds; to half-lifes close to the age of the universe.

The decay or disintegration process of a single atom implies a nuclear transmutation, in which the decaying nucleus (*parent nucleus*) transform into another one (*daughter nucleus*) with a different number of protons, neutrons or both. The physical processes that unstable nuclei follow to disintegrate are very different. For this reason, decays

are separated into subclasses depending on the physical process of disintegration they follow.

- **Alpha (α) decay:** an alpha decay takes place where the *parent nucleus* decays by emitting an alpha particle. An alpha particle is an Helium nuclei formed by two protons and two neutrons. Consequently, the *daughter nucleus* has two protons and neutrons less than the original. The excess of energy due to the decay is transferred to the alpha particle and the new nucleus in the form of kinetic energy.

- β^- **decay:** a β^- decay occurs in unstable isotopes with a high concentration of neutrons in the nucleus. An internal process transforms a neutron into a proton, and for conservation laws an electron and an antineutrino are ejected. The remaining isotope has the same atomic mass than the original one, but an atomic number one unit higher.

$$n \rightarrow p + e^- + \overline{\nu_e} \tag{1.11}$$

- β^+ **decay:** a β^+ decay is the contrary to the previous decay, it takes places in a nucleus rich in protons. In this case, protons converts into a neutron, and as a consequence, a positron and a neutrino are ejected out of the nucleus.

$$p \rightarrow n + e^+ + \nu_e \tag{1.12}$$

  Unlike electrons, positrons are unstable and annihilates as soon as they lose most of their kinetic energy. A positron at rest annihilates along a free electron in the medium, emitting two photons of 511 keV in opposite directions, due to conservation laws of energy and momentum. Isotopes that decay through this process are used in nuclear medicine in Positron emission tomography (PET). This technique makes use of the spatial correlations of the 511 keV photons emitted after a β^+ decay to estimate where the decays are produced.

- **Electron capture:** it is a process in which a proton-rich nucleus absorbs an inner atomic electron to change a proton for a neutron. The neutron remains in the nucleus and only a single neutrino is ejected. This process does not emit ionizing radiation.

$$e^- + p \rightarrow n + \nu_e \tag{1.13}$$

These are the most common decay process of radioactive isotopes. However, the mentioned ejected particles are not the only radiation emitting by these decays. The *daughter nucleus* usually results in an excited level which decay to the ground state emitting photons. The decay of these excited levels follows the same expression of equation 1.10 and they also have an associated half-life. The usual values of the half-lifes of these excited states are extremely short ($< fs$). In the previous section, it has been mentioned that protons can populate some of this excited levels due to inelastic scattering or nuclear reactions. The decay behavior of these states is the same regardless of how they are populated. Therefore, the decay will follow the exponential law with a half-life of the order of femtoseconds, which in terms of any real-life application, the emissions can be considered instantaneous. That is the reason why these emissions are also known as Prompt-Gamma when they are directly populated by an ionizing beam.

1.1.4 Cross-Section

Cross-section is the magnitude which indicates the probability that a specific process will take place when a certain kind of radiation (photons, protons, waves ...) interacts with matter [Knoll, 2011]. Cross-section is usually denoted as σ and it is expressed in units of area, specifically barns ($10^{-28}\ m^2$). Each reaction channel has an energy threshold, below which it is physically impossible for the reaction to occur. Above this threshold, the reaction can occur, and the probability of its occurrence as a function of the incident energy is given by the cross-section. Unlike the energy threshold, which can be theoretically calculated, the cross-section is challenging to predict with theoretical models, and as a result, specific experiments are required to determine it accurately.

Another magnitude related to cross-section is the yield production (Y). It expresses the probability that a single proton induces a certain reaction in a specific medium. As it is shown in the following formula, yield production depends on the atomic density of the material (ρ_{at}), the initial and the final proton energy, the reaction cross-section (σ) and the stopping power (dE/dx).

$$Y = \rho_{at} \int_{E_0}^{E_f} \sigma(E) \left(\frac{dE}{dx}\right)^{-1} dE \tag{1.14}$$

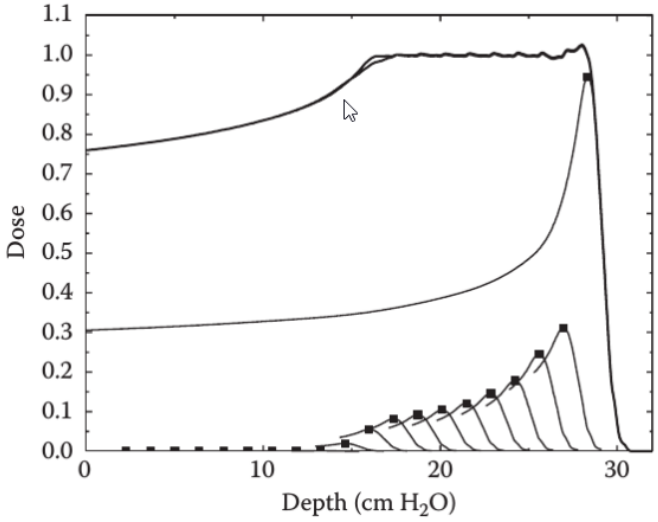

Figure 1.4: Spread out Bragg peak (SOBP) calculated as a superposition of several proton beams with different energy. The result is a flat dose over a region of more than 10 cm.

1.2 Proton therapy

Proton therapy is a radiotherapy technique that uses proton beams as external ionizing radiation to treat cancer [Mohan and Grosshans, 2017; Paganetti, 2011; Tian et al., 2017]. Its therapeutic potential was discovered in 1946 [Wilson, 1946], but it was not until 1954 at Berkley Radiation Laboratory that the first patient was treated. At that time, proton accelerators had several drawbacks, as for instance their price and their size. It took 36 years until 1990, when the first proton therapy facility began operating in a hospital, specifically at Loma Linda Hospital University Medical Center [Mohan and Grosshans, 2017].

1.2.1 Deposited dose

The remarkable surge in popularity of proton therapy can be attributed to the unique manner in which protons deposit their energy within patients. As previously discussed, the depth dose profiles of protons exhibit distinctive characteristics, including a low, relatively flat dose region at the entrance, a prominent dose peak at the end of their range (known as the Bragg peak), and negligible dose deposition beyond the proton range. This distinctive dose distribution enables the concentration of a significant portion of the deposited dose within a specific region. This breakthrough in radiotherapy represents a

significant advancement, as it allows for the escalation of radiation dose in tumor areas while concurrently minimizing the dose administered to healthy tissues.

However, the BP from a monoenergetic proton beam only spans a few millimeters, which is not enough to cover a tumor area. To solve this issue, several proton beams, whose Bragg peaks altogether generate a flat dose over the whole tumor region, are combined (see Figure 1.4). The combination of proton beams to obtain this benefit is known as *Spread out Bragg peak* (SOBP). As a consequence of the use of SOBP, the dose ratio between the Bragg Peak and the entrance decreases, but even so, the dose in the SOBP (which would cover the tumor area) is higher than in healthy tissues.

1.2.2 Advantages over traditional radiotherapy

Traditional radiotherapy uses photon and electron beams to treat cancer. In the case of photons, the deposited energy as a function of depth follows an exponential decay (equation 1.5), as it is shown with a dotted line in Figure 1.5 [Knoll, 2010; Paganetti, 2011]. Photons are a good choice to irradiate very deep tumors because of its high penetration capability, but as we are no able to irradiate with the maximum dose at a given depth, we need to use a lot of different beams whose superposition produces a hot spot of dose in the tumor area, at the expense of irradiating the surrounding healthy tissues [And, 1999].

Electrons are charge particles whose stopping power is defined by the Bethe formula (Eq. 1.8) [Knoll, 2010]. However, due to its very low mass, their dose profile does not show a high dose peak at the end of their range. On the contrary, the dose depth profile of electrons is characterized by a high dose peak at the entrance and a rapid fall after it [Kawachi, 1975; Paganetti, 2011]. Because of that, electrons are a good option to treat superficial tumors, but they can not be used for depth tumors due to its short range.

Proton therapy harnesses the advantages of both photons and electrons while mitigating their respective drawbacks. In Figure 1.5, the red line represents the Spread-Out Bragg Peak (SOBP) of a proton therapy treatment. The SOBP plays a pivotal role in irradiating the tumor area with a high dose while simultaneously minimizing the dose deposited in the surrounding healthy tissues. An essential advantage of proton therapy is that, unlike photons, there is no dose deposition beyond the proton range. This characteristic ensures that radiation is precisely confined to the target area, facilitating superior dose conformity in comparison to traditional techniques. As a result, reduced

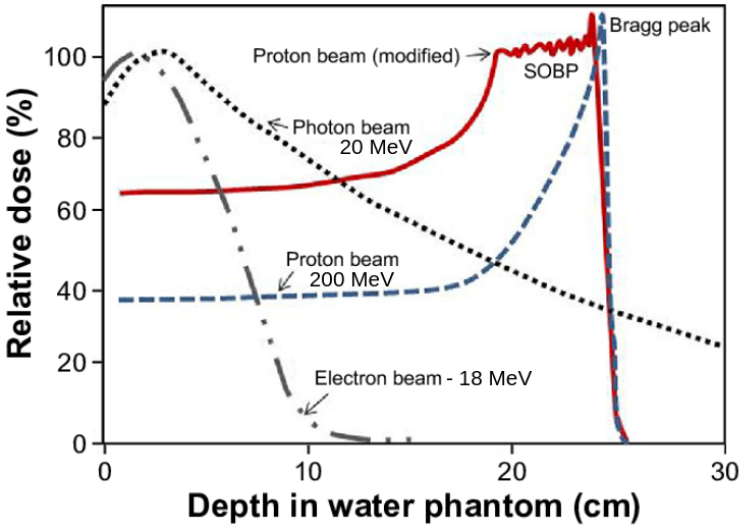

Figure 1.5: Dose profiles of photon (dotted line), electron (dotted-dashed line) and proton (dashed line) beams. Protons present a clear advantage over both techniques. They have a high penetration capability, but at the same time, its dose is lower at the surface. This allows to conform the dose better than in traditional techniques.

radiation doses are administered to healthy tissues, and certain radiation-sensitive organs can be effectively spared. This improved dose conformity translates to a better recovery outlook with a reduced likelihood of generating secondary effects, making proton therapy a superior alternative to traditional radiotherapy techniques [Paganetti, 2011].

1.2.3 Proton treatment plan optimization

Proton treatment plan optimization is a critical aspect of proton therapy that aims to deliver the highest radiation doses to the tumor while minimizing exposure of surrounding healthy tissues [McGowan et al., 2013; Langen and Zhu, 2018]. The process of proton treatment plan optimization involves several key considerations and steps to ensure that the treatment plan is tailored to the individual needs of each patient. One of the primary considerations is the determination of the Planning Target Volume (PTV) and Clinical Target Volume (CTV).

To determine the CTV, imaging techniques such as CT scans or MRI are used to obtain detailed images of the tumor and surrounding tissues. These images are then analyzed by the radiation oncologist and dosimetrist to determine the gross tumor volume

(GTV) which simply includes the visible tumor volume. However, the determination of the GTV is not an exact step. As a consequence, the total irradiation volume is expanded to include possible tumor spreads undetectable on medical imaging. This new expanded GTV is the Clinical target volume (CTV).

Range uncertainty is another important factor to consider in proton treatment plan optimization [Paganetti, 2012; Carabe et al., 2012]. Factors such as patient movement, patient positioning or anatomical modifications can introduce some level of uncertainty in the range of the proton beam, which may affect the accuracy of the treatment. Range uncertainties will be explained in detail in the next section, but for now, it is important to note that these uncertainties that may affect the delivered dose are addressed using a safety margin around the CTV. These safety margins depend on the individual patient, but are generally considered to be 3 mm plus 3% of the proton range, which can increase the CTV in all directions by 1.5 cm in the worst case [Paganetti, 2012]. The expanded CTV due to uncertainties is the PTV, which represents the volume of tissue that needs to be treated with the prescribed dose to achieve the desired treatment outcome. In radiotherapy, the fundamental assumption behind the PTV concept is that the shape of the dose distribution is largely unaltered by the underlying changes of the patient anatomy. However, in proton therapy this concept makes no sense as proton range deviations imply significant dose deviations in the irradiated region.

Another important consideration in proton treatment plan optimization is the identification of Organs at Risk (OARs) [McGowan et al., 2013]. OARs are organs that are close to the tumor and may receive some radiation dose during treatment. It is important to limit their exposure to radiation as much as possible to minimize the risk of side effects. The radiation oncologist and dosimetrist work to design a treatment plan that delivers the maximum radiation dose to the tumor while minimizing exposure to OARs.

Proton beam modulation is another key consideration in proton treatment plan optimization [Paganetti, 2011; McGowan et al., 2013]. Proton beams can be modulated in a variety of ways to shape the dose distribution and deliver the radiation to the tumor while sparing surrounding healthy tissues. Techniques such as Intensity-Modulated Proton Therapy (IMPT) and Pencil Beam Scanning (PBS) can be used to create a very precise dose distribution that conforms to the PTV, which takes into account all possible deviations from the plan.

Pencil Beam Scanning (PBS) is the most used technique to modulate the proton beam nowadays [Kooy et al., 2010]. In PBS, a narrow proton beam is scanned across the tumor in a pattern that matches its shape, with the beam turned on and off as it moves across the target area. This results in a highly precise dose distribution that conforms to the shape of the tumor. PBS is particularly useful for treating irregularly shaped tumors, as it can deliver a highly conformal dose while minimizing exposure to surrounding healthy tissues.

On the other hand, Intensity-Modulated Proton Therapy (IMPT) [Moreno et al., 2019] is an advanced form of proton therapy that uses multiple proton beams of varying intensities to deliver radiation to the tumor. IMPT optimizes the intensity of each proton beam to create a highly precise and conformal dose distribution within the target volume. It takes into account the varying tissue depths and densities, allowing for precise dose deposition while minimizing radiation exposure to healthy tissues. While PBS is a specific technique used for proton beam scanning, IMPT is a broader concept that encompasses various methods for intensity modulation in proton therapy, including PBS. IMPT can utilize pencil beam scanning or other techniques to achieve the desired dose distribution within the target volume. The implementation of PBS-IMPT is gaining importance and may become the main technique in the coming years [Vítek et al., 2021].

Robustness techniques play a crucial role in enhancing the reliability and effectiveness of treatment plans in proton therapy [Paganetti, 2011; Langen and Zhu, 2018]. As proton therapy involves the delivery of radiation with high precision, accounting for uncertainties and variations becomes imperative to ensure accurate dose deposition and minimize the risk of under- or over-irradiation. Robustness techniques aim to address these uncertainties by optimizing treatment plans that can withstand the potential challenges introduced by factors such as range uncertainties, organ motion, and patient setup errors. Two commonly used approaches in robustness optimization are worst-case robustness and probabilistic robustness.

- **Worst-case Robustness [Fredriksson and Bokrantz, 2014; Yang et al., 2019]**. This technique involves optimizing treatment plans by considering the worst-case scenarios of uncertainties, such as range uncertainties and organ motion. Safety margins are incorporated to account for these uncertainties, ensuring

adequate dose coverage of the target volume even under unfavorable conditions. Worst-case robustness aims to provide a plan that remains effective and reliable despite the presence of uncertainties.

- **Probabilistic Robustness [Teoh et al., 2017]**. Unlike worst-case robustness, probabilistic robustness incorporates statistical distributions of uncertainties into the treatment planning process. Instead of focusing solely on worst-case scenarios, this approach considers a range of possible outcomes based on probability distributions. Probabilistic robustness aims to optimize treatment plans that have a high likelihood of success across various possible scenarios, accounting for the inherent uncertainties in proton therapy.

1.2.4 Proton range uncertainties

Uncertainties in the proton range are a major challenge in proton therapy [Paganetti, 2012; Carabe et al., 2012]. Taking them into account in treatment planning involves the use of proton range uncertainties in the planning, to ensure the robustness of the plan in the face of possible deviations due to them [McGowan et al., 2013; Antolak and Rosen, 1999]. This is a step backwards in proton therapy since its main advantage is the compact conformation of the dose, and we cannot apply it to its full capacity because of these extra margins. On the contrary, it is necessary to irradiate healthy tissue around the tumor to ensure its total coverage, which implies a substantial increase in the possibility of generating side effects.

Dose uncertainties are not exclusive to protons. They are present in all radiotherapy techniques, but their impact is almost negligible in all of them except proton therapy [Knopf and Lomax, 2013].Figure 1.6 shows the impact of similar deviations in three different dose profiles: 1) single photon beam, 2) single proton beam and 3) SOBP. In the case of photons it can be noted that the deposited dose in the tumor region (red) almost does not vary from case to case, the tumor is covered equally in all cases and the dose beyond the tumor is identical. Therefore, photon dose uncertainty related to the same origins as range uncertainty in proton therapy does not imply a real impact in the delivered dose. This is the reason why the concept of PTV is not used in proton therapy. Unlike photon radiotherapy, where the irradiated Planning Target Volume

(PTV) is not significantly affected by anatomical changes, proton therapy is sensitive to such modifications, potentially resulting in substantially different deposited doses.

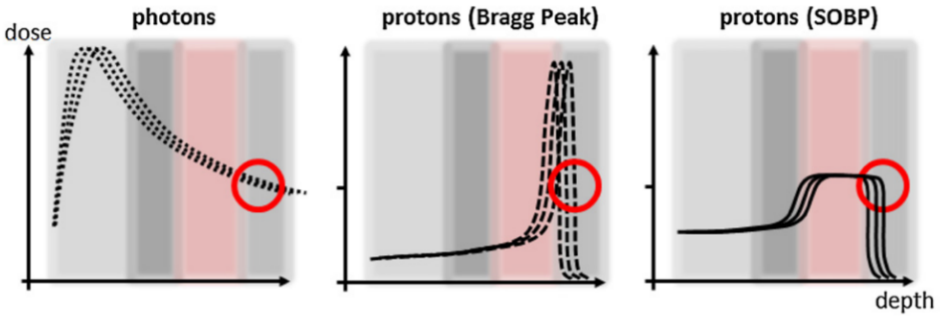

Figure 1.6: Representation of range issues in radiotherapy. On the left, the plot shows that dose deviations using photons are negligible. In the middle and in the right, it is shown that range deviations are critical in proton therapy.A deviation of just a few millimeters can imply the delivery of a significant part of the dose out of the tumor area and onto healthy tissues.

However, the situation changes drastically when protons are used. The dose profiles of a single proton beam show how a minimal deviation implies that the entire dose of the Bragg peak is deposited outside the tumor area. Applying the same to a real dose in a patient (SOBP), these deviations can lead to a general shift of the irradiated area, which implies an incomplete coverage of the tumor. Apart from this, deviations imply an overirradiation of the area posterior or anterior to the tumor, depending on whether the shift involves that the proton range increases or decreases. The solution to these problems is taken into account in robustness techniques, which use the potential range deviation to generate an irradiation plan which ensures the coverage of the CTV even in the worst-case scenario [McGowan et al., 2013; Langen and Zhu, 2018].

The selection of beam arrangements in proton therapy is also dictated by the need to minimize the impact of range uncertainties. An improved understanding of proton range could enable the use of more *adventurous* field directions that really take advantage of the steeper distal fall-off to shield critical organs, while reducing the healthy irradiated tissue. As shown in Figure 1.7, the above planning strategies for proton therapy can have different sensitivities towards range uncertainties, as illustrated by three possible plans for irradiating the same lung tumor next to the heart (OAR). Plan (a) represents the ideal scenario, where just one field is used for irradiation, resulting in minimal dose to healthy tissue but a high risk of irradiating the heart. Plan (b) closely resembles a

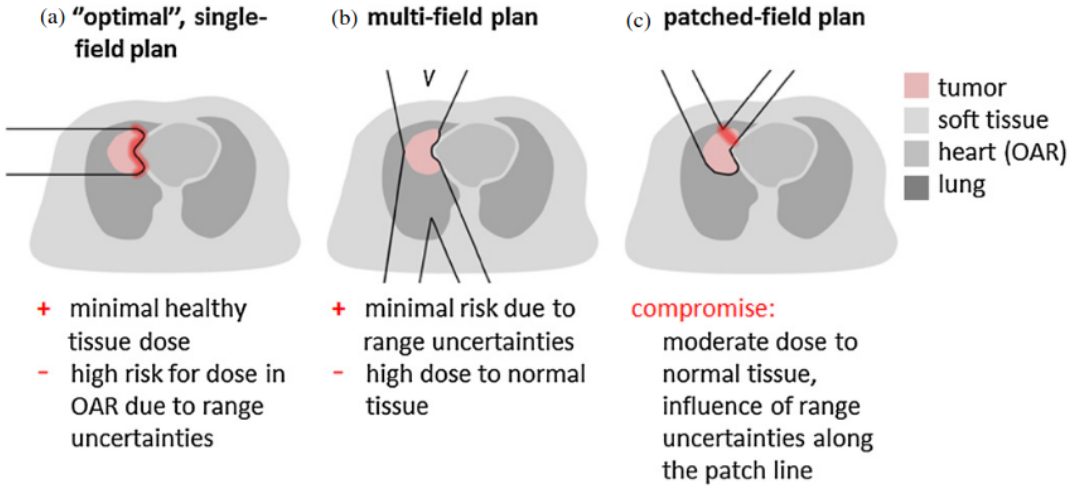

Figure 1.7: The potential impact of range uncertainties on proton therapy and the sensitivity of different planning strategies to these uncertainties [Knopf and Lomax, 2013].

real-life scenario, where three different fields are used to avoid irradiating the heart at the expense of irradiating much more healthy tissue. Plan (c) represents an intermediate approach, balancing the dose to healthy tissue with safety margins to OARs. Due to the uncertainties in proton planning, the second case is often chosen in practice to ensure tumour coverage and non-irradiation of the OAR, although it is known that the ideal plan is that of scenario (a).

Range uncertainties come from many different sources of error. In 2012, a study was carried out by Paganetti [2012], in which all the information available at the time on the different sources of uncertainty and their impact on planning was compiled. In this same work they also estimated the reduction of the uncertainties by simply implementing Monte Carlo simulation codes in planification. Nowadays, Monte Carlo methods are used clinically and within commercial treatment planning systems (such as RayStation). However, the proton range uncertanties using Monte Carlo methods are still quite important. The results of the work presented by Paganetti [2012] are shown in Table 1.1. The sources of range uncertainties are separated in two groups: 1) Those which are independent of dose calculation, such as the patient setup or the beam repeatability. 2) Those which are related to the dose calculation. The most relevant results in this table are the total uncertainties, which range from 2.7%+1.2 mm in the best case to 4.6%+1.2 mm in the worst. Considering that Monte Carlo simulators have

Source of range uncertainty in the patient	Range uncertainty without Monte Carlo	Range uncertainty with Monte Carlo
Independent of dose calculation		
Measurement uncertainty in water for commissioning	±0.3 mm	±0.3 mm
Compensator design	±0.2 mm	±0.2 mm
Beam reproducibility	±0.2 mm	±0.2 mm
Patient setup	±0.7 mm	±0.7 mm
Dose calculation		
Biology (always positive) ^	+~0.8%	+~0.8%
CT imaging and calibration	±0.5%[a]	±0.5%[a]
CT conversion to tissue (excluding I-values)	±0.5%[b]	±0.2%[g]
CT grid size	±0.3%[c]	±0.3%[c]
Mean excitation energy (I-values) in tissues	±1.5%[d]	±1.5%[d]
Range degradation; complex inhomogeneities	−0.7%[e]	±0.1%
Range degradation; local lateral inhomogeneities *	±2.5%[f]	±0.1%
Total (excluding *, ^)	2.7% + 1.2 mm	2.4% + 1.2 mm
Total (excluding ^)	4.6% + 1.2 mm	2.4% + 1.2 mm

Table 1.1: Estimated proton range uncertainties and their sources and the potential of Monte Carlo for reducing the uncertainty by Paganetti [2012]

not yet been implemented in planning, we can estimate the safety margins that are currently applied to CTV to be around 3.0% of the proton range plus 1.2 mm.

Much effort has been devoted since then to reduce these uncertainties as much as possible, but with one drawback, each of the items in Table 1.1 must be studied separately. There are studies that have tried to better calibrate the CT imaging for example [Bär et al., 2017; Wohlfahrt and Richter, 2020], or to improve the calculation of stopping power values in human patients [Zhengrong Liang et al., 2008; Poludniowski et al., 2015; Zhang et al., 2019; Medrano et al., 2022]. However, despite all the efforts, uncertainties in the proton range remain a serious concern nowadays.

There is a totally different approach to this problem, namely the use of range verification techniques [Verburg and Seco, 2014; Hueso-González et al., 2018; Zou et al., 2018]. These techniques make use of secondary photons that are induced by protons to estimate the dose that has been deposited in the patient. Implementing these techniques in proton therapy can significantly enhance treatment precision and safety. As a result, it may lead to reduced reliance on parameters employed in robustness techniques to mitigate proton range uncertainties. Moreover, it opens up the possibility of utilizing more innovative and sophisticated treatment fields, ultimately yielding improved treatment plans that offer greater benefits to the patient [Paganetti, 2011; Knopf

and Lomax, 2013; Zou et al., 2018]. By implementing real-time monitoring techniques, the reduction of safety margins can be effectively compensated for. These monitoring techniques provide continuous feedback on the location and deposition of the radiation dose in the patient, allowing any deviations from the irradiation plan to be immediately identified. The combination of online image guidance and adaptive plans enables the opportunity of using online adaptive planning in real-time during the irradiation.

The application of these techniques in the clinical setting would be a major breakthrough. Proton treatments would be much more precise and the amount of healthy tissue irradiated would be considerably reduced. The problem is that these techniques are relatively new and not fully developed. The work of this thesis focuses on the development of a series of tools and ideas with the aim of improving these techniques towards making their clinical use feasible. Before showing the work developed it is important to know and understand what these verification systems are and how they work.

1.3 Proton Range Verification Techniques

Proton range verification techniques attempt to estimate the proton range and the deposited dose using secondary emissions, in most cases, secondary radiation from proton nuclear reactions [MacKay, 2018; Paganetti, 2011]. Independently of the secondary emissions used for the verification, they all work in the same way. First, protons travel through the patient producing emissions that are measured with specific systems. After that, the measured data is analyzed and, in order to estimate proton range and dose, it is compared with the expected scenario based on MC simulations or similar approaches.

In this section, we discuss in detail the use of Positron Emission Tomography (PET) and Prompt-Gamma (PG) emissions for proton range verification. Both of them use secondary radiation from nuclear reactions. In the case of PET, we are interested in the β^+ isotopes which decay inside the patient, emitting two 511 keV photons. On the other hand, PG uses high energy photons emitted by excited nucleus as a result of a nuclear reaction or an inelastic scattering. These techniques are two of the most promising along with protoacoustic [Freijo et al., 2021], which instead of secondary radiation uses thermo-acoustic waves produced by protons depositing energy.

Proton range verification using PET and PG is the main topic of this thesis. Along this work, we will present different applications which would improve the implemen-

tation of these techniques in clinical scenarios. But firstly, it is important to properly introduce these proton range verification techniques in order to understand the motivation and the objective of the several research lines carried out in this thesis.

1.3.1 PET for range verification

Positron emission tomography is a very common tool for medical imaging in cancer diagnosis [Reske and Kotzerke, 2001; Almuhaideb et al., 2011]. The main physics principle that rules how it works is the decay of β^+ unstable isotopes, also known as PET isotopes. A β^+ isotope disintegrates by its own, emitting a positron (e^+). This e^+ annihilates along a free electron in the medium emitting two antiparallel 511 keV photons. A PET scanner detects these photons and PET image reconstruction methods are able to obtain the spatial distribution of these emissions, which is the same, where β^+ isotopes decay [Herraiz et al., 2006; Boellaard, 2009].

This technique can be used for proton range verification because protons produces β^+ isotopes in patients by nuclear reactions. Therefore, if we are able to perform a PET image of the irradiated area during or after the irradiation, it is possible to obtain the spatial distribution of the induced β^+ isotopes by protons. Once the PET image is done, the next step is to obtain the estimation of the proton range and the deposited dose from it. As we have mentioned in section 1.1.4, we are able to calculate the yield production of certain reactions knowing its reaction channels cross-sections. The yield formula (Eq. 1.14) relates the distribution of β^+ isotopes to the deposited dose, but it requires knowledge of the cross-sections of the reaction channels, which is the case for the most abundant reaction channel in natural tissue (Table 1.2) .One significant challenge in this step is the lack of an analytical solution for it. Although various methods have been proposed for estimating the dose and proton range from PET images, there is no absolute solution for this problem. In chapter 4, a detailed introduction to some of these methods is provided and we propose a new algorithm for estimating dose and proton range from PET images with submillimeter precision.

There is a very important property of the β^+ isotopes that must be studied carefully to perform the verification, the decay. It follows an exponential formula and it is ruled by the half-life ($t_{1/2}$), which indicates the time required for half of the atoms in a

Isotope	$T_{1/2}$ (min)	Reaction channel	Threshold energy (MeV)	CS integral <100 MeV (b·MeV)	References
^{11}C	20.364(20)	^{12}C(p,X)^{11}C	17.9	6.32	1, 2
		^{14}N(p,X)^{11}C	3.1	2.61	3
		^{16}O(p,X)^{11}C	23.6	1.26	3, 4
^{13}N	9.965(4)	^{14}N(p,X)^{13}N	8.9	1.88	5, 6
		^{16}O(p,X)^{13}N	5.5	0.65	3, 4
^{15}O	2.037(3)	^{16}O(p,X)^{15}O	14.3	5.44	4, 5, 7, 8

Table 1.2: Isotopes introduced in the MC simulation and subsequently used in the PET image reconstructions, along with their most representative properties. The half-life of the produced isotopes limits the usability of such isotopes for PET detection. The energy threshold and the cross-section (CS) integral value provide guidance of the dominance of each isotope next to the BP. References: 1)Measday [1966] 2)Whitehead and Foster [1958], 3)Takács et al. [2003], 4)Masuda et al. [2018], 5)Sajjad et al. [1985], 6) Hess et al. [2001], 7)Valentin [1965], 8)Akagi et al. [2013]

radioactive sample to decay. The decay formula is as follows,

$$A(t) = A_0 e^{-\lambda t} \qquad \lambda = \frac{t_{1/2}}{\log 2}, \tag{1.15}$$

where A_0 is the initial activity of a sample and λ is the decay constant. Looking at the properties of the PET isotopes produced in the human body in the Table 1.2, we observe they all have half-lifes of several minutes. Therefore, all of these isotopes are subject to the *wash-out* effect [Mizuno et al., 2003; Toramatsu et al., 2018, 2020]. It is a natural mechanism of the human body for which the isotopes generated are displaced from where they have been produced to other regions of the human body. The more time elapses, the greater the diffusion of PET isotopes generated by the protons. And therefore, the dose-activity relationship is much more complicated, since *wash-out* is not an easy effect to include in the simulations and induces very large errors.

Depending on the $t_{1/2}$ of the isotopes used for PET verification, the PET image can be obtained during or after the irradiation. Depending on when and where the spatial distributions of β^+isotopes is measured with a PET scan, we distinguish the following:

- **In-beam**

  In-beam PET verification is considered when the PET scan is placed somehow inside the treatment room, and it is possible to measure the PET activity during the irradiation without moving the patient [Knopf and Lomax, 2013]. This technique has an excellent advantage, we can measure the spatial distribution of the PET isotopes and verify proton range in real time during the irradiation. Furthermore, the *wash-out* effect impact is very low.

  However, there are several issues related to the high amount of secondary radiation, which do not come from β^+ isotopes that can saturate the detector. To accurately measure the secondary activity induced by the proton beam, it is necessary to develop sophisticated PET systems capable of detecting high rates of counts without malfunctioning. These systems must also be designed to be placed next to the proton beam to measure the secondary activity simultaneously with the irradiation. Another issue related to in-vivo PET verification is the low statistics due to the long half-life of the produced isotopes. During the first seconds after each beam delivery, only a few percentages of the total amount of produced isotopes decay, and a PET reconstruction algorithm needs a minimal number of detected 511 keV photons to obtain the spatial distribution with a decent quality.

- **In-room**

  In-room PET verification consist in measuring the PET isotope distribution in a patient just after the irradiation with a PET scanner in the same treatment room. The main advantages of this technique are that the patient maintains the position in which he/she was irradiated; and we can measure the β^+ emission for a long time, obtaining sufficient statistics for a good quality image, and therefore, a more accurate proton range estimation.

  Nevertheless, the disadvantages of this technique compared to *in-vivo* are significant. First, it is possible to verify the proton range, but after the irradiation. Deviations in proton range with respect to the plan can be identified, but we could not avoid them as the whole irradiation plan is already done. Secondly, measurements performed in a long period of time (several minutes) are subject to a high impact of the *wash-out* effect. The correlation between activity and dose becomes

more complicated, inducing errors and loosing accuracy in the estimations of dose and range.

- **After-irradiation**

  The third technique is similar to *in-room*, but instead of performing the PET image in the treatment room, the patient has to be moved to another room where the PET is placed. This technique has the same advantages as the previous one, and the disadvantages are also very similar, but the impact of the *wash-out* effect is even greater because more time elapses between the irradiation and the start of PET acquisition.

1.3.2 Prompt-Gamma for range verification

The use of Prompt-Gammas (PG) for proton range verification is one of the most promising techniques at the moment [Richter et al., 2016; Hueso-González et al., 2018; Draeger et al., 2018; Krimmer et al., 2018]. As it was already mentioned in section 1.1.2, PG are photons which are emitted as a consequence of the excitation of a nucleus in a nuclear reaction or an inelastic collision. Nucleus end in an excited level which decays with a half-life in the order of *fs*, which implies that the decay is instantaneous. This technique uses these PGs to verify proton range, similar to PET with β^+ isotopes.

Human body is mainly composed by oxygen and carbon, therefore, PGs produced in patients come mainly from the excitation of oxygen and carbon in inelastic collisions, and from excited nucleus as consequence of proton nuclear reactions. Emitted PGs from natural tissue have very high energy, between 2-7 MeV. And the two most abundance PG are the 4.4 and 6.1 MeV γ-lines which come from the first excited level of ^{12}C and ^{16}O respectively [Verburg et al., 2012], as an effect of inelastic interactions.

The use of PG for proton range verification have several advantages over all other verification techniques. The most important one is related with its instantaneous emissions. These emissions are produced only during the beam delivery and there is no residual activity after that. This allows for the measurement of induced PG by each beam separately, enabling the identification of its range without contamination from the secondary radiation of previous beams. Another advantage is that although the number of induced PGs is similar to that of β^+ isotopes, due to their very short $t_{1/2}$, PGs are emitted virtually instantaneously and can be measured in a very small fraction

of time. This implies that the lack of information and statistics is not a problem for this technique. All of this, make the use of PG a very promising technique for proton range verification. Its implementation in clinical settings would enable the identification of potential deviations in each planned beam independently and in real time during treatment. This advance would pave the way for real-time treatment plan adaptation [Albertini et al., 2020; Paganetti et al., 2021], offering the possibility to stop treatment in case of critical deviations.

However, this technique only started to be developed a few years ago [Verburg and Seco, 2014; Richter et al., 2016] and there are still some problems to be solved before it reaches its full potential [Krimmer et al., 2018]. The major challenge in PG verification systems is the high energy of the emitted γ. As the γ energy increases the efficiency for detecting them decreases. To increase the efficiency, PG verification systems often use large detectors. However, this means that current PG systems are large and difficult to implement in a proton facility.

At the moment, there are two different PG systems which have been tested in clinical scenarios [Hueso-González et al., 2018; Richter et al., 2016]. However, their set-ups and how they work are totally different from one another. We can consider them as two different techniques.

- **Promtp-gamma Imaging (PGI)**

  Prompt-Gamma Imaging measure the spatial distribution of PGs in the patient to verify proton range. A scheme of how it works is shown in Figure 1.8a. These techniques use what is known as a pinhole collimator. It consists of a piece of very dense metal that photons cannot trespass and a very narrow spot through which the PGs can travel unimpeded. This setup, as it is shown in Figure 1.8a, permits the correlation of every point of the detector with a certain position within the patient. A segmented detector measures how many photons have reached each point of the detector and a reconstruction algorithm estimates how many photons have been emitted along the proton path in the patient. The comparison between the measure data and the expected result determines the proton range [Richter et al., 2016].

- **Prompt-gamma spectroscopy (PGS)**

Prompt-gamma spectroscopy uses the PG spectral distribution to estimate the proton range [Hueso-González et al., 2018]. They use a collimator placed between the patient and the detector. It is formed by two big blocks of tungsten separated by few centimeters in such a way that only photons from certain regions reach the detector. These regions are always the Bragg peak area and a few centimeters from the flat dose of the protons (see Figure 1.8b). The role of this collimator is to reduce the total amount of secondary radiation that reaches the detector and to ensure that the secondary radiation comes from the Bragg peak area. Large detectors with high photon detection efficiency are placed behind the collimator. These detectors must be large enough to ensure the measurement of high energy photons to obtain the PG energy distribution of each proton beam. Similar to PGI, the measure spectral distribution is compared with the expected one to estimate the proton range.

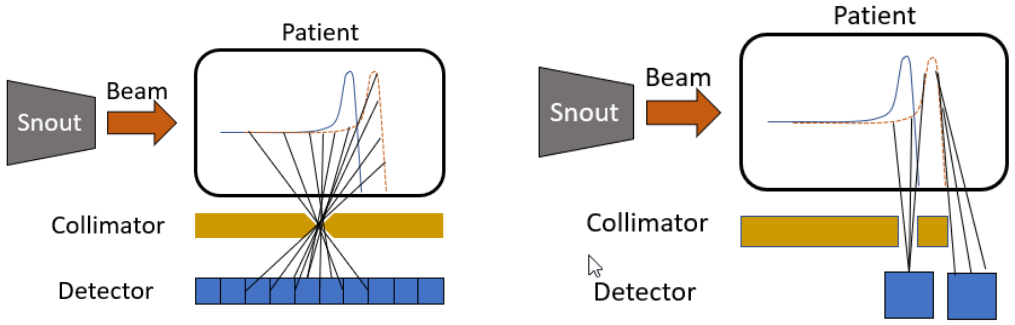

(a) Prompt-gamma imaging (PGI) **(b)** Prompt-Gamma spectroscopy (PGS)

Figure 1.8: Prompt-Gamma spectroscopy (PGS) and Prompt-Gamma imaging (PGI) schemes.

1.4 Radiation Detection

Ionizing radiation can be detected using special set-ups specifically developed for this purpose. These installations are generally formed by three components: 1) The detector in charge of stopping and measuring the ionizing radiation. 2) The component which converts the signal produced in the detector into an electrical pulse. 3) An acquisition system, capable of collecting, analyzing and storing all the pulses in the computer.

These kinds of set-ups are very common in cross-section measurements where it is important to detect as much ionizing radiation (photons, electrons, neutrons ...) as possible. In chapter 3 several cross-sections reaction channels have been studied. A set-up based in the previously mentioned configuration was developed to carry out the experiments. In this section, the basics of the three components of an usual radiation detection set-up are explained, with particular attention to the systems used in this thesis.

1.4.1 Inorganic Scintillator Detectors

Inorganic scintillators are used as detectors because they are able to transform ionizing radiation into a certain quantity of photons in the visible spectrum, proportional to the deposited energy by the incident particle. Atoms from an inorganic scintillator are excited when ionizing radiation interacts with them. As a consequence, the material scintillates, re-emitte radiation in the form of light. These photons are totally invisible to the detector because they do not have enough energy to excite any electron in the medium [Knoll, 2010]. Therefore, they will escape the detector, making it possible to collect them. The number of collected visible photons is proportional to the energy deposited in the detector. The main characteristics which define a detector are the followings.

- **Photon Yield:** this property indicates how many photons are produced in the crystal per unit of deposited energy by the incident ionizing radiation. A large photon yield implies smaller statistical errors in the determination of the exact value of the deposited energy.

- **Spectra Range Emission:** it defines the energy of the emitted photons and it is important when choosing the detector for an specific experiment. For example, in our case, if PMTs are to be used, these photons must be emitted in the visible range of light.

- **Decay Constant:** a single incident particle excites atomic levels. The de-excitation of all these states occurs through an exponential decay process ruled by a decay constant characteristic of each material (similar to nuclear decays explained in section 1.1.3). Because of this, the emitting photons are distributed in

time generating a pulse. The shortest the decay constant, the less probable that two pulses overlap. The effect produced by the superposition of several pulses, due to the arrival of two or more particles in less time than the decay constant is named pile-up. Figure 1.9 shows the typical shape of pulses generated by any type of particle along with an example of pile-up where two pulses are overlapped. Processing pile-up events is much more complicated than a single pulse and they are usually discarded. This is the reason whyshort decay constants lead into a better time resolution and reduce the loss of events due to pile-up.

- **Z Effective:** an important property of detectors is their efficiency to stop and detect radiation. In the case of γ rays, crystals with a high effective Z number are sought because the probability of a photon depositing all its energy increases with the Z of the material.

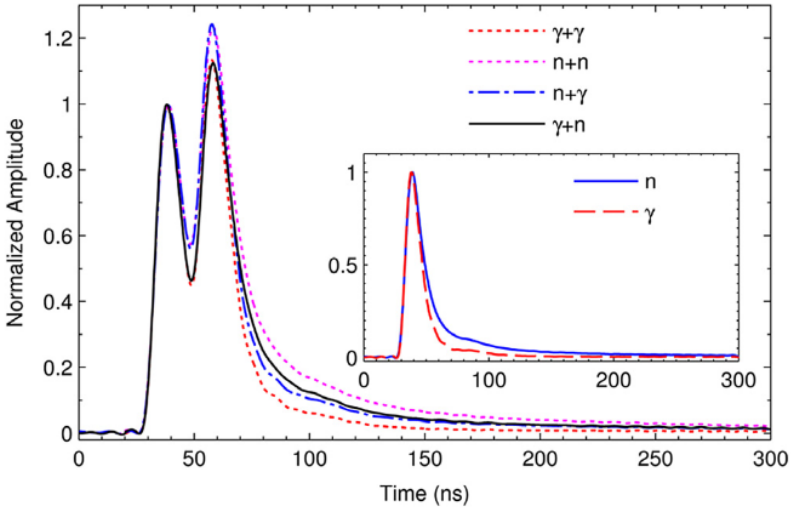

Figure 1.9: Shape of single and pill-up pulse events produced by the interaction of γ and neutrons emissions in a scintillator detector ($LaBr_3$ [Luo et al., 2018].

1.4.2 Light Collection System - Photo Multiplier Tubes

The light produced by the detectors must be collected and transformed into an electrical pulse so that an acquisition system can analyze it. The device in charge of converting the light into an electric signal is a photodetector, which generates an electric pulse whose charge is proportional to the number of incident photons. Considering that the

number of photons is proportional to the deposited energy, the pulse charge will also be proportional to the deposited energy. The two most common photodetectors are the photo multiplier tubes (PMT) and the silicon photomultiplier (SiPM). In this work, we focus on PMTs because they are the photodetector implemented in every set-up of chapter 3.

A PMT consists in a vacuum tube that converts the incident light into an electric signal [Knoll, 2010; Luo et al., 2018; Jagtap et al., 2019]. A PMT is structured in different parts, each one with an specific function. At one end of the tube where photons arrive, a photosensitive material (photocathode) is placed, which converts inci- dent photons into single electrons through the photoelectric effect. The tube is a vacuum chamber in which a high voltage is applied between both extremes, accelerating the electrons produced by the photocathode. Additionally, there are several metal plates (dynodes) along the tube which generate a cascade of electrons each time that an accelerated electron collide with it. At the beginning there is only an electron per each visible photon. But after several collisions with the dynodes, these few electrons are converted into an electric signal. In the final stage of this reaction, the charge is collected in the anode at the end of the tube providing an electric signal which is proportional to the deposited energy in the detector.

1.4.3 Acquisition system

The acquisition system is in charge of collecting and analyzing the electric signal. In this process, they convert these signals into numerical values that can be related to energy and stored in certain devices. There are two kinds of acquisition systems: the analog and the digital pulse processing. The analog method uses several devices to amplify the signal, modify its shape or apply any property to it. The second, which is the one used in this work, uses a single device which is able to process the signal by itself. This technique is known as digital acquisition system (DaQ) and was implemented in all the experiments of this work to obtain the time and energy of each pulse, with an accuracy of nanoseconds and eV respectively.

1.5 Monte Carlo methods

Monte Carlo (MC) methods involve any computational algorithm which is based in the random sample of a certain process to obtain numerical results [Kalos and Whitlock, 2008]. Although the random character of these algorithms, the MC can be applied to mathematical or physical deterministic processes, especially if their solution is very complex or even impossible to obtain with any other approach.

In physics, the use of MC methods is widely spread and they are implemented in almost every field. In this thesis, we will focus on MC methods applied to particle transportation. Every process in the particle transportation is stochastic. That means that the next step of the particle can not be predicted exactly, but it is possible to determine the probability of each of the interactions that can take place. Therefore, if the probability distributions of every interaction is well-known, we can use random sampling methods to calculate a possible solution for a single history or event. The simulation of many primary histories (using different seeds for the random number generation) produces as many different solutions as initial particles are simulated. The final result is the combination of all of these solutions, which leads into a reliable average value. This result has an assocaited standard deviation associated, which depends on the initial number of histories, the greater the number of events, the smaller the deviation [Reynaert et al., 2006].

Particle transportation Monte Carlo methods track each individual and initial particle as an independent event through the region of interest that has been previously defined. The solution induced by each event is stored, and the final solution is given as a combination of every individual result (average, sum, etc.). Along the tracking, the particle interacts in the medium it is traveling through. Using the interaction probability distributions and a random number generator, the MC calculates the distance that the particle travels before interacting (step-lenght) and the particle is propagated to this new position. After that, the method determines which interaction takes place based on their probabilities. This process is repeated over and over again with the remaining particle, the secondary particle if it is generated, or both [Reynaert et al., 2006]. This cycle ends when there is no remaining energy in any of the particles generated through the track, or the particles escapes from the region of interest.

There are a lot of new terms associated to a Monte Carlo method, (mentioned in the previous paragraph) which are the same regardless of the application field, and they must be explained in detail for a better understanding of this work.

- **Probability distribution functions:** they contain all the information related to the processes that appear in the simulation. In the specific cases of particle transportation, they must contain information of every physical process in the form of physics and mathematical models.
- **Random number generator:** the basis of a MC is its random character. A tool to generate random number uniformly distributed in the [0,1) interval is crucial for these methods [James and Moneta, 2020].
- **Sampling methods:** the sampling method is a tool able to transform a random number into a variable of the probability functions. A random number is not useful by itself. It needs to be implemented in such a way that its value represents a variable that can be used by the physical or mathematical probability distribution functions model. In the case of particle propagation, the sampling method is in charge of deciding which interaction takes place whitin all the possibilities [Reynaert et al., 2006].
- **Scoring methods:** they store the information of variables that impact the final result. For example, if we were interested in the energy of the photons that reach a certain detector, it would store information on the energy of those photons.
- **Error estimation:** it is important to determine the error and the accuracy of the results provided by the scoring methods. This error depends on the number of simulated events, and it is usually given by the standard deviation [Reynaert et al., 2006].

Another important part of Monte Carlo methods is their optimization. These algorithms are usually very slow and they need a lot of computational time to provide results with acceptable errors. Because of that, there are two additional concepts related to the optimization of these methods that are explained in the following points.

- **Variance reduction techniques:** methods which are implemented in MC simulators to increase their efficiency [García-Pareja et al., 2021].

- **Parallelization techniques:** the parallelization of the program is implemented to accelerate the simulations, and it can be applied if each event is independent of the others. The greater the number of events that can be simulated at the same time, the greater the reduction in computational time.

A new Monte Carlo for high-energy photon transportation is proposed in chapter 6. In this chapter, a full detailed explanation of this code is presented, explaining most of the implementations of the previous concepts.

In several parts of this thesis, different Monte Carlo simulators will be used for various purposes. For example, in chapter 4 TOPAS will be used for the calculation of deposited dose and activation of proton beams. In chapter 6 Penmain will be used for the validation of the proposed MC. At this point, we introduce both mentioned MC simulators for a better understanding of future sections.

1.5.1 TOPAS

TOol for PArticle Simulation (TOPAS) [Perl et al., 2012; Faddegon et al., 2020] is a particle transport Monte Carlo tool based on Geant4 [Agostinelli et al., 2003] specialized and developed for particle therapy physics. This MC is able to implement several physics models to adapt to certain situations, but its main goal is to transport particles in the standard electromagnetic model. This model covers the energy range from 0 to 1 GeV for most of the particles. However, TOPAS was specifically developed for medical physics. The ideal energy range in the case of hadrons is from 0 to 300 MeV, and for photons and electrons the ideal case should not exceed 10 MeV.

In this thesis, proton-induced activation plays a crucial role, and it is important to have a tool that can accurately calculate it TOPAS does not include activation scorers by default, but it permits including additional scorers developed by the user. In our case, specific TOPAS scorers were developed for the calculation of β^+ activations map during the simulation. These scorer is based on the yield formula [Krasnov, 1974], adapted to a MC code (1.16) [España et al., 2021]:

$$Y(\overline{\mathrm{E}}) = \rho_{at}\sigma(\overline{\mathrm{E}})dx \tag{1.16}$$

where σ is the cross-section, ρ_{at} is the atomic density, dx is the step-length of the particle and $\overline{\mathrm{E}}$ is the mean energy of the particle at each step of the path. This ex-

pression calculates the yield production of a specific isotope in every proton step in the simulation. The accumulation of these probabilities in voxels generates the volumetric activation distribution. This method provides results with significant statistics using much lower number of initial protons than in conventional simulations, which reduces considerably the computational time.

1.5.2 Penmain

Penmain is a Monte Carlo (MC) simulator for electron-photon transport in complex material structures. It is based on PENELOPE [Salvat, 2013] and it uses the PENGEOM to describe the geometry of the simulation. Although it implements PENELOPE, it only uses some of the routines and database that it provides to optimize the simulation. The input is very simple, it permits to define the source, the geometry, the material composition of the objects in the geometry and the scorers. There are only two available scorers, the spectra of the particles which incise external faces of a certain body and the spectra of the energy deposited in a body. All this makes this program very efficient for studying the response of certain detectors to ionizing particles in complex scenarios..

1.6 Graphics Processing Units (GPU)

A graphics processing units (GPU) is a complementary part of a computer which was originally developed for memory manipulation to accelerate different computational processes, such as the creation of images and their display on monitors. The GPU was developed in view of the impossibility of increasing the number of threads and cores of CPUs in the '80s' [Pratx and Xing, 2011]. Several companies in the computer industry demanded more computational power for high parallel task which could not be solved efficiently with CPUs of the time. This situation boosted the graphic industry to develop in 1990 a new specialized electronic circuit (named graphics processing units) capable of carrying out thousands of process at the same time [Fatica and Ruetsch, 2014]. As the name suggests, GPUs were initially developed for processing graphics in a computer. However, their properties were also attractive for other sectors, which led to the development of application program interfaces (API) such as NVIDIA CUDA [NVIDIA et al., 2020] or OpenCL. These APIs made it possible to develop programs that can run on GPUs, which enabled highly parallelization-intensive work to be carried

out. The parallelization implies a huge acceleration of previous codes and algorithms, which make programs faster and more efficiently.

Both the medical physic sector and Academia implemented the GPU programming early, and since then it has only gained popularity. However, it has been in recent years that its development has taken a great leap forward, thanks to advances in the computing power of GPUs. The implementation of GPU has led to faster medical workflows and more accurate results, thanks to the acceleration of the codes and its substantial computational speed [Després and Jia, 2017]. All these benefits have made GPUs suitable for new codes and algorithms to be implemented on them, whenever convenient. The GPU programming has been applied in many different fields of the medical physics, such as dose planning [Pratx and Xing, 2011; Aland et al., 2019], image reconstruction [Pratx et al., 2009; Després and Jia, 2017; Onecha et al., 2022] and particle MC simulations [Badal and Badano, 2009; Ibáñez et al., 2021; Lee et al., 2022].

The implementation of particle track Monte Carlo codes on GPU is highly advantageous. As discussed in the previous sections of this chapter, Monte Carlo codes for particle transportation simulate each initial event independently of one another. This implies that it would be possible to simulate many events at the same time without compromising the final result. This is exactly what a GPU does, parallelize the computational effort into many different and simultaneous events. GPU implementation of particle-tracking MC code can result in execution time increases by a factor of 1000 over the same code on CPUs [Ibáñez et al., 2021]. The same is applicable to image reconstruction algorithms, in which an independent computational process associated to each pixel of the image must be performed. The parallelization of these computations increases program speed execution when implemented on GPU [Galve et al., 2019a; Onecha et al., 2022].

The GPU programming has an important role in this thesis. Two different codes have been developed based on parallel computing acceleration with GPUs. Both have been implemented in two different languages for GPU programming, CUDA Fortran [Fatica and Ruetsch, 2014] and CUDA C [Sanders and Kandrot, 2010]. The frist one is a GPU code for proton dose image reconstruction from medical images is proposed in chapter 4. The second, is the GPU MC simulator for high-energy photons (Prompt-gammas) and is also presented in chapter 6.

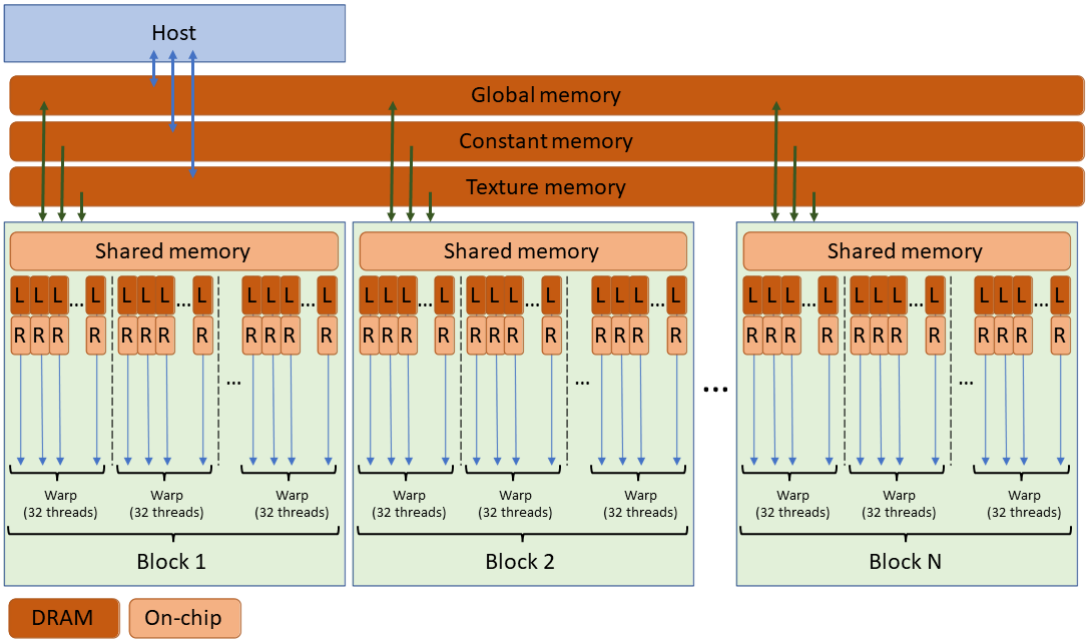

Figure 1.10: Scheme of the NVIDIA GPU architecture.

1.6.1 CUDA GPU Arquitecture

CUDA is an hybrid programming model that connects the central process unit (CPU) with the graphic process unit (GPU), in such a way that the CPU is able to call GPU kernels to carry out certain taks [NVIDIA et al., 2020; Fatica and Ruetsch, 2014; Sanders and Kandrot, 2010]. This connection between CPU and GPU is based on the CUDA architecture from NVIDIA, which separates in different memory access levels all the information that threads from GPU needs to perform the required processes. The scheme of this architecture is shown in Figure 1.10. Generally, in CUDA architecture the CPU is known as Host and everything inside the GPU is referred to as Device. Host and device are connected between them, but they are two different processes and memory units. The host works as usual and it is in charge of filling the device memory (global, constant and texture memories). In the device, thousands of threads work at the same time and routine but in different memory locations.

An important concept in GPU programming is the term coalescence. This concept is related to the fact that although each GPU thread works in a different memory location, there is a possibility that at certain point of the whole program, two or more

threads try to modify the same memory direction at the same time, which may lead into erroneous results. The optimal performance of a GPU program would be that each thread works over a certain chunk of memory that no other thread uses. This is what is understood as coalescence, and although in some cases it is impossible to achieve, we always have to look for the most optimal way to make this happen. In the case that two or more threads try to modify the same memory location atomic operations must be implemented. These are usual operations, such as additions or subtractions, which are queued by the GPU so that one operation carried out by a specific thread is not performed until the previous thread finishes its operation. This solves the problem that a bad coalescence may induce because two or more threads can not modify the same memory at the same time, but it loses the essence of parallelization since threads are queued and do not act at the same time. These operations must be avoided unless there is no other option.

When programming in GPU, there are several considerations related to the CUDA architecture and how host and device communicates, that must be taken into account to reach the most optimal version of the code. Threads are grouped in blocks and, in turn, these are grouped in grids. Therefore, each thread can be identified as its block (i) and grid (j) indexes. Furthermore, inside each block threads are organized in groups of 32 threads (warps). The main property of warps is that every thread of the same warp work in single-instruction multiple thread (SIMT) model. This indicates that a warp's threads carry out the instructions in lockstep.

The second important consideration when programming in GPU is related to the memory levels and how fast threads can read information from them. First, memory is divided in dynamic random-access memory (DRAM) and on-chip memory. DRAM is the general memory of the device which can be accessed by the host and the device itself. It is the contrary of on-chip memory because DRAM is physically separated from the thread processor chip.

The DRAM is also divided in 4 different memory levels.

- **Global memory:** the global memory is the most general level and can be read and written by both the device and the host. It is the largest memory space, but at the same, the slowest to read.

- **Constant and texture memory:** in the next level, the constant and the texture memory can be read and written by the host, but they can only be read by the device. Although its space memory is much smaller than global memory, but it can be read much faster. These memory accesses are usually reserved for large amount of data which are repeatedly read during the code.

- **Local memory:** is a memory space in the global memory reserved for each thread specifically, and noth accessible by any other thread. The local memory is reserved only during the lifetime of the thread. Once the thread ends, its process this memory is released.

The second kind of memory in CUDA architecture is the on-chip memory. At the contrary of DRAM, it is physically located in the GPU multiprocessor chips, which makes it much faster to read by threads. However, its main limitation is that the available memory space for it is very limited. This memory can be divided in two different access levels.

- **Shared memory:** it is the block's private memory which can only be accessed by the threads in that block. The access to this memory is very fast for threads and it is usually used for thread communication.

- **Registers:** registers are private spaces of chips' memory,reserved for each thread. They speed up the reading of the local memory because they store the data and avoid repeating the same memory reading several times. If there are more local memory than registers, some of the latter, which will not be used in a while, are spilled to local memory, in order to make room for other variables that will be used more frequently in that part of the program.

Chapter 2

From Theory to Practice: Testing New Contrast Agents for Imaging Purposes

A contrast agent is any kind of substance or molecule that is introduced into a patient prior to the performance of medical imaging with the aim of improving its quality. The use of contrast agents is widely implemented in different imaging techniques such as MRI or CT, where gadolinium and iodine, respectively, are used as contrast agents to substantially enhance results [Hao et al., 2012; Strijkers et al., 2008], or in ultrasound imaging, where metallic spheres can be introduced in the human body to amplify sound waves [Versluis et al., 2020; Frinking et al., 2020]. Furthermore, the use of external radioactive isotopes is very common in PET imaging, β^+ isotopes, leading to 511-keV gamma photons, are needed to perform the images. These isotopes are not found naturally in human tissues and they must be introduced in the patient [Reske and Kotzerke, 2001]. In short, the introduction of substances into the human body to improve the quality of medical outcomes is common practice in clinical imagining methods.

Although the idea of using contrast agents in medicine is not new, its implementation in proton therapy is almost non existing. Different ideas on how to implement contrast agents in proton therapy have been proposed in the last few years [Fraile et al., 2016; Cho et al., 2016; España et al., 2022], but no practical solution has been reached yet. In this chapter, we present a proposal for utilizing specific isotopes as contrast agents in proton therapy. It is important to note that the contrast agent should not be mistaken

for the isotope itself, but rather the molecule or nanoparticle that encapsulates the isotope. The primary objective of the contrast agent is to serve as a marker, indicating the precise location of protons within the body. By incorporating such contrast agents, proton therapy can achieve enhanced accuracy and precision in delivering radiation to the tumor site, while concurrently minimizing radiation exposure to healthy tissues.

The isotopes proposed as potential new contrast agents aim to improve the accuracy of proton range estimation by PET or PG techniques. In order to define the most effective approach for improving these techniques, it is necessary to first understand their underlying principles and limitations. The opening section of this chapter provides a summary of the limitations associated with PET techniques for range verification, and outlines the key features that potential contrast agents should possess to address these limitations. The second section of this chapter provides a detailed discussion on PG verification techniques, highlighting their shortcomings and major drawbacks. Furthermore, potential solutions to address them are also presented using contrast agents. Finally, a candidate contrast agent suitable for PG techniques is proposed.

In the last section of this chapter, we present the first experimental proof of concept for contrast agents in proton therapy [España et al., 2021]. We describe the design and synthesis of the experiment carried out to test a novel contrast agent, water-18, and show that it can successfully enhance the contrast of tumor tissues in proton therapy. This groundbreaking proof of concept for contrast agents in proton therapy not only represents a significant advance in the field, but also provides strong support and justification for the work carried out throughout this thesis. The successful development and testing of this novel approach paves the way for further research into the use of contrast agents in proton therapy and opens up new possibilities for improving treatment outcomes for cancer patients. This proof of concept represents a significant step forward in the development of contrast agents for proton therapy and opens up new possibilities for improving the accuracy and effectiveness of this important cancer treatment.

Overall, this chapter offers a comprehensive analysis of the utilization of contrast agents in proton therapy, specifically for range verification purposes. The primary focus is to underscore the potential advantages of incorporating contrast agents in enhancing treatment accuracy and optimizing treatment outcomes. By exploring the implementation of contrast agents, this chapter provides valuable insights into the potential benefits and implications of this approach in the context of proton therapy.

2.1 Contrast agents in PET proton range verification

Positron emission tomography (PET) can be used for proton range verification as it was explained in the Introduction (section 1.3.1). We can use the emissions from β^+ isotopes induced by protons to acquire a PET image of the spatial distribution of the activity inside the patient. Analyzing these spatial distributions we can estimate proton range and deposited dose. However, certain limitations can complicate the analysis, and to overcome these limitations, the use of contrast agents is proposed.

Isotope	$T_{1/2}$ (min)	Reaction channel	Threshold energy (MeV)	CS integral <100 MeV (b·MeV)	References
^{11}C	20.364(20)	^{12}C(p,X)^{11}C	17.9	6.32	1, 2
		^{14}N(p,X)^{11}C	3.1	2.61	3
		^{16}O(p,X)^{11}C	23.6	1.26	3, 4
^{13}N	9.965(4)	^{14}N(p,X)^{13}N	8.9	1.88	5, 6
		^{16}O(p,X)^{13}N	5.5	0.65	3, 4
^{15}O	2.037(3)	^{16}O(p,X)^{15}O	14.3	5.44	4, 5, 7, 8

Table 2.1: β^+ isotopes induced in natural tissues when irradiated with protons, along with their most representative properties. The half-life of the produced isotopes limits the usability of such isotopes for PET detection. The energy threshold and the cross section (CS) integral value provide guidance of the prevalence of each isotope next to the Bragg Peak. References: 1) Measday [1966] 2) Whitehead and Foster [1958], 3) Takács et al. [2003], 4) Masuda et al. [2018], 5) Sajjad et al. [1985], 6) Hess et al. [2001], 7) Valentin [1965], 8) Akagi et al. [2013]

- **Isotope half-life ($T_{1/2}$).** Depending on the time when the PET image is performed, we need to use β^+ isotopes with a shorter or larger $t_{1/2}$. An ideal scenario for in-beam PET verification would be to use isotopes with very short half-lives (less than a second) to measure the majority of decays that occur between the delivery of two consecutive beams of the plan. On the other hand, for post irradiation techniques it is necessary the use of isotopes with longer half-lives (several minutes), which still produce emissions after the treatment has been done, at the expense of lower emission rates. The problem is that the human body is mainly composed by oxygen and carbon. Therefore, we have to use PET isotopes that come from the interaction of protons with them. The isotopes naturally produced

in greater abundance in a human body during a proton therapy treatment are shown in Table 2.1, with some of their main properties. We underline that all of them have long half-lives, which make them suitable for postirradiation techniques, but do not facilitate in-beam verification.

- ***Wash-out* effect.** It refers to the diffusion of the induced PET isotopes due to natural mechanisms. It implies that in the time between their production and their decay, β^+ isotopes move inside the patient to other parts within the body. Some isotopes remain localized in the place where they are produced, while others may migrate short distances of a few millimeters or a few centimeters, and in some cases, even move to other organs. It should also be noted that the longer the time elapsed since irradiation, the greater the diffusion. Therefore, natural isotopes produced in human body are prone to diffusion since they can remain in the human body for several minutes without decaying. Ideally, the best options to solve the *wash-out* issues would be the use of isotopes with a very short half-life, because they do not have time to move before decaying, or otherwise the use of β^+ isotopes that do not suffer from this effect.

- **Spatial correlation between induced PET activity and deposited dose.** The spatial distribution of β^+ isotopes produced by proton beams is driven by the yield (Eq. 1.14). If we know the cross section of a certain reaction channel and the energy loss in the media, we can obtain the spatial distribution of the produced isotopes. Looking at the energy threshold of the main reactions induced by protons in living tissue (Table 2.1) we observe that the only reaction that produces β^+ isotopes below 10 MeV is $^{16}O(p,X)^{13}N$. The rest of the reaction channels open up above 15 MeV, and they are dominant in the region between 30-60 MeV. This implies that most of the activity is far from the Bragg Peak (BP), being almost negligible under it. To illustrate this effect we show in Figure 2.1 the 1D spatial distribution of PET isotopes produced in a material similar to human tissue when it is irradiated with a 120-MeV proton beam. The bottom X-axis indicates proton beam depth in the irradiated volume and the upper X-axis the remaining beam energy at the correspondent depth. Most of the produced β^+ isotopes are concentrated at energies higher than 20 MeV, which corresponds to a distance of more than 1 cm less than the proton range. This is the reason why

there is a lack of activity just under the BP, which complicates the estimation of the proton range. Currently, PET proton range verification techniques use ^{15}O and ^{11}C activity to estimate proton range and the last centimeter of dose is extrapolated from the activity along the proton path. Therefore, there is no direct spatial correlation between activity induced on natural tissue and the deposited dose. These techniques are in principle reliable, but they are totally blind to any patient modification in the BP region, since they provide no direct information of the activity in order to identify it.

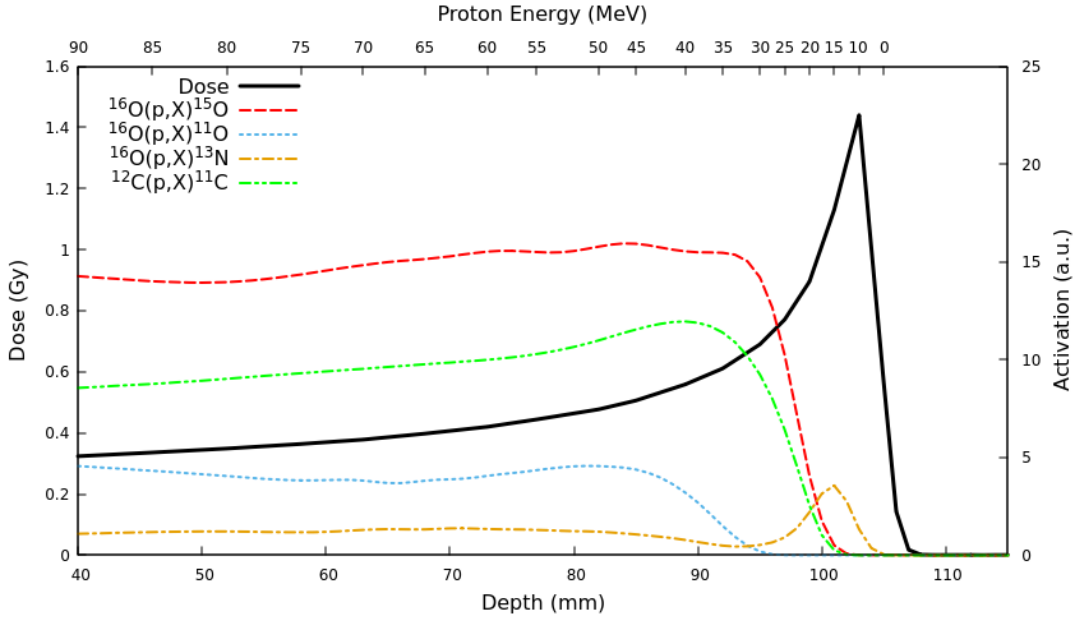

Figure 2.1: Cross sections of the main reactions in human tissues as a function of depth (low x-axis) and incident proton energy (upper x-axis). Most of the activity induced by protons in a patient are 1 cm far apart from the Bragg peak and almost no activity is produced close to it.

In view of the above shortcomings we turn to contrast agent for proton range verification using PET. They should be able to solve some of the issues discussed above in order to improve the accuracy of the proton range verification. Our idea of contrast agents is the use of compounds that produce β^+ isotopes when irradiated with protons, in a way such that the induced activity can solve some of the above problems. For this reason, we look for contrast agents that fulfil the following characteristics.

- **Production of β^+ isotopes at low energies just under the BP.** We have mentioned that one of the issues of this technique is the lack of activity in the last centimeter of the proton path (under the BP). Because of that, we require a contrast agent able to produce β^+ isotopes in this region. Therefore, the reaction channel must have a high cross section at energies below 10 MeV. Ideally, it should have a maximum cross section with a narrow peak centered at 5-7 MeV to induce activity only under the BP.

- **Administered in suitable amounts.** The contrast agent needs to be introduced into the body by a suitable route, in sufficient amounts to produce viable PET radioisotopes while being tolerable for the body.

- **Adequate half-life ($T_{1/2}$).** PET imaging is performed during proton irradiation, just after it, or after several minutes. In view of this, isotopes with a shorter or larger half-life are more suitable to obtain the best image possible in either scenario. To optimize in-beam measurements, it is desirable to use isotopes with very short half-lives that produce emissions immediately after each beam delivery, and ideally, have a half-life short enough to ensure that all emissions occur before the next beam. On the other hand, if we perform the PET image after the irradiation, we need isotopes with larger $F_{1/2}$ to ensure activity after several minutes.

- ***Wash-out* resistant isotopes.** The *wash-out* effect increases with the time that elapses since irradiation. Therefore, isotopes with a very short $T_{1/2}$ do not suffer from it, since they decay as soon as they are produced, without allowing time for *wash-out* to happen. On the other hand, long half-life isotopes suffer from this effect, and make the analysis and quantification of PET images much more entangled. That is why it would be interesting the use of certain compounds or isotopes which could stay at the location where they are produced, unaffected by *wash-out*.

Once the requirements for a compound to be considered as a contrast agent have been discussed, we search the Table of nuclides [Sonzogni, 2005] to find stable nuclei producing β^+ isotopes with the above requirements when irradiated with protons. Furthermore, we focus on low Z isotopes which we know that in low quantities are harmless to the human body, either because they are already part of it (^{23}Na, ^{39}K or ^{35}Cl), or

because they are already used as contrast agents in other medical techniques (^{11}B or ^{18}F). Table 2.2 shows the main characteristics of the candidates proposed as contrast agents: the stable target isotopes, the reaction channel, the β^+ induced nuclides, the energy threshold of the reaction (E_T) and the half-lives.

Isotope	Reaction	β^+ isotope	E_T (MeV)	$T_{1/2}$
^{11}B	(p,n)	^{11}C	3.02	20.364 min
^{18}O	(p,n)	^{18}F	2.57	109.77 min
^{23}Na	(p,n)	^{23}Mg	5.05	11.32 s
^{35}Cl	(p,n)	^{35}Ar	6.94	1.776 s
^{39}K	(p,n)	^{39}Ca	7.50	860 ms

Table 2.2: Proposed isotopes as contrast agents, with their main characteristic for this purpose. The first column is the stable isotope, the second one is the reaction that produces the β^+ isotope that we will us as contrast agent. In addition, the energy threshold of the reaction and the decay half-lives are shown in fourth and fifth column respectively.

2.1.1 ^{11}B

In this work we suggest boron as a potential contrast agent in proton therapy because of the production of ^{11}C when it is irradiated with protons. The cross section of the ^{11}B(p,n)^{11}B reaction exhibits a large peak centered at 6-7 MeV, which satisfies one of the main conditions of the proposed contrast agents. This implies that boron can produce a significant number of β^+ isotopes in the region under the BP.

The choice of boron as contrast agent is also encouraged because it is already used in boron neutron capture therapy [Nedunchezhian et al., 2016]. In this technique, the other boron stable isotope, ^{10}B, is introduced in the tumor area to kill it using the capture of thermal neutrons and subsequent release of α particles and ^{7}Li nuclei after the ^{10}B(n,α)^{7}Li reaction. We could use the same idea in proton therapy to improve the spatial distribution of PET emitters inside the patient.

Its use would be more suitable for post-irradiation verification due to the relatively long half-life of ^{11}C. However, it could also be used during treatment, but the number of acquisitions would be limited by the ^{11}C activity.

2.1.2 ^{18}O

The stable ^{18}O isotope of oxygen (natural abundance of 0.205%) is probably the most promising candidate as a contrast agent for several reasons. The first one is the production of ^{18}F when it is irradiated with protons. It is a β^+ emitter with a half-life of 110 minutes. Its cross section also has a high peak at low energies, centered at around 6 MeV, and it is almost negligible above 40 MeV. This implies that most of the isotopes of ^{18}F would be concentrated under the BP.

Another reason that makes ^{18}O a good contrast agent is that in our most recent experiments, there is evidence that ^{18}F does not suffer *wash-out* [España et al., 2022]. On the contrary, most of the produced ^{18}F remains where it is produced, just in the BP area. This effect would allow us to measure it with a PET system after the irradiation for a long time without worrying too much about *wash-out*.

Finally, the contrast agent could be directly injected in the patient as water-18. Although there is no toxicity study for this molecule we think that results could be positive because ^{18}F is usually incorporated in a PET radiotracer (FDG) which has been tested to not be toxic for patients. however, a specific toxicity study should be performed to approve water-18 as contrast agent.

2.1.3 ^{23}Na, ^{35}Cl & ^{39}K

These three isotopes are very similar. They all produced β^+ emitters trough reactions channels with energy threshold below 10 MeV and the produced isotope half-lives are in the order of seconds, being ^{35}Ar the fastest to decay. However, it is the only one for which cross section measurements do not exist in bibliography. Experimental cross section measurements for ^{23}Na and ^{39}K exist up to 10 MeV and they both have a significant intensity for PET verification.

These isotopes, apart from its properties as contrast agents, were chosen because they naturally form part of the human body. However, its concentration must be increased to use them as contrast agent and we need more information on production yields and cross sections for all of them.

2.2 Contrast agents in PG proton range verification

The use of prompt gamma-rays emitted during a proton irradiation has the potential to make it possible to estimate the proton range with a high accuracy. The popularity of this technique has increased in recent years since it solves two of the main issues of PET, the lack of count rate and the wash-out effect because of the delay of the β^+ emissions. However, there are some aspects of the naturally emitted PGs that limit the potential of the technique. The use of contrast agents would help to reduce these issues. In order to determine the properties of the ideal contrast agents for PG proton range verification, we have to previously introduce its limitations.

- **Emission of high-energy γ-rays.** Human body is composed mainly by oxygen and carbon. Therefore, we are limited to the use of PGs that arise from them, or other secondary isotopes produced in certain reaction channels with less intensity. The most abundantly emitted γ-rays from a patient during a proton therapy treatment are shown in Table 2.3 with the reactions that produce them. The energies are all above 2 MeV and the most intense are the inelastic (p,p') reactions, which lead to the emission of 4.44-MeV and 6.13-MeV photons from carbon and oxygen, respectively. The use of high-energy photons is a limitation because of the lower detection efficiency. To address this challenge current PG detection setups use large detectors to increase the efficiency as much as possible. This makes the acquisition systems much larger, less manageable and more expensive.

- **High count rates.** Prompt-gammas are emitted during beam delivery. Therefore, we need an acquisition system capable of measuring them during the beam-on period. The problem is that the total amount of secondary radiation (PG, neutrons and secondary protons) is so big that detectors easily saturate. In addition, related to the disadvantage highlighted in the previous point, the use of large detectors to increase the efficiency of high energy photons implies that more secondary radiation reach them.

- **Spatial effects.** Due to the nature of nuclear reactions, nuclear spin polarization induced by the proton beam leads to angular correlations of the emitted gamma radiation. Therefore, the angular distribution of prompt γ-rays is not necessarily

γ-ray E (MeV)	Reaction on ^{16}O	Reaction on ^{12}C
2.00	^{16}O(p,xγ)^{11}C	^{12}C(p,xγ)^{11}C
2.74	^{16}O(p,p'γ)^{16}O	
4.44	^{16}O(p,xγ)^{12}C	^{12}C(p,p'γ)^{12}C
5.24	^{16}O(p,xγ)^{15}O	
6.13	^{16}O(p,p')γ)^{16}O	
6.18	^{16}O(p,x)γ)^{15}O	

Table 2.3: Main prompt γ-rays induced by proton beams in patients. The first column is the energy of the emitted γ-ray in MeV. The second and third columns are the reactions that produce these PG from oxygen and carbon. Information extracted from NuDat 2.0 [Sonzogni, 2005].

symmetric with respect to the beam direction, and different count rates will be observed depending on the location of the detection setup.

In short, the main issue of PG proton range verification is related to high energy PGs emitted from natural tissues. The use of contrast agents that emit PGs at lower energies have the potential to tackle this challenge. The properties of the ideal contrast agent for PG proton range verification are described in the following.

- **Emissions of low-energy γ-rays.** We look for isotopes that emit PGs with energies below 2 MeV when irradiated with protons. The major advantage of using low-energy PGs lies in the increased detection efficiency. We have calculated the photopeak efficiency for the two most abundance PGs in human body and for 1 and 2 MeV for a cylindrical $LaBr_3$(Ce) detector with a radius of 1.5 inches and a height of 3 inches. The results in Table 2.4 show that the increment in efficiency reach up to a factor 10 in the case of the PGs close to 1 MeV in comparison with the 6.1 MeV from the oxygen. With respect to the 4.4 γ the improvement in the efficiency is almost a factor 3 for 2 MeV PGs and a factor 7 for 1-MeV γ-ray emissions. This overall improvement in efficiency could enable the development of new PG detection systems with smaller detectors, resulting in a more compact and cheaper setup than the current ones.

Energy (MeV)	Efficiency (%)
6.18	1.51
4.44	2.63
2.0	7.17
1.0	15.32

Table 2.4: Intrinsic photoelectric efficiency of a cylindrical $LaBr_3(Ce)$ detector with a radius of 1.5 inches and a height of 3 inches.

- **PG emissions under the BP.** The spatial correlation of activity and dose is important. Therefore, as we do in PET, we are interested in isotopes whose emissions are concentrated at low proton energy beams. The ideal case would be a high cross-section peak centered around 5-10 MeV and almost negligible at higher energies. We will find this kind of cross-sections in inelastic collisions (p,p') or in reaction channels with very low energy thresholds. We have studied the nuclear chart to find those isotopes that fulfil these conditions.

2.2.1 Use of ^{18}O as a PG emitter

We have introduced oxygen-18 in the context of PET, but ^{18}O is also suitable as a contrast agent for PG proton range verification. When irradiated with protons, it emits four PGs with the ideal contrast agent properties (Table 2.5). The 1982 keV PG comes from the inelastic collision of a proton with the ^{18}O, and therefore, its energy threshold is very low as the excited nuclear level is also 1982 keV. The other three γ-lines come from the excitation of the ^{18}F in the reaction channel $^{18}O(p,n\gamma)^{18}F$. The energy threshold of this reaction is very low (2.5 MeV). Because of this, the emission thresholds of the PGs will be below 5 MeV, since the excited levels that emit them are all below 1.1 MeV. In addition, as it was mentioned in section 2.1.2, ^{18}O can be introduced in the patient as water-18 without any risk.

The main challenge associated to this technique resides in the fact that PG measurements must be performed during the beam-on period, which complicates the experimental set-up. Therefore, there are far fewer experimental yield measurements for PG emissions than for β^+ delayed γ-rays. Natural PG emitted from oxygen and carbon have been previously measured[Dyer et al., 1981; Lang et al., 1987; Lesko et al., 1988;

E_γ (keV)	Reaction	Isotope	Level (keV)	E_T (MeV)
937.20	(p,nγ)	^{18}F*	937.20	3.5
1041.55	(p,nγ)	^{18}F*	1041.55	3.6
1080.54	(p,nγ)	^{18}F*	1080.54	3.6
1982.07	(p,p'γ)	^{18}O*	1982.07	2.0

Table 2.5: Main properties of the 4 studied prompt γ-rays coming from the irradiation of ^{18}O. The reaction channel, resulting isotope, the excited energy level and the energy threshold

Kiener et al., 1998], but there is no data at all about PG emission from ^{18}O when it is irradiated with protons. In chapter 3 we have measured production yields and deduced cross sections up to 10 MeV.

2.3 Experimental proof of concept for contrast agents

The main idea of the proposed contrast agents is to generate activity in the most distal part of the dose, where there is no natural activation. This idea had never been tested before, and because of that, we performed an experiment to prove the concept of contrast agents in proton therapy and their potential [España et al., 2021]. In this experiment, water-18 was used. A cylindrical phantom filled with distilled water and water-18 in different regions was irradiated with protons. The final goal was the observation with a preclinical PET system the differences in the activation between natural water and water-18. In the following we describe the experimental setup, the expected results according to Monte Carlo simulations and the most relevant results.

2.3.1 Experimental setup

The experimental setup is composed by two different pieces. The first one, and the most relevant, is a 3D-printed hollow cylindrical phantom with a 50 mm diameter and 80 mm of height with 1-mm walls. The material used for its construction is polylactic acid (PLA, (C3H4O2)n). From the other side of the large external emptied cylinder, 7 smaller cylindrical containers of 6-mm of diameter have been constructed, which can then be filled with different materials (see Figure 2.2). The external cylinder was filled

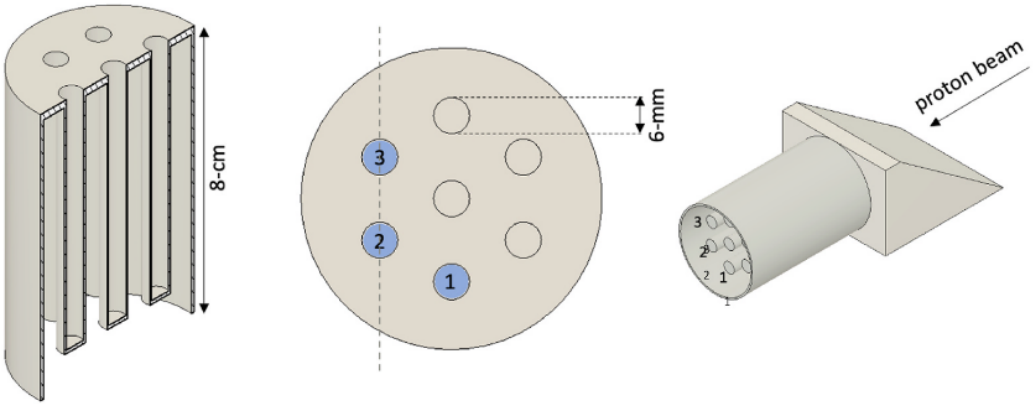

Figure 2.2: Scheme of the irradiated phantom. It is a hollow cylinder filled with gelled water. It is composed by another 7 smaller hollow cylinders which are filled with different compounds. Cylinders marked in blue are filled with 10% atomic ^{18}O-enriched water, mixed with a 1% of agarose to gel the liquid. The phantom was irradiated using a wedge-shaped high-density polyethylene block to generate a different proton energy beam at each point of the cylinder using only a monoenergetic irradiation field.

with distilled water mixed with 1% of agarose, which gels the mixture and thus avoids the typical diffusion within a liquid. To ensure the contents of the cylinder remained securely contained, a cover was placed over the opening and sealed with duct tape. Three of the cylindrical hollows (blue cylinders in Figure 2.2) were filled with 10% atomic ^{18}O-enriched water mixed with a 1% of agarose to gel the liquid, and cover with a thin plastic and tape.

The second piece is a wedge-shaped high-density polyethylene (HDPE) block whose thickness varies between 10 and 60 mm with a 45-degree angle (see Figure 2.2 for details). It is placed next to the phantom to decrease the beam energy and produce a different proton range along the transversal direction of the phantom. In this manner the proton range is different in each of the inner cylinders and we can analyze the impact of contrast agents at several energies in a single irradiation.

The irradiation consists of a mono-energetic proton field of 100 MeV delivering 20 Gy at the Bragg peak in a single irradiation. The dose level is higher than clinical doses by a factor of 10. This high dose was chosen to ensure that the produced activity was enough to perform the analysis without concern of the signal-to-noise ratio. This irradiation was performed at the West German Proton Therapy Center (WPE) where they have an IBA ProteusPlus, a 230-MeV isochronous cyclotron. After the irradiation

the phantom (without the wedge) was measured in a preclinical off-line β-CUBE PET scanner [Krishnamoorthy et al., 2018], and the measurement lasted 12 hours. A CT scan of the phantom was also performed after the irradiation to correlate the PET activity images with it.

2.3.2 Simulations

To understand the outcome of the experiment the expected effect was simulated using TOPAS. For that purpose, dose and activation profiles were calculated using a 100 MeV proton beam travelling through distilled water and water-18 (50% of $H_2^{18}O$). The results are shown in Figure 2.3, which illustrate how the doses are exactly the same in both cases. On the contrary, the activity profiles change a lot when, instead of distilled water, we irradiate a mixture of distilled water and water-18. A huge peak of activity appears in the most distal part of the proton range, just under the Bragg peak.

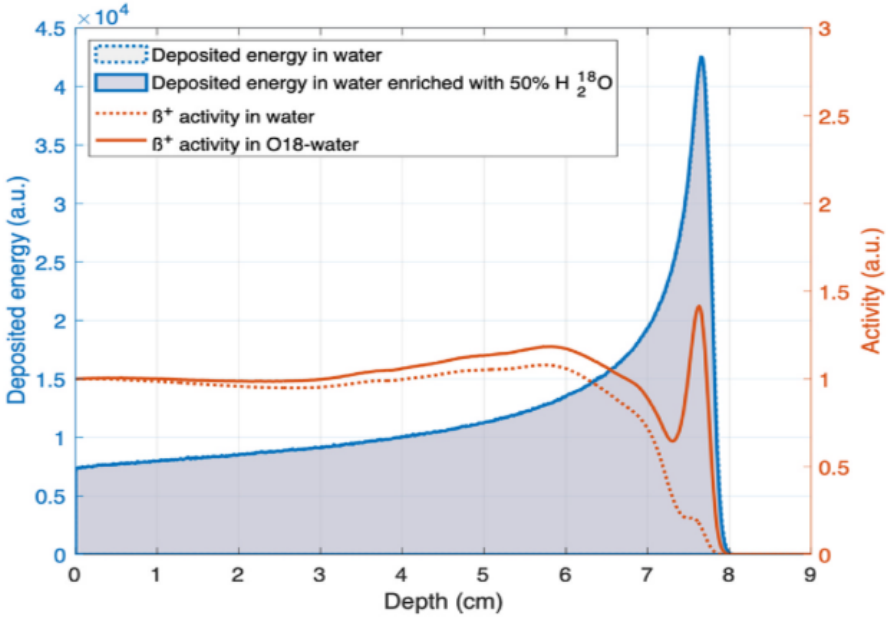

Figure 2.3: Dose and activity profiles produced by a 100 MeV proton beam in distilled water and in enriched water with 50% of $H_2^{18}O$. The dose profiles do not suffer any modification due to the ^{18}O. However, the activity profiles change drastically. The total amount of activity die to β^+ isotopes drastically increase under the Bragg peak thanks to $H_2^{18}O$.

To simulate the entire phantom, including the wedge, the same proton beam used in the experiment was employed in the TOPAS software (as described in Section 1.5.1).

The whole geometry was detailed and dose scores were stored. The activation was also necessary, and it was included in the simulation using our own developed scorers (described in section 1.5.1) and the mentioned cross-sections values in Table 2.1 for natural isotopes. For the ^{18}O(p,n)^{18}F reaction channel, we introduced the validated cross-section values from the International Atomic Energy Agency (IAEA) [Tárkányi et al., 2019; Hermanne et al., 2021].

2.3.3 Results

The main results from this experiment are the PET activity distribution. Figure 2.4 shows the activity at different time intervals (red), the dose (blue) and the CT of a slide which covers cylinders 2 and 3, centered at the dashed line in Figure 2.2. The time intervals chosen for this graph are each of the first 4 hours from the start of the measurement. These intervals were chosen to analyze the activity distribution as a function of time. The isotopes created in greatest abundance throughout the phantom are those produced from oxygen, such as ^{15}O, ^{13}N and ^{11}C with half-lives of 2, 10 and 20 minutes respectively. These isotopes dominate the activity map during the first hours, but as time goes by, their contribution will diminish and the one that will start to prevail will be ^{18}F because its half-life is much longer (110 minutes). Furthermore, the ^{15}O, ^{13}N and ^{11}C are produced in any region where oxygen is available, which is actually the whole phantom. However, the ^{18}F will be only produced in those regions filled with ^{18}O-enriched water, i.e., the 6-mm cylinders that are marked with a white dotted line in the images.

The experimental results can be successfully reproduced by the Monte Carlo, and the activity is as initially expected. In the first hour, the contribution of ^{18}F is negligible. The distribution of activity is almost uniform throughout the irradiated area, except in the most distal area of the dose (Bragg peak) where it is apparent that there is no activity on the dose. The activity distribution in the second hour shows an slight change. Some activity becomes visible in the most distal part of the small cylinder filled with water-18 due to the contribution of ^{18}F. The most relevant results come from the PET images during the third and fourth hour after irradiation. In these cases, there is activity in the most distal part of the cylinders, overlapping this activity with the high dose associated to the Bragg peak. In the fourth hour, when basically the whole activity from natural oxygen has disappeared, and the only contribution that remains is

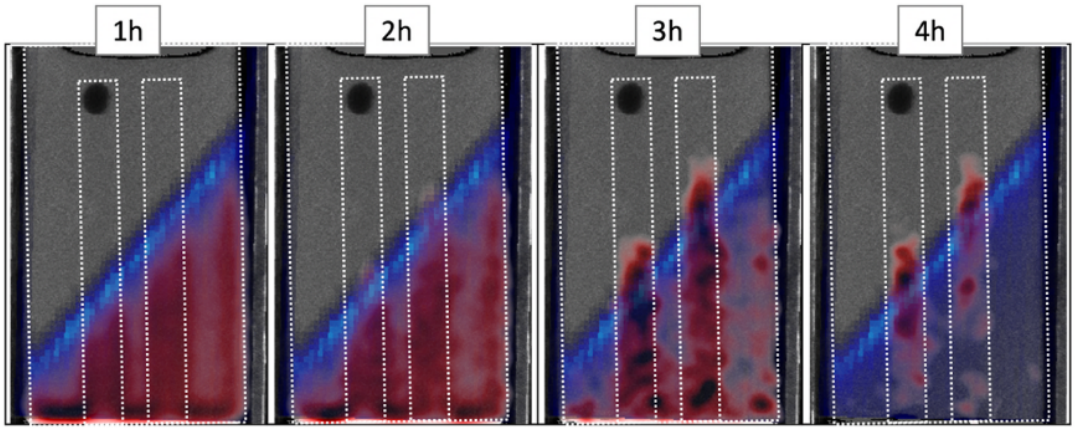

Figure 2.4: PET images obtained from the measurements of the irradiated phantom. From left to right, the PET images associated to the first four hours of measurement are shown in red, over the theoretical dose calculated with TOPAS in blue. Both images are plotted over the CT of the phantom. The white dashed lines indicate the contours of the narrow cylinders.

coming from ^{18}F, we can appreciate that there is only activity in the most distal part of the proton range. It is important to emphasize that there is no physically possible that activity exists beyond the dose. The observed deviations in activity from the planned values can be attributed to the possibility of gel movement during the time interval between irradiation and PET scanning. Although the material used in the phantom is in the form of a gel, there may still be some degree of diffusion or displacement. It is important to note that the phantom was transported from the irradiation room to the PET scanner, which was located in a different area of the building. During this period, it is possible that the gel within the phantom may have shifted from its original irradiated position, resulting in the observed discrepancies in activity compared to the planned values.

From the images shown above, it is shown that PET activity fulfil our expectations of generating activity in the most distal region of the proton range, but we still need to move to a more quantitative analysis and address how well or how poorly they match the Monte Carlo results using TOPAS. The analysis has been focused on the PET activity from the second hour after irradiation. Simulated PET activity has been calculated from the Monte Carlo activation maps from each of the isotopes, to which we have applied the half-life of their respective isotope to calculate the total contribution during the

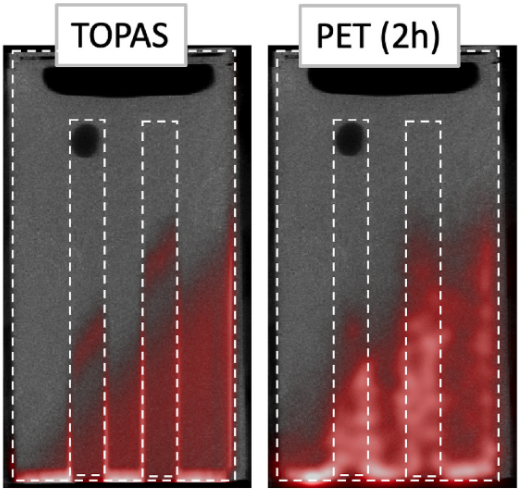

Figure 2.5: Right: Theoretical activity distribution calculated with TOPAS. Left: PET image from the second hour of the experiment. The activity from ^{18}F is located in the most distal part of the narrow cylinders. This activity can be observed in both theoretical and experimental images, confirming our capability to identify PET activity and assuring that the extracted dose is reliable enough.

second hour. Figure 2.5 shows Monte Carlo (TOPAS) and experimental PET activity distribution (red) associated to the second hour of the measurement. Both results are quite similar, which means that the available cross-sections are quite accurate. The main differences between images are the noise that it is introduced in the PET image due to the low count rate and a gap of activity in the narrow cylinders. This gap appears due to the lack of information of the reaction cross sections for ^{18}O(p,n)^{18}F beyond 25 MeV. As it will be explained in the next chapter, this is one of the reasons that encouraged us to measure the ^{18}F production cross sections at energies above 30 MeV.

2.4 Discussion

The techniques for proton range verification have a great potential by themselves, but their capabilities can be enhanced even further with the use of contrast agents as proposed in this chapter. Contrast agents have the potential to reduce uncertainty error sources, improve activity distribution maps, or introduce new emissions with different energies that allow for new approaches to the technique.

For PGs, the use of certain isotopes for contrast agents can produce less energetic

photons that are easier to detect, which could lead to a drastic change in the technique and the development of new verification systems specifically for these new emissions. Moreover, the efficiency of the current PG detection system to detect PGs from ^{18}O is 10 times higher than from natural emissions, which is a significant step forward. For PET contrast agents, several candidates have been proposed for all the PET verification possibilities (online, in-room, or offline), which could mitigate the *wash-out* effect and the absence of spatial correlation in the distal part of the proton range.

The proof of concept presented in this chapter, demonstrating the successful use of contrast agents in proton therapy, marks a significant milestone in the field. This experimental evidence supports and justifies the work carried out throughout this thesis. The integration of contrast agents into clinical practice could greatly enhance the ability to visualize and target tumor tissue during proton therapy, ultimately improving patient outcomes. Further research and development in this area will be necessary to optimize the use of contrast agents and fully realize their potential in proton therapy, starting with the measures of cross-section of these candidates to enable their study as contrast agents. Nonetheless, the results presented in this chapter provide a strong foundation for continued exploration and innovation in this exciting field.

Chapter 3

Experimental Production Yields of Contrast Agents

As discussed in early chapters, the knowledge of the production of radioisotopes able to generate the emission of photons (prompt or delayed) form the basis of proton range verification techniques. Cross-sections play a crucial role in determining the feasibility of using a particular isotope for proton range verification [España et al., 2011]. In this thesis, we propose the use of contrast agents as external substances which are activated when they are irradiated with protons. The first requisite to studying the potential of a particular isotope is to know the cross-section of the reaction channel that generates the radiation to be used for verification.

However, in the majority of the isotopes proposed as contrast agents, there is a lack of experimental data, which limits their study as a potential contrast agent in proton therapy. Therefore, a crucial step in the search for contrast agents is the measurement of their cross-sections, which can be done using various experimental techniques, such as the activation technique [Fraile et al., 2016; Rodriguez et al., 2021] By measuring the cross-sections, we can determine the probability of the reaction occurring as a function of the proton energy. Once the cross-sections are determined, the data can be incorporated into Monte Carlo simulations to evaluate the impact of the contrast agent on the activity emissions, either in terms of spatial distribution or in terms of energy spectrum, and how this affects the accuracy of the range estimation.

Among all the proposed reactions in the previous chapter, some of them, such as ^{18}O(p,n)^{18}F, are very well-known and have been studied in detail, because they have

other applications where the knowledge of the cross-section is essential too. Nonetheless, the measured energy range is often limited to the purposes of those studies and they do not cover the whole energy range of proton therapy (0 to 230 meV). On the other hand, there are reaction channels, such as the ^{35}Cl(p,n)^{35}Ar or the PG emissions from ^{18}O(p,Xγ), which have never been studied before, and we have no information at all about them. Because of that, we have carried out a series of experiments to measure cross-section values of those channels for which we do not have any information, or to complete those channels that have been previously measured but not over the entire energy range of interest.

In this chapter, we first study which of the proposed reaction channels have been previously measured and if so, in which energy range. We will use this information to justify the experiments that we have carried out, the reactions channels that we have measured and the energy range we have focused on. We will then provide a detailed explanation of the three experiments we conducted, which include measurements of cross-sections for low-energy β^+ isotopes, high-energy β^+ isotopes, and low-energy PG emissions.

3.1 Existing cross-section data

The knowledge of productions yields is essential in various fields of physics such as astrophysics and nuclear structure, and in certain aspects of nuclear medicine. In the last 70 years, thousands of experiments have been carried out to measure cross-sections and production yields of many reaction channels with interest in any fields, and all of these data are stored in online databases, such as EXFOR [Otuka et al., 2014] or JANIS [Soppera et al., 2014]. As a first step, we have made a literature survey using these databases to identify which of the potential contrast agents have been measured and if so in which energy range.

Among the proposed reactions, the one that has been studied the most is the ^{18}O(p,n)^{18}F. The reason is that ^{18}F is the most widely used radioisotope for PET imaging, and it is generated using this reaction. Figure 3.1 shows 7 different data sets for its cross-section, covering up to a proton incident energy of 25 MeV. The red line is the recommended data set by the International Atomic Energy Agency (IAEA) obtained from a validation study in which the experimental cross-section measurements

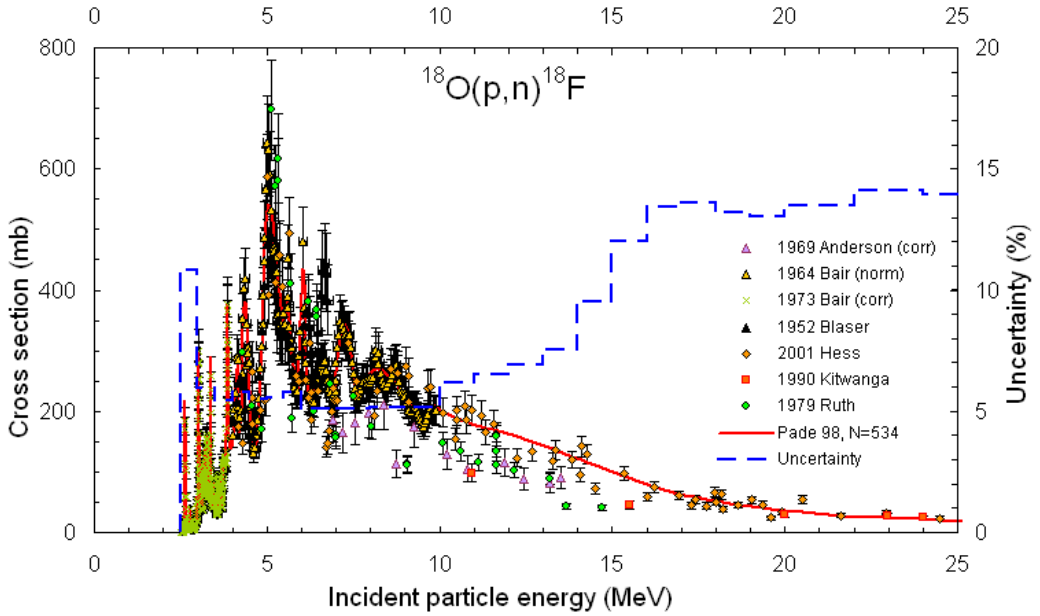

Figure 3.1: Cross-section measurements of the reaction channel $^{18}O(p,n)^{18}F$ up to 25 MeV. Red line determine the recommended data set by the International Atomic Energy Agency (IAEA), obtained as a validation study with all the data represented in the figure. The uncertainty of this evaluation is plotted with a blue dashed line. References: [Anderson et al., 1969; Bair, 1973; Hess et al., 2001; wa Kitwanga et al., 1990; Ruth and Wolf, 1979].

were taken into account. Since it was studied specifically for this purpose, there is no data available above 30 MeV. Although this energy range largely covers the distal end of the proton range, proton therapy uses proton beams up to 250 MeV, so it would be a clear advantage to have cross-section information up to this energy to cover the whole energy range. However, from the available data, it can be noted that the cross-section meet all the requirements mentioned in section 2.1.2. The energy threshold is very low, and the cross-sections shows a very intense peak centered at 6 MeV, and it is very low above 20 MeV.

As well as a PET contrast agent, we also proposed ^{18}O for PG verification. The challenge with PG measurements is that they must be performed during the beam-on period, which presents complications for the experimental setup and its limitations. Therefore, there are far fewer measurements for PG emissions than for β^+ isotopes. There are a few experiments which measured the PG emitted from oxygen and carbon for astrophysical purposes [Dyer et al., 1981; Lang et al., 1987; Lesko et al., 1988; Kiener et al., 1998], but there is no data at all about PG emission from $^{18}O(p,X\gamma)$.

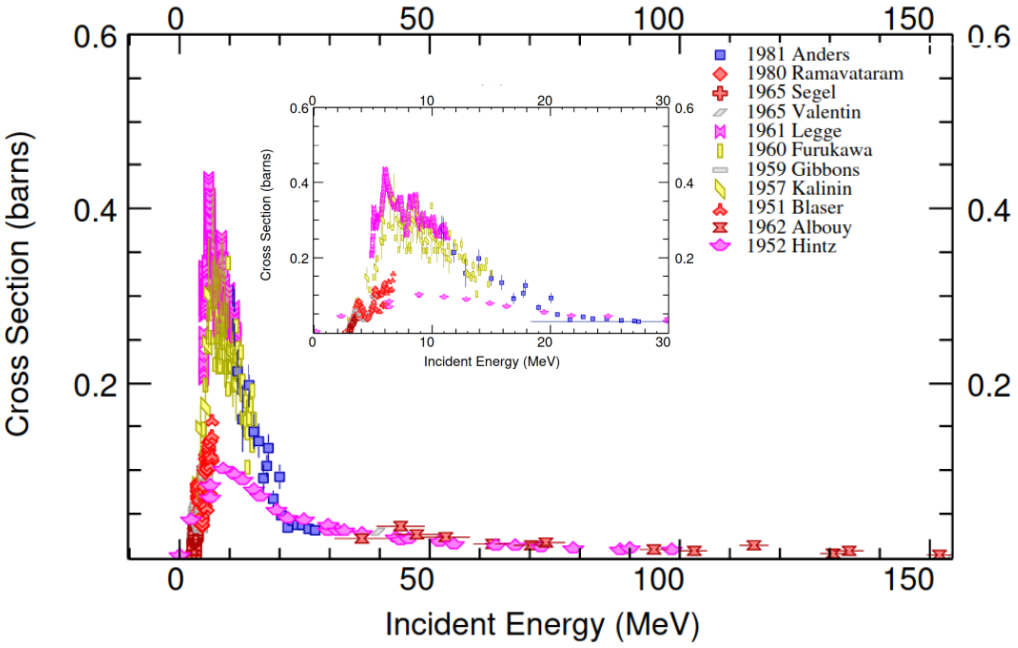

Figure 3.2: ^{11}B(p,n)^{11}C cross-section measurements available at EXFOR up to 150 MeV. There is also a zoom plot of the energy range between 0 and 30 MeV. In it, we can identify all the requirements that we have set for potential contrast agents. Low energy threshold around 3-4 MeV and a peak with its maximum at 8 MeV. References: Anders et al. [1981]; Ramavataram et al. [1980]; Segel et al. [1965]; Valentin [1965]; Furukawa et al. [2013]; Gibbons and Macklin [1959]; Albouy et al. [1962]; Hintz and Ramsey [1952]

Another potential contrast agent with several cross-section measurements is the production ^{11}C from ^{11}B in a (p,n) reaction. Figure 3.2 shows some of the experimental data sets in EXFOR. As it can be seen, there are cross-section values up to 150 MeV which cover the most relevant part of energy range in proton therapy. Furthermore, this reaction channel has a high cross-section peak at very low energies. The figure with zoom at low energies shows how it is centered around 8-9 MeV and decreases very fast up to 20 MeV where the cross-section remains almost constant. There are discrepancies between the data on the maximum height of the peak of almost 400 %. Some experiments measure values up to 500 mb, while others only obtain values of just over 100 mb. However, in every case the cross-section fulfil all the requirements as a potential contrast agents. A high peak at very low energies and almost no β^+ production above 20 MeV.

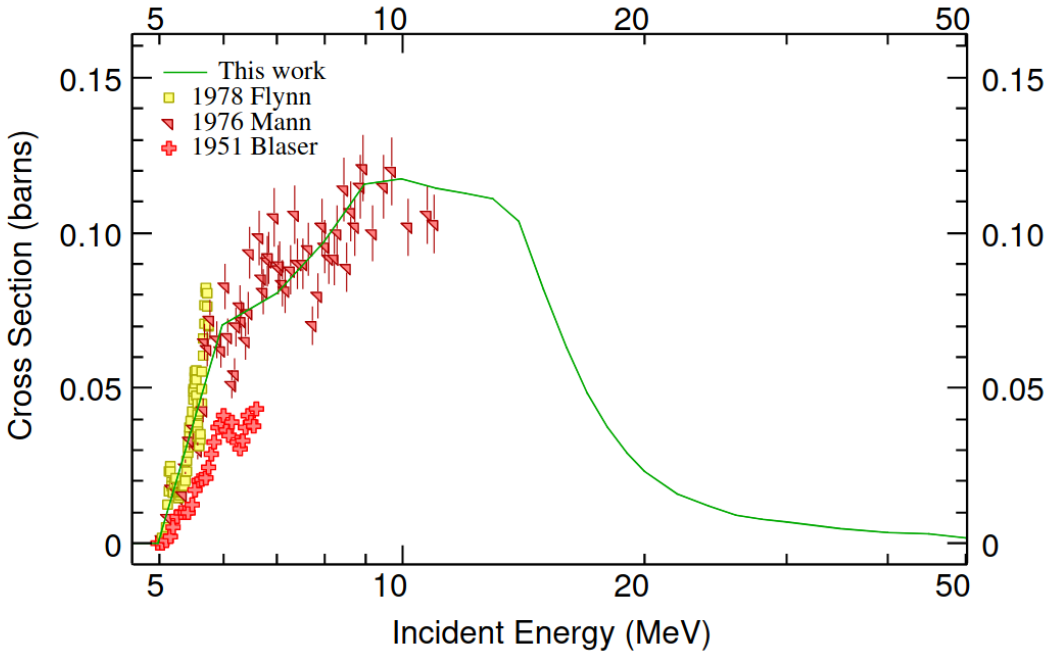

Figure 3.3: Cross-sections data sets from ^{23}Na(p,n)^{23}Mg available e in EXFOR. There are only experimental data up to 12 MeV. The green line is the theoretical estimation of the cross-section from 0 to 200 MeV. It uses a physical model and the experimental data to extrapolate the cross-section up to 20 MeV. The cross-section has an energy threshold close to 5 MeV and the maximum seems to be around 10-12 MeV. References: [Flynn et al., 1978; Mann et al., 1976; Kneff et al., 1975].

Moving on to the proposed contrast agents with short half-life β^+ emitters, the one with the most data sets is ^{23}Na(p,n)^{23}Mg. Cross-section data points from EXFOR are plotted in Figure 3.3. The energy threshold is very low ($\approx 5MeV$), it increases very quickly up to 150 mbarns and it seems that the tendency above 12 MeV is to decrease, but there are no experimental data to corroborate it. In the absence of experimental data, we will make use of cross-sections theoretical predictions to complete the energy range of interest. We have used TENDL-2021 [Koning et al., 2019], which uses experimental data (if they exist) and theoretical approach to estimate the cross-section up to 200 MeV. The theoretical cross-section predicted by TENDL for ^{23}Na(p,n)^{23}Mg is plotted in Figure 3.3 with a green line along the experimental data. The maximum is around 10 MeV. Furthermore, above 20 MeV the cross-section is very low.

The case of ^{39}K(p,n)^{39}Ca is very similar, with the exception that exists data from a single experiment. The energy threshold is again lower than 10 MeV and the exper-

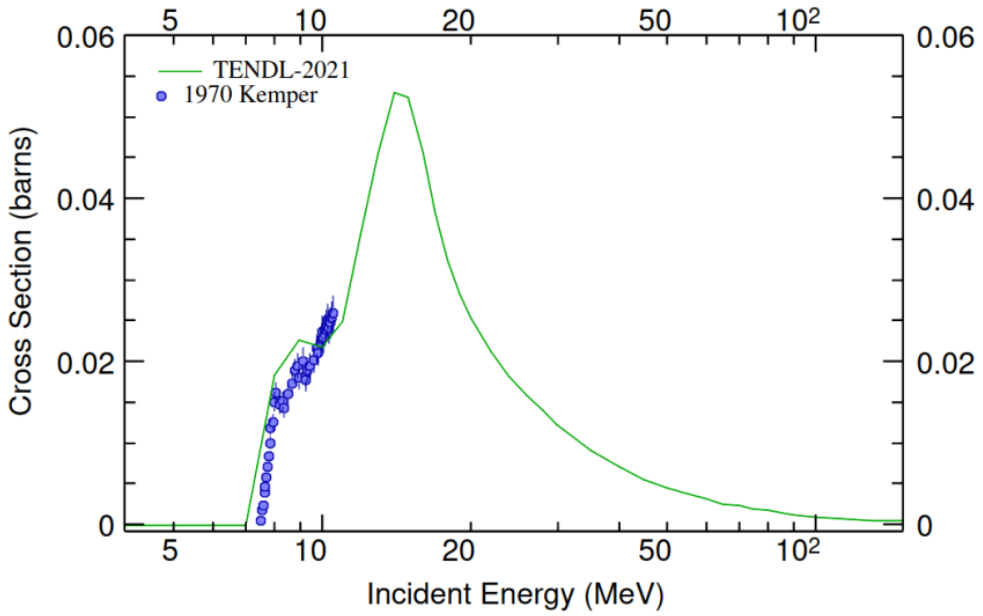

Figure 3.4: Cross-sections data sets from ^{39}K(p,n)^{39}Ca available in EXFOR. There are only one experimental data set up to 12 MeV. The green line is the theoretical estimation of the cross-section. It uses physical model and the experimental data to extrapolate the cross-section up to 200 MeV. The cross-section has an energy threshold close to 7 MeV and the maximum seems to be around 15 MeV. Reference [Kemper et al., 1970].

imental cross-section increases quickly up to 12 MeV. From this point only available information is the TENDL theoretical cross-section. Figure 3.4 shows the only available data set up to 12 MeV and the theoretical prediction. There is a peak centered at 15 MeV and the cross-section decreases slowly and its intensity is not negligible up to 100 MeV. However, although it is not the ideal behavior for a contrast candidate it still holds certain potential. Furthermore, while the peak intensity is lower for ^{39}Ca compared to ^{23}Mg, it is important to note that the $t_{1/2}$ of ^{39}Ca is 10 times shorter than that of ^{23}Mg. Therefore, in terms of activity after beam delivery, both isotopes exhibit similar levels.

The last candidate as contrast agent with short half-life β^+ emitters is the reaction ^{35}Cl(p,n)^{35}Ar. No experimental data is available for his one. In this case, we have only the information from TENDL (see Figure 3.5). We can appreciate that the peak maximum is expected to be around 15 MeV and the end of the tail around 50 MeV. These values are slightly high for an ideal contrast agent, but still its very short half-life make it a good candidate.

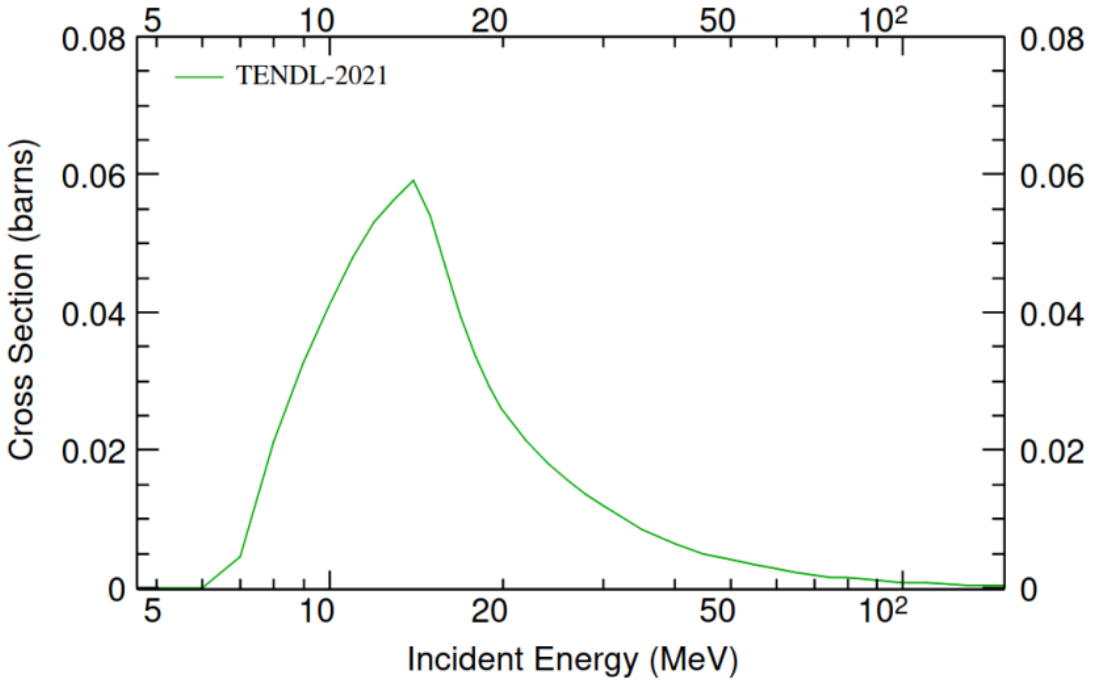

Figure 3.5: Theoretical estimation of the ^{35}Cl(p,n)^{35}Ar cross-section. There is no experimental values of this reaction. TENDL estimates that the energy threshold is around 7 MeV and the peak maximum close to 15 MeV.

3.2 Performed Experiments

Once we had obtained all the available information, it was decided to conduct three distinct experiments to further enhance the experimental cross-section data for the proposed contrast agents. The outcomes of these experiments will contribute significantly to our understanding of the contrast agents properties and their potential applications in proton range verification techniques.

1. **High energy for β^+**

   The ^{18}O(p,n)^{18}F reaction has been extensively mapped up to 30 MeV, providing valuable cross-section data within that energy range. However, above 30 MeV, there is a lack of available data. To address this gap, we conducted a series of cross-section measurements at various energies ranging from 50 MeV to 200 MeV. This comprehensive approach allowed us to cover the entire energy range and obtain valuable data points where there was previously a dearth of information.

By filling this knowledge gap, our measurements contribute to a more complete understanding of the ^{18}O(p,n)^{18}F reaction and provide crucial data for proton-induced reactions at higher energies.

2. **Low energy for β^+:**

   We made the decision to measure three specific reactions that produce β^+ isotopes with relatively short half-lives, covering the energy range up to 10 MeV. The first reaction selected was ^{39}K(p,n)^{39}Ca, for which only one data set existed. By conducting additional measurements of this reaction, we aimed to validate and corroborate the previously obtained data. In addition, we chose to map the cross-section of the reaction channel ^{35}Cl(p,n)^{35}Ar, as this particular reaction had never been measured before. Lastly, we included the well-known ^{23}Na(p,n)^{23}Mg reaction in our experimental plan to serve as a crosscheck and provide a reference point for comparison.

3. **Low energy for PG**

   There are no data at all of PG induced by protons in ^{18}O. Because of that we decided to perform an experiment to fully map the cross-section and angular distribution of the emitted PGs up to 10 MeV.

3.3 Experimental methods

All the experiments carried out in this thesis required detection systems with similar properties: 1) High detection efficiency to obtain good statistics. 2) Good response time to minimize the count losses and avoid pile-up at high rates. 3) Remarkable energy resolution to resolve peaks with similar energies. The use of a detector system based on fast inorganic scintillator crystals meets all these requirements (see Section 1.4). Because of that, we have used the same detection system in all experiments, with the only difference that the experimental setup and the placement of the detectors with respect to the sample was adapted to the needs of each experiment.

A system based on $LaBr_3$(Ce) crystals developed by V.Vedia [Vedia et al., 2015] for fast time measurements were chosen for these experiment because it meets all our requirements. These detectors have a truncated cone geometry with a nominal height of 3.8 cm and upper and lower bases with diameters of 2.5 and 3.8 cm respectively. They

are all coupled to Hamamatsu R9779 fast photomultiplier tubes (PMTs). The signal generated by these detectors can be processed by two CAEN model digital acquisition systems (DAQ), namely 5720b and 5751. The 5720b has a sampling rate of 250 MS/s, providing a precision of time of 4 ns. On the other hand, the 5751 has a higher sampling rate of 1 GS/s, offering a precision of time of 1 ns. The data are stored in list mode and for each event we have information on energy and time with an accuracy of ns. This DAQ is capable of processing up to 1M counts per second and the detectors can handle more than 10M counts per second without pill-up. However, the count rate bottleneck of this detection system is the PMTs, which start to malfunction above 100k counts per second. For this reason, we limit the total count rate to 60k counts per detector to ensure good performance of the detection system.

3.4 High-Energy Yield Measurements for ^{18}O(p,n)^{18}F

The only reaction channel studied in this experiment is the $^{18}O(p,n)^{18}F$. The induced β^+ isotope in this reaction is the ^{18}F with a half-life of 109.77 minutes. Because of its long half-life, irradiated samples must be measured for a long time, ideally more than 10 times the half-life, to ensure that 99.9 % of the produced radioactive nucleus. In this section, the cross-section of ^{18}O(p,n)^{18}F has been measured for several energies between 50 and 230 MeV, using very thin $H_2^{18}O$ sample as a target, which allowed us to perform this cross-section measurements in transmission because the proton beam travels through the sample with almost no energy loss.

3.4.1 Experimental facility

The experiment was carried out at the Quironsalud proton therapy center (Madrid, Spain). The facility is equipped with an IBA Proteus-ONE system, consisting of a compact synchrocyclotron (S2C2) with an internal RF frequency in the 60-90 MHz range. The single-room proton therapy system delivers protons with energies up to 230 MeV with a pulse repetition rate and width of 1 kHz and 10 µs respectively. It is equipped with a 270^{o} gantry that allows us to irradiate perpendicular to the patient table, which enables several ways to carry out the experiment.

3.4.2 Target

The chosen target for the experiment was a liquid sample composed by 70% of $H_2{}^{18}O$ and 30% of distilled water (water-18), containing both ^{16}O and ^{18}O. As a result of the irradiation, several reactions which produced β^+ isotopes occurred. Table 3.1 lists all the reactions observed in this experiment, along with the main properties of the induced β^+ isotopes."

Target	Reaction	β^+ Isotope	$T_{1/2}$
^{18}O	(p,n)	^{18}F	109.77 *5* min
^{16}O	(p,X)	^{15}O	122.24 *16* s
	(p,X)	^{13}N	9.965 *4* min
	(p,X)	^{11}C	20.364 *14* min

Table 3.1: Reaction channels that appear in the experiment irradiating water-18. The first column show the stable isotopes in target. The third column show all the β^+ isotopes induced with its half-life and the reaction that produces them. Information obtained from Sonzogni [2005].

3.4.3 Irradiation and Calibration

The beam delivery was perpendicularly to the patient stage and it allowed us to use a liquid sample without any risk. The container was a cylindrical vessel of 1.2 cm diameter and 450 μL were used to fill it, which corresponds to 2 mm height of water. Beam and target alignment was performed using the beam laser, and once it was aligned, we fixed the position of the target so that it could be reproduced in subsequent measurements. After each irradiation, the water-18 sample was transferred to a another Eppendorf container with an efficiency of 98% and transported to the detector setup in a separate room for measurement.

We have irradiated a total of 6 samples of water-18 at different energies between 50 and 170 MeV (see Table 3.2). In every case, we deliver several thousands of monitor units (MU) to the sample. However, for this experiment, it is essential to know the exact number of protons that travel through the sample. There are two important factors to take into account in the conversion of MU to protons in target. 1) The conversion of MU to number of protons depend on the beam energy. 2) The beam size changes with

Energy (MeV)	MU	σ_x (mm)	σ_y (mm)	Dose/MU (Gy)
50	9000	4.78	4.91	9.03E-02
70	3011	8.44	9.04	9.12E-02
90	9000	6.08	5.98	7.78E-02
110	3000	4.27	4.16	5.87E-02
130	9000	3.85	3.73	6.04E-02
170	9000	3.17	2.95	6.67E-02

Table 3.2: Beam properties and irradiation characteristics at all the energies. For every energy, we show the delivered monitor units (MU), the sigma of the beam spread in both directions, the deposited dose for MU.

the energy and it is bigger than the sample. Therefore, we need a systematic process to estimate the number of protons in the sample. Before each of the irradiations, we also irradiate a radiochromic with 100 MU (8-12 Gys depending on the energy) to obtain from them the beam size, the deposited dose and the number of protons by monitor unit (MU), using the calibration carried out by Sanchez-Parcerisa et al. [2021]. Finally, comparing the beam properties with the sample size we obtained the exact number of protons that reach the sample.

3.4.4 Experimental set-up

The experimental set-up was mounted in order to measure the decay of the ^{18}F which has a half-life of 109.7 minutes. Initially, the possibility of measuring the irradiated sample in the same room where it was irradiated was considered. However, this approach presented several limitations. Firstly, it would have required the treatment room to be disabled for an extended period of time, preventing additional irradiations during the entire 18.1-hour measurement. The solution to this problem was to separate the experiment into two different setups, one for the irradiation inside the treatment room, and a second room, free from beam background, was used to measure the irradiated samples over several hours

Detectors are positioned so that the activity of every single sample is detected by a single detector, but just in case, lead shielding blocks were installed to avoid detection interferences with the other irradiated samples. We manufactured with a 3D printer

specific supports for the vessels with the irradiated water-18 and for the calibrated sources, so that the center of both was in the same place to within 1 mm uncertainty.

The set-up was calibrated using an ^{152}Eu source and its holder placed at the front face of each detector to obtain calibrations in energy and efficiency for every detector individually. At this point, the main issue is that the irradiated sample is not a point source, but an eppendorf with 450 μL of irradiated water placed in the front face of the detector. In order to correct this factor we have carried out two different simulations using *Penmain*, a Monte Carlo simulator based on PENELOPE and specifically developed for detector response, to calculate the relative efficiency in this setup between the point source and the eppendorf. Both simulations include a realistic definition of the experimental set-up and differ in the source, one of them includes a point source and the other one a source with the eppendorf geometry. It is important to note that the positron range was not taken into account because 99% of them annihilates in the sample or in the vessel. The eppendorf efficiency was determined to be 84.1 $\pm$ 2.3 % of the point source efficiency. This factor is included in the cross-section analysis.

3.4.5 Data Acquisition and Measurements

We have only used one acquisition period for the irradiated samples. This measurement starts 15 minutes before the irradiation of the first water-18 sample and ends 24 hours later when there is no activity from the targets. This data acquisition provides time and energy information of every event detected by the 8 detectors. The time resolution of the experiment is precise to the nanosecond, while the energy measurement is in keV.

In addition to the sample measurements, several additional runs were conducted to ensure accurate calibration and minimize background contamination. Firstly, a dedicated calibration run was performed using ^{152}Eu as the energy reference for each detector. This calibration step was crucial in accurately determining the energy values associated with the measured signals. Secondly, a separate run was carried out to measure the background radiation in the secondary room where the experimental setup was located. This background measurement was conducted both with and without the beam on, allowing for the identification and mitigation of any potential background contamination resulting from the beam.

3.4.6 Analysis

The final goal of this experiment is to obtain the cross-section of $^{18}O(p,n)^{18}F$ at the irradiated energies. However, from the experimental data we can only measure the Yield production using the following equation

$$Y(E) = \frac{A}{I^{\gamma}\epsilon_t\phi\left(1-e^{-\lambda t_{irr}}\right)\left(1-e^{-\lambda t_m}\right)e^{-\lambda t_c}} \tag{3.1}$$

where A is the initial activity of ^{18}F in the measured data, I^{γ} is the intensity emission of the studied γ-ray, ϵ_t is the efficiency of the detector, ϕ is the proton flux during the irradiation, λ is the decay constant of ^{18}F and t_{irr} is the irradiated time, t_m is the measured time and t_c is the cool-down time between the end of the irradiation and the beginning of the measurement.

I^{γ} is extracted from the decay information. In the case of the 511 keV of the ^{18}F, its intensity is 193.46(8)%. The flux is calculated from the irradiated radiochromics as described in the previous sections. The efficiency is obtained from the measurements with the calibrated source of ^{152}Eu. Finally, we need to calculate the initial activity (A) of ^{18}F in each sample excluding all other contributions. To do that, we first extract from the raw data the count rate in the energy window of the 511 keV peak. The energy window is determined as the center of the Gaussian $\pm$ 3σ. For every sample, we fit the decay in this energy window to 4 different exponential functions and a constant which describe the background, as it is shown in Figure 3.6 for the irradiation of water-18 wit a 70 MeV proton beam. We are able to reproduce the whole decay of the sample, identifying the contribution of ^{15}O and ^{18}F perfectly. Contributions from ^{11}C and ^{13}N were indistinguishable in our data due to the need to remove part of the data in the region where they dominate. This was caused by an undesired placement of radioactive samples next to the set-up, which introduced background and affected data accuracy during that period of time. Despite this, we were able to obtain the ^{18}F contribution without any inconvenience.

Once the initial activity is obtained, we must use its relation to the cross section given by

$$Y = \rho_{at}\int_{E_i}^{E_f}\sigma(E)\left(\frac{dE}{dx}\right)^{-1}dE, \tag{3.2}$$

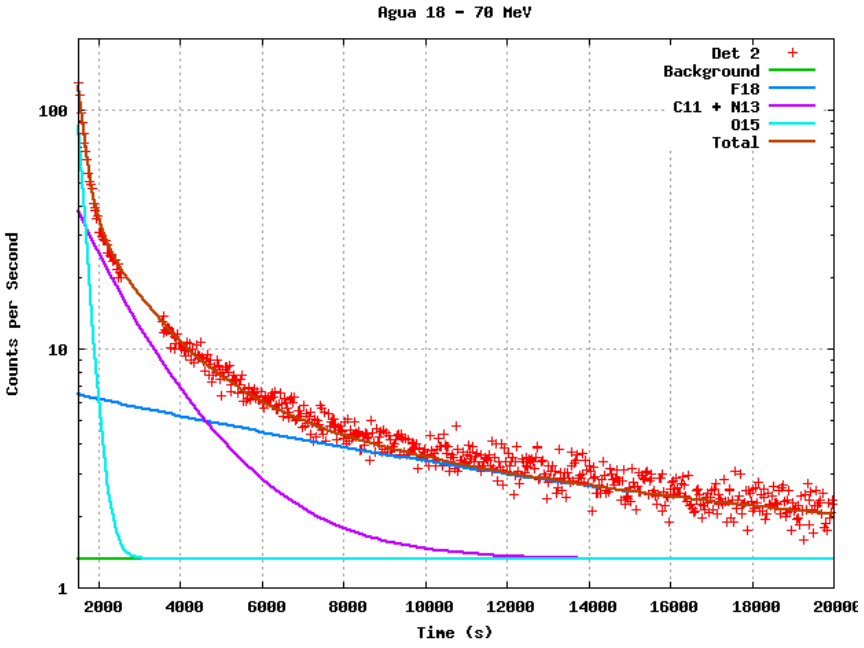

Figure 3.6: Decay of the water-18 sample irradiated with 70 MeV. Red dots are the experimental data. With lines of different colors, the decay of each isotope is plotted along the total decay as sum of all of them. There is a gap of data close to 3000 s because of the contamination of the experimental set-up by radioactive sources. ^{18}F constant decay was fitted to 109.3 ± 0.6 minutes and the reference value is 109.77 ± 0.5.

where ρ_{at} is the atomic density of the medium, dE'/dx is the stopping power, E_i is the initial energy of the incident particle and E_f the final energy. However, we can't use this expression to obtain the cross-section because there is no analytical solution for it and some other approach must be considered.

In this experiment, we have used a 2-millimetre-thin water-18 sample. This means that the energy lost by the incident protons is less than 2.5 MeV in every case, which is small enough to use the thin or transmission approximation of the previous expression. If the energy loss is very low, we can adapt it as follows with $\Delta E = E_i - E_f$ and $\overline{E} = (E_i + E_f)/2$

$$Y = \rho_a \sigma(\overline{E}) \left(\frac{d\overline{E}}{dx}\right)^{-1} \Delta E \tag{3.3}$$

which can be easily adapt to give

$$\sigma(\overline{E}) = \frac{Y\left(\frac{d\overline{E}}{dx}\right)}{\rho_a \Delta E} \tag{3.4}$$

An important part of the analysis is the estimation of the uncertainties of the cross-sections values. Uncertainties are obtained from a combination of statistical and systematic errors which appeare during the experiment and also during the data analysis. Related to the experiment, there are several sources of uncertainties. One of them is the number of protons which went through the sample. Since we calculated it from a radiochromic the value is not totally precise and because of that we assumed a 5% error for this value. Another source of uncertainty related to the experimental set-up is its efficiency. Its related uncertanity was asumed to be a 5% of the obtained values. However, we need to include the correction factor applied to the fact that the target is not a point source as the ^{152}Eu. Taking into consideration both the experimental efficiency and the correction factor from simulations, the total uncertainty for the efficiency is estimated to be 8

Apart from the experimental uncertainties, there is a source of uncertainty related to the data analysis, but its impact is less than the previous ones. This uncertainty come from the fittings of the decays to calculate the initial activities. The fitted variables have an associated errors which, although not very high ($\approx 1\%$), are taken into account.

The error propagation has not been done using a regular technique. These techniques are well-known and extended, but there are some limitations that might lead to overestimation of the final results. Instead, we have used a frequentist inference approach and made a nuisance analysis. It consists in the calculation of the same result a very large number of times, using as input the value of each variable random normally distributed within their uncertainty limits [Cowan, 2019]. The final result is calculated as the mean of all the obtained values and its error as the standard deviation of the whole data set.

3.4.7 Results

We have irradiated several water-18 samples at different energies, but we expect to see similar spectra in every case because the induced isotopes only emit 511 keV photons. Therefore, the spectra should have only one peak at that energy over the background. The background spectrum and the spectrum of the water-18 sample irradiated with a 70 MeV proton beam are compared to confirm this statement. Figure 3.7 shows how both spectra are almost identical except for the 511 keV peak and its Compton contribution. In the background, we can identify 4 peaks The most intense is the 1460 keV from the

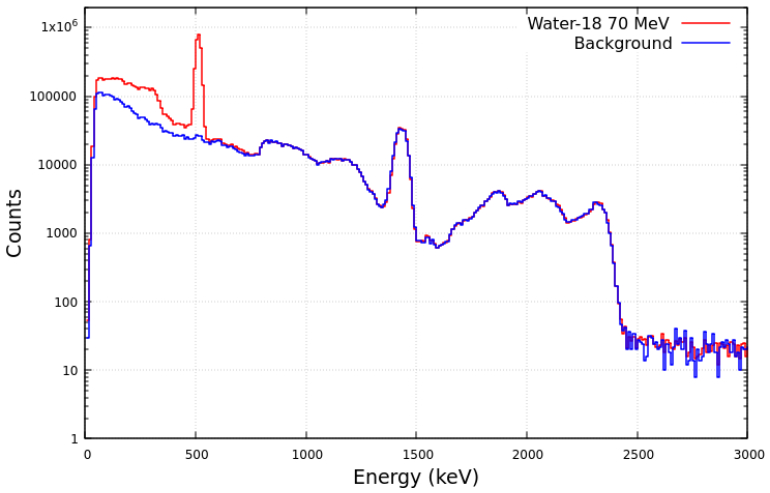

Figure 3.7: The red spectrum is related to the water-18 sample irradiated with a 70 MeV proton beam. In blue the background is plotted. It is shown that the only difference between both spectra is the 511 keV photopeak and its Compton contribution. All the peaks above it are due to internal activity of the $LaBr_3$(Ce) crystals.

natual presence of ^{40}K, and the other three, that are around 1.7 MeV and 2.5 MeV, come from alpha emissions in the decay of ^{227}Ac, which is always present in these detectors as contaminant [Vedia et al., 2015].

The first step of the actual analysis was to determine the initial activity of ^{18}F for each of the irradiated samples. We follow the same procedure explained in section 3.4.6 to calculate it. Table 3.3 shows the obtained results for the initial activities with their corresponnding error for each sample. Activity values are not very high, but still, we were able to perform the fits decay with a high accuracy. We can deduce from the results that the relative errors do not exceed 1%. Yield values for each irradiation are calculated using equation 3.1 and its error is obtained from the same formula following the nuisance analysis previously mentioned. The stopping power values with the errors were extracted from NIST database. Finally, the cross-section results are obtained from equation 3.4 and their errors using the nuisance analysis. The numerical results are shown in Table 3.3.

As mentioned above, the available data at this energy range is very limited. We have plotted the results obtained from this work along with all the previous data available in Figure 3.8. There is only one measurement at high energies, specifically at 150 MeV performed by Dostrovsky et al. [1968]. Our results differ significantly from this

Energy (MeV)	Initial Activity (s^{-1})		Yield (10^{-6})		CS (mbarn)	
	Value	Error	Value	Error	Value	Error
48.8 ± 1.2	382.5	1.2	101	32	8.6	3.0
69.3 ± 0.70	5.99	0.68	60.2	1.0	3.16	0.31
89.45 ± 0.55	95.02	0.21	36.0	2.3	3.02	0.19
109.60 ± 0.40	37.40	0.19	27.7	1.8	2.32	0.15
129.64 ± 0.36	115.40	0.24	22.1	1.4	1.86	0.12
179.75 ± 0.25	106.43	0.23	13.38	0.85	1.124	0.062

Table 3.3: Main results of the experiment. Initial activity extracted from decays (see figure 3.6. Yield production per 10^6 incident protons and the final value of the cross-sections in mbarn.

value. However, it is important to note that our experiment was specifically designed to measure the reaction channel $^{18}O(p,n)^{18}F$. Furthermore, our data also show a decreasing trend as energy decreases. If we scale our results to the previous measured value at 150 MeV, we find that the cross-section at 50 MeV is larger than at 30 MeV. Taking into account all of these factors, we believe that our results are more reliable and accurate for the energy range studied.

3.5 Thick-target yield measurements at low energies for β^+ contrast agents

In this experiment, the cross-sections of the proposed contrast agents for *in-beam* PET verification have been measured. NaCl and KCl salt targets have been irradiated with protons to study the ^{23}Na(p,n)^{23}Mg, the $^{39}K(p,n)^{39}Ca$ and the $^{35}Cl(p,n)^{35}Ar$ reaction channels. The produced β^+ isotopes disintegrate following the exponential decay ruled by their $t_{1/2}$ and the measurement of these decays will be used to calculate the thick-target yields. The cross-section from ^{23}Mg is well-known, and it will be used in this experiment as a cross-check to ensure the validity of the measurements and the realibit of MC simulations to take into account the positron range. On the other side, cross-sections from ^{39}K and ^{35}Cl have not been studied as precisely. The aim of this experiment for p-induced reaction is to validate the only previous measurement for the

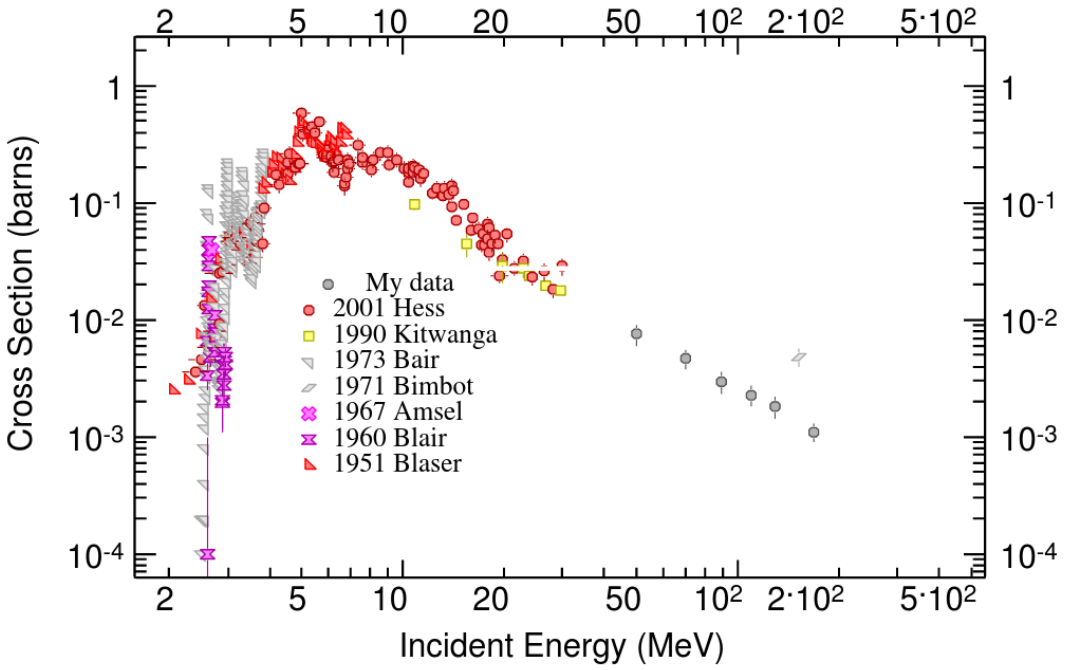

Figure 3.8: Cross-sections results of this experiment in gray dots. We have also plotted all the available data in EXFOR. The tendency of the results in this experiment perfectly correlates with the tendency of previous experimental data.

^{39}K, and to provide new data for ^{35}Cl, which has never been measured before. This will allow for a more comprehensive understanding of the behavior of these two isotopes, and have important implications for future research in this area.

3.5.1 External microbeam line - CMAM

Out of the 6 available experimental beam lines at CMAM, we chose the external microbeam line because it permits to irradiate samples in the air and to mount a set-up with several detectors close to the beam nozzle. Furthermore, this line has two properties that make it the ideal line for this experiment. The first one is that the beam presents a normal distribution described by sigma of a few hundred microns. Therefore, almost 99% of the protons are delivered in a spot with a diameter of less than 1 millimeter, allowing the consideration of point source approximation in the analysis. The second reason is the ability to modulate the beam intensity, ranging from a few nanoAmperes to nearly one microAmpere. This feature enables us to select an optimal

Target	β^+ Isotope	Reaction	$t_{1/2}$ (s)	Thres. (MeV)	γ (keV)	Intensity (%)
NaCl	^{23}Mg	^{23}Na(p,n)	11.317 *11*	5.05	511.0	199.9 *3*
					440.5	7.85
	^{35}Ar	^{35}Cl(p,n)	1.7756 *10*	6.94	511.0	199.84 *12*
KCl	^{39}Ca	^{39}K(p,n)	0.8596 *14*	7.46	511.0	199.851 *7*
	^{35}Ar	^{35}Cl(p,n)	1.7756 *10*	6.94	511.0	199.84 *12*

Table 3.4: Low β^+ reactions studied in the experiment with its main characteristics: half-life ($t_{1/2}$), energy threshold and main γ emissions with their intensities.

beam intensity that ensures sufficient emission counts for reliable measurements, while avoiding detector damage or saturation of the acquisition system.

This beamline is also very interesting because it can be fully controlled remotely from the control room. There is a motorized platform having an active area of 40×40 cm2 which can be moved remotely with a precision of 0.5 millimeters. This, together with the use of video cameras, allows for remote alignment of the beam with the target and real-time monitoring of the target during irradiation. In addition, the beam position is minimally affected by changes in beam energy, making it possible to perform measurements without entering the experimental room. However, periodic alignment adjustments were made between the target and the beam to ensure the accuracy and efficiency of the experiment.

3.5.2 Targets and Alignment

As proof of principle for very short $t_{1/2}$ prompt PET isotopes we chose natural salts for our experiment, specifically NaCl and KCl samples were chosen to perform this experiment. We generate solid tablets from these salts using a compressor. The tablets weigh one gram and have a cylindrical shape with a diameter of 13 mm and a height of 3.0-4.0 mm depending on the material. The irradiation of these samples produce the reactions in Table 3.4.

The alignment between the target and the beam was achieved using a luminescent material that emits blue light when irradiated with protons. The setup was carefully aligned to ensure that the beam impinged precisely at the center of the targets. Although no deviations were anticipated when changing the beam energy, the alignment

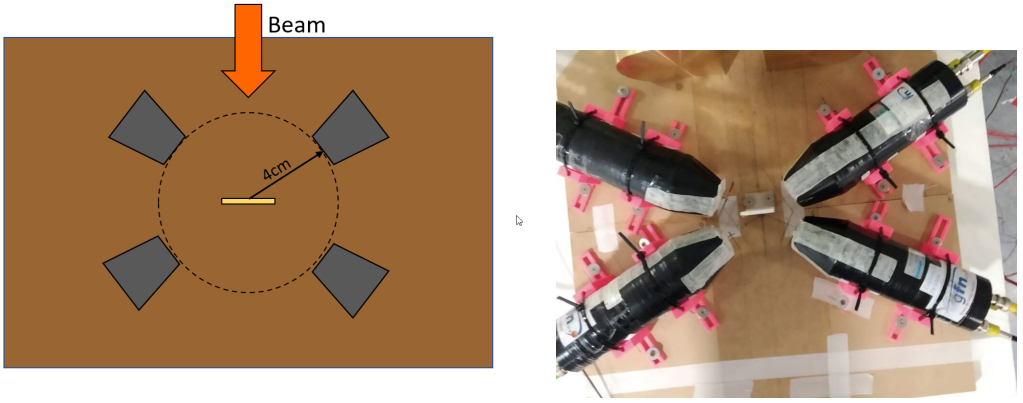

(a) Scheme **(b)** Set-up

Figure 3.9: Scheme of the experiment setup. In the center is placed the target 4 cm far from each of the detectors ($LaBr_3$). Detectors are placed at 60, 120, 240 and 310 degrees with respect to the beam direction to measure the angular distribution of the emitted PGs. They are fixed with 3D-printed supports to the table, so the experiment is totally reproducible. They are also coated with black tape to protect them from the light.

process was repeated multiple times to confirm this assumption. Furthermore, during the irradiation, the beam position could be directly determined as a dark mark appeared on the tablets exactly where the beam was impinging. This real-time visual feedback further ensured the accuracy of the beam positioning throughout the experiment.

3.5.3 Experimental set-up

The purpose of this experiment is measuring β^+ isotopes which emits two 511 keV photons in opposite directions when they decay. The experimental set-up was designed in order to take advantage of this spatial correlations, just as PET scanners do, facing detectors to measure both photons in coincidence. Because of this reason, our experimental set-up is composed by 4 detectors placed at 60, 120, 210 and 300 degrees with respect to the beam directions, so that they are facing each other two by two (see Figure 3.9). The target is placed in the center, 4 centimeters far from the front face of the detectors. This configuration will allow measuring in coincidence only emissions from the target, removing any background contribution due to the beamline activation. However, the coincidence detection efficiency was very low and could not be used in the analysis.

Energy (keV)	Efficiency (%)				Energy resolution (%)			
	Det 1	Det 2	Det 3	Det4	Det 1	Det 2	Det 3	Det4
121.8	1.23	1.49	1.21	1.39	27.8	30.0	16.9	15.63
244.7	0.91	0.90	0.83	0.89	12.15	13.73	9.09	8.22
344.3	0.71	0.73	0.65	0.70	9.15	10.65	6.99	6.33
511.0	0.47	0.46	0.43	0.46	6.87	6.95	5.01	4.98
778.9	0.31	0.32	0.30	0.31	5.16	5.81	3.83	3.78
964.0	0.26	0.25	0.26	0.23	4.35	4.84	3.51	3.31
1408.0	0.21	0.20	0.21	0.19	4.03	4.41	3.31	3.03

Table 3.5: Experimental efficiency and energy resolution of each of the detectors for every γ-lines from ^{152}Eu. Remarked the efficiency and the resolution at 511 keV. In the case of efficiency it was interpolated from the experimental data.

The efficiency of this set-up has been measured using a calibrated ^{132}Eu source to determine the exact efficiency of each detector-PMT pair. We measure this source for more than 12 hours, which allows us to obtain the efficiency from 144 to 1406 keV with high accuracy. Using the same measurement, we also calculate the energy resolution of each detector individually as the full width half maximum (FWHM) divided by the energy peak. The results of efficiency and energy resolution resolution are shown numerically in Table 3.5 together with the interpolated data for the 511 keV.

3.5.4 Irradiation and Calibration

The targets were irradiated with proton energies ranging from below the energy thresholds up to 10 MeV. Table 3.4 provides the energy thresholds, with the lowest threshold being 5.05 MeV for NaCl and 6.94 MeV for KCl. The reaction channel with the lowest energy threshold, ^{23}Na(p,n)^{23}Mg, has been extensively measured in previous studies and will serve as a crosscheck for the other measurements. To ensure comprehensive coverage of the energy range, measurements were conducted in 0.5 MeV steps from 5 to 7 MeV. For energies above 7 MeV up to 10 MeV, where the other two reactions become physically possible, the steps were further reduced to 0.25 MeV to obtain more accurate cross-section values for these reactions.

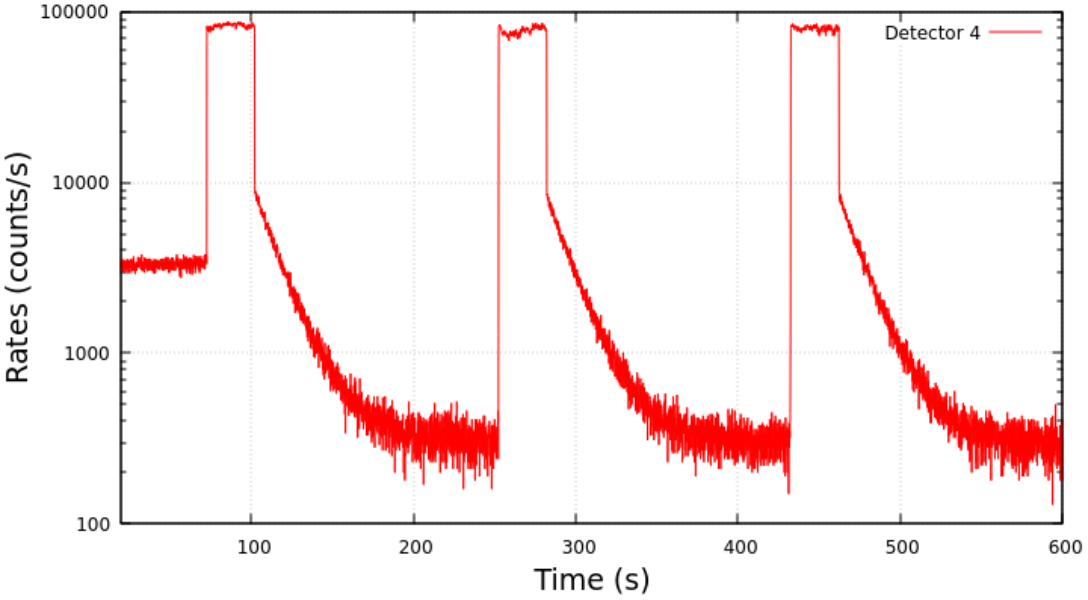

Figure 3.10: Rates during the irradiation of a NaCl sample with 7 MeV. Three decays are dominated by the ^{23}Mg ($t_{1/2}$). Rates during the irradiation reach values of 80-90 KHz, but as soon as the beam is off, the rates decrease sharply and during the following minutes a smooth decay is observed. The high rates before the first cycle are due to the Faraday cup which is placed closed to the setup.

Independently of the beam energy, the process for irradiation is the same. First, the background was measured with the target in position for 5 minutes to identify possible contaminants or background from the beam line. After this time, the target is irradiated for a time equivalent to 3 times the half-life of the longest produced PET isotope in the sample, 30 seconds for the NaCl and 10 seconds for the KCl. After the irradiation process is complete, the activated samples were measured for a time equivalent to ten half-lives of the isotope with the longest half-life, which ensures that more than 99.9% of the generated isotopes have decayed. To increase up the statistics of the measurement, this process was repeated several times and the final results were calculated as the accumulation of all the decays from each cycle. As an example, the measured total rates obtained during the irradiation of a NaCl sample with a 7 MeV proton beam are shown in Figure 3.10.

The beam current was measured before and after each irradiation with a Faraday cup placed at the end of the beam line. This Faraday only works by stopping the beam, therefore, there is no beam current information during the irradiation. Beam

current values were measure just before and after each irradiation to check the stability of the beam. As an additional cross-check, the measure rates, which are proportional to the current, were studied after each irradiation to identify current deviations during the irradiation. If any of these two validations noted an unstable behavior the measurement was repeated.

3.5.5 Analysis

The analysis of the measured data to obtain the thick target yields is similar to that of the previous experiment (section 3.4.6). However, there was one crucial difference: the non-thick approximation was not applicable in this case due to the complete stopping of the beam in the target.

The first step is the extraction of thick target yields using the yield formula (Eq. 3.1). Since measurements were performed online, no cool-down time needs to be considered. Furthermore, the measured time is long enough ($t_m > 10t_{1/2}$) to consider the full integration of the activity, thus is contribution is not taken into account. Thus, these terms can be neglected resulting in the following expression

$$Y(E) = \frac{A}{I^{\gamma}\epsilon_t\phi\,(1 - e^{-\lambda t_{irr}})} \tag{3.5}$$

where A is the initial activity of the β^+ isotope, ϵ_t is the efficiency of the detectors, ϕ is the proton flux, and I^{γ} the emission probability of the studied emission.

The initial activity (A) was calculated using the accumulated decays of the irradiated samples. For each energy and sample, the decay was fitted to two exponential functions with different *lambda* parameters, associated with each of the isotopes present in the decay: ^{23}Mg and ^{35}Ar in the NaCl; and ^{39}Ca and ^{35}Ar in KCl samples. In the same way as in the previous experiment, this fitting is not performed using the total rates, but the rates in the energy window of the 511 keV peak. This energy window was defined as the center of the Gaussian $\pm\, 3\sigma$. The fits for both samples irradiated with 9.5 MeV are shown in Figure 3.11 along with the initial activities obtained from the fit. The results show that measured data fit well to the decay of two independent components in both cases. However, in the case of NaCl, the intensity of the ^{35}Ar component is comparable to the background levels, and there is a 50% margin of error, which leads us to exclude these results from the analysis of this channel. The production of ^{35}Ar and ^{39}Ca will be

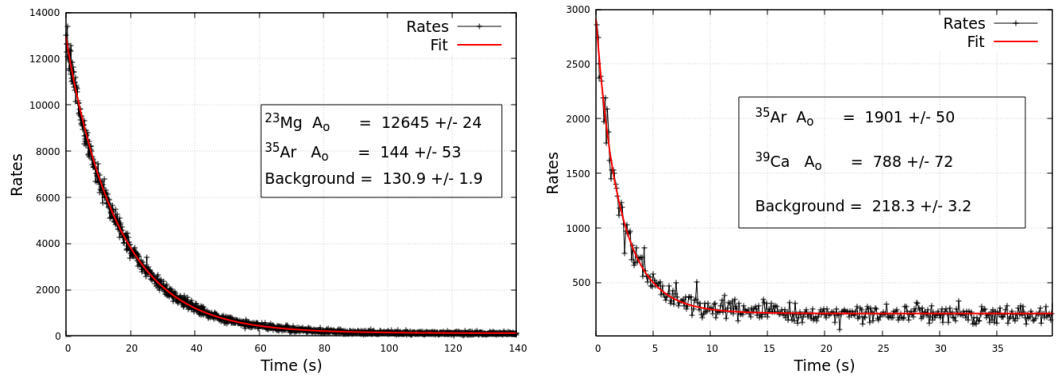

(a) NaCl - 9.5 MeV **(b)** KCl - 9.5 MeV

Figure 3.11: Accumulated decay for the NaCl and KCl samples irradiated with a 9.5 MeV proton beam. In red, the fits to an exponential decay with two components with the half-lifes of each β^+ isotope fixed. The obtained initial activities and the background from the fits are show in the graphics.

studied using KCl and NaCl will be used only as a cross-check due to the production of ^{23}Mg.

Once the initial activity is obtained, yields are obtained from equation 3.5. The total yield production is given by the mean value, because the spatial distribution of the 511 keV photons emitted in a β^+ decay is isotropic. The last step in this analysis is the calculation of the cross-section from the total yield production. The correlation between these two quantities is described by the following expression, which cannot be used directly without first applying some approximation.

$$Y = \rho_{at} \int_{E_i}^{E_f} \sigma(E') \left(\frac{dE'}{dx} \right)^{-1} dE', \tag{3.6}$$

In this experiment, the thick target approximation is applied. This approach is valid if the target is thick enough to stop the whole beam, and also if the measured energies are close enough to one another to assume a linear behavior of the stopping power. The thickness of the targets used in this experiment ranges from 1.5 to 2 millimeters, while the maximum range of protons in the most energetic case is less than one millimeter. Additionally, the energies used for irradiation are separated by no more than 0.5 MeV. These factors ensure that all the protons are stopped in the target and that the stopping power behaves linearly within the range of measured energies. This approach allow us to calculate the cross-section values with the thick target approach using two consecutive

yield measurements

$$\sigma(\overline{\mathrm{E}}) = \frac{Y(E_2) + Y(E_1)}{(E_2 - E_1)\rho_{at}} \left(\frac{d\overline{\mathrm{E}}}{dx}\right) \tag{3.7}$$

where E_2 is the highest energy, E_1 the lowest and $\overline{E}$ the average. The uncertainty of the cross-section was calculated using a nuisance analysis.

Positron annihilation

Positron annihilation deserves special attention in this experiment. The emitted positrons in the β^+ decays studied in this section have considerably high energies (Table 3.6). The ranges associated to these energies are several millimeters in NaCl and KCl, which implies that emission of the 511 keV photons, as a consequence of the positron annihilation, can not be considered a point source where the beam impinged the target. In addition, the large range of the emitted positrons may lead to the positron escaping the target and annihilating in the air or in any component of the set-up. All of this results in a loss of efficiency with respect to that calculated using the ^{152}Eu point source, which needs to be corrected.

Isotope	Mean Energy (keV)	End-point (keV)	Branching
^{23}Mg	1143.84 *19*	2594.0 *4*	7.84 % *11*
	1353.91	3034.18 *3*	92.08 % *11*
^{35}Ar	1691.20 *35*	3724.9 *7*	1.23 % *3*
	2284.46 *35*	4944.1 *7*	98.16 % *5*
^{39}Ca	2558.27 *30*	5502.5 *6*	99.92 % *3*

Table 3.6: Main properties of positrons emitted in the studied reactions: average energy, end-point energy and branching ratio.

It must be noted that this effect only applies to the 511 keV photons. Gamma-rays from nuclear excited levels will be emitted from where the reaction took place, and the point source approximation can be still considered. Therefore, the presence of any other gamma-ray can be used to correct the efficiency loss at 511 keV, comparing the ratio between the detected 440 keV and 511 keV counts with the expected theoretical value. However, the only reaction that has any identifiable emission other than the annihilation photons is the ^{23}Mg, which also emits a 440 keV with a 7.85 % branching

ratio. The expected value for the ratio of both peaks is 0.039, while the experimental is 0.055 ± 0.002. Only about 70% of the 511 keV photons emitted are detected.

A similar correction is required for the ^{35}Ar and the ^{39}Ca. In the absence of experimental data, the use of simulations is necessary. We recreate the experimental set-up to simulate with *Penmain* the efficiency of each detector in two different scenarios for each isotope: 1) A point source of 511 keV photons placed in the center of the target, which emulates the efficiency obtained from the experimental measurement with the ^{152}Eu. 2) A positron source placed at the front face of the target, recreating the experimental scenario. The positron source has an energy spectrum ruled by the details of Table 3.6. The comparison of these two results provides the number of 511 keV photons that are lost due to the positron range. These simulations have also been performed for the ^{23}Mg as crosscheck.

The results obtained from the experimental data and simulations are shown in Table 3.7. The values obtained for the ^{23}Mg indicate a great match between the experiment and simulations. This gives reliability to simulations, enabling its use in the other cases. An error of 5% was assumed for the simulated parameters. These corrections were introduced in the analysis as part of the efficiency.

Isotope	511 keV Efficiency	
	Simulations	Experimental
^{23}Mg	72 %	69.8 ± 2.5 %
^{35}Ar	42.6 %	-
^{39}Ca	39.6 %	-

Table 3.7: Experimental and simulated percentage the emitted 511 keV photons detected

3.5.6 Results

The main results of this experiment are the cross-sections values calculated for the production of ^{35}Ar and ^{39}Ca. In order to validate these measured cross-sections, we first used the reaction channel ^{23}Na(p,n)^{23}Mg as a benchmark. Figure 3.12 shows in green the cross-sectional values obtained in this work and some of the previous measurements available in the EXFOR database. The results from this experiment are

in good agreement with previous measurements, which indicates that the experiment was carried out correctly and therefore its results are reliable.

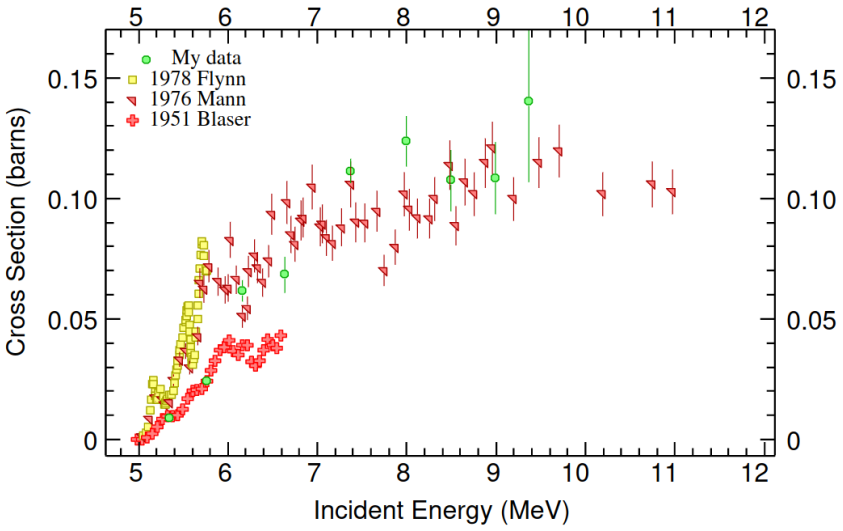

Figure 3.12: ^{23}Na(p,n)^{23}Mg Cross-section measurements in this work (green) along some of the available previous measurements in EXFOR.

The ^{35}Cl(p,n)^{35}Cl has never been measured before and the only available estimation of the expected values is the theoretical calculation by TENDL. Figure 3.13 shows the obtained cross-sections values in this experiment along the TENDL estimation. The results do not coincide with the theoretical calculation, but are in the same order of magnitude.

The last studied reaction is the ^{39}K(p,n)^{39}Ca, which has already been measured once up to 12 MeV. Figure 3.14 shows the data measured in this experiment (red), the data from the previous experiment (blue) and the theoretical estimate of TENDL (black line). The results do not agree exactly with either the experimental data or the TENDL estimation. It must be noted that only in the two most energetic cases the fitting identify two components in the decay with the half-lifes as a free parameter (see Figure 3.11b). At lower energies, the fit only identify the decay of ^{39}Ca fixing its $t_{1/2}$, which could have introduced biased information, leading to erroneous initial activities from ^{39}Ca. Therefore, the results for this channel are not totally reliable and the experiment should be repeated using a target in which this only channel contributes to the activity.

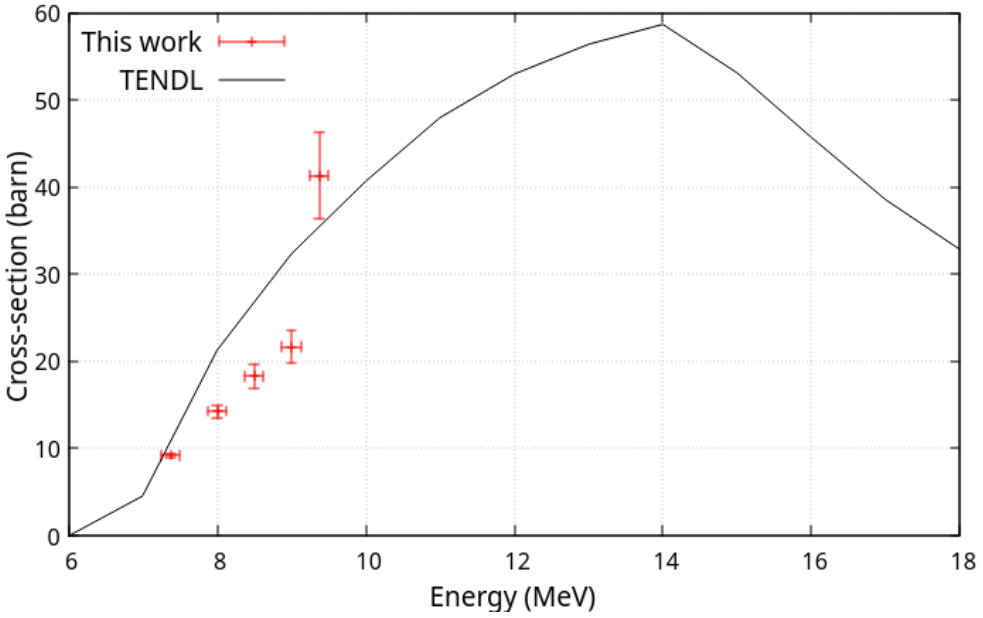

Figure 3.13: ^{35}Cl(p,n)^{35}Cl Cross-section measure in this experiment in red along the theoretical prediction by TENDL.

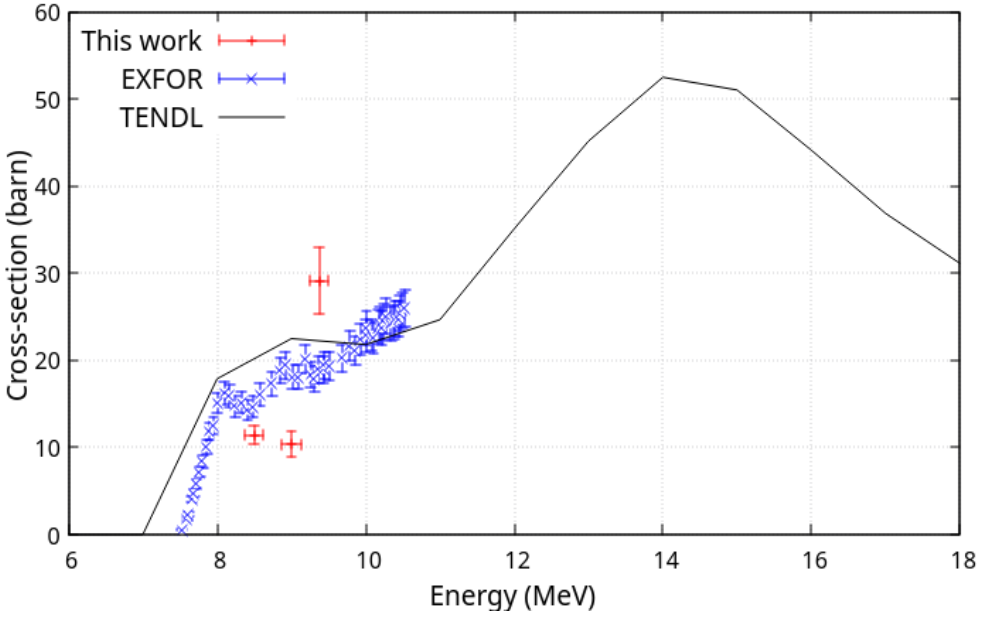

Figure 3.14: ^{39}K(p,n)^{39}Ca Cross-section measurements in this work in red together with the only other available measurement (blue) and the theoretical forecast of TENDL (black line).

3.6 PG thick-yield measurements at low energies

In this thesis, we propose the use of ^{18}O as PG contrast agent, which has never been studied before. A comprehensive experimental campaign was conducted at CMAM with the objective of thoroughly mapping the cross-sections and angular distribution of prompt gamma (PG) emissions yield originating from ^{18}O nuclei under proton incident energies below 10 MeV. Five different PG have been identified, measured and studied. Among the five incident proton energies considered in the experiment, three of them were in proximity to 1 MeV, while the remaining two energies were 1.9 MeV and 5.3 MeV, respectively. In addition to mapping the yield production, we successfully obtained measurements of the angular distribution of the emitted prompt gammas.

3.6.1 External micro beam-line - CMAM

This experiment was carried out at the Centre for Micro Analysis of Materials (CMAM) in Madrid. In this facility there is a 5-MV tandetron capable of producing protons beams up to 10 MeV. They have 6 different beam-lines, each one specifically mounted with certain characteristics for different purposes. Among all of them, we chose the micro beam-line for similar reasons as in the experiment for low cross-sections of β^+ emitters.

The horizontal beam spatial distribution follows a normal distribution described by sigma of a few hundreds of microns, which enables the consideration of the point source approximation in the analysis. Another notable advantage of this beamline is its capability to modulate the beam intensity across a wide range, spanning from a few hundred pA to several nA. This remarkable feature allows for precise control over the beam intensity, enabling the generation of an optimal count rate in the detectors at any time. Finally, we also made use of the 40x40 cm^2 motorized and remote controlled platform to perform alignments from the control room.

3.6.2 Target and alignment

The objective of this experiment was to study water-18, which is a mixture consisting of 70% $H_2^{18}O$ and 30% $H_2^{16}O$. To conduct the experiment, the water-18 sample was placed in a cylindrical plastic vessel with a volume of 600 μL and a radius of 3 millimeters. The narrowness of the container results in a high surface tension, ensuring that the liquid remains confined even when the vessel is positioned horizontally. This is essential

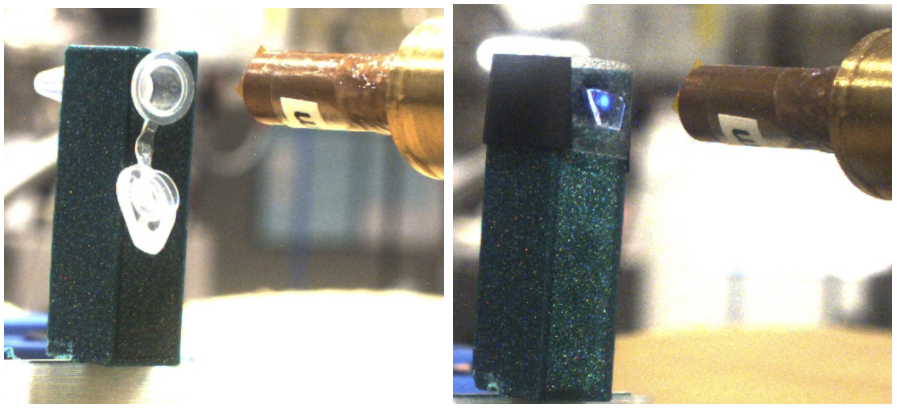

(a) Sample **(b)** Alignment

Figure 3.15: Experimental setup. a) Vessel colocation in a 3D-print support placed at the geometrical centre of the set-up, 10 cm far from each of the detectors. b) Alignment set-up with a fluorescence material due to proton irradiation at a low energy beam (2 MeV). This process was systematically repeated along the experiment to ensure the aligment.

because both the liquid sample and the proton beam need to be aligned horizontally to the ground, as depicted in Figure 3.15a. The vessel was filled with 450 μL of water-18, which allowed the liquid to be in proximity to the opening while preventing any risk of leakage. Since the focus was on the prompt gamma (PG) emissions, the same sample was used for multiple measurements as the residual activity from β^+ emitters did not affect the online measurements. However, for safety purposes, the target was replaced once the radioactive levels reached a certain intensity.

The alignment between the beam and the target is essential because it must reach the water-18 inside the vessel without touching its walls. The alignment was performed using a quartz layer, a luminescent material that emits blue light when it is irradiated with proton (see Figure 3.15b). The beam size is small enough to travel through the vessel opening to the water-18 without touching it. The platform position was fixed once the alignment was performed and cross-checked it several times during the experiment. This rigorous approach ensured that the beam consistently and accurately targeted the desired location, maintaining the reliability and precision of the experimental measurements.ed.

3.6.3 Experimental set-up

The main goal of this experiment is the measurement of angular distributions and the yield productions of PG emissions coming from the irradiation of ^{18}O during irradiation. The detector system is shown in Figure 3.16a. Detectors and target are fixed over a wooden board thanks to 3D-printed holders. Detectors front face are 10 cm far from the irradiated target and rotated 15^{o}, 40^{o}, 90^{o} and 115^{o} with respect to the beam direction (Figure 3.16b) to obtain the angular distribution of Prompt-Gammas.

Contrary to previous sections, the detection system in this experiment was set to measure γ-rays up to 7 MeV. Therefore, it was necessary to calibrate the spectrum and to determine the detection efficiency of the set-up up to 7 MeV. A source of ^{152}Eu was used for both calibrations up to 1408 keV, the highest energy emitted by this source.

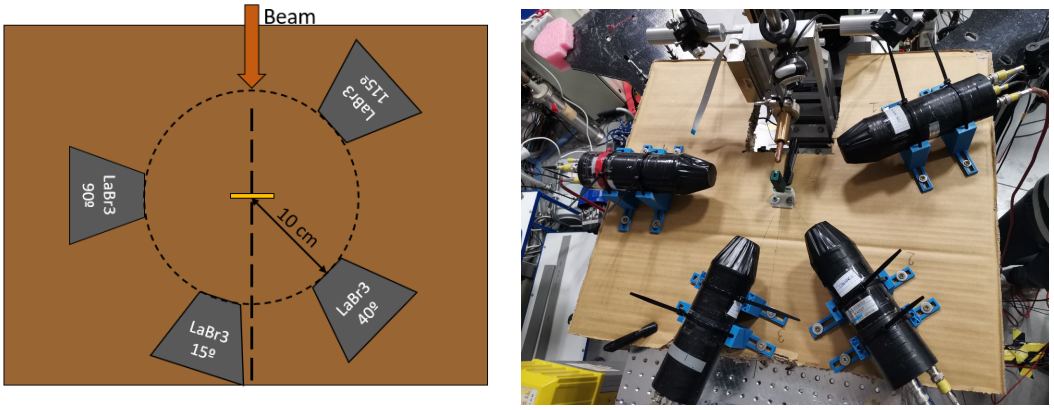

(a) Scheme Set-up **(b)** Set-up

Figure 3.16: Image and scheme of the experiment setup. In the center is placed the vessel support 10 cm far from each of the detectors ($LaBr_3$). Detectors are placed at 15, 40, 90 and 115 degrees with respect to the beam direction to measure the angular distribution of the emitted PGs. They are fixed with 3D-printed supports to the table, so the experiment is totally reproducible. They are also coated with black tape to protect them from the light.

- **Energy Calibration**

The energy calibration of the whole energy range was performed using the ^{152}Eu measurements and high energy known γ-rays, the 4.44 MeV γ-line from ^{12}C, the 6.13 γ-line MeV from ^{16}O, which are easily identifiable in water and plastic samples. $LaBr_3$(Ce) spectrums are usually calibrated following a quadratic equation for the whole energy

range, but the result of a single fit to the entire spectrum plotted in 3.17 clearly demonstrates that it fails to accurately fit the data. To solve this issue, two different quadratic calibrations were conducted, each one tailored to the corresponding low and high energy ranges.The energies employed in these calibrations are illustrated in Figure 3.17, along with the low and high energy fits which cross at 2566 keV. The final calibration is given as a combination of both fits. The low energy fit is applied from 0 keV until where it crosses with the second fit for high energies at 2566 keV. From this point, the high energy calibration is applied to the spectrum.

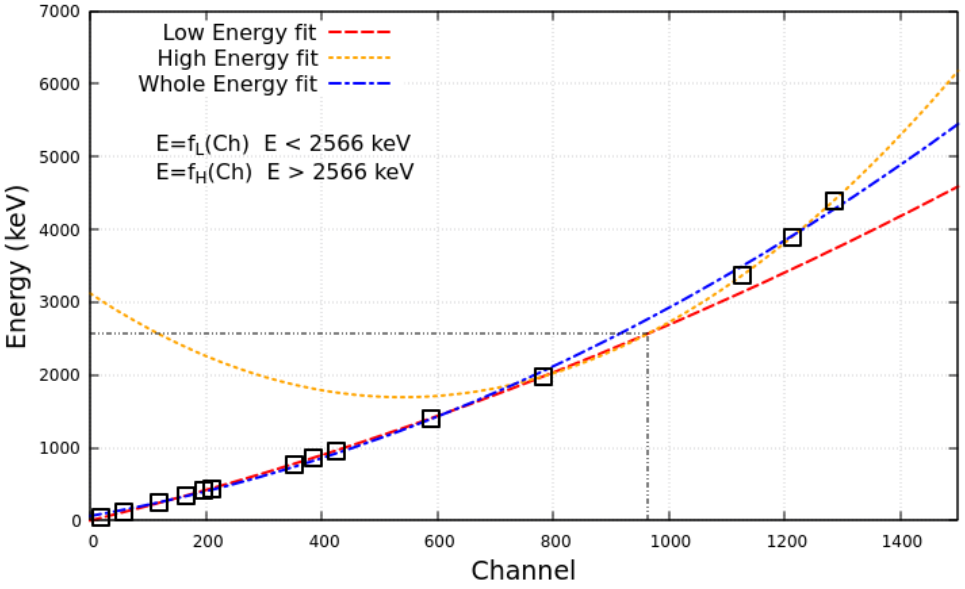

Figure 3.17: Spectrum energy calibration from 0 to 7 MeV. Black square dots represents the channel-energy correlation extracted from a ^{152}Eu spectrum and from the irradiation of a plastic material mainly composed by carbon.The red dashed line represents the fit using only the data below 2 MeV, while the orange dotted line represents the fit over this energy range. On the other hand, the blue solid line represents the fit of the entire interval using a single function, which does not provide a good fit to the data.

- **Efficiency Calibration**

The set-up efficiency was also determined experimentally using the same ^{152}Eu source up to 1408 keV. There was no calibrated source available for higher energy emissions, necessitating the theoretical calculation of efficiency using Monte Carlo (MC) simulations. The setup was replicated in a Monte Carlo simulator called *Penmain*, based on PENELOPE [Salvat, 2013], to conduct simulations and calculate the full energy

detector efficiency at various energies. The selected simulated energies covered the entire energy spectra up to 7 MeV and were aligned with experimental measurements at lower energies to ensure comparability. This way, it is possible to contrast if simulated efficiencies match the efficiencies at low energies to use them at high energies.Figure 3.18 displays the experimental efficiencies (represented by blue dots) obtained from the ^{152}Eu source, as well as the simulated efficiencies (represented by red dots) from Penmain. The perfect alignment of the two datasets at low energies indicates the reliability of the simulated results at higher energies.

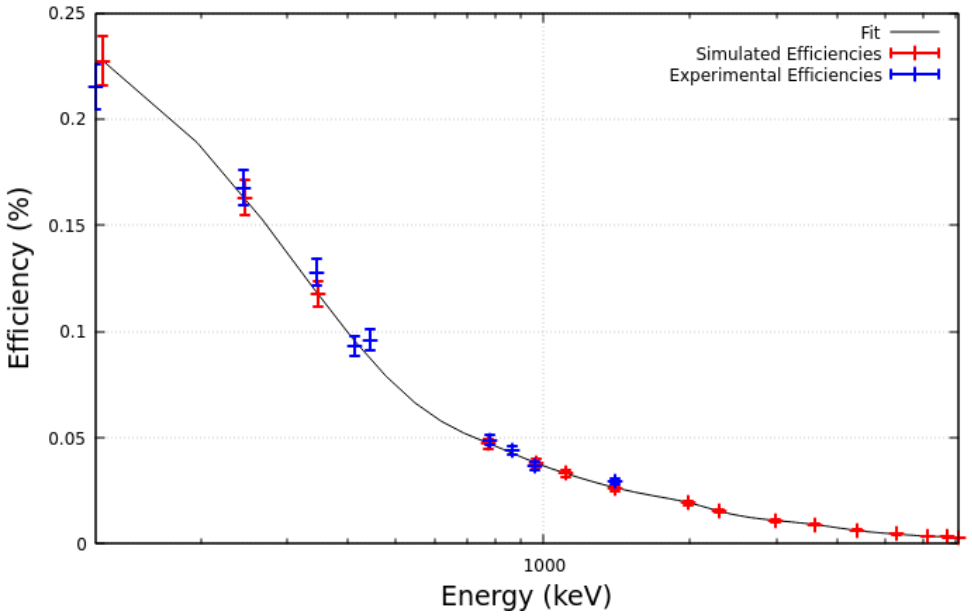

Figure 3.18: Detector efficiency as function of energy. Blue dots present the experimental values obtained from the spectrum of a calibrated ^{152}Eu source. Red dots are the simulated efficiencies obtained using *Penmain*. The line is a fit to the simulated results to obtain the efficiency of the set-up at any energy.

3.6.4 Irradiations

The water-18 was irradiated with protons from 3 to 10 MeV in 0.25 MeV steps, and the same procedure was followed in every measurement. The measurement began with a 3-minute measurement of the background, followed by a 5-minute irradiation of the target. The beam current used in this experiment are between 0.5 and 30 nA depending on the beam energy, in order to maintain the count rate in each detector stable between 10k-

20k counts per second. Beam intensity could not be measured during the irradiation, so it was recorded just before and after of each irradiation. As an additional cross-check, the count rate during the irradiation was taken into account. If some of these two tests indicated that the intensity varied during the irradiation, the measurement was repeated.

Distilled water was also irradiated from 3 to 10 MeV, but in this case with 1 MeV steps. The purpose of these measurements was to identify the specific gamma-ray lines originating from ^{16}O which also appear in the water-18 irradiations.

3.6.5 Analysis

The final aim of the experiment is to calculate the experimental values of the cross-section and angular distribution. However, from the experimental data, it is only possible to obtain the γ-ray production yields, which can be related to cross-section as it was explained in section 1.1.4 using the following equation.

$$Y_{tot}(E) = \rho_{at} \int_{E_0}^{E_f} \sigma(E) \left(\frac{dE}{dx}\right)^{-1} dE \tag{3.8}$$

The first step of the analysis is the determination of the production yields for each PG. The more general expression for the yield production of radioactive samples (equation 3.1) can be adapted to this case by simply considering the prompt emissions.

$$Y_\theta(E) = \frac{N}{\epsilon \phi t_{irr}} \tag{3.9}$$

where $Y_\theta(E)$ is the yield production of the detector placed at θ degrees with respect to the beam direction. N is the number of counts in the photo peak, ϵ is the full energy efficiency at γ-line energy, ϕ is the proton flux and t_{irr} is the irradiation time. The total number of counts in the photopeak (N) was calculated by fitting to Gaussian with background. In the case of 1040 and 1080 keV, the two peaks partially overlap, but it is still possible to resolve them using a two Gaussian fit, as shown in Figure 3.19.

Uncertainties and errors of variables in equation 3.9 were studied carefully as a combination of statistical and systematic errors. ϵ_t and N errors were obtained from experimental data fit. In the case of the efficiency values at high energies calculated with MC simulations, a systematic error of a 5% was assumed because statistical errors from simulations were too low. Irradiation time has a systematic error below 0.1 seconds, as

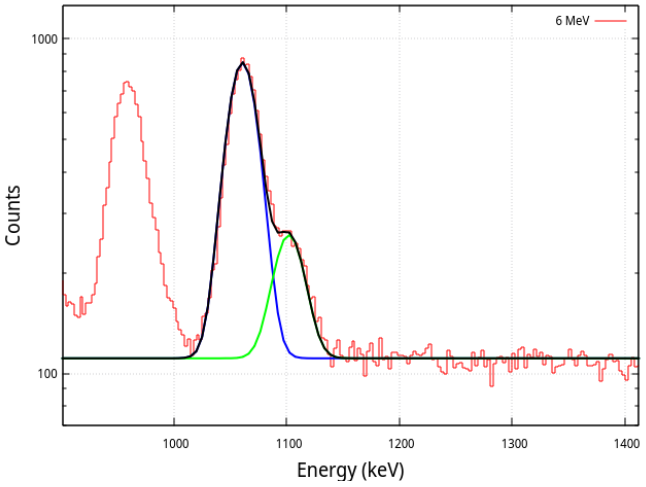

Figure 3.19: Double Gaussian fit of the 1040 and 1080 keV gamma-lines coming from the irradiation of water-18. The energy resolution of the detectors is enough to resolve both peaks and to study its contribution separetly.

we are able to determine the beginning and the end of the irradiation with the count rate with high accuracy. Th source uncertainty with the highest impact is the beam current. Its systematic error is 0.1 nA, but an additional 5% of the current value was assumed due to the current beam instability. At low energies, where a high beam current was used for sample irradiation, the relative error remains at the assumed 5%. However, at high energies, where the beam current has been reduced to 0.5 nA, the relative error increases significantly to 30%.

PG emissions induced by an ionizing beam are not isotropic, but will have a certain angular distribution with respect to the beam direction [Dyer et al., 1981]. The angular distribution of a PG induced by an ionizing beam is given by

$$W(\theta) = \sum_{l=0}^{l=L} a_l P_l(cos(\theta)) \qquad l = even, \tag{3.10}$$

where θ is the angle with respect to the beam direction, P_l are the Legendre polynomials and L is the smaller of these two values: 1) twice the spin of the decaying state; 2) twice the multipolarity of the gamma ray [Dyer et al., 1981]. This equation shows that angular distribution depends only on the even Legendre polynomials, which means that the emission is symmetric with respect to the specific direction given by the beam. Furthermore, most of the gamma lines studied in this work have a L value no greater

γ (keV)	Reaction	Isotope	Level (keV)	J^π	M (γ)	L
937.20 *6*	p,p'γ	^{18}F	937.20	3^+	E2	4
1041.55 *8*	p,nγ	^{18}F	1041.55	0^+	M1	2
1080.54 *12*	p,nγ	^{18}F	1080.54	0^-	E1	2
1982.07 *9*	p,nγ	^{18}O	1982.07	2^+	E2	6
5269.16 *14*	p,$\alpha\gamma$	^{15}N	5270.15	$5/2^+$	M2+E3	6
5237.82 *14*	p,α	^{15}N	5298.82	$1/2^+$	E1	2

Table 3.8: Main properties of the 6 studied gamma-lines coming from the irradiation of ^{18}O. For each of them we how in this table the reaction channel, the resulting isotope, the excited energy level, the spin of this level, the multipolarity transition and the obtained L value.

than 4 (see Table 3.8), which implies that equation 3.10 never has more than three components and it is possible to fit it with 4 experimental values associated to different values of $|\cos\theta|$. That is the reason why detectors are placed at 15º, 40º, 90º and 115º (equivalent to 65º). The parameters a_l are obtained from the fits and they determine the angular distribution. The total yield is calculated as the integral over the space of equation 3.10, which is always $4\pi a_0$ independently of the L parameter.

$$Y_{tot} = 4\pi a_0 \tag{3.11}$$

The last step in the analysis is the calculus of the cross-section using the expression 3.8, which correlates total yield and cross-section. In the experiment, we use the thick target approximation:

$$\sigma(\overline{\mathrm{E}}) = \frac{Y(E_2) + Y(E_1)}{(E_2 - E_1)\rho_{at}} \left(\frac{d\overline{\mathrm{E}}}{dx}\right) \tag{3.12}$$

where E_2 is the highest energy, E_1 the lowest and $\overline{E}$ the average. The uncertainty of the cross-section was calculated using a nuisance analysis.

3.6.6 Identification of γ-rays

The identification of γ-rays is an important part in the analysis of the experimental data. This process must be done carefully because all the emissions do not come from the target. The beam line is activated during the irradiation, and there could also be

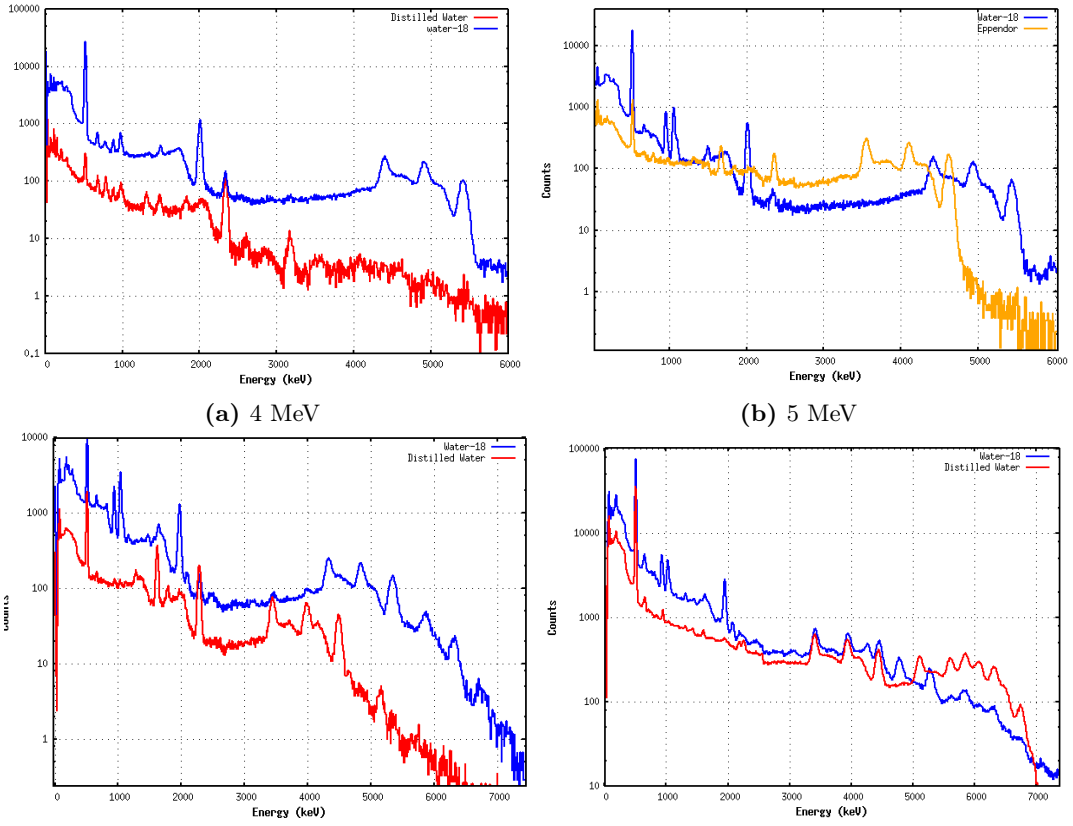

(a) 4 MeV **(b)** 5 MeV

(c) 7 MeV **(d)** 10 MeV

Figure 3.20: Gamma-ray spectra observed for the bombardment of the water-18 target with several proton energy beams. The target and the energy beams are shown.

contaminants in the sample which induce additional PGs in the spectrum. In order to identify every peak in the spectra and determine the expected PGs in Table 3.8, a detailed study has been carried out using irradiations from 4 to 10 MeV on three different materials, distilled water, water-18 and plastic.

Figure 3.20 illustrates four of the spectra employed in the γ-ray identification process. The first image shows the measured spectra of water-18 and distilled water with 4 MeV protons. Four low intensity peaks are observed in both spectra between 600 and 1000 keV. These γ-lines are associated to the beam line activation, which introduces them as background component. Apart from them, there is a high intensity peak at 2.3 MeV in both spectra, which has been related to the first excited level of ^{14}N. This isotope appears as a contaminant and its presence also explain the peak at 1.6 MeV. In the water-18 spectra, 4 peaks are identified which do not appear in distilled water. One

Energy (keV)	Target	Reaction	Q-value
184	^{18}O	(p,n)^{18}F*	-3559.6
940	^{18}O	(p,n)^{18}F*	-3378.3
1041	^{18}O	(p,n)^{18}F*	-3479.3
1081	^{18}O	(p,n)^{18}F*	-3529.3
1635	^{14}N	(p,p')^{14}N*	-3948.1
1982	^{18}O	(p,p')^{18}O*	-1982.9
2312	^{14}N	(p,p')^{14}N*	-2312.8
4439	^{12}C	(p,p')^{12}C*	-4439.8
5270	^{18}O	(p,α)^{15}N*	-1291.2
5298	^{18}O	(p,α)^{15}N*	-1219.4
6128	^{16}O	(p,p')^{16}O*	-6129.3
6323	^{18}O	(p,α)^{15}N*	-1219.4

Table 3.9: Every γ-line identified in the spectrum with information of the parent nucleus, the reactions which produce them and the Q-value of each reaction.

of them, very close to 2 MeV, is the 1984 keV γ-line from the first excited level of ^{18}O. The other three peaks are related to the 5.3 MeV γ-line from the first excited level of ^{15}N and its single and double escape peaks. This isotope is produced from water-18 in the ^{18}O(p,α)^{15}N reaction channel.

Four new peaks were identified from the irradiation of water-18 and a predominantly carbon-based compound in the second figure. The 4.44 MeV PG from ^{12}C first excited level is visible in the spectrum, along with its two escape peaks. Water-18 spectra shows 3 peaks close to 1 MeV which were not observed at 4 MeV. These peaks are the 940, 1040 and 1080 from the first three nuclear levels of ^{18}F. The third image show sthe spectra of distilled water and water-18 samples irradiated with 7 MeV. In the water-18 spectra a peak close to 6.2 MeV is observed. It was assigned to the second excited level of the ^{15}N. The last image corresponds to irradiation of water and water-18 with 10 MeV. No additional peaks are observed from the water-18 sample. However, in the distilled water spectra, both the 6.1 MeV and 6.7 MeV peaks from the first and the second excited levels of ^{16}O are clearly visible. Identified peak and the reaction that induces it are shown in Table 3.9.

3.6.7 Results: Angular distributions

Angular distributions have been calculated for every PG emitted from the irradiation of ^{18}O. In the case of 1040 and 1080 keV PGs, yield values from the detector number 3,

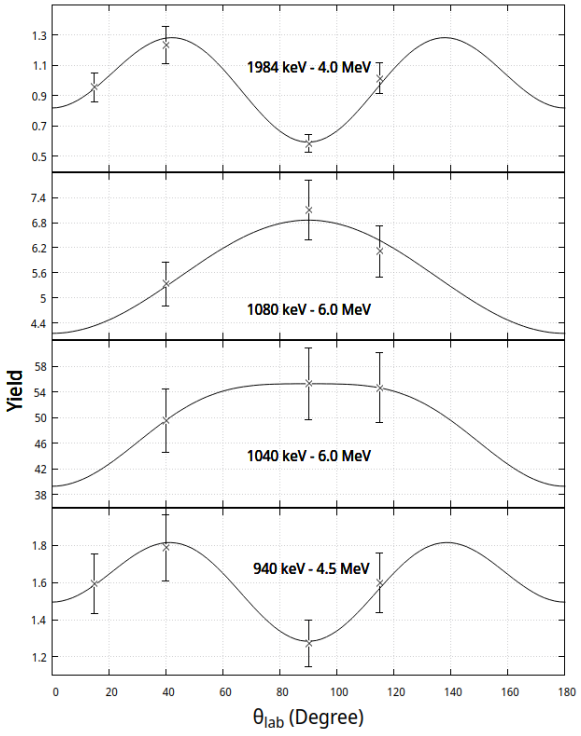

Figure 3.21: Gamma-ray angular distribution observed for the bombardment of the water-18 with several proton energy beams. The gamma-ray energy and the energy used for irradiation in each case are shown in each graph.

placed at 15^{o} with respect to the beam direction, had to be removed from the analysis because due to the deterioration of the energy resolution in this detector, it was not possible to resolve both peaks.

The distributions have been obtained independently for each energy separately and the experimental results of all a_l parameters are show in the Appendix A.1. Figure 3.21 displays the angular distribution of each PG at the lowest energy in which they can be determined in the spectrum. This approach ensures that all emissions arise from the direct population of the level excited by the proton beam. Angular yields values has a low uncertainty, and because of that, the fitted a_l parameters also have low errors.

Looking in more detail at the form of the angular distributions, we can relate each of the gammas with its electromagnetic transition multipolarity (Table 3.8). In the case of the 1040 and 1080 keV gammas with a M1 and E1 transition, a maximum emission at 90 degrees was expected. On the other hand, in the case of the gamma lines of 940

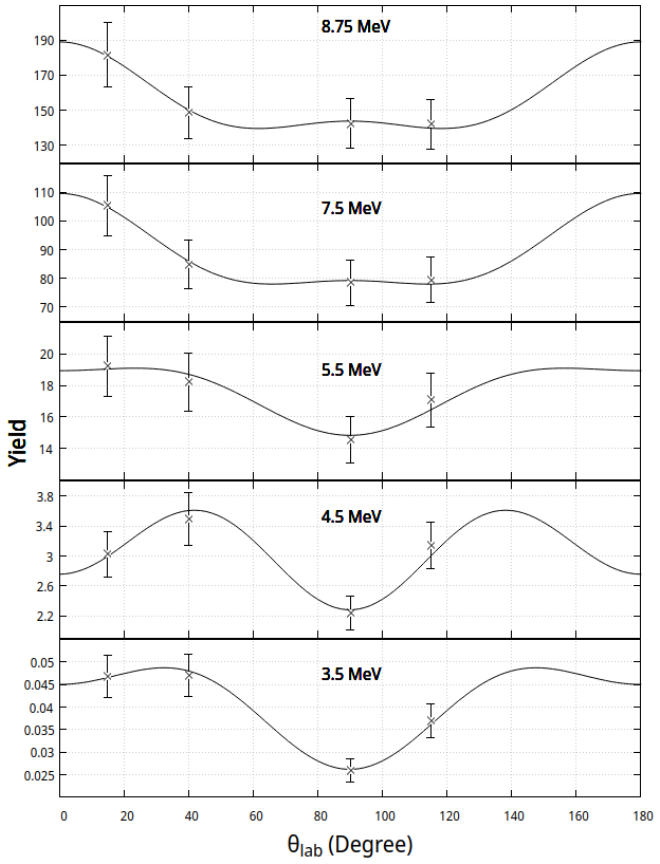

Figure 3.22: Gamma-ray angular distribution observed for the bombardment of the water-18 with several proton energy beams. The gamma-ray energy for every case is 1984 keV and the energy used for irradiation in each case is shown in each graph.

and 1982 keV, both have an E2 multipolarity and the expected maximums should be at 45 and 135 degrees. In every case, the fits represent the experimental data. This indicates that the multipolarity induced by the beam is well described by the equation 3.10 and the assumptions of Dyer et al. [1981].

The analysis of angular distributions led to an unexpected result, the angular distribution changes as the incident energy increase. Previous and similar experiments [Dyer et al., 1981; Lang et al., 1987; Lesko et al., 1988; Kiener et al., 1998] do not mention this behavior, but they did appreciate it. This effect has been observed in every γ-ray emission. Figure 3.22 shows the specific case of the 1984 keV PG emitted from the first excited level of ^{18}O. Its transition is an M2, so the expected distribution should present two maximum emission peaks at 45^{o} and 135^{o} as it is observed at incident energies

of 3.5 and 4.5 MeV. However, as the energy increase, this shape is fading away. We attributed this phenomenon to the population of the 1984 keV level from nuclear levels with higher energies. The angular distribution is given by the momentum transfer from the beam to the excited level. But if it is indirectly populated from more energetic levels, the momentum transfer disappear and the angular distribution changes.

3.6.8 Results: Yields and Cross-sections

Experimental yield values were calculated from angular distributions using equation 3.11. Figure 3.23 shows the experimental yields obtained in this experiment for the 940, 1040, 1080 and 1984 γ-rays.

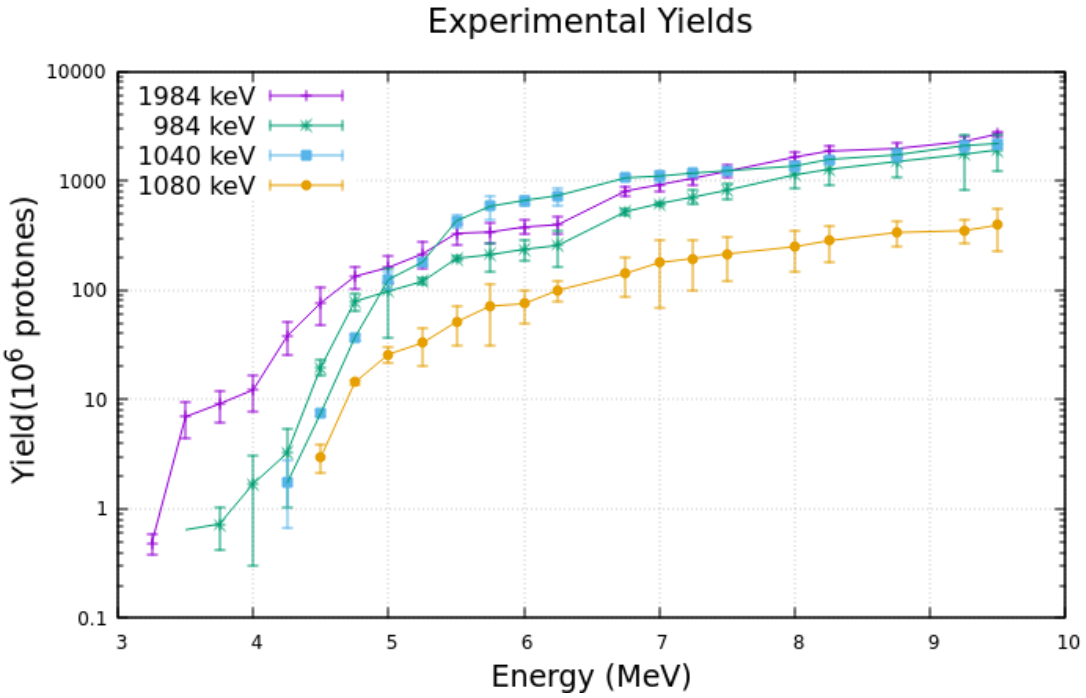

Figure 3.23: Yield production obtained in this work for the 984, 1040, 1080 and 1984 keV γ-lines.

Cross-sections values were calculated from yields using equation 3.12, The obtained results are plotted in Figure 3.24. Errors are below a 10 % of the main value in every case except for the 1080 keV γ. This particular case exhibits higher errors due to the lower number of counts in the photopeak and partial overlap with the 1040 keV peak. Despite these limitations, the uncertainties obtained for the cross-section measurements

are comparable to those observed in previous experiments [Dyer et al., 1981; Lang et al., 1987; Lesko et al., 1988; Kiener et al., 1998].

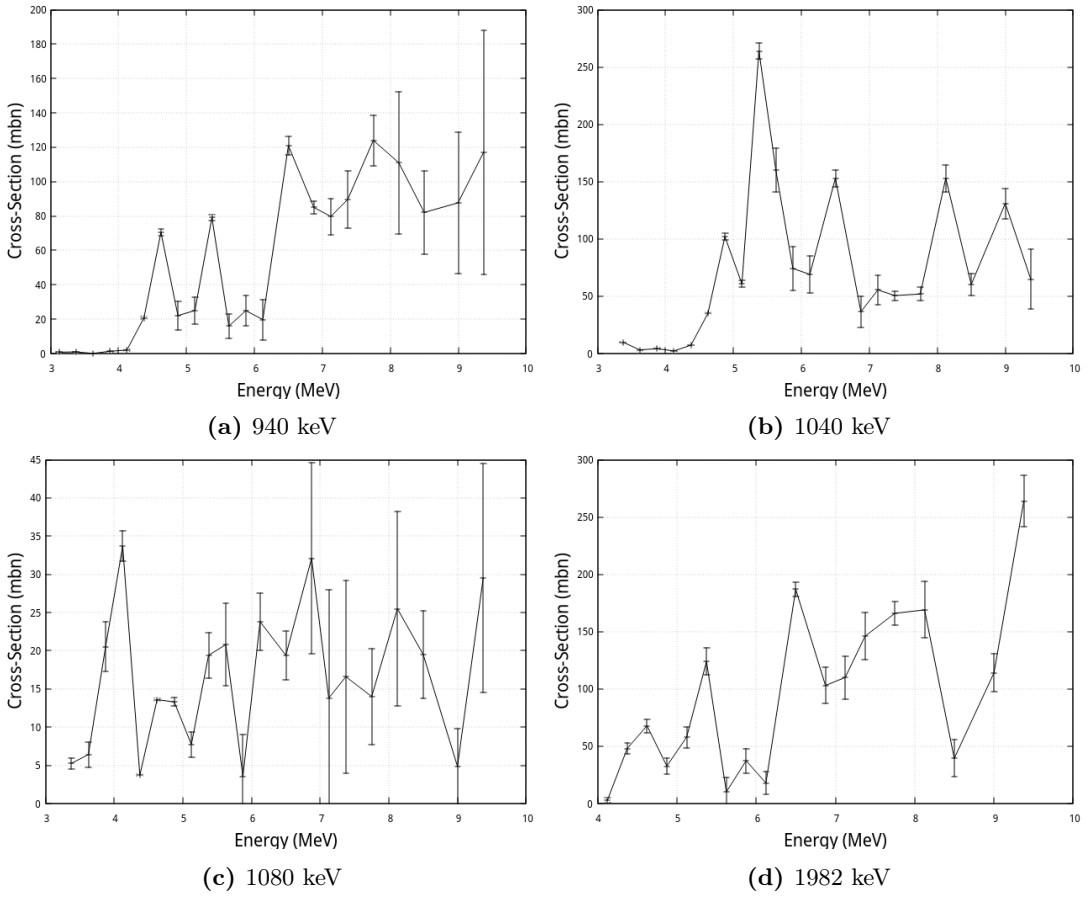

(a) 940 keV **(b)** 1040 keV

(c) 1080 keV **(d)** 1982 keV

Figure 3.24: Absolute cross-section measurements obtained in this work for the 984, 1040, 1080 and 1984 keV γ-lines.

3.6.9 Results: 5.3 MeV PG

The case of the 5.3 MeV γ-ray studied in this experiment is presented separately due to its special nature. This emission has a very interesting property, its Q value is positive, so that it can be measured at incident energies as low as 3.5 MeV. Additionally, the 5.3 MeV photopeak consists of two distinct PGs that are indistinguishable: the 5.270 MeV PG originating from the first excited level of ^{15}N, which has a multipolarity of M2+E3, and the 5.298 MeV PG originating from the second excited level of ^{15}N, which has a multipolarity of E1. As a consequence, this peak must study as a E1+M2+E3 emission

multipolarity. This case is beyond the limitations of our experimental set-up and can not be well fitted with only four yield-angle pairs of data. Even so, the fit was carried out usign the first four terms of equation 3.10, but only the a_0 parameter was taken into account for the yield and corss-section calcualtion. The angular distribution obtained from the fit was not considered.

Figure 3.25 shows the measured yields and cross-sections obtained from this experiment. This is the first time that this emission is studied, so there is no available data to compare with. Yield values show how the energy threshold of this reaction is very low. The 5.3 MeV γ-ray is detected with an incident energy of just 3.5 MeV. Errors in cross-section values are slightly high due to several uncertainties sources: 1) The peak is the sum of two contributions, 2) the efficiency is obtained with MC simulations and 3) the background in this region at high energy beams is complicated to adjust and extract.

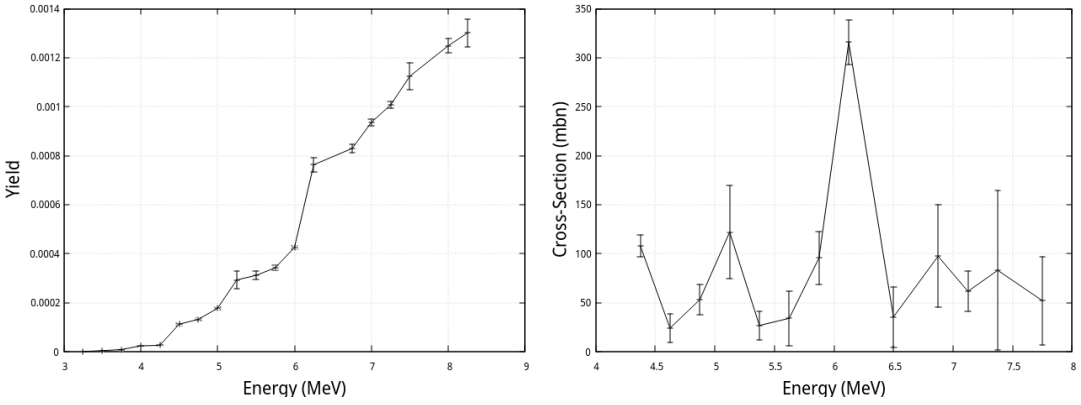

(a) Yield **(b)** CS

Figure 3.25: Absolute yield and cross-section measurements for the 5.3 MeV γ-line from the two first levels of ^{15}N.

3.7 Discussion

Three experiments have been carried out to measure production yields from the irradiation of potential contrast agents with protons. The aim of these experiment is the calculation of the cross-sections of the proposed contrast agents, whose knowledge is crucial in further investigation abut its implementation in clinical scenarios.

3. EXPERIMENTAL PRODUCTION YIELDS OF CONTRAST AGENTS

One of the studied reactions is the ^{18}O(p,n)^{18}F which has been extensively studied up to 30 MeV, but there is a notable lack of information and research available at higher energies. The experiment performed at QuirionSalud has allowed us to measure the cross-section of this reaction at several energies between 50 and 180 MeV. These measurements cover the whole energy range relevant in proton therapy, which enables it to be studied as a contrast agent (Chapter 5).

A second experiment has been performed to calculate cross-sections of the three proposed contrast agents with short half-lives. The ^{23}Mg has been used as cross-check because its cross-section up to 12 MeV is well-known, and the most relevant results are those from the ^{35}Ar and ^{39}Ca, which had hardly been studied before. Results from all of these reactions show that cross-sections are relatively high at low energies, which is one of the properties required for PET contrast agents. Future investigations should aim to study cross-sections up to at least 100 MeV to cover the relevant energy range for these contrast agents in proton therapy.

The last experiment focused on the measurements of PG production yields from ^{18}O when irradiating with protons. We were able to determine and analyze four γ-rays with energies below 2 MeV and very low energy thresholds ($<$3 MeV). Angular distributions and cross-sections were obtained from experimental data. Results show that all of these PG meets all the requirement mentioned in section 2.2, but its study at higher energies must be carried out to confirm its potential use in range verification. In addition, in this experiment we identified a 5.3 MeV γ-line with a 3.5 MeV energy threshold which may be useful in current systems. Overall, ^{18}O shows a great potential to improve PG verification techniques and further investigation are already planned to verify this assumption.

Chapter 4

Dictionary-based software for proton range verification

Proton range verification techniques are developed with the final aim of reaching the full potential of proton therapy, by delivering a high dose to the target while sparing as much healthy tissue as possible. As discussed in previous chapters, the use of secondary radiation provides several tools for proton range verifications. Nevertheless, the detection of secondary radiation is only the first step towards the verification of the proton range in a clinical scenario. The next and more complicate step is the estimation of the proton range and deposited dose from the measured radiation. Most of the current systems rely on the comparison of the experimental data with expected results based on simulations.

Ideally, the best option would be to measure the deposited dose and proton range simultaneously. There are several proposed methods to estimate the proton range using PET activity images [Masuda et al., 2019] and PG measurements [Richter et al., 2016; Hueso-González et al., 2018]. However, there are only methods that estimate dose from PET images, but it does not exist any tool capable of doing that from PG measurements yet. Some of these methods are introduced in the following section, along their advantages and limitations.

In this chapter, a new methodology to estimate the proton range and the deposited dose from measured secondary radiation is proposed. It has been tested using simulated PET images related to a realistic clinical scenario, but it could be adapted to any kind of measured information which can be associated to the deposited dose, such as PGs

emissions, neutrons, etc. This methodology is based on a fast dose reconstruction algorithm implemented in Graphics Processing Units (GPU), which is able to obtain dose from PET images in milliseconds and with high accuracy (< 1 mm), enabling *in-beam* verification.

4.1 Introduction and Motivation

PET and PG systems are able to detect secondary radiation generated by protons in irradiated regions leading to activation maps that can be correlated to the deposited dose [Zhu and Fakhri, 2013; Paganetti and Fakhri, 2015]. However, the main challenge for PET and PG dose verification is the derivation of accurate dose maps from experimentally measured activity maps [Paganetti, 2012; Knopf and Lomax, 2013; Parodi and Polf, 2018], due to the fact that activation and dose are correlated to different physical processes [Parodi et al., 2005; Paganetti and Fakhri, 2015].

Activation and dose maps can be calculated using MC simulators as they both depend on the proton properties (energy, fluence, etc.), but yield activation is also related to the cross-section of the reaction channel (equation 1.14) and dose is given by the Bethe-Block (energy loss) formula (equation 1.8). They are two different processes which are not directly related, and there is no analytical method of switching from one to the other. Indeed, in the few clinical implementations of PET proton range verification [Zhu et al., 2011; Parodi et al., 2013], dose was not derived from activity, but instead measured activity maps were directly compared with the expected activity derived from Monte Carlo simulations. Any reported deviations were used to flag potential inaccuracies in dose delivery caused by range uncertainties. While this approach can indeed detect range errors with relative success [Zhu et al., 2011; Parodi et al., 2013], it reduces the ability to perform a full reconstruction of the delivered dose maps, which would in turn allow for online planning adaptations that could make up for any observed under/overdosage.

Over the last few years, a few methods have been proposed to estimate dose from PET images. The basic idea is the same for all of them, they correlate PET activity maps with dose maps. The main difference between them is how they approach this correlation. They are individually discussed in what follows.

- ***Filtering approach* analytical method**

  The first method proposed and the only one fully implemented in a clinical scenario is the one presented by Parodi et al. in 2006 [Parodi and Bortfeld, 2006], and it took 13 years to be applied in a real case [Masuda et al., 2019, 2020]. This method uses the *Pencil Beam* (PB) approach [Hong et al., 1996] to transform PET activation maps to deposited dose. The main idea behind this method is to fit the observed PET images to complex equations which describe the proton transportation (based on the analytical PB approximations) and the nuclear activation processes. The derivation of these equations arises from the combination of the *Pencil Beam* analytical expressions, the yield production formula and the cross-sections values of the main reaction channels that produce β^+ isotopes [Parodi and Bortfeld, 2006]. The final expressions relate activity to dose, allowing the fitting of PET images to generate an estimate of the equivalent deposited dose. Some of the fit parameters are precalculated, allowing dose reconstruction to be completed in just a few seconds after the PET image is available. However, the use of approximate analytical expressions for dose calculation is a significant drawback of this approach, which results in less accuracy compared to a Monte Carlo-based approach.

  This method has been tested experimentally using a 190 MeV pencil beam and a SOBP with a maximum beam energy of 190 MeV with homogeneous phantoms [Masuda et al., 2019]. Monte Carlo (MC) simulations were also introduced to evaluate the accuracy in the reconstruction of dose for treatments based on clinical CT [Masuda et al., 2020]. The results of these validations show a precision of 2 mm in the proton range estimation, and better than 10% local dose reconstruction. The main inconvenience of the method is its high dependence on noise. PET images associated to a 2-Gy irradiation are extremely noisy and this effect is extrapolated to dose. The presence of noise in reconstructed dose makes difficult its evaluation and the proton range estimation.

- **Machine-learning algorithms**

  The implementation of recurrent neural networks has been used for correlating PET activity and proton dose [Liu et al., 2019; Li et al., 2019]. A theoretical study [Liu et al., 2019] showed the prospective accuracy better than 1 mm in proton

range estimation, which is very promising, but the method has been investigated only in 1D.

- **Minimization of the sum of squared errors**

  A new dose-reconstruction method (for carbon ion beams) has been proposed by Rutherford *et al.* [Rutherford et al., 2020]. It uses the well-known minimization of the sum of squared errors between the expected ground truth activities and PET images to obtain the deposited dose. The results show a high accurate dose estimation. However, similar to the *filterign approach* method, this method also seems to be sensitive to the noise in the PET images. The produced deposited doses are noisy which could lead to inaccuracies in the proton range estimation.

All the methods discussed above can calculate dose from PET images, but each of them has limitations. An optimal approach would be to use Monte Carlo (MC) simulations to achieve high accuracy, with processing times of less than a second, and minimize the impact of noise in the PET image. However, none of the current methodologies can meet all these criteria.

In this work, we propose a novel 3D dose reconstruction method using the full power of Monte Carlo simulations [Paganetti et al., 2004; Mairani et al., 2013], but decoupling the time-demanding simulation steps from the reconstruction phase, allowing thus to implement the method near real-time. The database is formed by the individual contribution to dose and activity of each of the pencil beams of the treatment plan, which we call Dose-Activity Dictionary (DAD). Generating the DAD is a time-consuming process but, as mentioned before, in a clinical setting, it could be carried out in the time between the CT becomes available and the moment when the first treatment fraction is delivered. This precalculation step separates realistic simulation of expected activation in a patient CT (using Monte Carlo transport codes) from dose reconstruction, which considerably reduces the amount of time required for the latter. Our algorithm, when fed with a measured PET image, uses the existing DAD to find the linear combination of activities of pencil beams that best fits the observed PET image. Then, the same linear combination is used to derive the most probable absorbed dose map. This entire process, from the availability of the PET image to the estimation of the deposited dose, takes less than a second.

This method has several advantages. The first and most important one the increased accuracy of Monte Carlo calculation (over analytical methods), which is implemented in the DAD calculation. Another benefit is the use of activity maps for individual pencil beams which, combined with precalculation of dose kernels, can help identify problematic areas within the irradiated volume which may have received a significantly different dose than the expected from the treatment plan. Last but not least, the reconstructed dose distributions are noiseless, allowing to estimate proton ranges with much higher accuracy than in previous works.

The main objective of this chapter is to illustrate the applicability of the proposed method in a clinical situation, with a particular emphasis on how the deposited dose and the time between dose deposition and PET measurement impact the quality of the reconstructed dose maps. Both factors affect directly the PET image quality and therefore, the quality of the reconstructed dose maps [Parodi and Polf, 2018]. To prove the viability of this method under realistic clinical scenarios, we show how the new program is capable to detect submillimetrical deviations induced by several sources of uncertainties.

4.2 Methods

4.2.1 Workflow

The workflow of this method describes the whole process, since the treatment plan is defined until the estimated dose from the PET images is available. This process can be separated in several steps.

1. **Dose-Activity Database calculation:** this step can be performed as soon as the treatment plan is available, which usually occurs at least 24 hours prior to treatment. The simulation of every beam in the plan is simulated with a detailed Monte Carlo simulator, from which we obtain both the dose and the activation of each pencil beam separately. The simulation must be finished before the treatment begins.

2. **Activity reconstruction:** after or during the irradiation, the β^+ activity induced by protons must be recorded with a PET system. The recorded PET data is analyzed to find the linear combination of precalculated pencil beams from the

Isotope	$T_{1/2}$ (min)	Reaction channel	Threshold energy (keV)	CS integral <100 MeV (b·MeV)	References
^{11}C	20.364(20)	^{12}C(p,x)^{11}C	17882.10 *11*	6.32	1, 2
		^{14}N(p,x)^{11}C	3132.27 *6*	2.61	3
		^{16}O(p,x)^{11}C	23582.59 *6*	1.26	3, 4
^{13}N	9.965(4)	^{14}N(p,x)^{13}N	8928.4 *3*	1.88	5, 6
		^{16}O(p,X)^{13}N	5547.3 *3*	0.65	3, 4
^{15}O	2.037(3)	^{16}O(p,x)^{15}O	14286.5 *5*	5.44	4, 5, 7, 8

Table 4.1: Isotopes introduced in the MC simulation and subsequently used in the PET image reconstructions, along with their most representative properties. The half-life of the produced isotopes limits the usability of such isotopes for PET detection. The energy threshold and the cross-section (CS) integral value provide guidance of the dominance of each isotope next to the BP. References: 1)Measday [1966] 2)Whitehead and Foster [1958], 3)Takács et al. [2003], 4)Masuda et al. [2018], 5)Sajjad et al. [1985], 6) Hess et al. [2001], 7)Valentin [1965], 8)Akagi et al. [2013]

DAD that can reproduce it more accurately. The convergence of this method is controlled by a χ^2 test, which determine the validity of the final solution.

3. **Dose estimation:** if the χ^2 test is satisfactory, the linear combination derived from the activities can be applied to the doses in the DAD to calculate the delivered dose. This calculated dose is compared with the reference dose in order to detect potential deviations or errors in the delivery.

4.2.2 Dose-Activity database calculation

The Dose-Activity Dictionary (DAD) is calculated by simulating every beam in the treatment plan using the patient CT as input. The Monte Carlo code TOPAS (TOol for PArticle Simulation) [Perl et al., 2012] (section 1.5) is used for this purpose. The deposited dose and the simulated activities for each isotope are stored separately in order to be able to recreate PET images at any time interval, correcting for the specific half-life of each beta emitter. The simulated activation of each isotope is filtered and smoothed to introduce into the DAD the PET system response. This effect depends on the e^+ energy and the PET geometry and detection properties. The PET response is independent for each PET system employed but, in most cases, a 3D-Gaussian filter

point spread function (PSF) is suitable [Zhu et al., 2011; Parodi et al., 2007] to reproduce it. The PSF must be determined in advance, and it is specific for each PET system, but this procedure is straightforward and needs to be performed only once for a given PET scanner. Realistic MC simulations [Abushab et al., 2016; Lopez-Montes et al., 2019] combined with reconstruction codes [Galve et al., 2019b] help us reproduce the PET signal under realistic conditions. The comparison between the simulated activities and the realistic PET images made it possible to characterize the PET system response as a 3D-Gaussian filter point spread function (PSF).

4.3 GPU MLEM & Simulated Annealing (MSA) Algorithm

In this thesis, the GPU MLEM & Simulated Annealing (MSA) Reconstruction Algorithm has been developed. It uses a maximum likelihood estimation method (MLEM) and a Simulated Annealing (SA) functionality, to reconstruct the deposited dose in an irradiated region from activity maps obtained from PET systems. For this purpose, this algorithm uses the information in the Dose-Activity database to find the combination of pencil beam which best fits the PET activity map. It has been implemented on a GPU to reduce the reconstruction time to less than one second and to be able to apply it in real time during treatment.

- **MLEM** is an iterative algorithm based on the principle of likelihood maximization for parameter estimation. It has been previously implemented in several fields where optimizations problems are required, such as physics, economy or biology [Ma et al., 2013; Maxim et al., 2016]. The main idea of this algorithm is to start from a flat image, with no prior information, and iterate pixel-by-pixel maximizing the loglikelihood until the obtained result maximized the likelihood between the reference data and the input image.

  The novelty of the developed method lies in the fact that, instead of reconstructing the input image pixel-by-pixel, we optimize the linear combination of certain maps that contribute to every pixel independently. The maps used for this optimization are the beam activity maps in the DAD, and after the reconstruction, the algorithm associates the coefficient that best fits the PET image to every beam. In order to implement this approach, the general MLEM equation has been used.

This allows us to obtain the linear combination of precalculated beams that maximizes the log-likelihood function [Shepp and Vardi, 1982].

$$c_i^{n+1} = \frac{c_i^n}{\sum_j A_{ij}} \sum_j \frac{A_{ij} \cdot d_j}{\sum_i c_i^n \cdot A_{ij}} \tag{4.1}$$

Where:

- j is the pixel index in the irradiated region.
- i is the index of each pencil beam in the DAD.
- c_i^n is the coefficient of each beam at iteration n: value that multiplies the associated activation and dose image.
- d_j is the data input activation (PET image).
- A_{ij} is the activity stored in the DAD database. Every pixel data of the ROI image (j index) of each beam of the Dictionary (i index).

- **The Simulated Annealing (SA)** is used to find the best solutions in some combinatorial optimization problems in which it is required to find some set of parameters $\overline{X} = (X_1, X_2, ..., X_N)$ that minimizes some function f($\overline{X}$) [Rutenbar, 1989]. The SA algorithm modifies these parameters randomly and evaluates the result using a *cost function* to assess whether the new answer is better than the previous one. This algorithm iteratively uses the best solution from the previous step to minimize the *cost function* up to a certain predetermined limit. In this specific case, the function would be a linear combination of the activity maps associated with each beam, where the parameters are the contribution coefficients to the linear combination for each beam, and the "cost function" which is minimized in the process is the χ^2 test.

The MSA algorithm, as any other reconstruction algorithm, requires an initial solution to begin with the optimization process which, in our specific case, is a combination of beams in the plan. In a general situation the initial solution must be chosen carefully because the final result is, in general, highly dependent on it. Neutral solutions, in which every parameter takes the same value, are commonly used as initial input. The main advantage of this approach is to ensure that the final solution is not biased by any a priori information. However, this option slows down the convergence and increases

the required time to reach the best solution. Furthermore, in proton therapy the expected solution is well-known, since the energy, the position and the dose deposited by each beam in the plan are known with high precision. The use of this a priori information speeds up the convergence without losing the generality of the method. For this reason, an intermediate initial solution between the uniformity and the canonical solution (planned) is selected as initial distribution. From here on, we will refer as "a priori information" to the initial solution that combines information from the expected solution (initial coefficient beam value 1) and the more general case (initial coefficient beam value 0.5).

The implementation of both algorithms (MLEM and SA) is flexible and it offers several options. One possibility is to use only one of the two algorithms for the whole process. The other option is the combination of both algorithms, so they are applied consecutively in a cycle of the iterative process as XX iterations of MLEM, followed by YY iterations of SA. This cycle is repeated until the *cost function* is minimized. The use of MLEM and SA at the same time implies that the χ^2 is minimized, while the log-likelihood function is maximized. This optimization method avoids getting stuck in local suboptimal solutions of either algorithms, which usually improves the results that both methods provides separately.

A figure of merit is required to assess the reliability of the obtained dose/activity maps. And adaptation of the χ^2 test was specifically developed to control and evaluate the results provided by the MSA algorithm

$$\frac{\chi^2}{\nu} = \sum_i \frac{(A_{i,truth} - A_{i,reco})^2}{A_{i,truth} + C} \tag{4.2}$$

where i is the index of each pixel, $A_{i,truth}$ is the PET input image data set and $A_{i,reco}$ is the reconstructed data. Two normalization constants were included to adadpt the χ^2 test to our case. The ν constant is related to the degrees of freedom. Its function is to normalize the test, so that the planned solution extracted from the DAD provides a value of χ^2 close to 1 when compared to the best possible simulated PET image. The C constant is in charge of regulating the PET image background. Its value is equal to a 5% of the maximum activity in the PET image, which is the smallest threshold that suppress the background noise without interfering with the final result

4.4 Benchmark Study

A benchmark study has been carried out to validate the new proposed method for proton range verification. The main goal of this benchmark is to test of the MSA algorithm in a simulated clinical scenario, in which the proton range is verified using a PET system. For this purpose, a realistic prostate treatment plan with protons has been chosen to perform this study using the Siemens mMR Biograph [Delso et al., 2011] as PET system. We have adapted this case to different clinical scenarios to test how the deposited dose and the time between dose deposition and PET measurement affect the quality of the results. In adittion, the response of the method to minimal deviations in the proton range due to different sources of uncertainties has been studied.

4.4.1 Creation of Dose-Activity Dictionary (DAD)

The Dose-Activity Dictionary was created from a realistic treatment plan of a prostate CT [Craft et al., 2014] segmented in 24 biological materials, following Schneider *et al.* [Schneider et al., 2000]. It was generated using matRad [Wieser et al., 2017] covering the target volume defined in the CT with two lateral and opposed beams. Only one of the two fields was taken into account as the objective of the benchmark is the proton range verification. The treatment is composed of 927 spots with energies between 130 and 190 MeV, which cover the PTV homogeneously. The spatial distribution is the usual in clinical beams and it is described by a Gaussian with sigma values of 2.1 mm and 2.8 mm in X and Y transverse directions, respectively.

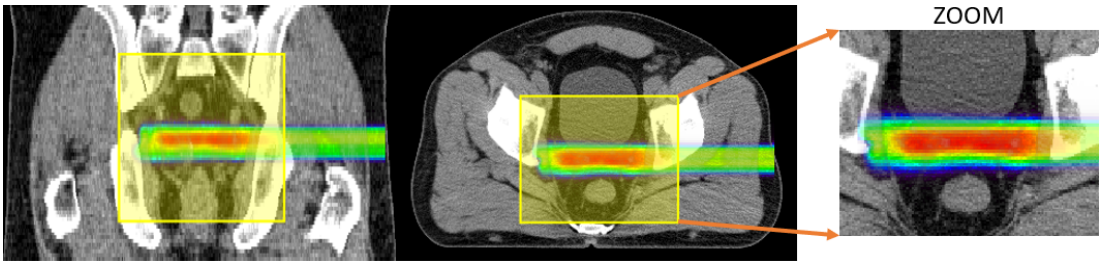

Figure 4.1: Deposited-dose map of the single-field plan, as calculated by matRad [Wieser et al., 2017], over a prostate CT. The optimization results in a set of 927 beams of energies between 130 and 190 MeV. The yellow box represents the ROI chosen for this work, i.e. only dose and activity points inside this region were used to generate the Dose-Activity Dictionary (DAD), to save memory and computational resources.

Therefore, the DAD is composed by 927 data sets, each of them containing dose and activity of every β^+ isotope produced in the human body (Table 1.2) for every beam. TOPAS simulated pacakage was used to generate them using 10^6 histories per beam. Beams were simulated from outside the patient as shown in Figure 4.1, but only the data in the region of interest (ROI) marked with a yellow box were storage in the DAD. The ROI occupies a volume of 150x60x70 pixels of 2x2x1 mm^3 (XYZ), with finer grid size in the propagation direction to calculate proton range with more accuracy. This region includes the whole dose deposited in the tumor area and its vicinity. The total amount of memory required to store the complete DAD is 9.2 GB and the required time to calcluate it in a cluster with 10 nodes and up to 160 threads is about 6 hours.

4.4.2 Simulation of PET images

The PET images were simulated based on proton activation simulation and using the Siemens mMR Biograph [Delso et al., 2011] system, which is used in the day-to-day practice of nuclear medicine as PET scanner for diagnostic. It is composed of 8 rings with 56 detector blocks and 8x8 lutetium oxyorthosilicate crystals (4x4x20 mm) per block. It covers a transverse field of view (FOV) of 59.4 cm and an axial FOV of 25.8 cm. The energy resolution of this scanner is 14.5% at 511 keV and the energy window was set in 430-560 keV. Figure 4.2 shows the scheme of the scanner and the prostate CT in three different planes.

PET signals used in this benchmark were obtained from simulations performed in the Ultra-fast MC PET simulator [Galve et al., 2020], a GPU- accelerated Monte Carlo for photon transport specifically developed for PET purposes. It includes all the physics related to the positron range, photon interactions and detector response. In the simulations, the deposited dose and the time interval of the PET measurements were taken into account. The simulated PET signals were reconstructed using the Ordered Subsets Expectation Maximization algorithm with a maximum a priori regularization (MAP-OSEM) [Hudson and Larkin, 1994; Bettinardi et al., 2002]. These steps include normalization to correct for variations in detector response, attenuation correction to account for the attenuation of photons through the patient's body, scatter correction to account for photons scattered within the body, and resolution modeling with the point spread function (PSF) to improve image sharpness.

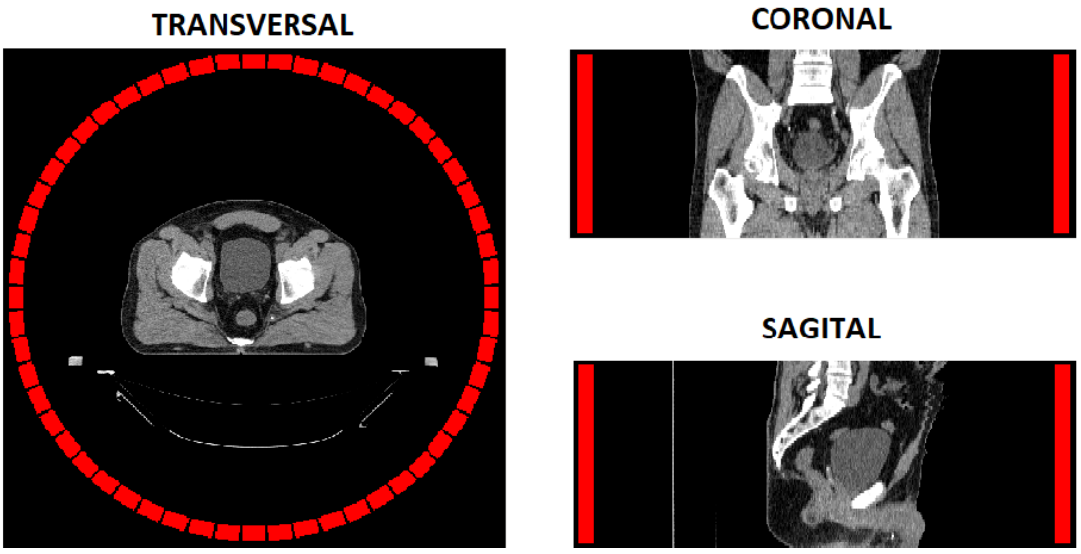

Figure 4.2: Siemens Biograph mMR system (red) used for the photon simulation by the Ultra-fast Monte Carlo PET simulator [Galve et al., 2020] to obtain realistic PET signals. The prostate CT chosen to validate the method is represented at the same geometrical position with respect to the PET as it was used to simulate the photon transport.

4.4.3 Test Scenarios

The proper functioning of the DAD MSA-Algorithm was tested in several scenarios using the treatment plan and the PET system previously described.

1. **The compromise between dose and quality of the reconstructions**

   Delivered dose is proportional to the total amount of protons. Therefore, the increase in dose also implies an increase in the amount of β^+ activation induced by protons. The quality of the PET image depends on the total amount of detected events, so the quality of the PET image depends on the delivered dose. The method must provide reliable results using a dose no larger than what is typically delivered in a single treatment fraction, which usually ranges from 1 to 2 Gy at the BP. Therefore, it is important to ensure that the method can provide accurate dose estimations even at these low doses.

   To test the dependence of the results with the dose, a proton beam from the dictionary, with a range of 21 cm in water, was used to generate the PET image and its associated reconstructed dose. This was done for delivered doses ranging

0.01 to 10 Gy at the BP. The total amount of PET activity was used to perform the reconstruction of the PET image. The upper limit of 10 Gy was set because beyond this point, the quality of the result does not improve any further with an increase in dose.

2. **Dependence between image reconstruction quality and the PET data acquisition time.**

   Similarly to the previous case, the acquisition time directly affects the quality of the results because the number of detected emissions by the PET system depends on it. To test the viability of the method in online and offline scenarios an analysis was carried out. The delivery dose is composed by all DAD beams with energies between 179 and 180 MeV. In this case, the delivered dose was fixed to 1 Gy (realistic scenario) and two different acquisition times were used to reconstruct the dose: in-room (up to 1 minute post irradiation) and offline (10 to 30 minutes post-irradiation).

3. **Sensitivity to anatomical changes.**

   There are clinical scenarios where interfractional anatomical changes occur. In order to mimic a realistic situation, density modifications have been applied to certain CT regions in the beam path. The modification of the density implies variations in the proton range which may lead to a delivered dose that differs from what was initially planned [Lomax, 2008; Hui et al., 2008; Yang et al., 2020]. It is important that the proposed method is able to identify them. To study the sensitivity of the program to range deviations, two scenarios were created in adittion to the reference one. In both cases a 10% density increase was considered in certain regions. In the first case, the increase was applied to the whole ROI (CT-Altered-Box), causing a maximum range shift of 8 mm. In the second case the modification of the dose was applied to a slice of 1 cm perpendicular to the beam direction (CT-Altered-Slice), introducing a range shift of just 0.6 mm.

4. **Spread out Bragg peak (SOBP).**

   In a realistic clinical scenario, the administered dose covers the target volume with a uniform dose by combining several pencil beams with different energies (SOBP). To test the DAD MSA-Algortihm in a completely realistic scenario, a set of 144

beams from the planned with energies between 160 and 180 MeV has been used to recreate a SOBP at the prostate. To represent the clinical scenario as realistically as possible, the deposited dose was set to 1 Gy at the SOBP and the acquisition time was assumed to be 10 to 40 minutes after irradiation.

4.4.4 Metrics

The accuracy of the method will be described by a set of metrics that compare the reconstructed dose to the reference dose (ground truth). The combination of these metrics and its analysis must flag and identify possible range deviations or changes in the deposited dose with respect to the planned one.

1. **Range estimation**

   The estimation of the proton range is essential in any proton range verification technique. This method includes the calculation of the R_{90}, R_{50} and R_{10} parameters. These R# indicates the location along the beam direction where the dose is a #% of the maximum value at the Bragg Peak [Schuemann et al., 2014; Tommasino et al., 2017], which are usually used to define the proton range. These R# parameters are calculated along the Z axis for every point of XY plane which contributes to the dose. The comparison of the R# derived from reconstructions with the R# obtained from the reference dose are used to create "Range Deviation" histograms. The analysis of these histograms will tell us how accurate is the reconstruction and which is the precision of the estimation.

   The obtained results from the range estimation analysis must be compared with the current uncertainties applied in proton treatment plan, with the aim of testing whether the accuracy of this technique is higher than that applied in clinical cases. Figure 4.3 shows typical range uncertainty margins applied at different proton centers. The 3.5% + 1 mm safety margin is applied at the Massachusetts General Hospital [Paganetti, 2012]. Centers such as the MD Anderson Proton-Therapy Center in Houston, the Loma Linda University Medical Center and the Roberts Proton Therapy Center at the University of Pennsylvania use safety margins defined as 3.5% + 3 mm [Paganetti, 2012]. The center with the lowest safety margins is the University of Florida Proton Therapy Institute with 2.5% + 1.5 mm, which it still implies an uncertainty of 5 mm for a 20 cm proton range (175

MeV in water). It must be noted that these centers may apply bigger margins in specific treatment scenarios.

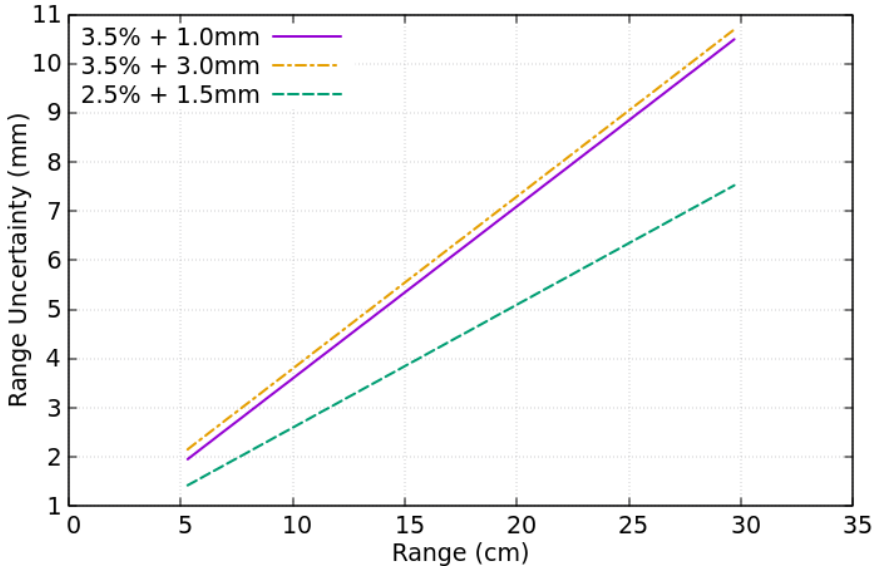

Figure 4.3: Typically applied range uncertainty margins in proton therapy treatment planning applied at the MGH (3.5%+1 mm), the MD Anderson ProtonTherapy Center in Houston (3.5%+3 mm), the Loma Linda University Medical Center (3.5%+3 mm), the Roberts Proton Therapy Center at the University of Pennsylvania (3.5%+3 mm) and the University of Florida Proton Therapy Institute (3.5%+1.5 mm).

2. **Pixel-by-pixel dose deviation**

   The deviation of the reconstructed dose with respect to the planned dose map is calculated as the relative error between them [Masuda et al., 2020]

$$RE_{Dose} = \frac{D_i - D_{i,ref}}{max_i(D_{i,ref})} \cdot 100 \tag{4.3}$$

   being $D_{i,ref}$ the i-th voxel of the reference dose and D_i the i-th voxel of the reconstructed dose. This parameter provides a quantitative value of the similarity between the reconstructed dose and the predicted dose.

3. **Gamma-analysis**

   The gamma-analysis has been adapted as descried by Low et al. [1998]. This metric quantifies the agreement between the reference and the measured dose maps in terms of distance and relative difference pixel-by-pixel. One of the main

limitations of this test is the presence of noise in the problem map distribution, which may lead to erroneous solutions [Huang et al., 2014; Miften et al., 2018; Cohilis et al., 2020]. However, the reconstructed doses by the MSA algorithm are noiseless. This makes gamma analysis a suitable and reliable test to use as a metric to verify results. The γ criteria is defined as

$$\gamma(r_m) = min\{\Gamma(r_m, r_c)\}\forall\{r_c\} \tag{4.4}$$

where Γ is defined as

$$\Gamma(r_m, r_c) = \sqrt{\frac{r^2(r_m, r_c)}{\Delta d_M^2} + \frac{\delta^2(r_m, r_c)}{\Delta D_M^2}} \tag{4.5}$$

with

$$r^2 = |r_m - r_c| \qquad \delta^2 = D_{rec}(r_m) - D_{ref}(r_c) \tag{4.6}$$

and r_m is the position of the pixel of the reconstructed dose image, r_c is the pixel of the reference dose image, $D_{rec}(r_m)$ and $D_{ref}(r_c)$ are the pixel value of the reconstructed and reference dose respectively.

In this test a value below 1 indicates a satisfactory result for a specific pixel. The values of Δd_M and ΔD_M were set to 1 mm and 3% of the maximum dose respectively (gamma 1mm-3% with dose global criteria). Only voxels with dose values greater than 5% of the maximum dose are considered for analysis. This limit was established to prevent the inclusion of background contribution that may produce gamma-analysis results that do not align with the actual outcomes. To ensure a reliable reconstruction of both the entire dose and the end of the proton range, which is particularly crucial in proton therapy, this metric was applied separately to the entire dose image and the fall-off region (i.e., the end of the Bragg peak). As a result, independent assessments of the accurate reconstruction of these two critical areas were obtained.

4.5 Results

4.5.1 Dose dependence

The quality of the results as a function of the deposited dose has been studied using PET map distributions associated to a 180 MeV pencil beam of the plan, which was simulated and reconstructed assuming 0.1, 1.0 and 10 Gy. Figure 4.4 shows the three mentioned simulated activity maps (PET images) and the reconstructed dose obtained from them and Figure 4.5 details the reconstructed dose profiles, including a zoom of the fall-off region. The reconstructed doses are almost indistinguishable from the planned dose in the cases above 1 Gy delivery. The reconstructed dose associated to 0.1 Gy overestimates by 5% the dose along the beam profile. This effect is visible in the dose deviation histogram (Figure 4.6d) because it mainly contributes to the RE_{DOSE} with values close to 2%.

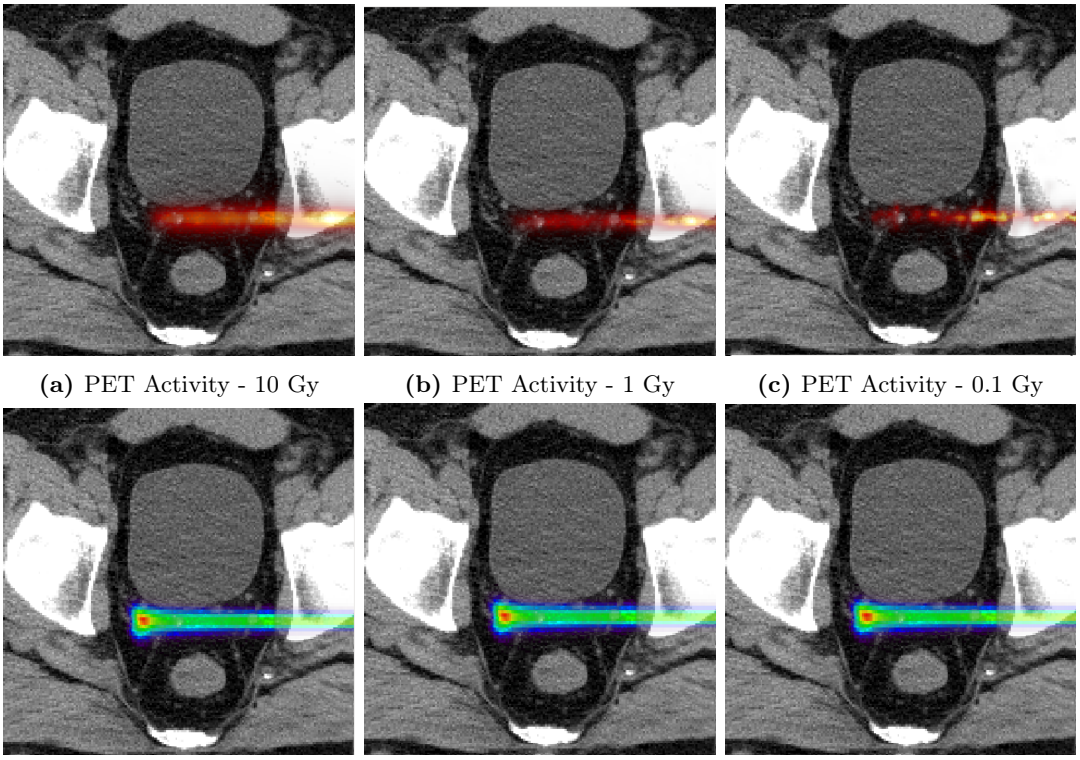

(a) PET Activity - 10 Gy **(b)** PET Activity - 1 Gy **(c)** PET Activity - 0.1 Gy

(d) Dose - 10 Gy **(e)** Dose - 1 Gy **(f)** Dose - 0.1 Gy

Figure 4.4: Simulated PET images (a-c) and its associated reconstructed doses (d-f) related to a 180 MeV from the treatment plan with different doses from 0.1 Gy to 10 Gy.

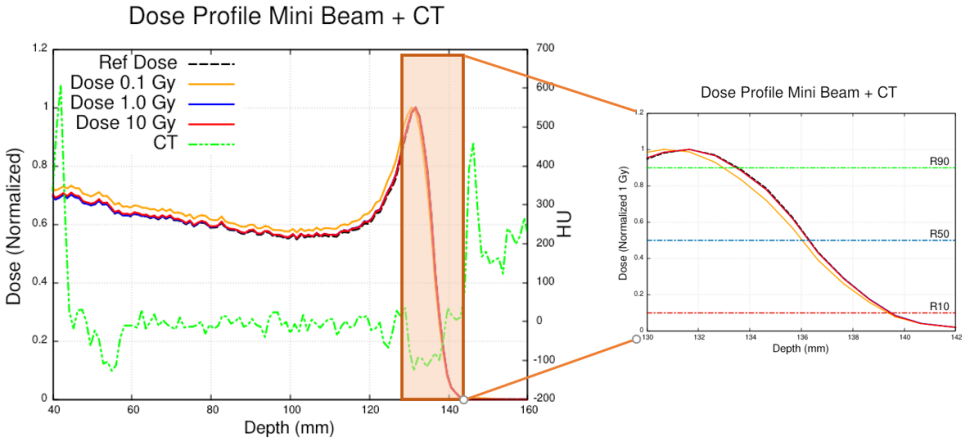

Figure 4.5: Central dose profiles of the doses reconstructed from PET activities associated to 10, 1 and 0.1 Gy, presented along the groundtruth (reference) dose. A zoom of the fall-off region of the Bragg peak (orange box) is also shown.

A precise analysis of the quality of the results were performed using the range and dose histograms deviations and the mean and sigma values that were obtained from them. These results are shown in Figure 4.6 and Table 4.2. The table also shows the gamma-analysis for each of the three reconstructed doses. The results are consistent with the first conclusions extracted from the dose profiles. The range and dose deviations from the doses above 1 Gy are almost zero, no range deviations higher than 0.2 mm are appreciated in the histograms. For dose deviations, the maximum discrepancy for the RE_{DOSE} is 3%. In the case of 0.1 Gy, the results are worse. The range histograms (Figure 4.6) show deviations up to 1 mm and the mean values for the R90 and R50 are 0.5 and 0.25 mm away from the expected one. The uncertainty associated with a 180 MeV proton beam in a human body is determined by its range, which is approximately 20 cm. Depending on the specific proton center, the corresponding uncertainty is typically within the range of 5-7 mm. When comparing these values with the results obtained using the proposed technique, it becomes evident that this approach offers significantly higher accuracy across all the studied doses. Furthermore, the gamma-analysis also indicates that the reconstructed doses with 1 and 10 Gy are almost identical to the reference dose, with values of 99.99 % in both cases. The gamma analysis decreases down to 96% with the 0.1 Gy reconstructed dose as expected. We underline here that 0.1 Gy is a very low dose and the results are still comparable with those where a clinical dose, or higher, were used.

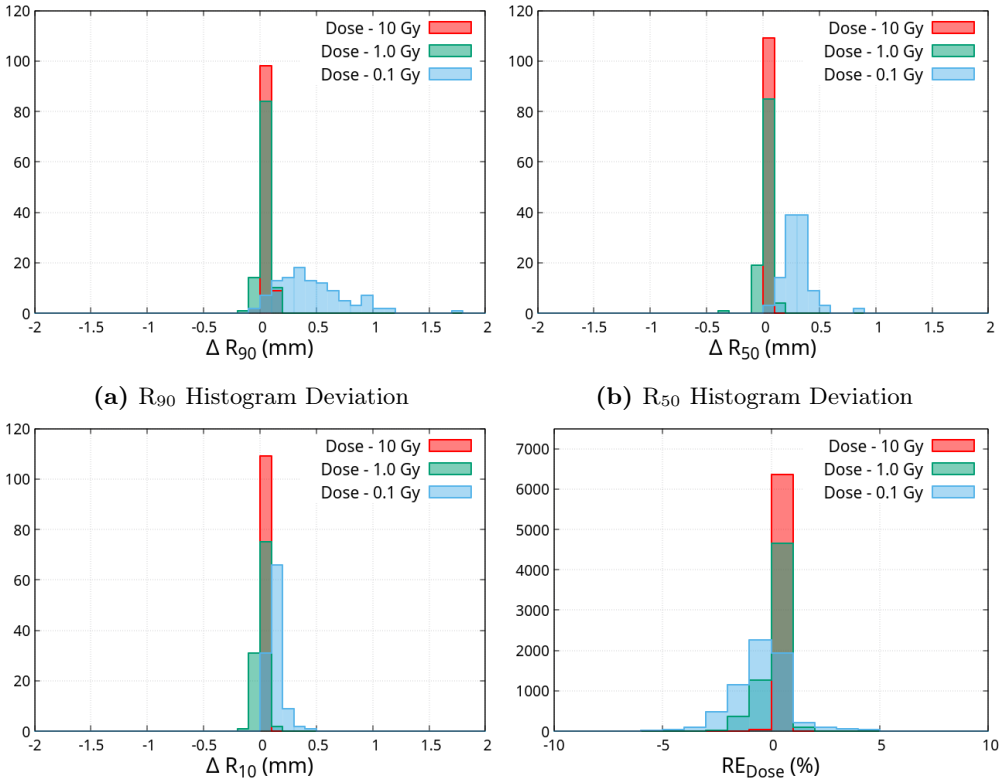

(a) R_{90} Histogram Deviation

(b) R_{50} Histogram Deviation

(c) R_{10} Histogram Deviation

(d) Dose Histogram Deviation

Figure 4.6: a-c) Range deviation histograms calculated from the dose map distributions, comparing the R# values of the reference dose with the related values from the reconstructed ones (see Equation 4.3).The R_{90} (a), R_{50} (b) and R_{10} (c) resulting for 10 Gy(green), 1 Gy (blue) and 0.1 Gy (red) histograms are plotted together. d) Dose deviation histograms of the three reconstructed doses.

Dose (Gy)	ΔR_{90} (mm)		ΔR_{50} (mm)		ΔR_{10} (mm)		RE_{DOSE} (%)		Gamma analysis
	Mean	σ	Mean	σ	Mean	σ	Mean	σ	1 mm-3%
10	0.01	0.03	0.00	0.00	0.00	0.00	0.00	0.07	99.9
1	0.00	0.05	-0.02	0.06	-0.03	0.05	-0.32	0.61	99.99
0.1	0.43	0.37	0.25	0.12	0.09	0.07	-0.94	1.32	95.62

Table 4.2: Mean and sigma values of the range and dose deviation histograms (Figure 4.6) obtained from the noise dependency study using three different doses (10, 1 and 0.1 Gy) for the same irradiation.

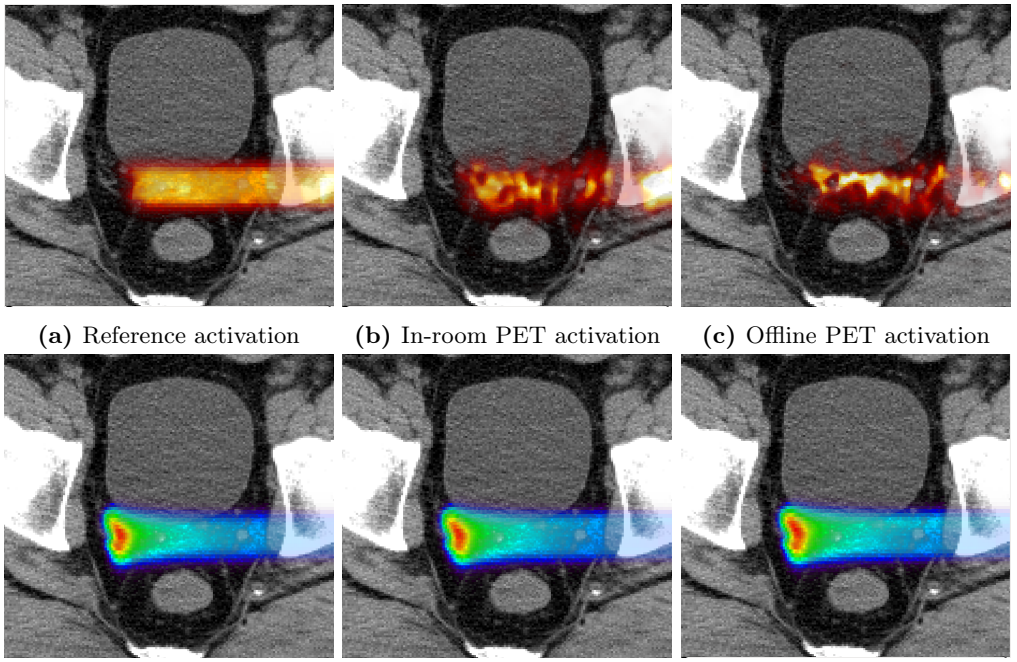

(a) Reference activation **(b)** In-room PET activation **(c)** Offline PET activation

(d) Reference dose **(e)** In-room dose **(f)** Offline dose

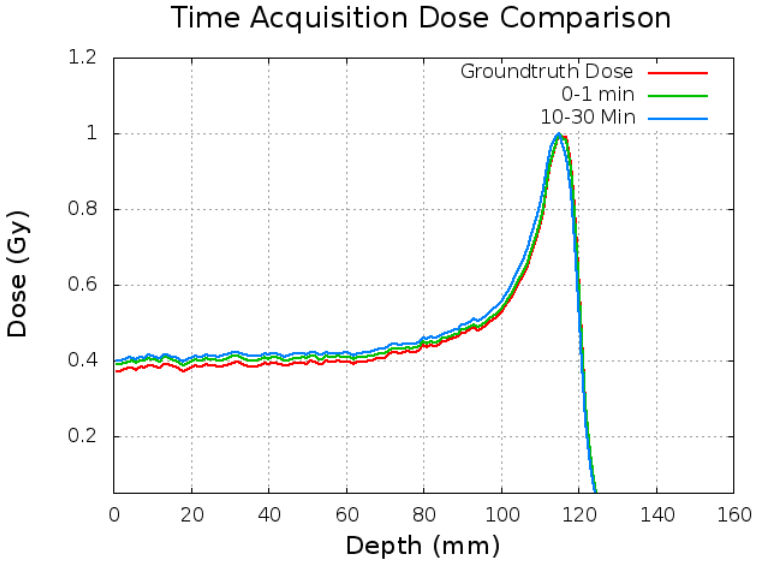

(g) Offline dose

Figure 4.7: a & d) Simulated activation and dose obtained as a combination of every pencil beam of 180 MeV comprised in the plan calculated from the prostate CT. b) PET image associated to the in-room modality with a time acquisition from 0 to 1 minute after the irradiation. e) Reconstructed dose from the PET image of the in-room modality. c) PET image associated to the offline modality with a time window of 10-30 min after irradiation. f) Reconstructed dose from the PET image of the offline modality. g) Central dose profiles of the groundtruth, in-room and offline doses.

4.5.2 Acquisition time dependence

The dependence of the result on the PET acquisition time is studied in this section using two different activations, associated to the same deposited dose of 1 Gy, but related to two different acquisition schemes: in-room PET (simulated measurement 0-1 min after irradiation) and offline PET (10-30 minutes after the dose delivery). Both PET images were calculated using the simulation code and reconstruction algorithm described in section 4.4.2. Reference dose and activation maps from the Monte Carlo code are displayed alongside reconstructed dose and activation maps in Figure 4.7. Initially, reconstructions were carried out starting from a homogeneous distribution of beam coefficients.

Range and relative dose deviation histograms are shown in Figure 4.8 and the mean and standard deviation values associated with them are displayed in Table 4.3. Based on these results, there are two visible effects in the reconstructed doses.

Firstly, the reconstructed doses slightly overestimate the dose along the entire proton path until the end of its range, which in turn underestimates the dose in the Bragg peak (BP). This effect implies a deviation of the R# of a few millimeters. However, the results of the reconstructed doses are satisfactory, since 90% of the pixels suffer a deviation below 5% in any case, which is caused by the overestimation of the coefficients of low-energy beams.

Secondly, the range histograms obtained from the in-room scenario show a deviation that is not related to a Gaussian distribution. This implies that the reconstructed dose from a PET image associated with a dose of 1 Gy with a 1-minute acquisition is not suitable, at least using a uniform distribution of coefficients as an initial input.

Time (min)	Decays	Dose (Gy)	ΔR_{90} (mm)		ΔR_{50} (mm)		ΔR_{10} (mm)		RE_{DOSE} (%)	
			Mean	σ	Mean	σ	Mean	σ	Mean	σ
0 - 1	$6.3{\cdot}10^5$	1	0.54	0.77	0.35	0.59	0.09	0.35	-0.64	2.71
10 - 30	$1.19{\cdot}10^6$	1	0.49	0.19	0.31	0.09	0.16	0.08	-1.96	2.45

Table 4.3: Principal parameters of the reconstructed doses of both acquisition modalities (0-1 min and 10-30 min after the irradiation) are presented in this table. Mean and sigma values are derived from the histograms in Figure 4.8

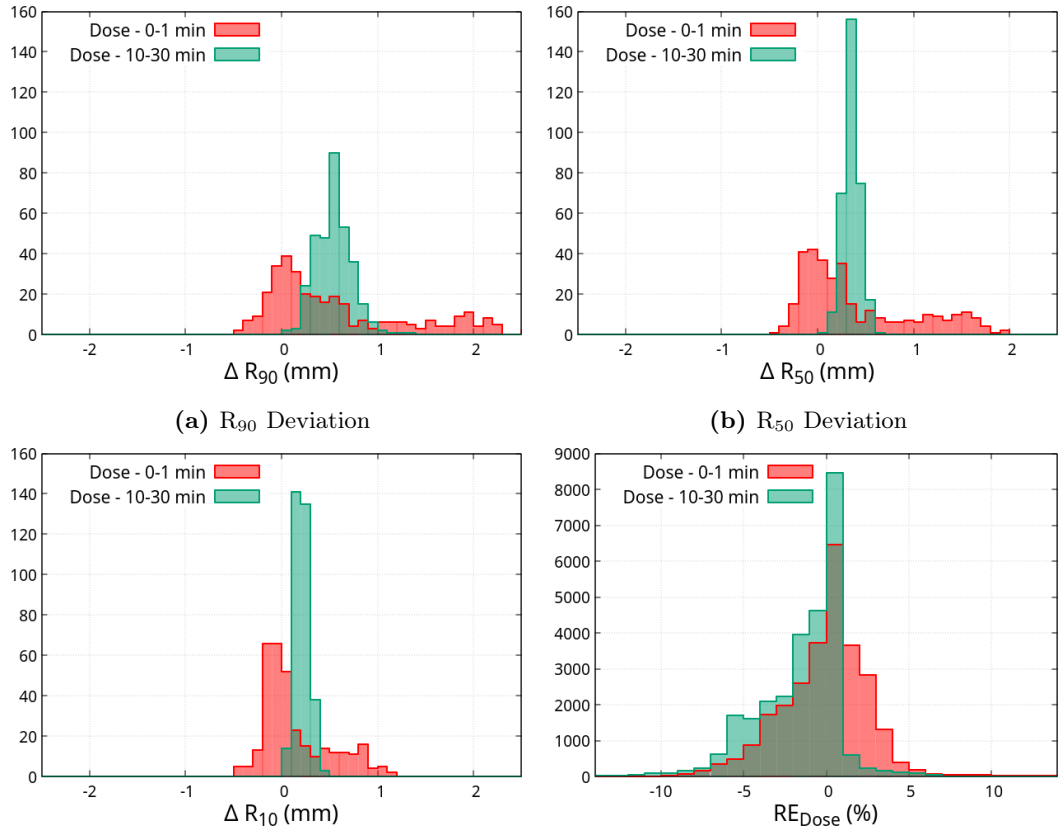

(a) R_{90} Deviation

(b) R_{50} Deviation

(c) R_{10} Deviation

(d) Dose Deviation

Figure 4.8: Range (R_{90}, R_{50} and R_{10}) and dose deviation histograms obtained by the comparison of the reference dose with the reconstructed doses of each acquisition modality: in-room (0-1 min, red) and offline (10-30 min, blue).

In order to improve the previous results, the same study was repeated introducing as a priori information the same coefficient distribution that was used to generate the reference dose. The most relevant results from this second analysis are shown in Table 4.4. The results indicate a substantial improvement in the reconstructed doses in comparison with the previous case, where uniform coefficient distribution was used as input. This methodology solves the two previous problems. The blurring effect in the dose is significantly reduced in this proposed methodology, allowing for sub-millimetric precision in range reproduction in both in-room and offline PET scenarios. The use of the expected coefficient distribution as a priori information clearly improves the results. However, this a priori information could theoretically imply a loss of generality and lead to erroneous reconstructed doses if anatomical changes are present in the patient. It

is important to verify that the use of a priori information in reconstruction still allows identifying and detecting dose deviations due to anatomical changes in the planning CT. For this purpose, the next section focuses on the ability of the DAD-MSA algorithm to detect anatomical changes in the patient when a priori information of the delivery dose is implemented in the method.

Dose 1.0 Gy - Planned Beam Distribution as Input

Time range	Dose	ΔR_{90} (mm)		ΔR_{50} (mm)		ΔR_{10} (mm)		RE_{DOSE}(%)	
(min)	(Gy)	Mean	σ	Mean	σ	Mean	σ	Mean	σ
0 - 1	1.0	0.08	0.42	0.09	0.47	-0.16	0.48	-0.62	2.21
10 - 30	1.0	0.04	0.36	0.12	0.52	0.09	0.32	-0.35	1.23

Table 4.4: The reconstructions of both time modalities were performed again using the expected distribution of coefficients as input. The mean and sigma values of the ΔR_{90}, ΔR_{50} and ΔR_{10} and dose deviation histograms obtained with this method can be seen in this table. The results show a great improvement in the range deviation in comparison with the results in Table 4.3. The dose is better reproduced as well.

4.5.3 Detection of anatomical variations in planning CT

The reconstructed doses together with their respective CTs for the 3 cases described in section 4.4.3 are shown in Figure 4.9: reference case, altered box (10% global density increase, leading into a range shift of 8 mm) and altered-slice (10% density increase in a 1-cm slice, causing a shift of 0.6 mm in the proton range). In this case, the initial input of coefficient distribution for the reconstruction includes a priori information of the treatment plan. A dose of 1 Gy at the BP deposited by a 180 MeV pencil and an offline scheme (10 to 30 minutes PET time acquisition) were assumed in each of the three scenarios.

Figure 4.9d shows the dose profiles from the reconstructed doses and the ground truth dose when there is no anatomical modifications. It is visible from the image that the doses differ one from the others, and that the range is also different in each scenario. The numerical analysis of these deviations is shown in the form of the R_{50} deviations histograms in Figure 4.10, and the statistics of these distributions are presented in Table 4.5. The table show both the calculated and the expected ΔR_{50} values for each of the

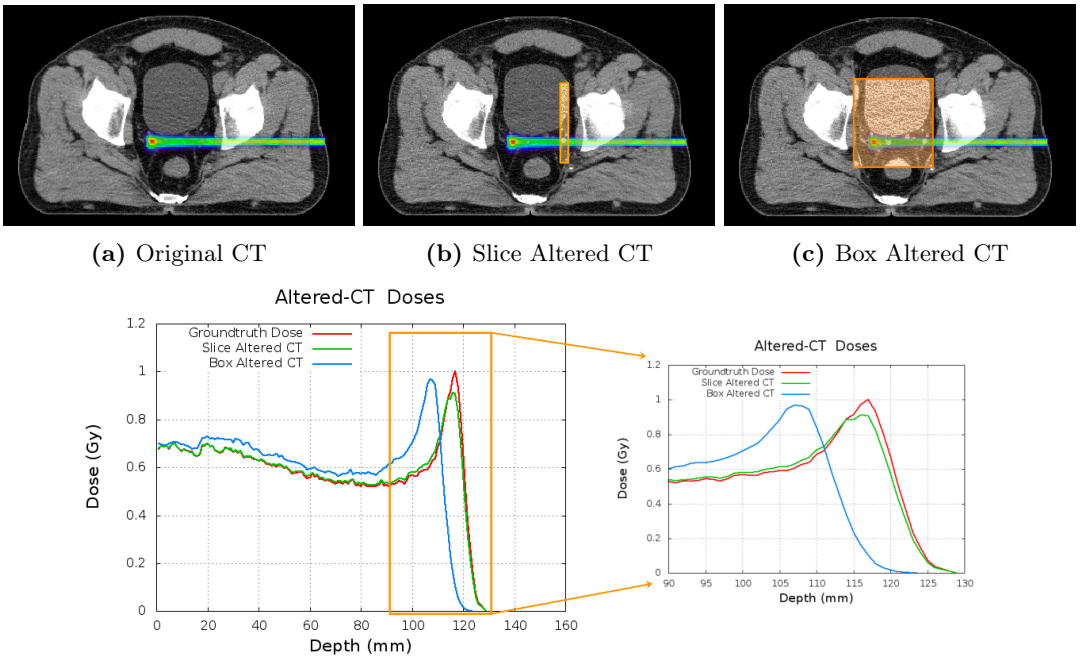

(a) Original CT **(b)** Slice Altered CT **(c)** Box Altered CT

(d) Central dose profiles

Figure 4.9: Reconstructed dose overlying planning CTs for the three cases under study for the detection of anatomical variation in planning CT. No altered region (a), slice altered region generating a 0.6-mm deviation in proton range (b) and box altered region generation a 8.0-mm deviation in proton range (c). Altered regions with a density increment of a 10% are marked in orange. d) Central dose profiles of the groundtruth dose and the reconstructed dose maps from altered CTs.

scenarios. In addition, the table also presents the gamma-analysis results of the entire region and the fall-off dose area. These results indicate that the use of both metrics under study (range deviation and gamma analysis) are suitable to potentially identify and detect range deviations below one millimeter.

Results obtained from the R_{50} analysis of reconstructed doses for slice- and box-altered CTs clearly show how the expected deviations are well identified. The histograms are already different at first sight, but when they are analyzed in detail, it becomes obvious that their mean values match perfectly with the expected deviations due to the density modifications on the planning CT.

The gamma analysis can be used to detect deviations in the dose delivery, specifically if it is applied in the fall-off region of the Bragg peak, because it is the region used for the estimations of the proton range. In the box-altered case where an 8 mm range shift

is introduced, we can appreciate how more than 70% of the considered voxels still pass the test. However, if the gamma analysis test is applied only to the fall-off region this number decrease up to a 5%, clearly identifying a problem in the deposited dose in this area. Comparing the reference case with the slice CT, the gamma analysis decreases from 92% to 84%. All these results indicate that appropriate thresholds can be found to flag potential delivery errors in reconstructed doses with the DAD-MSA algorithm.

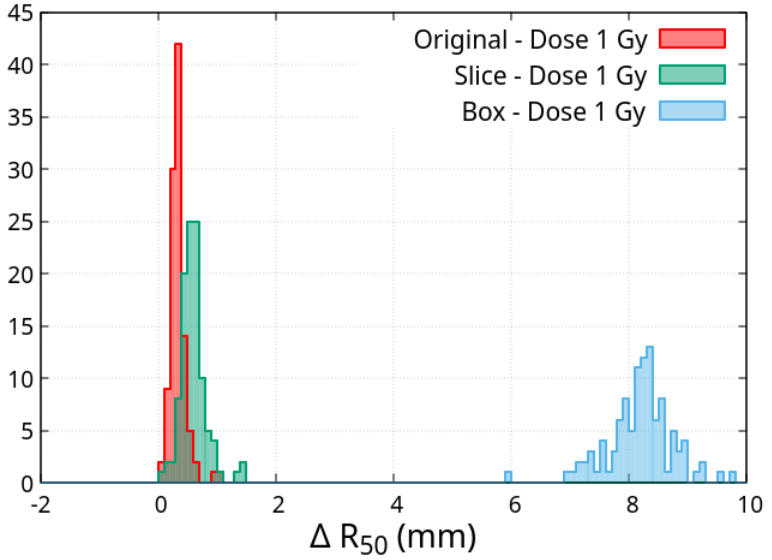

Figure 4.10: R_{50} deviation histogram comparing the reference dose with the reconstructed doses from the three scenarios in the study of detection of anatomical variations. Original CT - expected no deviation (red), the slice-altered CT - 0.6 mm expected deviation (green) and the box-altered CT - 8.0 mm expected deviation (blue).

Case	ΔR_{50} (mm)		Expected	Gamma 1 mm-3%	
	Mean	σ	ΔR_{50} (mm)	Total	Fall-off
Original CT	0.13	0.14	0.00	93.99%	92.40%
Slice CT	0.55	0.22	0.61	83.20%	84.24%
Box CT	8.14	0.56	8.03	72.33%	5.87%

Table 4.5: The most significant parameters of the anatomical variation detection study are shown in this table. Mean and sigma values obtained from the histograms of Figure 4.10 with the expected values indicate the precision in the range determination. The gamma 1 mm-3% test shows the quality of the overall region and the fall-off region of the reconstructed dose.

4.5.4 SOBP

In this section, we test the MSA-DAD method to reconstruct a Spread Out Bragg Peak (SOBP), representing a more realistic clinical case than the previous ones. To create the SOBP covering the prostate CT, 144 pencil beams from the Dictionary were used. In this case, a scenario with a 1 Gy dose delivery and a time window of 10-30 min after the irradiation for the PET acquisition was assumed. For the reconstruction, a priori information of the planned dose was implemented overweighing the pencil beams that contribute to the reference SOBP. The reference dose, reconstructed dose and the PET activity obtained from the simulation are illustrated in Fig 4.11. The central dose profiles and the range deviation histograms are also shown in this image. The analysis of these histograms is presented in Table 4.6 along with the gamma analysis (2 mm3%) applied to the entire dose and the fall-off region.

The results demonstrate excellent agreement between the reference dose and the reconstructed SOBP. The measurements also show a strong correlation between the expected and reconstructed doses. However, the program has a tendency to overestimate lower energy beams, leading to a small deviation in the flat dosage, which is evidently seen in the dose profile. The range prediction in the R_{50} example is essentially excellent, and its range deviation distribution never deviate more than a millimeter from the expected value. Taking into account that the expected value is 122 mm, deviation is less than 0.83% of the proton range. The R_{10} is poorly resolved due to low statics in the PET picture, which prevents the approach from accurately adjusting the most distant part of the dose where background has the same activity levels than the one induced by protons. The deviation of the R_{90} is caused by the overestimation of low energy beams. However, it is worth noting that the obtained results exhibit a level of accuracy that surpasses the uncertainties typically associated with this beam in treatment planning. Specifically, for a Spread-Out Bragg Peak (SOBP) with a maximum energy of 185 MeV, the corresponding uncertainty ranges between 5.2-7.3 mm, varying slightly depending on the treatment center. In comparison, the results obtained through the proposed technique demonstrate a significantly higher level of precision. Furthermore, according to the gamma test analysis, the reconstruction of the dose is accurate across the entire volume and even better in the fall-off area, which is used to estimate the proton range.

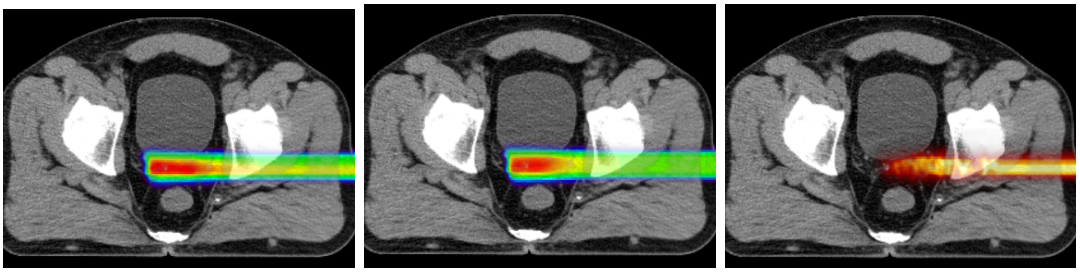

(a) Reconstructed Dose **(b)** Reference Dose **(c)** PET simulated Image

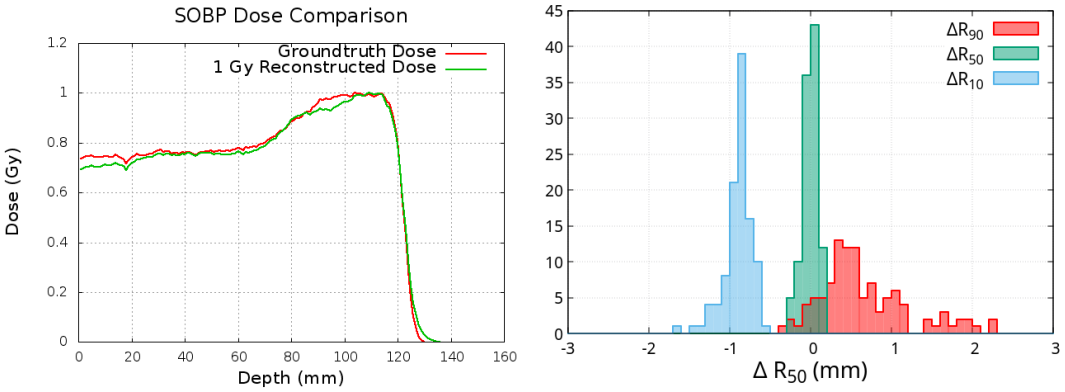

(d) Dose Profiles **(e)** $\Delta R_{\#\#}$ Histograms

Figure 4.11: a) Reconstructed dose from a PET image of a 1 Gy SOBP irradiation. b) SOBP ground truth dose as a result of the combination of 144 pencil beam of a treatment plan. c) PET simulated image associated to the SOBP, as a result of the acquisition time window of 10-40 min after the a 1 Gy irradiation. d) Central dose profiles of both reference and reconstructed data. e) Range deviation histogram obtained by comparing the groundtruth dose with the reconstructed one.

Dose 1.0 Gy - Planned Beam Distribution as Input

Decays	R_{90} (mm)		R_{50} (mm)		R_{10} (mm)		Gamma 2 mm-3%	
	Mean	σ	Mean	σ	Mean	σ	Total	Fall-off
$3.58{\cdot}10^5$	0.61	0.56	-0.056	0.097	-0.94	0.17	88.52	92.53

Table 4.6: Statistical results of the range deviation histogram in Figure 4.11 and the gamma test analysis by comparing the groundtruth and the reconstructed doses.

4.6 Discussion

In this thesis, the DAD-MSA algorithm is proposed as an alternative to the existing methods which reconstruct the delivered proton dose from PET images, such as the *filtering approach* [Parodi and Bortfeld, 2006] and the use of deep learning [Liu et al., 2019; Ma et al., 2020]. The MLEM & Simulated Annealing (MSA) approach is implemented in GPU and it is based on a Dose-Activity Dictionary (DAD) database. The DAD-MSA algorithm is natively three-dimensional and can be applied over any clinical scenario, independently of the beam pulse, the PET time acquisition or the beam delivery technique. It provides naturally noiseless dose distributions by design, which gives it a distinct edge over previous techniques [Masuda et al., 2020; Ma et al., 2020] and makes it easier to analyze range distributions and spot any delivery mistakes.

In light of the dose-dependency analysis, we conclude that our method will be capable of accurately recreating dosages larger than or equivalent to 1 Gy. In simpler scenarios where only one beam is delivered, the reconstruction has been successful simply using an irradiation of 0.1 Gy. It should be noted that the conditions under which this reconstruction has been carried out are far from those of a clinical scenario, in which a 0.1 Gy irradiation may not be enough to properly reconstruct the deposited dose from PET images. However, this conclusion must be taken after testing it in an experimental validation. Even so, this dose of 0.1 Gy is probably more than enough to reconstruct simple doses with very few beams or in phantoms where there is no biological effect on activation, which could be enough to detect issues in the beam delivery.

Based on the obtained results from the PET acquisition modality analysis, both *in-room* and *off-line* PET schemes might be used to verify the proton range and the deposited dose using the DAD-MSA algorithm. Although the offline approach produces slightly better results, both strategies have been demonstrated to be viable for dose reconstruction, provided that a priori information from treatment planning is used as an input to the reconstruction algorithm. However, it is worth noting that the offline PET version produces slightly better results due to the higher total amount of detected counts. Nevertheless, it should be considered that the biological wash-out effect has not been taken into account in this study, which can affect the accuracy of the reconstructed dose distribution [Mizuno et al., 2003; Parodi et al., 2007; Ammar et al., 2014; Bauer et al., 2018; Toramatsu et al., 2018]..

The results obtained from the dose dependency and PET acquisition time analysis represent a breakthrough in comparison with results in previous works [Masuda et al., 2020; Ma et al., 2020]. Best results so far were obtained with irradiations associated to 2-6 Gy and time PET acquisitions carried out 10-15 minutes after the end of the treatment. In this work, reconstructed doses and proton range estimation were obtained with comparable accuracy than previous results, but using doses lower than 1 Gy and assuming the PET acquisition during the first minute after the irradiation.

Our application of the DAD-MSA method employing a priori knowledge from treatment planning has shown to be efficient at identifying anatomical changes [Lomax, 2008; Carabe et al., 2012; Paganetti, 2012] leading to different dose distributions in a realistic clinical scenario. Assuming conditions of a realistic treatment plan in which 1Gy is delivered per fraction and a PET offline acquisition is carried out, the DAD-MSA algorithm has been able to identify range shifts smaller than 1 mm for an absolute proton range of 122 mmm, which implies a deviation less than 1% of the proton range. Furthermore, the 3D dose maps reconstructions allow us to perform a more in-depth analysis of the provided results, such as the gamma-analysis or the proton range estimation along the Z axis in every point in the XY plane. The result of these test would enable the treatment team to choose potential plan modifications for subsequent sessions to account for delivery errors. Considering that the reconstruction can be done instantaneously, error detection parameters would be available during treatment if the PET acquisition was performed during irradiation. This would enable experts to identify deviations from the plan during irradiation rather than after it has been completed. Finally, the proposed MSA algorithm was tested over a more complicated and realistic scenario reproducing the deposited dose by a SOBP. In this case, the reconstructed dose also shows good agreement with the reference dose, which reinforces the potential shown by this method for implementation in real clinical cases.

From a technical point of view, there is some room for improvement in certain aspects of the dose reconstruction algorithm, which we leave for future works. A tendency to overestimate the contribution of lower energy beams has been observed, resulting in the underestimation of the proton range in some cases. The MSA algorithm is not able to establish a zero contribution for the lower energy beams, which although they do not contribute to the simulated activity because they are not part of the delivery dose, they can be part of the final solution, since all the activity they produce is present in

the irradiated region. On the other hand, high-energy beams are often avoided since any activity contribution that goes outside the scope of the PET pictures is severely penalized in the χ^2 calculation. A potential improvement on the method would be to introduce this effect, adding a correction factor to the χ^2 value in the optimization to avoid the over estimation of low energy beams and the penalization of high-energy beams. Furthermore, the biological *wash-out* effect [Parodi et al., 2007; Ammar et al., 2014; Bauer et al., 2018; Toramatsu et al., 2018; Mizuno et al., 2003] (i.e., diffusion of β^+ isotopes in patient body after irradiation) was not included in this work. The impact of *wash-out* on online and in-room techniques is possibly insignificant. However, its impact on offline acquisition should be carefully examined by constructing a time-dependent version of the Ultra-fast MC PET simulator that takes into account patient *wash-out*.

Chapter 5

PET range verification with Water-18: A Clinical Perspective

5.1 Introduction and Motivation

This chapter brings together the work presented in previous chapters, with the aim of testing the viability of contrast agents in proton therapy. In the second chapter, the main potential contrast agents were proposed for PET and PG range verification. The third chapter summarizes in section 3.1 all the cross-section available for the proposed contrast agents that were previously measured in other works. Using this information, we planned a few experiments to measure the cross-sections of those channels that were not measured to the entire clinical energy range, such as the $^{18}O(p,n)^{18}F$. Once the required cross-section were measured, the next step would have been the application of contrast agents in a clinical scenario. To do this, we developed a tool capable to transform a PET image or a PG spectrum into an image of deposited dose, which has been presented in chapter 4. Several tests have shown the capability of this algorithm to estimate the deposited dose, using PET images as input, with high accuracy to different clinical scenarios, demonstrating results from this software are reliable.

It should be recalled that the main interest of PET contrast agents is the introduction of activity in the most distal region of the proton path, just off to the Bragg peak. The purpose of this chapter is to test the advantages that this implies. Analyzing proton range estimations results from the previous chapter, in which the DAD-MSA algorithm was tested, we can not expect a high improve of the accuracy of the reconstructions.

The precision is better than a millimeter, and to improve it is complicated. However, we do expect a significant improvement with the use of water-18 identifying deviations that are not visible using only the activity produced by natural isotopes. In those cases in which the anatomical modification take place at the end of the proton path, where there is no information in the form of activity induced by natural isotopes, it is not possible to detect and identify the deviations in the proton range. The use of contrast agents may provide the solution to this issue because the additional activity that they induced at the end of the proton range can be used to identify deviations in the last millimeters.

To verify our assumption, we conducted a study in a clinical scenario involving the irradiation of a head CT scan with fictitious air bubbles using a proton therapy treatment plan. The air bubbles were strategically placed at two different positions: one at the entrance of the proton beam and the other just off the Bragg peak. Our main objective was to assess the effectiveness of the DAD-MSA algorithm, with and without the use of contrast agents, in accurately detecting and quantifying the deviations caused by these air bubbles in the proton range. Specifically, we expected to observe minimal differences in the proton range estimations when the air bubble was positioned at the entrance. In contrast, when the air bubble was placed right next to the Bragg peak, we anticipated that the deviation would only be identifiable with the use of contrast agents, whereas relying on activity from natural isotopes would lead to completely wrong predictions. By comparing the results obtained under these conditions, we aimed to validate the significance of contrast agents in accurately identifying and characterizing deviations in the proton range.

5.2 Methods

5.2.1 Dose Activity Dictionary - Head CT

A head treatment plan was chosen for this study. As a final step the Dose-Activity Dictionary was calculated following the same procedure described in chapter 4. First, a treatment plan was created using a clinical head CT segmented in Hounsfield Units [Schneider et al., 2000]. The plan was generated using matRad [Wieser et al., 2017] covering the target volume, which was already defined in the CT, with a single field as it can be observed in Figure 5.1. The plan is composed by 625 beams with energies

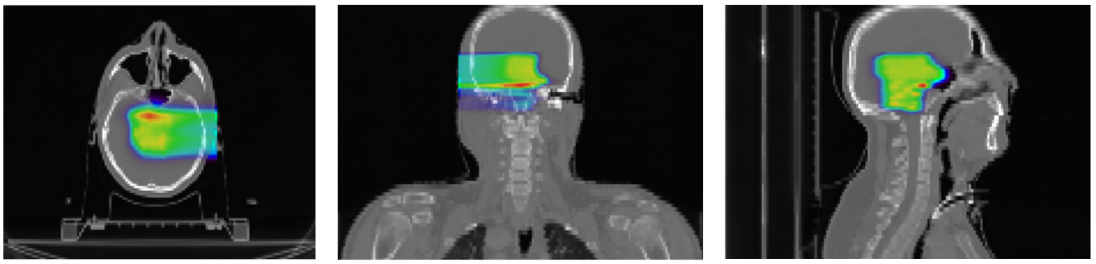

Figure 5.1: Deposited-dose map of the single-field plan, as calculated by matRad [Wieser et al., 2017], over a prostate CT. The optimization results in a set of 625 beams of energies between 70 and 140 MeV. The resulting deposited dose is plotted over the CT.

between 70 and 140 MeV. The beam spatial distribution is described by a Gaussian with sigma values of 0.21 cm and 0.28 cm in X and Y transverse directions, respectively. The beam travels along the Z direction.

Every beam in the plan was simulated with TOPAS in order to calculate the deposited dose and the activation of each isotope produced by each of the beams separately. In these simulations, we have assumed a 10% ^{18}O in the irradiated area to introduce the contrast agent activation. This change does not imply any modification in the dose [España et al., 2021], which is very useful as we can escalate the contributions from ^{16}O and ^{18}O as needed without affecting the deposited dose. The region of interest (ROI) covers all the deposited dose and activity production and occupies a volume of 70x50x140 pixels of 2x2x1 mm^3 (XYZ, finer grid size in the propagation direction). Activation maps were calculated using our own TOPAS scorers described in section 1.5.1 and the cross-sections mentioned in Table 1.2 for ^{16}O and ^{12}C reactions. The reaction channel ^{18}O(p,n)^{18}F cross-sections were also introduced. Below 30 MeV, the cross-section values certified by the IAEA were used [Tárkányi et al., 2019], and above 30 MeV we use an interpolation of our experimental results for this channel obtained in section 3.4.

The activity stored in the DAD is not the simulated activation, but the associated image that would be produced by the PET system. To take into account the PET response a ponit spread function (PSF) is applied to the simulated activation by TOPAS. In this scenario, the Siemens mMR Biograph PET system is used to perform the theoretical imaging and therefore the PSF is applied to the activation maps calculated by TOPAS.

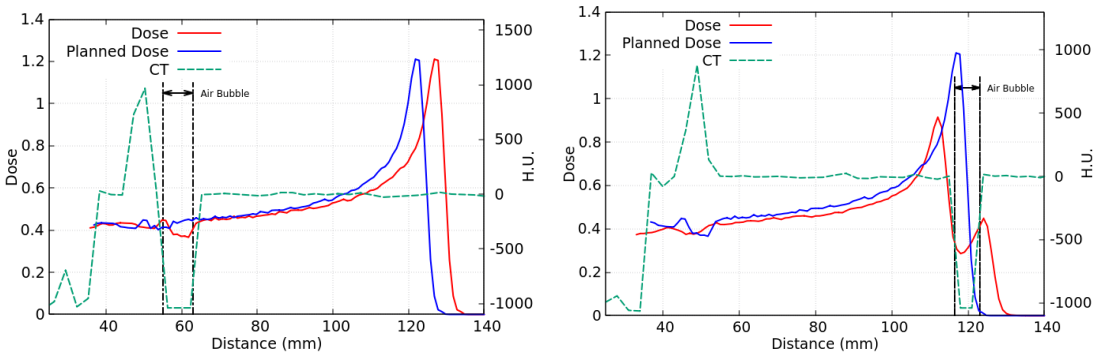

Figure 5.2: Planned (blue) and expected (red) doses from both scenarios where an air bubble were virtually introduced in the proton path. CT profiles with the air gaps due to air bubbles are also plotted in greens dashed lines.

5.2.2 Test scenarios

Two different scenarios have been used to test the potential of contrast agents. In both scenarios, an air bubble of 5.0 mm diameter was inserted in the patient CT in two different positions. In one case, the air bubble was placed at the entrance of the proton path, and in the second case, it was located just close to the Bragg peak where there is no activity. These modifications induce a range deviation. This effect can be observed in Figure 5.2, where the expected dose with no CT modification is plotted in blue, along with the resulting dose using the modified CT in red. The image on the left side shows the case where the air gap is at the entrance of the proton beam in the patient. As a result, the BP is deviated 3 millimeters from where it was expected to be. On the right side image, where the air gap is at the end of the proton path, the Bragg peak splits into two different peaks. The first one is placed where the planned BP was expected and the second one 5-6 millimeters far away.

These two modified doses have been reconstructed from activation data and analyzed, in order to assess wether the MSA algorithm is capable of identifying them with and without ^{18}F. To carry out this test we generated 2 different PET images for each scenario: 1) the activation that would be produced in the patient without contrast, 2) the activation assuming that 10% of ^{16}O has been replaced by ^{18}O. In both cases we have assumed a 3 Gy dose at the BP produced by a single beam of the treatment plan with an energy of 120 MeV.

We chose a theoretical *offline* scenario where the measurements were carried out in the time interval of 10-40 min after the irradiation. In addition, we implemented the *wash-out* effect using the mathematical model proposed by Toramatsu et al. [2018, 2020]. This model describes how the ^{15}O, ^{13}N and ^{11}C diffuse through the body and allow us to calculate how much activity will remain in the irradiated region after a certain period of time. This model did not study the diffusion of ^{18}F. However, in a study carried out by España et al. [2022], it was determined that ^{18}F does not diffuse outside the cells in living tissues by fast mechanism and it remains inside the cell on the order of hours. The final consideration is that 60% of ^{13}N, 50% of ^{11}C and 85 % of ^{18}F remain in the irradiated area. ^{15}O is disregarded because its contribution is negligible 10 minutes after the irradiation.

PET images were generated following the same procedure as described in section 4.4.2. The resulting PET activity distributions were used to estimate the deposited dose with the DAD calculated using the CT for planning, without the air bubbles. The MSA algorithm reconstructs the dose associated to these PET images, so we expect the MSA algorithm to be able to recover the "wrong" doses and identify that there have been deviations from the initial plan. Furthermore, we will analyze the impact of contrast agents in the verification in order to determine their applicability in proton range verification.

5.3 Results

5.3.1 Air gap at the entrance

This case represents a possible clinical scenario in which a 5 mm diameter air bubble appears in the patient after the generation of the CT used for planning, near the entry point of the proton beam in the planning volume. . This induces a non-expected shift on the proton range, which implies an erroneous deposition of the dose compared to what was planned. The dose associated to this scenario has been reconstructed from two simulated PET images, one with contrast agents and the other does not.

The reconstructed doses with contrast agent (red) and without it (blue) are shown in Figure 5.3 along with the planned/expected dose and the deposited dose in the modified CT. The results clearly show how the MSA algorithm is able to detect the range shift with and without the contrast agent, with similar accuracy. Table 5.1 show the ΔR_{50}

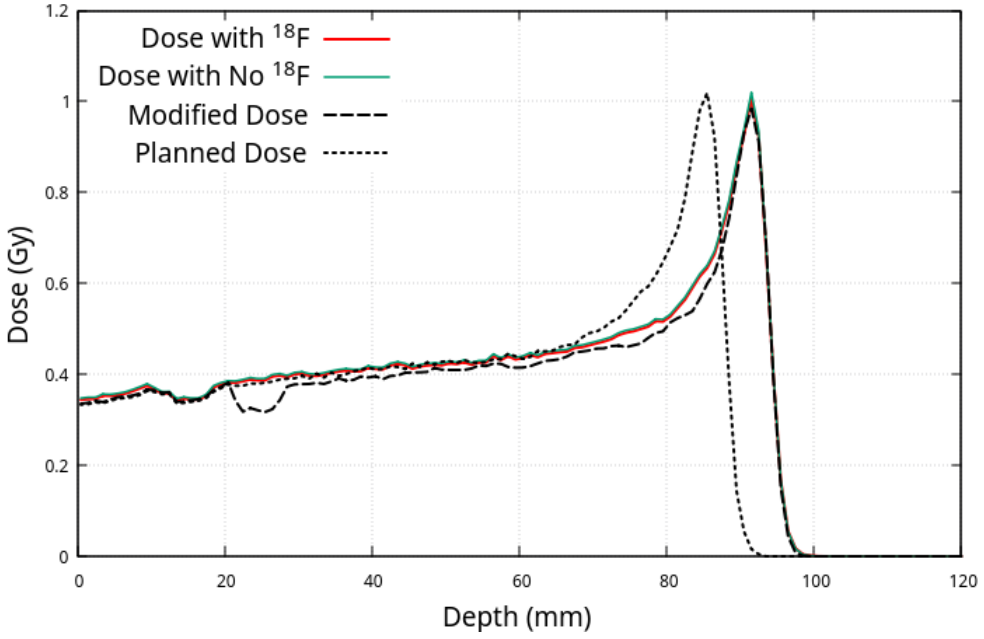

Figure 5.3: Reconstructed doses with and without ^{18}F in red and blue respectively, in the case where the air gap is located at the entrance. Figure shows these two reconstructed dose along with the planned dose and the real expected dose. Both doses estimated from PET images with and without contrast agent identify and reproduce the dose deviation.

from each scenario, together with the results of the gamma analysis. The expected range deviation induced because of the air bubble is 6.14 mm, which perfectly match with the estimations from the reconstructed doses. In addition, the gamma analysis also shows that something is wrong with the reconstructed dose, specially the one focused on the fall-off region, where only the 10% of the pixels pass this test.

Case	ΔR_{50} (mm)		Expected	Gamma 1 mm-3%	
	Mean	σ	ΔR_{50} (mm)	Total	Fall-off
^{18}F	6.10	0.16	6.14	92.88%	10.12%
Natural	6.11	0.22		93.04%	11.02%

Table 5.1: The most significant parameters of the anatomical variation detection using contrast agents are shown in this table. Mean and sigma values obtained from the histograms of Figire 5.3 with the expected values indicate the precision in the range determination. The gamma 1 mm-3% test shows the quality of the overall region and the fall-off region of the reconstructed dose.

5.3.2 Air gap at thedistal edge

This scenario is similar to the previous one but, in this case, the air bubble is much deeper in the CT just under the Bragg peak. As a consequence, the Bragg peak splits into two smaller peaks (Figure 5.2). The resulting dose differs from what was planned, and we have used the PET images associated to activation maps with and without contrast agent to identify it.

Similarly to the previous case, the reconstructed doses are plotted in Figures 5.4, together with the planned dose and the real deposited dose in the modified CT. And Table 5.2 show the expected and the calculated $\Delta R_{\#\#}$ of each of the cases. Both reconstructed doses reproduce well enough the first peak, which is placed approximately 5.5 mm shorter than the planned BP and to which correspond ΔR_{90} and ΔR_{50} parameters. Comparing these two parameters between the case with and without water-18, it can be concluded that the natural activity reproduce with a little better accuracy the position of this first peak. However, this behavior drastically changes for the second peak, which is identified with the ΔR_{10} parameter. In this case, the reconstructed dose with ^{18}F performs much better, producing a more accurate representation of the actual deposited dose. Although it is unable to perfectly scale the peak splitting, it is still able to identify it to some extent. The expected value for the ΔR_{10} compare with the planned dose is 5.56. The reconstructed dose with water-18 provides a value of 5.98, which is very close to the expectation, while the value obtained from the case without contrast agent is -3.5 mm. This implies that the proton range is shorter than the planned one, when the reality is that the range is 5.56 mm larger. This erroneous estimation may lead to wrong appreciations and corrections of the plan, with all the harm that this entails for the patient. Therefore, the use of contrast agents in proton therapy is crucial for accurate dose reconstruction, as it helps to identify deviation in the last millimeters and improve the overall quality of the reconstructed dose.

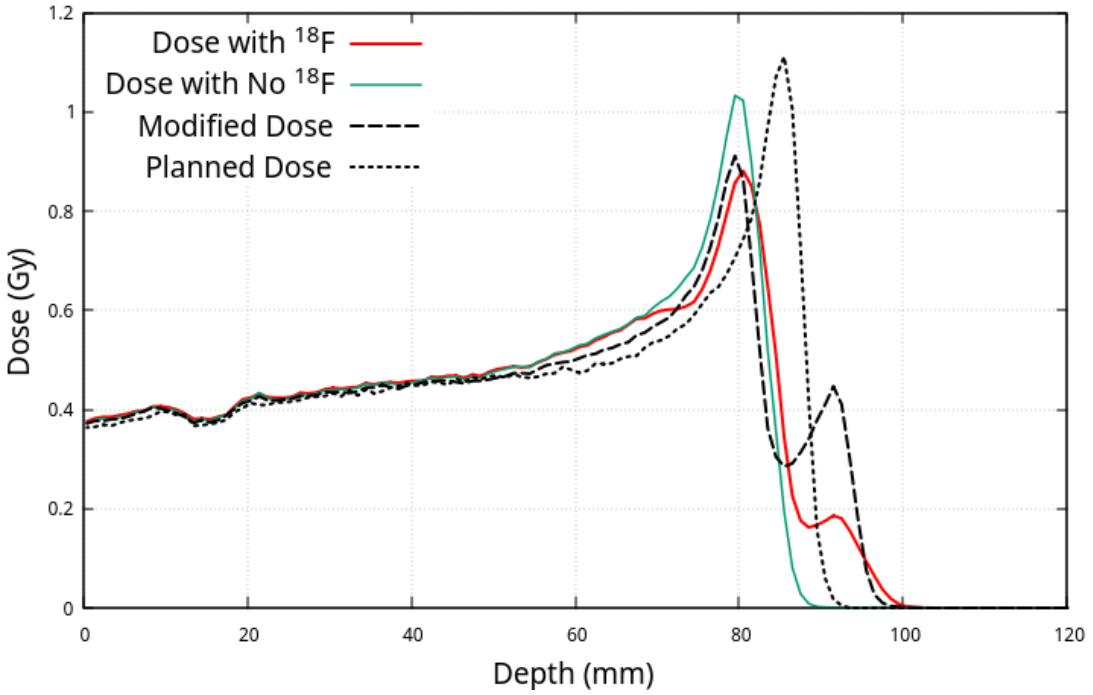

Figure 5.4: Reconstructed doses with and without ^{18}F in red and blue, respectively, in the case where the air gap is located at the Bragg peak. This figure also shows the planned dose together with the deposited dose in the modified CT. In this case, the deviation is only identified in the case where the contrast agent is implemented.

Case	ΔR_{90} (mm)			ΔR_{50} (mm)			ΔR_{10} (mm)		
	Mean	σ	Exp.	Mean	σ	Exp.	Mean	σ	Exp.
^{18}F	-3.99	0.47	-5.78	-3.05	0.24	-5.29	5.98	0.24	5.56
Natural	-5.10	0.61		-4.20	0.59		-3.53	0.30	

Table 5.2: Expected and calculated range deviation and gamma analysis from bubble at the entrance

Overall, the improvement in the reconstruction using ^{18}F is sizeable. Even if the reconstructed dose not reproduce exactly the actual result, the MSA algorithm is able to provide a result much closer to the groudn truth thanks to the presence of the contrast agent. The reason is related to the fact that ^{18}O generates β^+ isotopes much closer to the end of the proton range than ^{16}O. Therefore, anatomical changes in the most distal part of the proton path are only identifiable with the use of contrast agents. This results

highlights the great advantage of contrast agents such as ^{18}O over natural isotopes for range verification using PET.

5.4 Discussion

In this chapter, we have tested the advantages of using contrast agents in proton range verification techniques using PET systems. As it has been mentioned before, the principal property of our proposed contrast agents is the generation of β^+ isotopes at very low proton energies, which is the same, at the end of the proton range where there is no activity production from natural tissues. Our hypothesis was that if there were deviations in these last millimeters of the proton range, they would only be identifiable with the use of contrasts.

In order to test this idea, a study has been conducted using the DAD-MSA presented in Chapter 4 to calculate the proton range in two hypothetical scenarios. In these scenarios, an air bubble was introduced to create a deviation in the range, one located at the entrance of the beam and the other precisely at the Bragg peak. For each case, the dose was reconstructed both with and without water-18, to observe in which cases the contrast makes the difference. The results show that contrast agents do not play a very important role if the deviation is produced at an intermediate point of the proton range, since it can be identified with or without contrast. However, it has been demonstrated that in the second case, where the bubble is positioned precisely at the Bragg peak, resulting in a splitting of the peak, only the reconstruction with water-18 is able to accurately reproduce and identify this modification in the dose.

These results support our initial assumption, at the same time that they show that contrast agents are beneficial in proton range verification techniques, because they make it possible to identify deviations that may not be appreciable without them. The incorporation of contrast agents in proton range verification techniques represents a notable advancement, enabling precise localization of the complete Bragg peak. This is particularly valuable in rare cases where modifications occur directly at the Bragg peak, ensuring accurate identification and assessment of such deviations. Since the Bragg peak is responsible for the majority of the deposited dose, the ability to detect deviations in this region would prevent undertreatment of the tumor or exposure of nearby organs at risk, due to unexpected deviations in the proton range during treatment.

5. PET RANGE VERIFICATION WITH WATER-18: A CLINICAL PERSPECTIVE

The promising findings presented in this chapter regarding the effectiveness of contrast agents in proton range verification techniques have inspired us to explore additional options for implementing such agents. Further investigations should be conducted to evaluate the feasibility of using short half-life ($t_{1/2}$) contrast agents, which could facilitate beam-specific proton range verification using PET systems. Moreover, these encouraging results also motivate us to conduct future experiments aimed at assessing the potential application of contrast agents in PG verification systems and the associated benefits they may offer.

Chapter 6

Ultra-fast GPU Monte Carlo for Prompt-Gamma simulation

As discussed in Section 1.3.2 another promising technique for proton range verification in proton therapy is the use of prompt gamma radiation produced by proton-induced reaction in tissues. The use of prompt gammas-rays (PG) for proton range verification has been already tested, yielding promising results [Verburg and Seco, 2014; Hueso-González et al., 2018]. In the mentioned studies, range shifts of less than 2.0 millimeters using phantoms have been detected. The authors have also tested their PG verification system with components that resemble human lungs and hearts, resulting in range estimations with accuracies in the order of a millimeter. The results support the use of prompt gamma-ray detection for proton range verification in clinical scenarios.

Because the final goal of this technique is the *in-beam* verification of the proton range during the treatment, three conditions must be satisfied: 1) to have detection systems capable of measuring PGs. 2) to develop a fast reconstruction algorithms able to estimate range and dose, in less than a second. 3) A fast and efficient tool that simulates and generates all necessary a priori information for proton range verification algorithms. The first condition is already achieved. Two different PG system have been successfully tested [Hueso-González et al., 2018; Bello et al., 2020]. The second condition could be fullfiled with the implementation of our proposed DAD-MSA algorithm in chapter 4 to this technique. The third condition presents more challenges, especially if the intention is to introduce Monte Carlo simulations in the reconstruction algorithms. The total amount of PGs induced by a single proton beam can be estimated using

the nonelastic scattering probability tables calculated by Janni [1982] and validated by Polf et al. [2013]. These tables indicate that a 150 MeV proton beam in water has a 16.62 ± 3.66 % probability to interact via nonelastic scattering. A normal clinical beam of 150 MeV needs around 10^9 protons to deliver 1 Gy at the BP, which implies a total amount of PGs close to $1.6 \cdot 10^8$. Considering that a plan is composed by 1.000-10.000 beam, the number of photons to simulate would be around 10^{12}. In a conventional MC, the computational time required to carry out the whole simulation in a regular computer could be days or even weeks.

In this chapter, a new GPU-MC photon simulator is proposed to accelerate as much as possible the propagation of high energy PG. This work was developed at the Massachusetts General Hospital (MGH) and Harvard Medical School during a stay of six months. The MGH has one of the few PG verification systems that exists in the world [Verburg and Seco, 2014; Hueso-González et al., 2018]. The main objective of this work was to accelerate the simulation of the a priori information needed by the reconstruction algorithm to estimate the proton range. In previous versions of the available code at the MGH, the time required was always more than several hours, and with the new GPU-MC code this time was reduced to a few minutes.

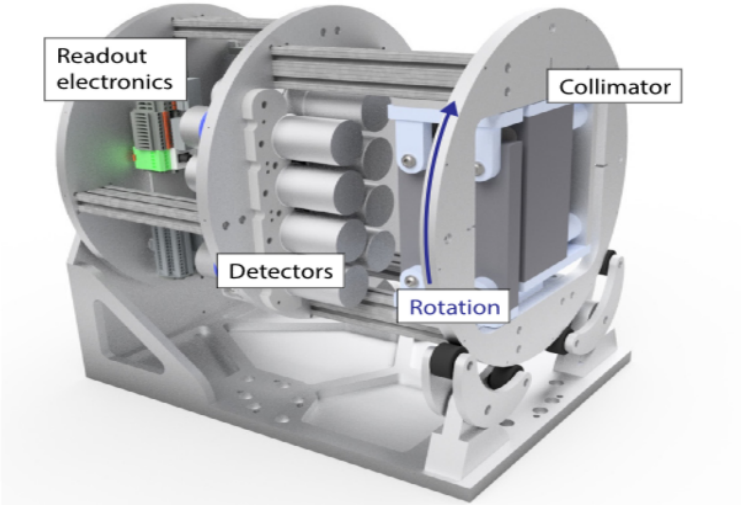

Figure 6.1: 3D model of the clinical prototype system, which can rotate around its axis according to the beam incidence angle. The tungsten collimator is visible on the front plane, the eight scintillation detectors in the middle and the readout electronics on the back plate [Hueso-González et al., 2018].

6.1 Introduction and Motivation

The development of the mentioned GPU-MC for high-energy photons is placed in the framework of the PG range verification system proposed by Hueso-González et al. [2018]. The detection system in composed by eight $LaBr_3(Ce)$ scintillator detectors and a tungsten collimator (Figure 6.1). The detectors have a cylindrical shape with a diameter of 50.8 mm and a length of 76.2 mm and each of them is coupled to a PMT. The detection system is capable of measuring the energy and the time arrival of the PG emitted by the irradiated target (PG spectroscopy technique, section 1.3.2) from a FOV of 120×320×320 mm^3, divided in 120x160x160 voxels. This system provides the energy-time spectra of PGs emitted from the FOV, which are used for the proton range estimation. In general terms, this process is carried out by a reconstruction algorithm that compares the characteristics of the measured data with the expected results, given by a detailed model of the expected gamma-ray emissions.

The generation of the expected gamma-ray model is a complex process, as it depends on the patient and the treatment plan. In the work carried out by Hueso-González et al. [2018] at the MGH, its calculation was divided in three different and independent processes. The convolution of the results provides the *Prompt gamma detection model* used by the reconstruction algorithm to estimate the proton range. The generation scheme of this model is shown in Figure 6.2, where the 3 independent processes can be observed.

1. **PG ray emissions production:** the first step is the simulation of the beam delivery to calculate how many prompt gamma emissions are produced and where. This step can be performed once the treatment is available. Furthermore, it is already implemented in GPU and the required time to calculate it is just a few minutes.

2. **Transmission probability:** this process calculates the probability that a prompt gamma-ray of a certain energy emitted from a pixel of the field of view reaches the collimator surface. In a common plan, the number of pixels in the FOV with PG emissions is around $250{\cdot}10^3$. Taking into account that 7 different energies between 1.3 and 6.6 MeV are considered by the reconstruction algorithm [Hueso-González

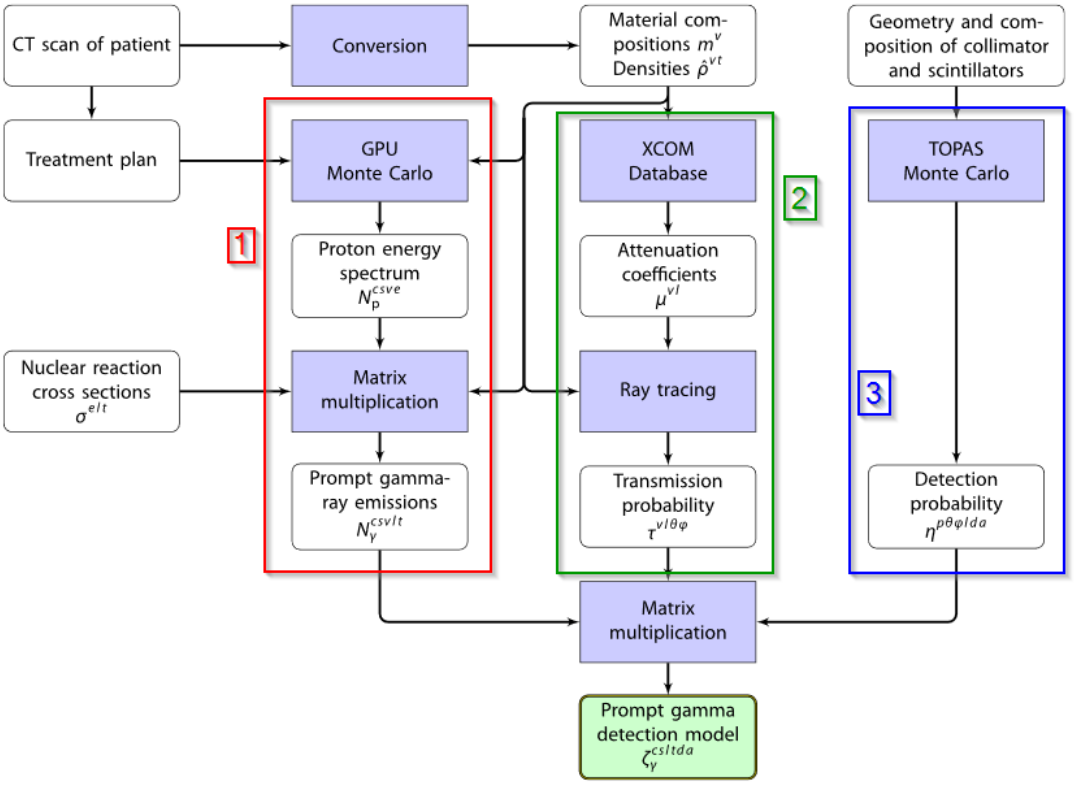

Figure 6.2: General scheme of the PG system verification model developed at the MGH [Hueso-González et al., 2018]. 1) Simulation pf the PG emissions production. 2) Simulation of PG transmission probability from where they are produced to the collimator. 3) Detector probability response independent of the patient scenario.

et al., 2018], 7 different energies with at least 10.000 photons each must be simulated to obtain acceptable statistics. The total number of simulated photons in this step rises to 10^{10}, which would take several hours or days on a normal computer running a standard Monte Carlo.

3. **Detection Probability:** this step is the only one that is independent of the clinical case. It provides information on the probability that a given photon reaching the surface of the collimator, with a specific energy and direction, will be detected by each of the eight detectors.

The final model of the expected prompt gamma emissions is given by the convolution of the three processes described above. The determination of the absolute proton range of a pencil-beam spot is achieved by minimizing the least square residuals between the

measured gamma-ray obtained through experiments and the corresponding data from by the prompt gamma detection model. This method was tested by Hueso-González et al. [2018] with promising results.

The main limitation of this method is that it takes a long time to calculate the PG transmission probability. In the version proposed by Hueso-González et al. [2018], they implemented a theoretical calculation of the photon attenuation, without taking into account secondary photon as a consequence of Rayleigh or Compton scattering. This approximation is valid because of the presence of the collimator, which stops almost every secondary photon. Even so, the program was still very slow and it took almost 2-3 hours to simulate the simplest case.

To solve all of these issues, a full GPU Monte Carlo code specifically developed for high-energy photon transportation has been developed in the framework of this thesis. It is based in some of the aspects of the Hybrid MC approach proposed by Ibáñez et al. [2021], which was specifically developed for dose calculation of low energy X-rays. In this work, this code has been adapted to high-energy photons and optimized for photon transport. In addition to the photon propagation, this code also includes the convolution of the prompt gamma-ray emissions and the detection probability with transmission probability, resulting in the PG Detection model.

6.2 Hybrid Prompt gamma Transportation (HPT) MC

The HPT-MC (Hybrid Prompt gamma Transportation - Monte Carlo) is a tool for the simulation of photons with energies comprise between 10 keV to 10 MeV across vowelized geometries. It uses a Woodcock MC algorithm [Woodcock et al., 1965; Carter et al., 1972; Badal and Badano, 2009] for the photon transport, which implies that the step length is given by the shortest mean free path (mfp) of all the present material in the simulation (see section 6.2.2 for further explanation). To address this assumption, in materials with a larger mean free path (mfp), it is necessary to incorporate an additional "virtual non-interaction" term. This correction helps compensate for the excessive interaction introduced by the Woodcock approach. The HPT-MC also includes some aspects of the Hybrid Monte Carlo approach proposed by Ibáñez et al. [2021] to accelerate the simulation. Specifically, the use of precalculated databases with the angles and energies of the ejected particles after Compton and Rayleigh interaction

has been implemented. In this way, these parameters are read from the databases after each interaction instead of calculating them. This implementation makes the simulation more efficient and increases its speed by a factor 100. Furthermore, this option allows us to introduce the physics from any conventional MC that permit to extract/calculate these databases. In this work the databases were generated from PENELOPE [Salvat, 2013] models.

This code has been implemented in GPU, which implies the parallelization of the problem. Generally, an ionizing particle transport MC is able to parallelize the simulation of each of the stories as they are completely independent of each other. Consequently, a GPU MC is capable of simulating thousands of particles at the same time. However, this scenario is not the ideal for the ongoing problem. The ultimate goal of this tool is to calculate the transmission probability of a photon with a specific energy from every voxel in the field of view (FOV) to the surface of the collimator. Because of that, the parallelization has been implemented at the voxel level, allowing for simultaneous processing of multiple voxels. In this way, the host code (CPU) only calls the device code (GPU) once for each voxel, and inside the GPU each thread simulates an arbitrary number of photons with the same initial energy and position but different directions. This method reduces the number of calls to the GPU and the number of times data is copied from device memory to host memory, which leads to an optimal use of the computational time. In addition, the utilization of this method eliminates the need for atomic sums on the GPU, as each thread is responsible for updating only its respective voxel. Avoiding such operations helps to prevent bottleneck, thereby making the code more efficient. The use of atomic operations in GPU slows down the code significantly as they queue operations so that two or more threads do not overlap updating the same memory address, which may lead to erroneous results.

The HPT-MC has been implemented and adapted to the specific case of the MGH PG verification system to accelerate the simulation of the PG transportation from where they are produced to the front face to the collimator. The overall workflow of the code is shown in Figure 6.3. The program begins reading and loading in memory all the simulation parameters, the precalculated tables for Compton and Rayleigh interactions, the input seeds for the random numbers, the prompt gamma-ray emission model and the detection probability model. Once the initialization is done, the code calculates the most optimal combination of blocks (N) and threads (M), considering that the parallelization

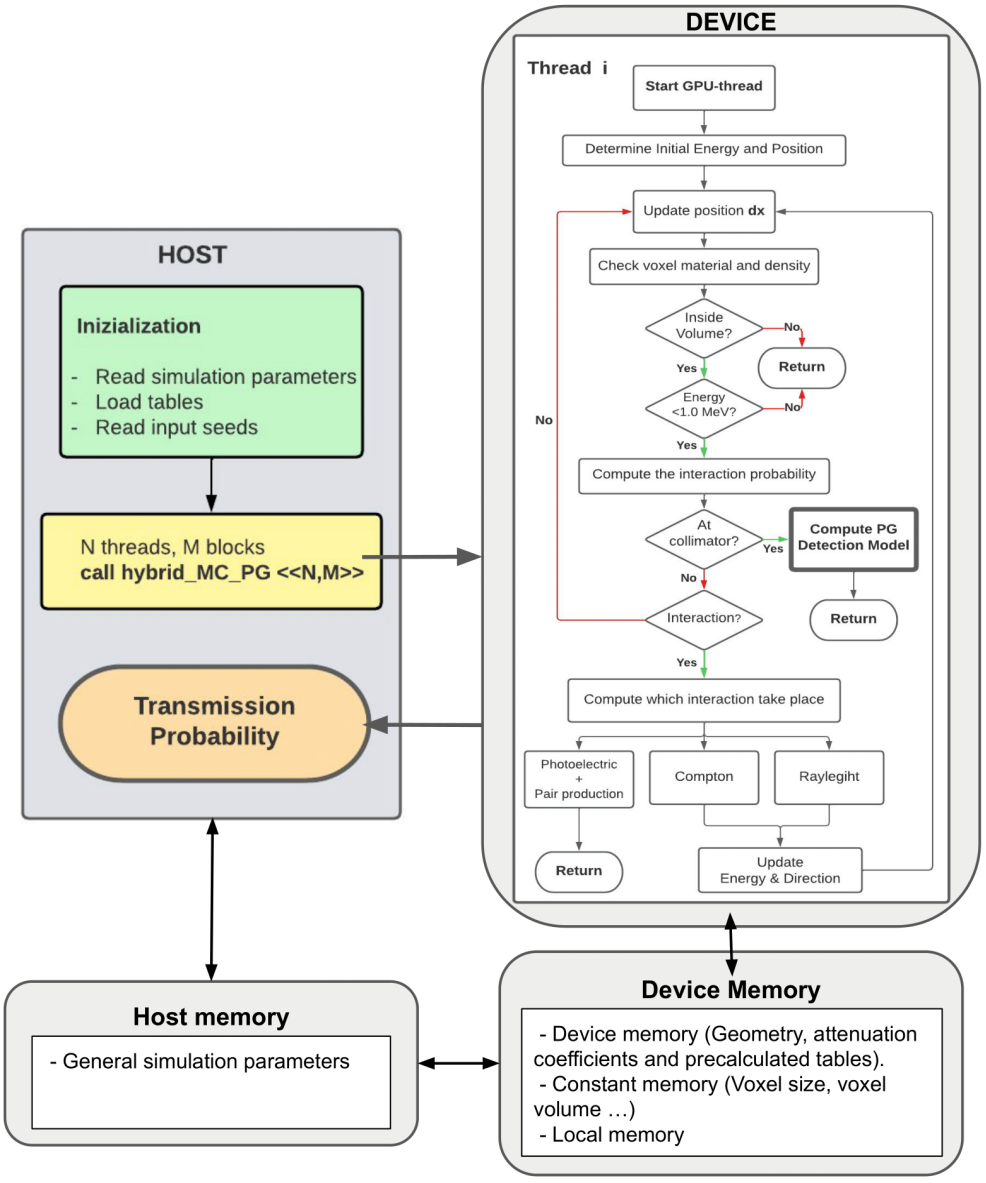

Figure 6.3: Overall workflow of the Hybrid Prompt gamma Transportation - Monte Carlo

is done over the voxels with non-zero activity contribution, information given by the prompt gamma-ray emission model. At this point, the GPU starts to work. Each thread simulates an arbitrary number of initial photons with the same energy and position, but with random directions. The photons are transported through the volume until their

energy is lower than the energy threshold, they are outside the volume, or they interact via photoelectric effect or pair production. When photons reach the collimator surfaces, their contribution to the final Prompt gamma detection model is calculated applying the detection probability model over the current properties of the photon, otherwise, if the photon do not reach the collimator its contribution to the model is considered zero (see section 6.2.3 for further explanation). Once all initial photons are simulated by each thread, the final Prompt gamma detection model is copied from the device to the host memory.

The verification system does not take into account any information from measured data with energy lower than 1.0 MeV. Hence, photons below 1.0 MeV are not considered in the simulation by setting the energy threshold of the simulation at 1 MeV. Ignoring these photons has no effect on the final result of the simulation, while significantly reducing the computation time. As a consequence, photons with lower energy than 1.0 MeV are rejected. Because of that, the pair production effect is combined with the photoelectric effect and considered as a single interaction. The two 511 keV photons produced during the pair production effect are not simulated, which is equivalent to the photoelectric effect from a simulation perspective. Combining both interactions as a single one improves the efficiency of the code without compromising the accuracy of the results.

In the following sections, each of the points will be detailed for a better understanding and comprehension of the code.

6.2.1 Input Parameters

The HPT-MC was specifically developed for the PG detection system at the MGH [Hueso-González et al., 2018], and for that reason the geometry has been fixed. However, the program can easily adapt to the irradiation conditions specific to each case. All it requires is a CT image of the target being irradiated and a mask, which is generated by the GPU proton MC and indicates the voxels that have the potential to produce activity. Apart from the variables specific to each case, the program must also load in memory all information related to the materials used in the simulation, including their density, photon interaction cross-sections, attenuation coefficients, and pre-calculated databases for photon interactions (Compton and Rayleigh). A database with more than

30 different materials (including all those related to Hounsfield units (HU) [Schneider et al., 2000]) was calculated and stored with all the information mentioned above.

6.2.1.1 Treatment Inputs - CT

The only inputs which depend on the treatment plan are the CT of the irradiated target and the mask of voxels with non-zero activity. The CT must be introduced in Hounsfield Units (HU) [Schneider et al., 2000] and its dimensions can not exceed the FOV volume (120x320x320 mm^3).

6.2.1.2 Treatment Inputs - Mask

The mask is obtained from the proton GPU Monte Carlo and identifies the voxels where activity is generated due to irradiation. Margins are added to the contour of the theoretical activity to detect any deviations that may lead to activity in unexpected regions. This mask is extracted from the prompt gamma-ray emissions model and it is not strictly required for the simulation, but it significantly reduces the simulation time while maintaining accurate range verification results. The transmission probability is calculated only for the voxels indicated by the mask, which typically reduces the number of voxels in the FOV from 2.34 million to around 500,000, saving about the 75% of the simulation effort.

6.2.1.3 Materials

Material information are read from a precalculated database with all the necessary information for the photon propagation. This database is formed by 30 different materials, of which 24 of them correspond to the 24 Hounsfield Units described by Schneider et al. [2000]. The rest corresponds to common material in these scenarios, such as the collimator material (Tungsten) and different kind of detectors ($LaBr_3$, NaI ...). For each material, the database stores the following information.

- **Photon mass attenuation coefficients**

  The photon transportation and its interactions with the medium are defined by the photon attenuation mass coefficients (μ) (Section 1.1.1). This magnitude allows calculating the interaction probability of a photon of a certain energy after traveling a certain length., such as photoelectric effect (μ_{ph}), Compton Scattering

(μ_C), Rayleigh (μ_R) or pair production (μ_{pp}). The sum of the probabilities of these four interactions results in the total mass attenuation coefficient (μ_{tot}). These parameters depends on the energy and they are stored in the database from 10 kev up to 10 MeV in 10 keV steps for each material. The μ values were extracted from PENELOPE and will conform what was defined as probability distribution functions.

- **Compton and Rayleigh tables**

  The ejected particles from inelastic (Compton) and elastic (Rayleigh) scattering are not calculated using internal routines. The properties of the ejected particles are read from precalculated tables. These tables are created from PENELOPE routines In the case of Rayleigh, they provide the angle scatter of the photon and in the case of Compton, a pair of energy-angle values. For each material, 100.000 possible cases were generated using these routines for both interactions and for energies between 10 keV and 10 MeV. The HPT-MC program reads the ejected photon properties from the tables using the following scheme,

  – $Rayleigh \rightarrow [\theta] = T(E_i, M, R)$

  – $Compton \rightarrow [E_f, \theta] = T(E_i, M, R)$

  where θ is the scattered angle, E_i is the initial energy of the photon, M is the material, R is a random number between [1-100k] and E_f is the scattered energy of the photon in the case of Compton scattering. These tables are at the same time part of the probability distribution functions, because they provide information of secondary particles, and a variance reduction technique because it increases the speed of the code.

6.2.2 Woodcock photon propagation

The tracking of photons is performed using the Woodcock algorithm approach [Woodcock et al., 1965; Carter et al., 1972; Badal and Badano, 2009]. This algorithm considers that the simulated particle is all the time in a reference material with a mass attenuation coefficient μ_{ref} , which is usually defined by the highest μ value among all the

materials in the simulation. Therefore, the step length (λ) along the whole simulation is the same and it is given by the following expression

$$\lambda = -\frac{ln(\epsilon)}{\mu_{ref}} \tag{6.1}$$

where ϵ is a random number between 0 and 1. This expression is the mean free path formula adapted to the random MC behavior.

As a result, every material in the simulation is defined as its own μ_{mat} value plus a fictitious μ_f, which always add up to μ_{ref} ($\mu_{ref} = \mu_{mat} + \mu_f$). The fictitious coefficient introduce a *virtual non-interaction* in which the photon continues its path without interacting with the medium. In this way, the excess of interactions due to the use of the highest μ_{ref} of the simulation is compensated.

In the Woodcock approach, the photon interacts at each step and it is necessary to determine which kind of interaction takes place among all the possibilities. This process is determined considering the probabilities of each of the interactions given by

$$P_{int} = \frac{\mu_i}{\mu_{ref}} \tag{6.2}$$

At each step of the simulation, an additional random number between [0-1) determines which interaction occurs based on the probabilities of each interaction. The possible interactions include:

- ***Virtual* Interaction:** the photon do not interact with the medium. It follows its path with the same energy and direction.
- **Photoelectric effect:** the photon is absorbed by the medium. The scattered electron is absorbed locally.
- **Compton scattering:** the photon transfers part of its energy to and electron in the medium. As a result, the photon changes its energy and its direction. The new simulation parameters are read from precalculated tables. The scattered electron is neglected.
- **Rayleigh:** the photon interacts with the medium, changing its direction, but without loosing energy. The new direction is read from tables.

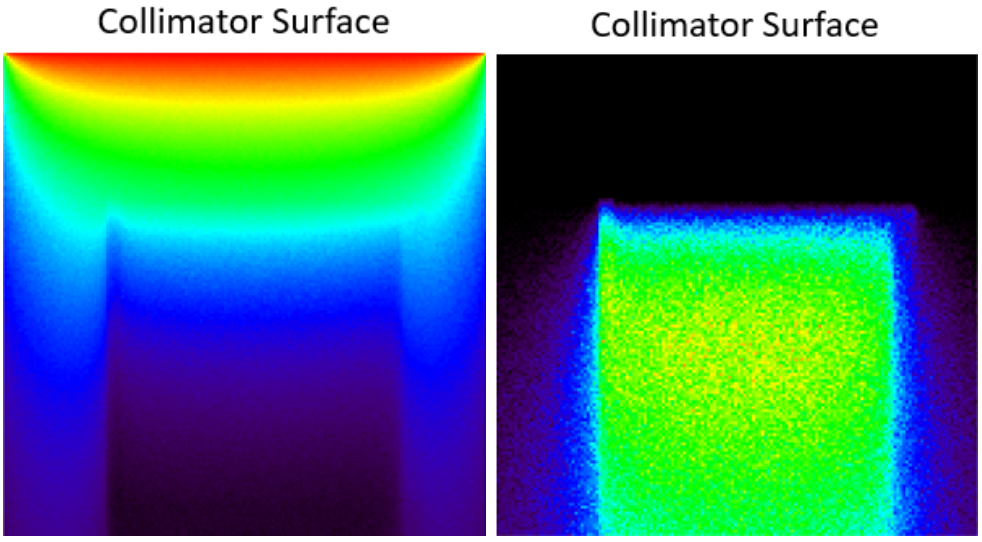

(a) Attenuation **(b)** Compton

Figure 6.4: Transmission probability model separated in two contributions. 1) Attenuation: indicates the probability that a photon emitted from a certain voxel reach the collimator surface with the initial energy. 2) Compton: indicates the probability that a photon reaches after loosing energy in a Compton interaction. Attenuation effect is more important though the eater than in air. On the contrary, only photons which travel through water contributes to Compton.

- **Pair production:** a photon annihilates in the medium generating an e^--e^+ pair. The 511 keV photons are assumed to be absorbed locally.

6.2.3 Prompt gamma detection model calculation

The Prompt gamma detection model is calculated as the convolution of the PG emission model, the transmission model and the precalculated detection model. The emission model is introduced as input (mask) and implemented before tracking photons in order to speed up the simulation and make it more efficient, simulating only those voxels with non-zero activity. The detection model is also included as input in the code, but it is only applied at the end of the simulation of each photon if it has successfully reached the collimator. The detection probability matrix is implemented based on the photon properties at the collimator, which provides its contribution to the final prompt gamma detection model. If the photon does not reach the collimator its contribution to the final model is zero.

The code also permits to simply calculate the Transmission probability model. If this option is chosen, the mask is not taken into account and every voxel is simulated, and the detection probability is neglected. It only stores information on whether the arriving photon has the main energy or whether it has less energy due to Compton interaction. Figure 6.4 shows an example of a sagittal plane of a Transmission probability model associated to 4.44 MeV PGs and a water phantom of 10x10x10 cm^3 (the rest of the volume is air). The contributions of photons which reach with the initial energy and those which lost energy due to inelastic scattering are separated. As it is expected, the attenuation effect is higher in water than in the air. On the contrary, only voxels whose emitted photons travel through the water phantom contribute to the Compton scattering

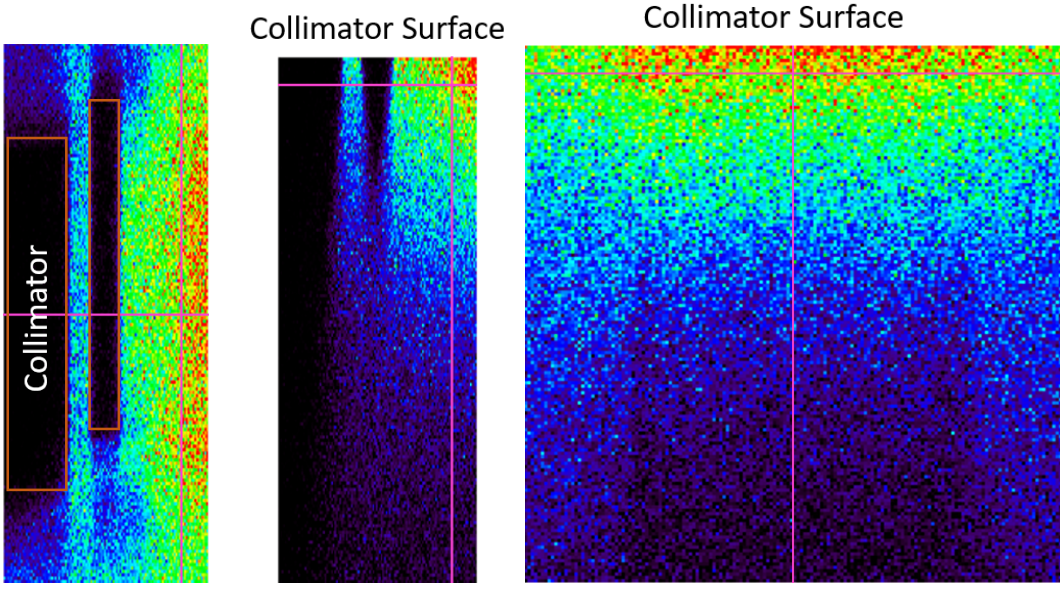

(a) Transversal **(b)** Frontal **(c)** Sagittal

Figure 6.5: Graphic representation of the 4.4. MeV PG detection model using as input a water phantom. Its detection probability has been calculated for every pixel in the FOV and the main patterns of the collimators are visible.

The Prompt gamma detection model associated to this same case is shown in Figure 6.5. In this scenario, the detection model has been applied to the photons which reach the collimator surface. The detection model includes information of the collimator and the detector efficiency. Considering that in the simulation, most of the photons do not deposit energy in the detectors, and therefore they do not contribute to the

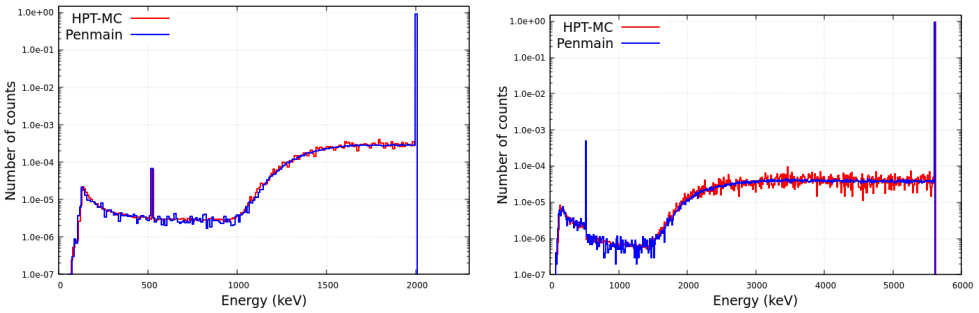

(a) 2.0 MeV Spectrum **(b)** 5.6 MeV Spectrum

Figure 6.6: Photon spectra calculated in the collimator surface with the HPT-MC in red and with Penmain in blue. The results from both codes are identical, but the simulation time is 1000 time less in the HPT-MC.

final model. The sagittal plane shows a similar shape than in the Transition model but with much lower statistics. In the transversal plane, the shape of the collimator is clearly visible because photons are not able to travel through it. Voxels in front of the collimator do not contribute to the final model, as their associated photons can't reach the detectors. Similarly, in the frontal plane the collimator positions are clearly visible, since there is no contribution in the voxels placed next to them.

6.3 Validation

The validation of the code has been carried out in two different steps. The first one consists in the comparison of the results of the HPT-MC with a validated Monte Carlo to ensure that the transportation of the photons is performed correctly. In the second step, the results of proton range verification from the overall program have been compared with the analogous results obtained with the previous version, which only takes into account the theoretical attenuation of the PGs. First, we study the results implementing only attenuation in the HPT-MC, which should be similar to the previous results. After that, the results were obtained with the full version of the MC and the improvements were analyzed.

6.3.1 Comparison with *Penmain*

A new developed Monte Carlo for particle simulation must be tested and compared with validated Monte Carlo programs. In this case, the HPT-MC has been developed with

the physics from PENELOPE, and for this reason the code to which we have compared it is *Penmain*, a MC simulator for photons, electrons and positrons, specialized in detector response based in PENELOPE. The comparison has been carried out reproducing the same scenario in both codes. The water phantom geometry shown in the previous section has been chosen for this purpose. Several simulations with initial photons of different energies have been performed. Photons are emitted from all over the phantom and the phase spaces file (PSF) in the surface of the collimator have been calculated. The properties of these PSFs (photon energy spectra) have been compared for 2 different energies, 2.0 and 5.6 MeV. Spectra from *Penamin* and HPT-MC are shown in Figure 6.6. Both results are practically the same which implies that the propagation of the photons is properly done with a much greater speed.

6.3.2 Proton range verification tests

The last step to crosscheck the proposed program was to reproduce the proton range verification results that were obtained with the previous version of the code using experimental data [Hueso-González et al., 2018]. In the previous version of the code, only attenuation was considered, and secondary particles were not tracked. To obtain consistent proton range estimation results with our code, the HPT-MC was modified to only consider attenuation and disregard the tracking of secondary particles.

The first case studied for the validation is the irradiation of a water phantom in which a deviation of zero millimeter was expected (*nominal scenario*). The phantom was irradiated using almost 500 different pencil beams which deposit an homogeneous dose over the whole phantom volume. By implementing the algorithm proposed by Hueso-González et al. [2018], the proton range estimation is conducted individually for each pencil beam, followed by a comparison with the expected range. This comparison yields the range shift, denoted as the range error (ϵ) in the figures. The resulting histograms illustrate the frequency of deviation from the expected range, indicating the number of individual beams that exhibit a certain distance from the expected values. Figure 6.7 shows the obtained histograms using the previous version of the code (Figure 6.7a) and the histogram calculated with the attenuation simulations with the HPT-MC (Figure 6.7b). The histograms generated from both versions of the code appear quite similar, suggesting that the collimator is effectively shielding the detectors from any secondary photons produced as a result of Rayleigh or Compton scattering.

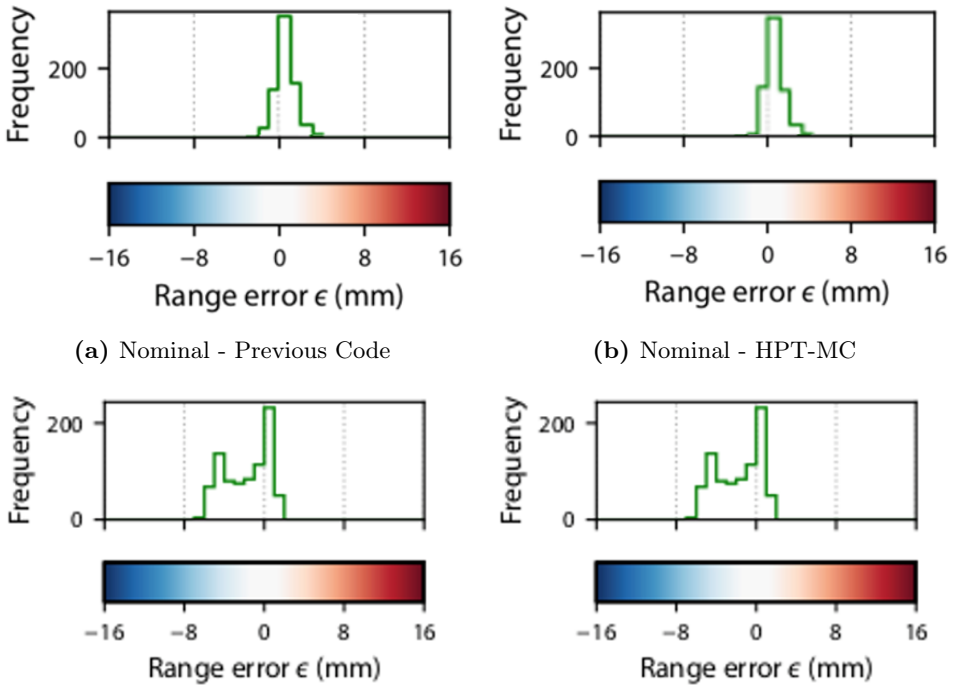

(a) Nominal - Previous Code

(b) Nominal - HPT-MC

(c) 5.5 mm deviation - Previous Code

(d) 5.5 mm deviation - HPT-MC

Figure 6.7: Deviation range histogram calculated in the nominal scenario and in the 5.5 mm shift case, using the previous code and the HPT-MC with only attenuation. Range error ϵ denotes the range shift and frequency is defined as the number of individual beams that exhibit a certain range shift from the expected values.

The second experimental case replicates the first scenario with a modification. Half of the phantom is covered with a range shifter which introduce a modification in the proton range of 5.5 millimeters. Figure 6.7 shows the range deviation histograms calculated using the previous CPU code (Figure 6.7c) and the new HPT-MC implemented in the GPU (Figure 6.7d). Both histograms look identical and they show how the distribution of the range is separately in two peaks. One peak is centered in 0.0 mm deviation and the other is centered at the expected deviation of 5.5 millimeter.

These results prove that the HPT-MC provides the same range estimations as the previous version of the code when it includes the same physics (only attenuation). It reproduces the results from a validated MC with high accuracy in the whole energy spectrum (1-7 MeV) relevant for the workflow for PG proton range verification developed at the MGH. The code has also been implemented in the general workflow in order to

reproduce previous results of proton range estimations. In these tests, the HPT-MC has been used to calculate the attenuation, as the previous code does, to replicate the same results that were obtained in the previous studies. The comparison of the results shows that the same range estimations are obtained with the new program. All this corroborates the good performance of the program and its possible incorporation into the workflow without any inconvenience. Although the time required to perform the simulations is not significant in the validation (to be studied in depth in the next section), the results obtained in these two cases are very promising. The total calculation time has been reduced from 3 hours to only 2 minutes. This implies an acceleration of the code by a factor of 100.

6.4 Results & Improvements

This section shows the main results obtained with the implementation of the HPT-MC in the PG proton range verification workflow and the improvements this entails. The implemented version was the most complete one that included the simulation of secondary photons (see section 6.2). Several cases were used to test the accuracy and the time required with the new version of the code in comparison with the previous version of the code. Three different scenarios were studied with this purpose. Two of them are the same as in the previous results, but instead of using the attenuation version of the HPT-MC, the full version with Compton, Rayleigh and pair production was used for the analysis. These two scenarios are used to test the capability of reproducing the correct expected proton range (*nominal* and *range shift* scenarios). The third case is a phantom composed of water and solid water (water like material made of carbon). It is used to test the ability of the new version of the code, with the full version of the HPT-MC, to estimate the concentration of oxygen and carbon in the irradiated target (*material composition* scenario). In addition, the study of the required time to perform the PG detection model is performed in every case.

6.4.1 *Nominal* scenario

This case is the same as in the previous section. The experimental data were obtained from the irradiation of a water phantom of 10x10x10 cm^3 with a homogenous dose using 525 pencil beams. The experimental data from the detected Prompt gamma-rays were

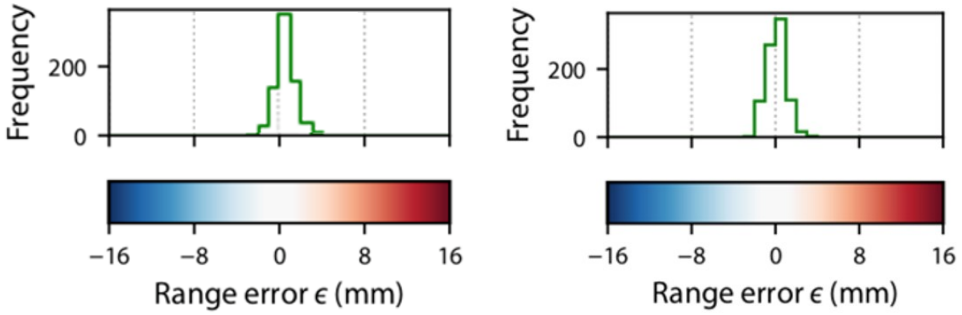

(a) Nominal - Previous Code **(b)** Nominal - Full version HPT-MC

Figure 6.8: Deviation range histogram calculated in the nominal scenario using the previous code and the full version of HPT-MC.

Code Version	Δ Range Deviation (mm)		Time (min)
	Mean	Error	
CPU previous version	0.45	0.08	169
GPU HPT-MC	0.49	0.09	3.8

Table 6.1: Range histograms numerical parameters and simulation time from the nominal case results

used to estimate the proton range using the previous version of the code and the one developed in this work, with the full version of the HPT-MC. The range deviations histograms of both methods are shown in Figure 6.8. The numerical properties of the deviation extracted from these histograms are summarized in Table 6.1 along with the required simulation time. Results show slight differences between the range estimations obtained with the previous code and with the implementation of the HPT-MC. The mean values of the range estimations are 0.45 and 0.49 mm with the previous version and the current one, respectively, when the expected value is 0.0 mm. The errors in both case are approximately 0.1 mm, therefore both values are compatible between them, although they are slightly deviated from the reference value. However, this range shift is less than half of a millimeter, which is much less than the current uncertainties in proton therapy [Paganetti, 2011].

In terms of computational time, improvements are much more relevant. Table 6.1 shows the computational time required to generate the PG detection model using the previous version of the code and the HPT-MC. Using the previous version of the code,

the time rises to almost 3 hours using a parallelized code in a single CPU with 32 cores. In contrast, using the HPT-MC the computational time is reduced up to 3.8 minutes using an NVIDIA RTX3090. This is a major breakthrough since the PG detection model can be calculated even with the most recent CT scan taken just prior to treatment.

6.4.2 Range shift scenario

Once the standard test has been verified we benchmarked the scenario where range shifts are induced. In this experimental test, half of the water phantom is covered by a plastic material that introduce a deviation of 5.5 mm in the proton range when the beam travel through it. As a consequence, we expect to detect two distinct Bragg peaks. One centered at 0 mm and the second one centered at the expected deviation of 5.5 mm. The proton range deviation histograms calculated using the previous code and the HPT-MC can are plotted in Figure 6.9. Histograms show similar results and the two peaks can be appreciated in both cases. The numerical analysis of these histograms is shown in Table 6.2. These results indicate that the range estimations obtained from both cases are similar and that the deviation can be detected with either of the methods. The small difference between the results suggests that the contribution of Compton scattering to the final result is minimal, as most Compton-scattered photons are stopped by the collimator and do not significantly contribute to the prompt gamma signal.

Similarly to the previous case, the improvements in the range estimation were not significant, since actually the room for improvements compared to previous results was not very large. The range estimation was determined with similar accuracies and precision in both cases. The most relevant result is the required time to calculate the whole PG detection model. The time decreases from almost 3 hours to only 4 minutes. This represents an improvement by a factor of 50, which allows the whole workflow to use the most recent information from the patient for the calculation of the PG detection model used in the range estimation.

6.4.3 Material Composition Estimation

The algorithm implemented in the workflow in Hueso-González et al. [2018] is capable of determining the quantity of carbon and oxygen in the irradiated region a the pencil beam. To test the capability of the program with the new HPT-MC to properly identify the oxygen and carbon concentration in the irradiated area by a pencil beam, a phantom

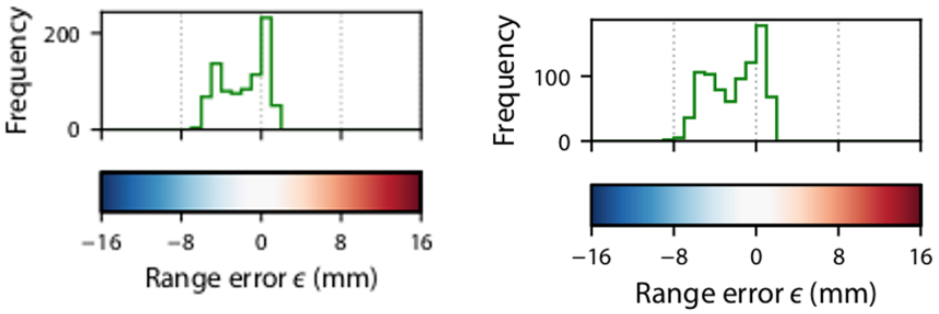

(a) Range Shift - Previous Code **(b)** Range Shift - HPT-MC

Figure 6.9: Deviation range histogram calculated in the 5.5 mm shift scenario using the previous code and the full version of HPT-MC.

Code Version	Range Deviation (mm)		Time (min)
	Center Peak	Shift peak	
CPU previous version	0.49 ± 0.11	5.78 ± 0.26	175
GPU HPT-MC	0.46 ± 0.15	5.96 ± 0.32	3.8

Table 6.2: Range histograms numerical parameters and simulation time from the 5.5 mm case results

of half water and half solid water was irradiated. The solid water is a water-like material mostly composed by carbon, with the property that the proton range is the same as it would be in water. In this way, the range estimation should produce a peak centered at 0.0 mm similar to the *nominal* case, but in half of the volume the program should have the capability to identify that half of the phantom is composed by carbon and in the other half by oxygen. Histogram deviation results calculated with the previous code and with the HPT-MC are shown in Figure 6.10 and Table 6.3 presents the numerical parameters of the histograms and the required time to calculate the range estimations. Similar to the rest of the cases, the histogram does not differ too much from the obtained with the previous results. However, the material composition estimation significantly improves.

Figure 6.10 also presents the oxygen and carbon estimation for evry pencil beam in the plan separetley. The material composition is represented by two squares with circles, one for oxygen fraction (blue) and one for carbon fraction (red), representing each beam

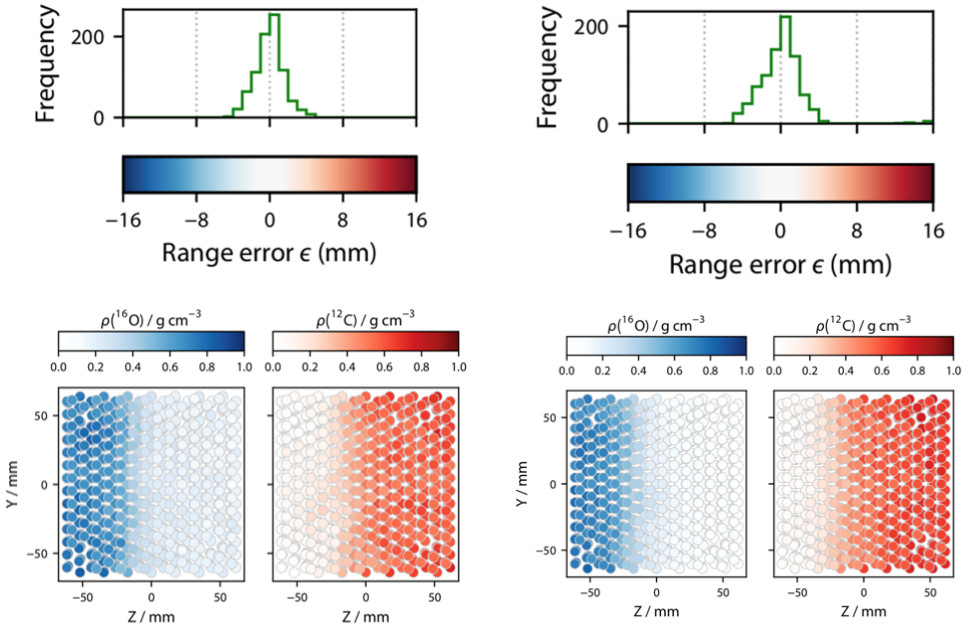

(a) Material Composition - Previous Code **(b)** Material Composition - HPT-MC

Figure 6.10: Deviation range histogram calculated in the solid water scenario using the previous code and the full version of HPT-MC. In this case, the material composition was also estimated using both methods. The material estimation for each beam is represented as the percentage of oxygen in blue and the carbon in red.

of the plan. The gradient from oxygen to carbon is generated by the beam's position, causing some beams radiate only water or solid water, while others radiate both. In both cases, the left side of the phantom is composed of water (oxygen), while the right side is composed of solid water (carbon). As it can be observed in Figure 6.10a, the previous code blurs the separation between the materials around Z=-10 mm, resulting in a curved line, while HPT-MC has the ability to accurately identify and separate the oxygen and carbon concentration, yielding in a straight line. This is a more accurate material composition estimation and reproduce better the expected results.

Material composition in Figure 6.10a shows that the oxygen contribution to the right side of the phantom, where there should be only carbon, is estimated to be close to 20%, and the same happens with the carbon in the left part of the image. The material contribution estimation using the previous version of the program has the disadvantage of not being able to completely subtract the oxygen or carbon contributions in regions where there should be none. However, the implementation of the HPT-MC, with the

Code Version	Range Deviation (mm)	Time (min)
CPU previous version	0.45 ± 0.46	188
GPU HPT-MC	0.26 ± 0.61	3.6

Table 6.3: Range histograms numerical parameters and simulation times from the solid and water-like plastic phantom irradiation using the previous code and the HPT-MC.

simulation of scattered photons, clearly improves this problem. Figure 6.10b shows that contribution intensities has decreased in those regions where they are not expected, specially in the case of the oxygen on the left side. The average contribution of 20% obtained in the previous case has been reduced to a value of 5%.

6.5 Discussion

The Hybrid Prompt gamma Transportation - Monte Carlo has been proposed in this chapter to accelerate the transportation of PGs as much as possible. This program was developed in the framework of the PG proton range verification system developed at the Massachusetts General Hospital [Verburg et al., 2012; Verburg and Seco, 2014; Hueso-González et al., 2018]. The development of this program comes from the necessity of calculating the PG detection model required for the proton range estimation in a shorter time and with similar accuracy. The previous version of the code introduced a theoretical calculation of the attenuation implemented in CPU, which made the code quite slow and did not include all the physics of photon. The HPT-MC is a full Monte Carlo simulation for high-energy photon transportation, which is based in some aspects of the XIORT-MC [Ibáñez et al., 2021] and to which different variance reductions have been introduced to increase its computational speed. Furthermore, the whole photon tracking is implemented in Graphics Processing Units (GPU) to parallelize the independent photon histories, which greatly accelerates the code even more.

The proposed method needed a benchmarking process to test its capacity to properly simulate the propagation of high-energy photons. This step has been performed comparing the results obtained from the HPT-MC with the results provided by *Penmain*, a validated MC based on PENELOPE. The obtained results from *Penmain* and the HPT-MC show that both programs provides similar outputs. This corroborates the

HPT-MC works properly and its results are reliable. However, the final goal of this new code is not the transportation of photons, rather its implementation in the framework of proton range verification system at the MGH. Because of that, a second step in its validation was required. This step consisted in reproducing the range verification performed in 2018 by Hueso-González et al. [2018] with our version of the HPT-MC code which only includes attenuation. The results from both methods should be the same and the results obtain in section 6.3.2 proved it. The overall benchmarking procedures validate the HPT-MC as a reliable Monte Carlo for high-energy photon transportation and its implementation in the proton range verification framework.

The most complex version of the HPT-MC was implemented in the PG verification system developed at the MGH. It was also tested using different experimental data sets and compared with previous results in order to identify the improvements it introduces. The range estimations obtained with this new version are similar to the previous results, which were already very precise, and no direct improvement is appreciated. The conclusion extracted from these results is that the collimator is stopping most of the photons that interact via Compton. In all the cases presented in this chapter, only about 5% of the photons arriving at the detectors previously interact with the medium via Compton. Moreover, their contribution is not very relevant for the final result, since almost no significant changes have been observed related to the range verification. Nonetheless, the inclusion of all photon interactions is necessary to obtain reliable results in any verification system, which gives this program a great potential to be implemented in any other system.

The most significant improvement introduced by the HPT-MC is the acceleration of the PG detection model calculation. A usual case related to an actual treatment plan with some thousands of beams has been accelerated by a factor between 50 and 100 depending on the case. The time in the previous version was around 3 hours for the calculation of the model and with the proposed method this time has been reduced down to 3 to 4 minutes. This acceleration is a major breakthrough since it is now possible to calculate the detection model using the most recent patient information, and even the CT scan performed just before irradiation can be used.

Furthermore, the HPT-MC also introduces a great improvement in the material composition identification. Previous version of the workflow were not able to accurately

determine the carbon and oxygen contribution of the irradiated region. The implementation fo the HPT-MC in the workflow has solved this issue. Results from section 6.4.3 show that the program is capable of separating and identifying the material composition with better accuracy. The Compton contribution, which seems to have no relevance in range verification, plays an important role in the identification of the composition of the irradiated material.

The HPT-MC far exceeds all the expectations initially set forth, which they were mainly related to the simulation time. In addition, some aspects of the PG system such as the material composition have considerably improved as a result of its implementation. Overall, the results and the improvements due to the development of the HPT-MC and its implementation on the PG system verification can be considered success.

The next step in the development of the HPT-MC entails implementing the detector response in the simulation. This advancement would eliminate the need for using the Detector response matrix, resulting in a significant reduction of memory load on the GPU without a substantial increase in simulation time. It is estimated that the time required to find and read the response for each of the 8 detectors in the matrix would be similar to the simulation time of the detector response itself. Moreover, incorporating this feature would enhance the code's flexibility to adapt to other verification systems. To validate this concept, a proof-of-principle experiment is scheduled to be conducted using an unshielded $LaBr_3(Ce)$ detector system at the GFN-UCM in the proton therapy center QuironSalus in Madrid. This experiment aims to test the detector response in a simple detection setup.

Chapter 7

Conclusions

This thesis has extensively revised PET and PG proton range verification techniques. The implementation of these techniques would imply a great breakthrough in proton therapy. However, it is important to acknowledge that there are several challenges that need to be addressed before the implementation of these techniques can become a reality. Throughout this work, we have proposed several ideas and tools to address this issues with promising results. In this chapter, the main contributions and conclusions are summarized.

Contrast Agents in proton therapy

The use of contrast agents has been proposed to improve the performance of proton range verification techniques and with the aim to make these techniques more suitable for proton therapy.

Contrast agents proposed for proton range verification using PET must produce β^+ isotopes in the most distal part of the proton range under proton irradiations, where no PET activity would be produced if only natural tissues are irradiated. For this reason, contrast agents for PET must present the following properties:

- The energy threshold of the reaction channel which produces the β^+ isotopes must be low enough to ensure the production in the distal part of the proton range, where the protons have small remaining energy ($<$10 MeV).

- The cross-section of the reaction channel must be high at low energies (<15 MeV) and ideally much smaller at high energies, resulting in a activation cross-section peak centered around 10 MeV.

- The $t_{1/2}$ of the produced β^+ isotope must be in accordance with the PET modality which will be used. For in-beam PET verification, we would favor short $t_{1/2}$ (<1 second), whereas for offline PET, it should be long enough to ensure activity for several minutes after irradiation. In the latter case, it is preferable that the chemical properties of the contrast agent and the activated residual is resistant to wash-out effect.

On the other hand, contrast agents for PG verification techniques must solve their main limitation, which is that they mostly produce very high energy γ rays, difficult to detect. The properties of the contrast agent which can solve this problem are:

- Production of low energy PG emissions (1-2 MeV) to increase the detection efficiency of current systems or to develop new, more compact and manageable systems that can maintain the same efficiency, but using lower energy emissions.

- These emissions must be produced in the most distal part of the proton range. Therefore, the cross-section must be similar to that described above for PET, with a high peak at low energies and negligible cross-section above 20-30 MeV.

The nuclei chart was studied in detail to determine potential contrast agents. After this study the proposed isotopes as contrast agents are: ^{18}O, ^{11}C, ^{23}Na, ^{35}Cl, ^{39}K.

The first experimental proof of concept was carried out to test the real potential of contrast agents. The irradiation of a homemade phantom with water-18 and its subsequent measurement in a preclinical PET, provided very promising results. The obtained PET images show the presence of activity in the Bragg peak region, meeting our expectations and ratifying our assumptions.

One has to remark that, very interestingly, the biochemistry of 18F produced from water-18 seems to allow for 18F being kept inside the cells where it is produced from quite some time, thus preventing fast wash-out for the fraction of 18F produced inside cells. In-ovo experiments have shown this [España et al., 2022].

Cross-Section Measurements

Three different experiments have been carried out in order to determine the cross-sections of the proposed contrast agents at different energies.

High energy measurements for PET isotopes

The cross-section of the $^{18}O(p,n)^{18}F$ reaction channel has been measured at various energies ranging from 50 to 230 MeV. The results indicate a smooth behavior of the cross-section in this energy range, making interpolation of the results feasible to map the entire interval. These cross-section data, along with the previous ones, allow us to map the complete energy range for proton therapy.

Low energy measurements for PET isotopes

Cross-section measurements have been conducted for the $^{23}Na(p,n)^{23}Mg$, $^{35}Cl(p,n)^{35}Ar$, and $^{39}K(p,n)^{39}Ca$ reactions below 10 MeV. The $^{23}Na(p,n)^{23}Mg$ reaction served as a cross-check for the experiment and simulations. The obtained results exhibited good agreement with both, thus validating the application of the simulation in the analysis and confirming the reliability of the results for ^{35}Ar and ^{39}Ca.

The $^{35}Cl(p,n)^{35}Ar$ cross-sections were measured for the first time, and it is consistent with theoretical estimations. The results obtained for the cross-section of the $^{39}K(p,n)^{39}Ca$ reaction channel are in acceptable agreement with previous data, but the accuracy of these measurements is low due to the low statistics. To improve the accuracy of this experiment, each of the reactions mentioned above must be studied again individually, using samples that only produce the specific reaction channel and not a combination of multiple reactions, since the overlapping of the decays complicates the analysis and induces errors that lead to a loss of accuracy.

Low energy measurements for PG isotopes

Prompt-Gamma emissions from ^{18}O under proton irradiation have been extensively studied below 10 MeV. Among the observed emissions, four distinct γ rays were identified. One of these γ rays originates from the $^{18}O(p,p'\gamma)$ reaction, while the remaining three are produced through the $^{18}O(p,n\gamma)^{18}F$ reaction. All these PGs have energies

below 2 MeV with energy threshold around 2-3 MeV, which meet of principal requirement for potential contrast agents in Prompt gamma verification. Furthermore, the angular distribution and the cross-sections of these γ-rays have been obtained thanks to the experimental setup specifically developed for this experiment. In addition, a 5.3 MeV PG was detected and analyzed. This γ-ray comes from the $^{18}O(p,\alpha\gamma)^{15}N$ reaction. Notably, the most significant characteristic of this emission is its remarkably low energy threshold of only 3.5 MeV. This indicates that it is generated in closer proximity to the proton range compared to other prompt-gamma emissions originating from natural tissues.

DAD-MSA reconstruction algorithm

Our proposed DAD-MSA algorithm for dose reconstruction from PET images shows great potential as a suitable tool for PET verification systems. It possesses all the main advantages of previously methods, such as fast execution time (<1 second), while also solving some of their main limitations. The reconstructed doses are noiseless, which allows for more accurate estimation and analysis of the proton range compared to any prior method.

The DAD-MSA algorithm has been tested on various realistic clinical scenarios with highly promising outcomes. The error in dose and proton range estimations obtained in each case were below the existing uncertainties in planning, which is the primary goal of proton range verification techniques. The next stage in the development of the DAD-MSA algorithm would be to validate in experiment the theoretical results presented in this thesis.

A very interesting future plan for this code is its implementation in the scope of PG verification. Several PG verification techniques estimate the proton range [Richter et al., 2016; Hueso-González et al., 2018], but none of them is able to estimate the deposited dose from PG measurements. The calculation speed and the accuracy showed in this thesis, make the MSA-DAD algorithm a great candidate to be implemented in PG systems. The algorithm's capabilities extend to real-time estimation of proton range and deposited dose during irradiation, and it can even generate the deposited dose during the intervals between each beam delivery, with the advantage of no residual activities from previous beams would interfere in the reconstruction.

Clinical advantages of PET contrast agents

Contrast agents hold strong potential for improving proton range verification using PET systems in a clinical scenario. In chapter 5, we have combined the idea of contrast agents, the measured cross-sections, and the DAD-MSA algorithm to identify range deviations with and without the contrast agent (water-18). Our results showed that, while the presence of water-18 contrast agent is not does needed to estimate deviations in the proton range from the plan, when these are induced by anatomical modifications in the middle of the proton path, however, in cases where the range deviation is caused by a modification in the most distal part of the proton beam (Bragg peak area), the identification of the range deviation is only feasible with the use of contrast agents. These findings suggest that contrast agents could significantly enhance the accuracy of range verification techniques, which have the potential to significantly reduce the safety mar- gins required due to uncertainties in the planning target volume (PTV). This, in turn, could improve the overall efficacy of proton therapy in cancer treatment by reducing the probability of healthy tissues being irradiated and minimizing the risk of potential side effects.

In conclusion, contrast agents have proven to be a valuable tool in proton range verification techniques. They enhance the visibility of tissues and structures during PET and PGI imaging, making it possible to identify deviations that may not be otherwise detectable. This allows for more accurate determination of the range of protons in tissue, which is critical for maximizing the therapeutic effect of proton therapy and minimizing damage to surrounding healthy tissues. As proton therapy continues to evolve, the use of contrast agents is likely to become even more important in ensuring the precise delivery of radiation to tumors.

HPT-MC for PG verification system

The Hybrid Prompt-gamma Transportation - Monte Carlo (HPT-MC) is a significant development in the field of prompt-gamma verification systems. It has been specifically designed for the PG verification system developed at the Massachusetts General Hospital, with the ultimate goal of implementing it in clinics. Unlike previous methods, the HPT-MC introduces a Monte Carlo simulation that accurately transports all the prompt gammas produced in a patient during proton therapy.

First, the HPT-MC was validated against established Monte Carlo codes, and after that, it was successfully integrated into the PG verification workflow. Once implemented in the verification system, it was tested to reproduce range estimations from experimental data already obtained with previous versions of the code. The results demonstrated a strong match with both the expected and the previously calculated ranges, thus confirming the validity and accuracy of the HPT-MC. Moreover, the computational speed of the new version is a significant improvement over previous models, with the PG detection model now being calculated in just a few minutes instead of the previous 2-3 hours. This improvement in computational speed is significant as it enables the PG model to be calculated with the latest medical information of the patient, including CT scans carried out in the same treatment room just prior to the irradiation, which increase the accuracy of the range estimations preformed by the PG verification system.

In the scope of this topic, the next stages of development for the HPT-MC involves the integration of the detector response into the simulation. Any other proposed prototype with the same purpose will face the same problem of simulating a huge amount of photons in the shortest possible time at some point. The incorporation of the detector response would enhance the code versatility to adapt to other verification systems, allowing verification and proof-of-concept tests to be carried out in a much simpler, less time-consuming and resource-intensive manner. This would give many research groups the opportunity to carry out studies related to verification with PGs, which they are currently unable to do because they do not have the necessary resources to carry out this type of work. The increase in the number of studies on this topic would accelerate its development and therefore its possible implementation in the clinical setting. To verify the implementation of the detector response, a proof-of-principle experiment is scheduled to be conducted at the GFN-UCM using an unshielded $LaBr_3(Ce)$ detector system. The experiment will take place at the proton therapy center QuironSalus in Madrid. The primary objective of this experiment is to assess the detector response in a simple detection setup and compare it against the simulations provided by the HPT-MC.

Final Conclusions

The ideas and tools presented in this thesis offer valuable insights into range verification techniques, improving their accuracy and making them easier to implement in actual clinical settings, which brings about numerous benefits to patients. The proposed ideas are related to two of the most relevant proton range verification techniques, PET and PG. However, these are not the only range verification techniques under study. The use of neutrons [Ytre-Hauge et al., 2019; Yabe et al., 2023] or ionoacustic waves [Assmann et al., 2015; Kipergil et al., 2017; Freijo et al., 2021] have been studied, but they have not been tested yet in patients. These techniques also offer valuable results, but they present several limitations which placed them a step behind PG and PET range verification systems.

In terms of PET verification techniques we have proposed two main new ideas to improve the accuracy of the results. The first one is the use of contrast agents (Chapter 2) which improve the activity map inside the patient producing β^+ isotopes in BP area, where there is no production from natural tissues. The second proposed idea is a new algorithm to reconstruct dose from PET images (Chapter 4). There are several similar programs based on analytical [Parodi and Bortfeld, 2006; Masuda et al., 2019] and Deep Learning (DL) methods [**?**Hu et al., 2020; Ma et al., 2020]. The analytical methods provide accurate results in a few seconds, but the implementation of pencil beam approximation instead of MC simulations the level of reliability of the results is diminished. In the case of DL methods the MC simulations are implemented and they are able to estimate the dose and the proton range in times similar to our DAD-MSA algorithm. however, they present an important inconvenient, their reconstructed doses are noisy which complicates the comparison against the ground-truth dose and the estimation of the proton range.

Regardless of the reconstruction algorithm, we have demonstrated that the detection of deviations in the final millimeters of the proton range is only feasible with the utilization of contrast agents. Every program which estimates the dose and the proton range uses the same PET signal, and the identification of anatomical modifications in the last millimeters of the proton range, which leads into range shifts, can not be detected by any of the mentioned algorithms because there is no information in form of

PET activity that they can use to identify it. However, the use of contrast agents introduce activity in the most distal area of the proton path, so proton range verification algorithms could be able to detect distal shifts. We have tested this theory (Chapter 5 combining the cross sections measurements performed in chapter 3 along with the DAD-MSA algorithm. Results show how the anatomical modifications in the BP area can only be identified with the use of contrast agents. This result has only been tested with the DAD-MSA algorithm and it should be studied using some of the rest of the proposed methods for dose reconstruction from PET images. However, since they all follow the same physical principle, the obtained results should be reproduced with the rest of the methods.

In this thesis, the study of PG verification techniques has also been conducted. In collaboration with the MGH, a GPU-based Monte Carlo for Prompt-Gamma has been developed, allowing the implementation of their Prompt-Gamma Spectroscopy verification system [Hueso-González et al., 2018] in real-time during treatment. There are a few more prototypes in the world which try to estimate the proton range from PG emissions. Some of them are based on Prompt Gamma Imaging [Richter et al., 2016], which has also been tested in patients [Berthold et al., 2021], and some others in Compton Cameras [Muñoz et al., 2021]. All of these systems provides similar proton range accuracies ($\approx 2mm$). However, the Prompt-Gamma Spectroscopy prototype at the MGH has a unique property, it is able to determine the material composition of the irradiated region.

All the mentioned prototypes face the same limitations and problems. One of them is related to the efficiency of the system due to the high energy of the emitted PG. In the work carried out by Muñoz et al. [2021] is said that the Compton Camera increase the efficiency in comparison with the other techniques which certain the efficiency is an issue. Even so, they need acquisition times between 30 and 120 minutes to obtain accurate estimations of the range. In this work, we have proposed the use of contrast agents also in PG verification system to solve this issue (Chapter 2). The contrast agent would introduce low energy prompt gamma emissions (1-2 MeV) which increase the efficiency of any detection system by a factor between 5 and 10. In chapter 3 the cross sections and the angular distribution of the PGs emitted from ^{18}O were studied. We were able to identify 4 different γ-lines with energies below 2 MeV and quite intense cross sections at low energies. The use of this contrast agent could mitigate the lack

of efficiency in some of the proposed prototypes, reducing the acquisition time and improving the accuracy of the reconstructed images and range estimations.

Another challenge encountered by PG verification systems is the need to simulate the anticipated response of the PG detection system in order to compare it with experimental data [Richter et al., 2016; Hueso-González et al., 2018; Muñoz et al., 2021]. This is a critical step as the expected results are used to estimate the actual range of the delivered proton beam. However, this process poses a challenge due to the time-consuming nature of the current tools used to calculate the detector response. In the case of the PG imaging technique [Richter et al., 2016; Berthold et al., 2021] they implement REGGUI [Sterpin et al., 2015] to simulate the detector response. REGGUI is an analytical software which calculates the production site of the PG emissions using the Ray Tracing approximation, and estimates the detector response using a fitted equation which produce the detector response taking into account the production site and the energy of the PG. However, the accuracy and the reliability of the results of an analytical method is not comparable to those results from MC simulators.

The development of the GPU-based Monte Carlo for Prompt-Gamma Transportation, as proposed in Chapter 6, offers a solution to the aforementioned problem. This code has the ability to transport over 300 million photons per second and estimate the response of the detection system. While initially implemented within the framework of the PG detection system at the MGH, it can be adapted for use with any of the mentioned PG prototypes, effectively reducing simulation time and improving accuracy. By combining this GPU-based MC approach for high-energy photons with recent proton GPU MC techniques like MOQUI [Lee et al., 2022], it becomes possible to simulate the detector response of virtually any system in just a matter of minutes. This opens up the potential for real-time image guidance during irradiation and the application of in-beam adaptive plans to enhance the robustness of proton therapy.

Outlook

The results achieved in this thesis are indeed promising, but it is important to acknowledge that there is still a significant journey ahead to achieve the ultimate goal of real-time and accurate verification of the deposited dose and proton range. While the

advancements made in this research contribute to the overall progress, further development and refinement are necessary to fully realize this objective.

We have demonstrated that the utilization of contrast agents in PET verification techniques holds the potential to facilitate the detection of range shifts in patients. However, it is important to note that our testing was conducted using ^{18}F as the PET isotope, which has a relatively long half-life of 109 minutes. This characteristic poses a challenge in terms of in-beam verification, which is the ultimate objective. To fulfill the necessary requirements for in-beam verification of the deposited dose using PET systems, our focus should shift towards utilizing contrast agents with short half-lives. This approach is crucial for achieving real-time and accurate verification, as shorter half-lives allow for more immediate assessment of the delivered dose during proton therapy treatments. By incorporating short half-life isotopes, we can overcome the challenges associated with long half-life isotopes and enhance the feasibility of in-beam dose verification using PET systems.

The proposed DAD-MSA algorithm has shown a great potential to reproduce the deposited dose and to estimate the proton range with high accuracy. However, all the results are based on simulations and they must be reinforced with experimental results. Furthermore, in-beam verification with PET presents an additional problem, there is residual activity from previous beams which complicates the verification. Another aspect to consider is the choice of PET image for verification. One approach is to accumulate all the decays since the first beam delivery, resulting in a PET image with a larger number of decays and potentially better image reconstruction quality. However, this approach may overshadow the activity contribution of more recent beams, which could affect the accuracy of range verification. On the other hand, using PET images from the last few seconds would prioritize the contribution of the most recent beams to the PET signal. However, these images may suffer from a lack of statistical data, making accurate dose reconstruction challenging. A thorough investigation is needed to determine the optimal compromise between these two scenarios in terms of range verification accuracy. This study will shed light on the best approach for PET image selection and provide valuable insights for improving range verification techniques in proton therapy.

The next step for the Hybrid Prompt Gamma Transportation (HPT) Monte Carlo is to further develop the code to make it a versatile Monte Carlo tool capable of simu-

lating the response of any Prompt Gamma (PG) detection system based on PG activity distribution maps. This requires adapting the code to calculate the deposited energy by photons and obtain the detector response without relying on precalculated databases. Additionally, the input options of the code need to be adjusted to accommodate the setup geometry, including collimators, detectors, and any other materials involved in the detector response. By implementing these enhancements, the code will enable the calculation of the PG system response in a matter of minutes. This advancement is crucial for in-beam proton range verification, as it allows for real-time assessment using the control CT performed just before irradiation.

Main contributions of this thesis

During the development of this PhD thesis, several results have been shared through publications in international journals and conferences related to this field. The significant contributions of this thesis are summarized below.

Published articles in indexed international journals

1. Samuel España, Daniel Sánchez-Parcerisa, Paloma Bragado, Álvaro Gutiérrez-Uzquiza, Almudena Porras, Carolina Gutiérrez-Neira, Andrea Espinosa, **Víctor V. Onecha**, Paula Ibáñez, Víctor Sánchez-Tembleque, José M. Udías & Luis M. Fraile. "In vivo production of fluorine-18 in a chicken egg tumor model of breast cancer for proton therapy range verification". *Scientific Reports* **12** (2022) 7075. https://doi.org/10.1038/s41598-022-11037-7

2. **V V Onecha**, P Galve, P Ibáñez, C Freijo, F Arias-Valcayo, D Sanchez-Parcerisa, S España, L M Fraile and J M Udías. "Dictionary-based software for proton dose reconstruction andsubmilimetric range verification". *Physics in Medicine & Biology* **67** (2021) 045002 https://doi.org/10.1088/1361-6560/ac4efc

3. A. Espinosa Rodriguez, **V.V. Onecha**, V. Sanchez-Tembleque, C. Gutierrez-Neira, M. García-Díez, P. Ibañez, S. España, D. Sanchez-Parcerisa, J.M. Udías, L.M. Fraile. "Can iodine be used as a contrast agent for protontherapy range verification? Measurement of the ^{127}I(p,n)^{127m}Xe (reaction) cross section in the 4.5–10 MeV energy range". *Radiation Physics and Chemistry* **185** (2021) 109485. https://doi.org/10.1016/j.radphyschem.2021.109485

4. Samuel Espana, Daniel Sanchez-Parcerisa, Paula Ibanez, Víctor Sanchez-Tembleque, Jose Manuel Udías, **Víctor V. Onecha**, Alvaro Gutierrez-Uzquiza, Claus Max-

imilian Backer, Christian Baumer, Ken Herrmann, Pedro Fragoso Costa, Beate Timmermann, Luis Mario Fraile. "Direct proton range verification using oxygen-18 enriched water as a contrast agent." *Radiation Physics and Chemistry* **182** (2021) 109385. *https://doi.org/10.1016/j.radphyschem.2021.109385*

5. Victor Sanchez-Tembleque, Daniel Sanchez-Parcerisa, **Victor Valladolid-Onecha**, Luis Mario Fraile & Jose Manuel Udias. "Simultaneous measurement of the spectral and temporal properties of a LINAC pulse from outside the treatment room." *Radiation Physics and Chemistry* **158** (2019) 1-5. *https://doi.org/10.1016/j.radphyschem.2019.01.002*

6. Miguel García Díez, Andrea Espinosa Rodriguez, Victor Sánchez Tembleque, Daniel Sánchez Parcerisa, **Victor V Onecha**, Juan A. Vera Sanchez, Alejandro Mazal, Luis Mario Fraile, Jose Manuel Udias. "Technical note: Measurement of the bunch structure of a clinical proton beam using a SiPM coupled to a plastic scintillator with an optical fiber". *Medical Physics* (2023) 1-7 https://doi.org/10.1002/mp.16333

Conference contributions and proceedings

Throughout this thesis, more than 25 contributions have been accepted for various conferences and workshops, in which I appeared as an author or co-author. In the following list, only those contributions in which I was the presenting author and those most relevant to the topic of this thesis are included.

Authors: **V.V. Onecha**, S. España, L.M. Fraile, J.M. Udías, H. Paganetti, J.M. Verburg
Title: Ultra-fast photon GPU MC for online proton range verification based in prompt gamma
Type: Oral
Congress: 2022 IEEE Nuclear Science Symposium, Medical Imaging Conference and Room Temperature Semiconductor Detector Conference
Date and place: Milan Meeting 08-13 November 2022

Authors: A. Espinosa Rodriguez, F.Arias Valcayo, **V.V.Onecha**, P. Ibáñez, M. García Díez, V. Martínez Nouvilas, S. España, D. Sanchez-Parcerisa, J.A. Vera Sanchez, A. Mazal, L.M. Fraile, J.M. Udias

Title: First steps towards on-the-fly dose reconstruction from in-beam PET activation
Type: Poster
Congress: 2022 IEEE Nuclear Science Symposium, Medical Imaging Conference and Room Temperature Semiconductor Detector Conference
Date and place: Milan Meeting 08-13 November 2022

Authors: **V.V. Onecha**, V. Sánchez-Tembleque, A. Espinosa-Rodríguez, P. Ibáñez, M. García-Díez, S. España, D. Sanchez-Parcerisa, G. Garcí, S. Viñals, J.M. Udías, L.M. Fraile
Title: Prompt-gamma measurements of ^{18}O as contrast agent for proton range verification
Type: Oral
Congress: 5th Annual European Nuclear Physics Conference
Date and place: Santiago de Compostela 24-28 October 2022
Link: https://indico.cern.ch/event/1104299/contributions/5055199/

Authors: **V.V. Onecha**, V. Sanchez-Tembleque, A. Espinosa-Rodríguez, P. Ibáñez, M. García-Díez, S. España, D. Sanchez-Parcerisa, C. Gutiérrez-Neir, G. García, S. Viñal, J.A. Vera, A. Mazal, J.M. Udías, L.M. Fraile
Title: Reaction cross sections of prompt-gamma and PET radioisotopes for range verification in proton therapy
Type: Oral
Congress: 15th International Conference on Nuclear Data for Science and Technology (ND2022)
Date and place: Online Meeting July 24–29, 2022
Link: https://indico.frib.msu.edu/event/52/contributions/650/

Authors: **V.V. Onecha**, P. Galve, P. Ibañez, A. Espinosa, S. España, D. Sanchez-Parcerisa, L.M. Fraile, J.M. Udías
Title: Dictionary-based ML-EM & Simulated Annealing (MSA) GPU-Algorithm for real time PET proton range verification
Type: Oral
Congress: 2021 Virtual IEEE Nuclear Science Symposium and Medical Imaging Conference
Date and place: Online Meeting 1-23 October 2021

Authors: **V.V. Onecha**, P. Galve, A. Espinosa-Rodriguez, P. Ibañez, D. Sanchez-Parcerisa, S. España, L.M. Fraile, J.M. Udias
Title: Identifying undetectable range deviations using Dictionary-based method and contrast agents

Type: Poster
Congress: 60th Annual Conference of the Particle Therapy CO-operative Group (PTCOG)
Date and place: Online Meeting July 2021

Authors: **V.V. Onecha**, P. Galve, P. Ibañez, A. Espinosa, D. Sanchez-Parcerisa, S. España, L.M.Fraile, J.M. Udías
Title: Dictionary based MLEM-algorithm for real-time proton range verification from PET data: submilimretic precision in clinical dose.
Type: Poster
Congress: 59th Annual Conference of the Particle Therapy CO-operative Group (PTCOG)
Date and place: Online Meeting 4-7 June 2021

Authors: P. Ibáñez, **V. Valladolid**, A. Villa-Abaunza, P. Galve, F. Arias, A. Espinosa, S. España, D. Sánchez-Parcerisa, L.M. Fraile, J. M. Udías
Title: Real time dose verification for proton therapy
Type: Oral
Congress: 59th Annual Conference of the Particle Therapy CO-operative Group (PTCOG)
Date and place: Online Meeting 4-7 June 2021

Authors: **V.V.Onecha**, A. Espinosa, V. Sanchez-Tembleque, P. Ibañez, S. España, D. Sanchez-Parcerisa, L.M. Fraile, J.M. Udias
Title: Cross section measurements of Contrast Agents: a promising solution to drawbacks of in-vivo dose verification technique
Type: Oral
Congress: III Jornadas RSEF/IFIMED de Física Médica
Date and place: Online Meeting 14-15 December 2020
Link:https://indico.ific.uv.es/event/5983/contributions/13894/

Authors: **V.V. Onecha**, P. Galve, P. Ibañez, A. Espinosa, S. España, D. Sanchez-Parcerisa, L.M. Fraile, J.M. Udías
Title: Dictionary based MLEM-algorithm for real time proton range verification from PET data: the virtue of contrasts
Type: Poster
Congress: 2020 Virtual IEEE Nuclear Science Symposium and Medical Imaging Conference
Date and place: Online Meeting 1-10 November 2020

Authors: **V. Valladolid Onecha**, P. Ibáñez, D. Sanchez-Parcerisa S. España, L.M. Fraile, J.M. Udías

Title: PET Imaging from Proton Activation with Contrasts and Correlation with Dose.
Type: Poster
Congress: Final MediNet Network Meeting
Date and place: Viena Meeting 7-9 October 2019
Link: https://medinet2022.medaustron.at/index.php/Meeting2019

Authors: **V. Valladolid-Onecha**, P. Galve, F. Arias, P. Ibañez, A. Villa-Abaunza, D.Sanchez-Parcerisa, S.España, J.L. Herraiz, L.M. Fraile, J.M. Udías.
Title: PET Imaging and Dose correlation from Proton Activation.
Type: Oral
Congress: Conference on Medical Accelerators and Particle Therapy
Date and place: Sevilla Meeting 08-12 September 2019

Authors: **V. Valladolid-Onecha**, P. Galve, F. Arias, P. Ibañez, A. Villa-Abaunza, D.Sanchez-Parcerisa, S.España, J.L. Herraiz, L.M. Fraile, J.M. Udías.
Title: PET Imaging and Dose correlation from Proton Activation.
Type: Oral
Congress: XXXVIIth Biennial Meeting of the Spanish Royal Society of Physics (RSEF)
Date and place: Zaragoza Meeting 15-19 July 2019
Link: https://eventos.unizar.es/20274/detail/bienalrsef2019.html

Authors: **V. Valladolid-Onecha**, P. Galve, F. Arias, P. Ibañez, A. Villa-Abaunza, D.Sanchez-Parcerisa, S.España, J.L. Herraiz, L.M. Fraile, J.M. Udías.
Title: PET Imaging and Dose correlation from Proton Activation.
Type: Poster
Congress: 58th Annual Conference of the Particle Therapy CO-operative Group (PTCOG)
Date and place: Manchester Meeting 10-15 June 2019

Appendix A

Tables from Chapter 3

A.1 Cross-Section Results

	Total gamma-ray production cross-section (mbarn)				
Energy (MeV)	940 keV	1040 keV	1080 keV	1982 keV	5300 keV
3.125				0.780(22)	
3.375	0.984(29)			9.88(44)	5.24(69)
3.625	0.120(51)			3.16(65)	6.4(16)
3.875	1.33(23)			4.28(84)	20.5(33)
4.125	2.02(39)	2.25(16)		33.7(20)	2.9(11)
4.375	20.81(53)	7.28(18)	3.71(10)	48.1(47)	109(11)
4.625	70.5(18)	35.09(56)	13.64(67)	67.9(59)	24(12)
4.875	22.1(84)	101.6(30)	13.33(54)	32.7(71)	53(15)
5.125	25.0(79)	60.8(31)	7.7(16)	58.0(92)	122(46)
5.375	79.1(15)	264.5(70)	19.4(30)	124(11)	26(14)
5.625	16.0(73)	160(19)	20.8(54)	12.1(83)	33(22)
5.875	25.0(88)	74(18)	3.5(12)	37(10)	95(27)
6.125	20(11)	69(16)	23.8(37)	18.0(80)	316(23)
6.500	121.4(52)	152.7(73)	19.4(32)	187(12)	35(31)
6.875	85.0(38)	36(12)	32(11)	103(15)	97(52)
7.125	80(10)	55(13)	14.3(76)	109(18)	61(20)
7.375	90(16)	50.7(41)	16(10)	146(21)	83(41)
7.750	124(15)	51.9(59)	14.0(60)	166(11)	52(31)
8.125	111(41)	152(12)	25(10)	169(25)	
8.500	82(24)	60.2(95)	20.3(5.7)	39(15)	
9.00	88(41)	131(13)	5.2(2.7)	114(17)	
9.375	117(61)	65(22)	30(13)	164(22)	

Table A.1: Prompt Gamma Cross-sections Results

A.2 Angular Coefficients a_i

940 keV

Energy (MeV)	a_0		a_2		a_4	
3.50	5.12E-08	*30*	1.33E-08	*43*	-2.51E-08	*71*
3.75	5.78E-08	*24*	1.71E-08	*34*	-2.79E-08	*56*
4.00	1.34E-07	*11*	-1.7E-08	*17*	-2.1E-08	*24*
4.25	2.57E-07	*17*	9.0E-08	*28*	-7.4E-08	*42*
4.50	1.578E-06	*23*	3.01E-07	*38*	-3.84E-07	*56*
4.75	6.25E-06	*10*	1.51E-06	*19*	-1.4E-07	*27*
5.00	7.78E-06	*48*	1.83E-06	*87*	-3.25E-07	*12*
5.25	9.574E-06	*57*	1.99E-06	*10*	-2.7E-07	*14*
5.50	1.5E-05	*84*	3.02E-06	*15*	-1.7E-07	*21*
5.75	1.7E-05	*48*	4.21E-06	*86*	-8.35E-07	*12*
6.00	1.9E-05	*37*	2.75E-06	*68*	3.8E-07	*94*
6.25	2.0E-05	*75*	4.0E-06	*13*	-1.53E-07	*18*
6.75	4.1E-05	*23*	6.55E-06	*43*	1.02E-06	*59*
7.00	4.9E-05	*18*	7.43E-06	*34*	3.6E-07	*47*
7.25	5.6E-05	*83*	8.5E-06	*15*	-6.66E-07	*20*
7.50	6.50E-05	*10*	9.0E-06	*19*	-7.67E-07	*27*
8.00	8.97E-05	*23*	1.10E-05	*41*	1.5E-06	*57*
8.25	1.0E-04	*28*	1.11E-05	*52*	3.4E-06	*71*
8.75	1.2E-04	*34*	1.10E-05	*61*	-6.07E-07	*84*
9.25	1.4E-04	*72*	1.3E-05	*13*	8.80E-06	*17*
9.50	1.5E-04	*56*	1.5E-05	*10*	6.77E-06	*13*

Table A.2: 940-keV prompt gamma angular distribution: a_i parameters.

1040 keV

Energy (MeV)	a_0		a_2	
4.25	1.365E-07	*84*	-1.2E-08	*21*
4.50	5.990E-07	*40*	-7.7E-08	*10*
4.75	2.925E-06	*17*	-4.2E-07	*45*
5.00	9.94E-06	*17*	-1.25E-06	*44*
5.25	1.431E-05	*80*	-1.56E-06	*20*
5.50	3.402E-05	*47*	-4.6E-06	*12*
5.75	4.64E-05	*11*	-3.0E-06	*30*
6.00	5.232E-05	*50*	-6.9E-06	*13*
6.25	5.80E-05	*10*	-3.8E-06	*26*
6.75	8.446E-05	*31*	-1.11E-05	*81*
7.00	8.78E-05	*10*	-1.13E-05	*26*
7.25	9.294E-05	*31*	-1.11E-05	*82*
7.50	9.778E-05	*33*	-9.88E-06	*87*
8.00	1.081E-04	*97*	-1.27E-05	*25*
8.25	1.239E-04	*44*	-1.71E-05	*11*
8.75	1.368E-04	*16*	-1.55E-05	*43*
9.25	1.663E-04	*18*	-1.75E-05	*49*
9.50	1.738E-04	*18*	-1.76E-05	*47*

Table A.3: 1040-keV prompt gamma angular distribution: a_i parameters.

1080 keV

Energy (MeV)	a_0		a_2	
4.50	2.356E-07	*67*	-6.2E-08	*17*
4.75	1.140E-06	*47*	-1.78E-07	*12*
5.00	2.060E-06	*33*	-3.88E-07	*87*
5.25	2.616E-06	*98*	-7.3E-07	*26*
5.50	4.06E-06	*16*	-1.53E-06	*43*
5.75	5.67E-06	*32*	-1.48E-06	*87*
6.00	5.95E-06	*20*	-1.81E-06	*53*
6.25	7.92E-06	*17*	-1.74E-06	*46*
6.75	1.127E-05	*44*	-2.1E-06	*11*
7.00	1.417E-05	*87*	-2.8E-06	*23*
7.25	1.545E-05	*74*	-3.0E-06	*20*
7.50	1.704E-05	*73*	-2.8E-06	*19*
8.00	1.983E-05	*79*	-4.0E-06	*21*
8.25	2.247E-05	*80*	-2.5E-06	*21*
8.75	2.665E-05	*70*	-5.1E-06	*18*
9.25	2.774E-05	*67*	-2.5E-06	*17*
9.50	3.12E-05	*13*	-4.3E-06	*35*

Table A.4: 1080 keV prompt gamma angular distribution: a_i parameters.

1984 keV

Energy (MeV)	a_0		a_2		a_4	
3.25	3.841E-08	*76*	1.68E-08	*12*	-1.02E-08	*18*
3.50	5.52E-07	*19*	2.57E-07	*27*	-3.30E-07	*46*
3.75	7.25E-07	*23*	3.15E-07	*32*	-4.32E-07	*55*
4.00	9.72E-07	*34*	3.67E-07	*48*	-5.21E-07	*80*
4.25	3.014E-06	*98*	7.3E-07	*15*	-9.8E-07	*23*
4.50	6.07E-06	*22*	1.33E-06	*37*	-1.39E-06	*54*
4.75	1.057E-05	*25*	1.94E-06	*42*	-1.70E-06	*61*
5.00	1.283E-05	*33*	1.86E-06	*58*	-1.14E-06	*82*
5.25	1.700E-05	*46*	3.31E-06	*81*	-1.4E-06	*11*
5.50	2.623E-05	*58*	4.8E-06	*10*	4.8E-08	*14*
5.75	2.701E-05	*59*	5.7E-06	*11*	3.2E-07	*15*
6.00	3.000E-05	*44*	5.52E-06	*82*	1.7E-06	*11*
6.25	3.148E-05	*56*	6.3E-06	*10*	5.3E-07	*14*
6.75	6.381E-05	*71*	1.34E-05	*13*	6.3E-06	*18*
7.00	7.31E-05	*10*	1.33E-05	*19*	8.3E-06	*26*
7.25	8.33E-05	*11*	1.59E-05	*21*	1.04E-05	*29*
7.50	9.73E-05	*12*	1.76E-05	*24*	1.04E-05	*32*
8.00	1.304E-04	*12*	2.09E-05	*24*	1.79E-05	*32*
8.25	1.478E-04	*18*	2.23E-05	*34*	1.89E-05	*46*
8.75	1.562E-04	*23*	2.31E-05	*44*	1.47E-05	*60*
9.25	1.817E-04	*21*	2.89E-05	*38*	7.5E-07	*53*
9.50	2.123E-04	*74*	3.86E-05	*13*	1.24E-05	*19*

Table A.5: 1984 keV prompt gamma angular distribution: a_i parameters.

List of Figures

List of Tables

References

(1999). Dose calculations for external photon beams in radiotherapy. *Physics in Medicine Biology*, 44:R99.

Abushab, K. M., Herraiz, J. L., Vicente, E., Cal-Gonzalez, J., Espana, S., Vaquero, J. J., Jakoby, B. W., and Udias, J. M. (2016). Evaluation of PeneloPET Simulations of Biograph PET/CT Scanners. *IEEE Transactions on Nuclear Science*, 63(3):1367–1374.

Agostinelli, S., Allison, J., Amako, K., Apostolakis, J., Araujo, H., Arce, P., Asai, M., Axen, D., Banerjee, S., Barrand, G., Behner, F., Bellagamba, L., Boudreau, J., Broglia, L., Brunengo, A., Burkhardt, H., Chauvie, S., Chuma, J., Chytracek, R., Cooperman, G., Cosmo, G., Degtyarenko, P., Dell'Acqua, A., Depaola, G., Dietrich, D., Enami, R., Feliciello, A., Ferguson, C., Fesefeldt, H., Folger, G., Foppiano, F., Forti, A., Garelli, S., Giani, S., Giannitrapani, R., Gibin, D., Cadenas, J. J. G., Gonzalez, I., Abril, G. G., Greeniaus, G., Greiner, W., Grichine, V., Grossheim, A., Guatelli, S., Gumplinger, P., Hamatsu, R., Hashimoto, K., Hasui, H., Heikkinen, A., Howard, A., Ivanchenko, V., Johnson, A., Jones, F. W., Kallenbach, J., Kanaya, N., Kawabata, M., Kawabata, Y., Kawaguti, M., Kelner, S., Kent, P., Kimura, A., Kodama, T., Kokoulin, R., Kossov, M., Kurashige, H., Lamanna, E., Lampen, T., Lara, V., Lefebure, V., Lei, F., Liendl, M., Lockman, W., Longo, F., Magni, S., Maire, M., Medernach, E., Minamimoto, K., de Freitas, P. M., Morita, Y., Murakami, K., Nagamatu, M., Nartallo, R., Nieminen, P., Nishimura, T., Ohtsubo, K., Okamura, M., O'Neale, S., Oohata, Y., Paech, K., Perl, J., Pfeiffer, A., Pia, M. G., Ranjard, F., Rybin, A., Sadilov, S., di Salvo, E., Santin, G., Sasaki, T., Savvas, N., Sawada, Y., Scherer, S., Sei, S., Sirotenko, V., Smith, D., Starkov, N., Stoecker, H., Sulkimo, J., Takahata, M., Tanaka, S., Tcherniaev, E., Tehrani, E. S., Tropeano, M., Truscott, P., Uno, H., Urban, L., Urban, P., Verderi, M., Walkden, A., Wander, W., Weber, H., Wellisch, J. P., Wenaus, T., Williams, D. C., Wright, D., Yamada, T., Yoshida, H., and Zschiesche, D. (2003). Geant4 - a simulation toolkit. *Nuclear Instruments and Methods in Physics Research, Section A: Accelerators, Spectrometers, Detectors and Associated Equipment*.

Akagi, T., Yagi, M., Yamashita, T., Murakami, M., Yamakawa, Y., Kitamura, K., Ogura, K., Kondo, K., and Kawanishi, S. (2013). Experimental study for the production cross sections of positron emitters induced from 12c and 16o nuclei by low-energy proton beams. *Radiation Measurements*, 59:262–269.

Aland, T., Walsh, A., Jones, M., Piccini, A., and Devlin, A. (2019). Accuracy and efficiency

of graphics processing unit (gpu) based acuros xb dose calculation within the varian eclipse treatment planning system. *Medical Dosimetry*, 44(3):219–225.

Albertini, F., Matter, M., Nenoff, L., Zhang, Y., and Lomax, A. (2020). Online daily adaptive proton therapy. *British Journal of Radiology*, 93.

Albouy, G., Gusakow, M., Poffé, N., Sergolle, H., and Valentin, L. (1962). Réactions (p, n) à moyenne énergie. *Journal de Physique et le Radium*, 23:1000–1002.

Almuhaideb, A., Papathanasiou, N., and Bomanji, J. (2011). 18f-fdg pet/ct imaging in oncology. *Annals of Saudi Medicine*, 31:3–13.

Ammar, C., Frey, K., Bauer, J., Melzig, C., Chiblak, S., Hildebrandt, M., Unholtz, D., Kurz, C., Brons, S., Debus, J., Abdollahi, A., and Parodi, K. (2014). Comparing the biological washout of β ⁺ -activity induced in mice brain after ¹² c-ion and proton irradiation. *Physics in Medicine and Biology*, 59:7229–7244.

Anders, B., Herges, P., and Scobel, W. (1981). Excitation functions of nuclear reactions producing11c. *Zeitschrift für Physik A Atoms and Nuclei*, 301:353–361.

Anderson, J. D., Bloom, S. D., Wong, C., Hornyak, W. F., and Madsen, V. A. (1969). Effective two-body force inferred from the (p , n) reaction on o 17 , o 18 , al 27 , and other light nuclei. *Physical Review*, 177:1416–1435.

Antolak, J. A. and Rosen, I. I. (1999). Planning target volumes for radiotherapy: How much margin is needed? *International Journal of Radiation Oncology Biology Physics*, 44:1165–1170.

Assmann, W., Kellnberger, S., Reinhardt, S., Lehrack, S., Edlich, A., Thirolf, P. G., Moser, M., Dollinger, G., Omar, M., Ntziachristos, V., and Parodi, K. (2015). Ionoacoustic characterization of the proton bragg peak with submillimeter accuracy. *Medical Physics*, 42:567–574.

Badal, A. and Badano, A. (2009). Accelerating Monte Carlo simulations of photon transport in a voxelized geometry using a massively parallel graphics processing unit. *Medical Physics*, 36(11):4878–4880.

Bair, J. K. (1973). Total neutron yields from the proton bombardment of o 1 7 , 1 8. *Physical Review C*, 8:120–123.

Baskar, R., Lee, K. A., Yeo, R., and Yeoh, K. W. (2012). Cancer and radiation therapy: Current advances and future directions. *International Journal of Medical Sciences*, 9:193–199.

Bauer, J., Chen, W., Nischwitz, S., Liebl, J., Rieken, S., Welzel, T., Debus, J., and Parodi, K. (2018). Improving the modelling of irradiation-induced brain activation for in vivo pet verification of proton therapy. *Radiotherapy and Oncology*, 128:101–108.

Bello, R. D., Martins, P. M., Brons, S., Hermann, G., Kihm, T., Seimetz, M., and Seco, J. (2020). Prompt gamma spectroscopy for absolute range verification of 12c ions at synchrotron-based facilities. *Physics in medicine and biology*, 65.

Berthold, J., Khamfongkhruea, C., Petzoldt, J., Thiele, J., Hölscher, T., Wohlfahrt, P., Peters, N., Jost, A., Hofmann, C., Janssens, G., Smeets, J., and Richter, C. (2021). First-in-human validation of ct-based proton range prediction using prompt gamma imaging in prostate cancer treatments. *International Journal of Radiation Oncology*Biology*Physics*, 111:1033–1043.

Bethe, H. (1930). Zur theorie des durchgangs schneller korpuskularstrahlen durch materie. *Annalen der Physik*, 397:325–400.

Bettinardi, V., Pagani, E., Gilardi, M., Alenius, S., Thielemans, K., Teras, M., and Fazio, F. (2002). Implementation and evaluation of a 3d one-step late reconstruction algorithm for 3d positron emission tomography brain studies using median root prior. *European Journal of Nuclear Medicine*, 29:7–18.

Boellaard, R. (2009). Standards for pet image acquisition and quantitative data analysis. *J Nucl Med*, 50:11–20.

Bär, E., Lalonde, A., Royle, G., Lu, H. M., and Bouchard, H. (2017). The potential of dual-energy ct to reduce proton beam range uncertainties. *Medical Physics*, 44:2332–2344.

Carabe, A., Moteabbed, M., Depauw, N., Schuemann, J., and Paganetti, H. (2012). Range uncertainty in proton therapy due to variable biological effectiveness. *Physics in Medicine and Biology*, 57:1159–1172.

Carter, L. L., Cashwell, E. D., and Taylor, W. M. (1972). Monte Carlo Sampling with Continuously Varying Cross Sections Along Flight Paths. *Nuclear Science and Engineering*, 48(4):403–411.

Cherry, S., Sorenson, J., and Phelps, M. (2012). *Physics in Nuclear Medicine*. Elsevier.

Cho, J., Campbell, P., Wang, M., Alqathami, M., Mawlawi, O., Kerr, M., and Cho, S. H. (2016). Feasibility of hydrogel fiducial markers for in vivo proton range verification using pet. *Physics in Medicine and Biology*, 61:2162–2176.

Cohilis, M., Sterpin, E., Lee, J. A., and Souris, K. (2020). A noise correction of the γ-index method for monte carlo dose distribution comparison. *Medical Physics*, 47:681–692.

Compton, A. H. (1923). A quantum theory of the scattering of x-rays by light elements. *Physical Review*, 21:483–502.

Cowan, G. (2019). Statistical models with uncertain error parameters. *The European Physical Journal C 2019 79:2*, 79:1–17.

Craft, D., Bangert, M., Long, T., Papp, D., and Unkelbach, J. (2014). Shared data for intensity modulated radiation therapy (imrt) optimization research: The cort dataset. *GigaScience*, 3.

Delso, G., Fürst, S., Jakoby, B., Ladebeck, R., Ganter, C., Nekolla, S. G., Schwaiger, M., and Ziegler, S. I. (2011). Performance measurements of the siemens mmr integrated whole-body pet/mr scanner. *Journal of Nuclear Medicine*, 52:1914–1922.

REFERENCES

Després, P. and Jia, X. (2017). A review of GPU-based medical image reconstruction. *Physica Medica*, 42(October 2017):76–92.

Dostrovsky, I., Gauvin, H., and Lefort, M. (1968). (p,xp) and (p,xpyα) reactions of 156-mev protons with light targets (a=11 to a=27). *Physical Review*, 169:836.

Draeger, E., Mackin, D., Peterson, S., Chen, H., Avery, S., Beddar, S., and Polf, J. C. (2018). 3d prompt gamma imaging for proton beam range verification. *Physics in Medicine and Biology*, 63:035019.

Dyer, P., Bodansky, D., Seamster, A. G., Norman, E. B., and Maxson, D. R. (1981). Cross sections relevant to gamma-ray astronomy: Proton induced reactions. *Physical Review C*, 23:1865–1882.

España, S., Sánchez-Parcerisa, D., Bragado, P., Álvaro Gutiérrez-Uzquiza, Porras, A., Gutiérrez-Neira, C., Espinosa, A., Onecha, V. V., Ibáñez, P., Sánchez-Tembleque, V., Udías, J. M., and Fraile, L. M. (2022). In vivo production of fluorine-18 in a chicken egg tumor model of breast cancer for proton therapy range verification. *Scientific Reports 2022 12:1*, 12:1–12.

España, S., Sánchez-Parcerisa, D., Ibáñez, P., Sánchez-Tembleque, V., Udías, J. M., Onecha, V., Gutierrez-Uzquiza, A., Bäcker, C. M., Bäumer, C., Herrmann, K., Costa, P. F., Timmermann, B., and Fraile, L. M. (2021). Direct proton range verification using oxygen-18 enriched water as a contrast agent. *Radiation Physics and Chemistry*, 182:109385.

España, S., Zhu, X., Daartz, J., Fakhri, G. E., Bortfeld, T., and Paganetti, H. (2011). The reliability of proton-nuclear interaction cross-section data to predict proton-induced pet images in proton therapy. *Physics in Medicine and Biology*, 56:2687–2698.

Faddegon, B., Ramos-Mendez, J., Schuemann, J., McNamara, A., Shin, J., Perl, J., and H., P. (2020). The TOPAS Tool for Particle Simulation, a Monte Carlo Simulation Tool for Physics, Biology and Clinical Research. *Physica Medica*.

Fatica, M. and Ruetsch, G. (2014). *CUDA Fortran for Scientists and Engineers*. Elsevier.

Flynn, D. S., Sekharan, K. K., Hiller, B. A., Laumer, H., Weil, J. L., and Gabbard, F. (1978). Cross sections and reaction rates for na 23 (p , n) mg 23 , al 27 (p , n) si 27 , al 27 (α , n) p 30 , si 29 (α , n) s 32 , and si 30 (α , n) s 33. *Physical Review C*, 18:1566–1576.

Fraile, L. M., Herraiz, J. L., Udías, J. M., Cal-González, J., Corzo, P. M. G., España, S., Herranz, E., Pérez-Liva, M., Picado, E., Vicente, E., Muñoz-Martín, A., and Vaquero, J. J. (2016). Experimental validation of gallium production and isotope-dependent positron range correction in pet. *Nuclear Instruments and Methods in Physics Research, Section A: Accelerators, Spectrometers, Detectors and Associated Equipment*, 814:110–116.

Fredriksson, A. and Bokrantz, R. (2014). A critical evaluation of worst case optimization methods for robust intensity-modulated proton therapy planning. *Medical physics*, 41.

Freijo, C., Herraiz, J. L., Sanchez-Parcerisa, D., and Udias, J. M. (2021). Dictionary-based protoacoustic dose map imaging for proton range verification. *Photoacoustics*, 21:100240.

Frinking, P., Segers, T., Luan, Y., and Tranquart, F. (2020). Three decades of ultrasound contrast agents: A review of the past, present and future improvements. *Ultrasound in Medicine Biology*, 46:892–908.

Furukawa, M., Ishizaki, Y., Nakano, Y., Nozaki, T., Saji, Y., Tanaka, S., Nakano, Y., and Nozaki, T. (2013). Excitation function for the reaction b11(p, n)c11 up to ep=15 mev and energy levels of c12. *https://doi.org/10.1143/JPSJ.15.2167*, 15:2167–2170.

Galve, P., Herraiz, J. L., Catana, C., and Udías, J. (2020). Gpu based fast and flexible iterative reconstructions of arbitrary and complex pet scanners: application to next generation dedicated brain scanners. Virtual 2020 IEEE Nuclear Science Symposium Medical Imaging Conference.

Galve, P., López-Montes, A., Udías, J. M., and López Herraiz, J. (2019a). Iterative Algorithm for Optimal Super Resolution Sampling. In *Springer Proceedings in Physics*, volume 225, pages 141–143.

Galve, P., Udias, J. M., Lopez-Montes, A., and Herraiz, J. L. (2019b). Super-iterative image reconstruction in PET. In Matej, S. and Metzler, S. D., editors, *15th International Meeting on Fully Three-Dimensional Image Reconstruction in Radiology and Nuclear Medicine*, number May, page 53. SPIE.

García-Pareja, S., Lallena, A. M., and Salvat, F. (2021). Variance-reduction methods for monte carlo simulation of radiation transport. *Frontiers in Physics*, 9:633.

Gibbons, J. H. and Macklin, R. L. (1959). Total neutron yields from light elements under proton and alpha bombardment. *Physical Review*, 114:571–580.

Hao, D., Ai, T., Goerner, F., Hu, X., Runge, V. M., and Tweedle, M. (2012). Mri contrast agents: Basic chemistry and safety. *Journal of Magnetic Resonance Imaging*, 36:1060–1071.

Hermanne, A., Tárkányi, F. T., Ignatyuk, A. V., Takács, S., and Capote, R. (2021). Upgrade of iaea recommended data of selected nuclear reactions for production of pet and spect isotopes. *Nuclear Data Sheets*, 173:285–308.

Herraiz, J. L., España, S., Vaquero, J. J., Desco, M., and Udías, J. M. (2006). First: Fast iterative reconstruction software for (pet) tomography. *Physics in Medicine and Biology*, 51:4547–4565.

Hess, E., Scholten, B., Coenen, H. H., Qaim, S. M., Takács, S., and Tárkányi, F. (2001). Excitation function of the 18o(p,n)18f nuclear reaction from threshold up to 30 mev. *Radiochimica Acta*, 89:357.

Hintz, N. M. and Ramsey, N. F. (1952). Excitation functions to 100 mev. *Physical Review*, 88:19–27.

Hong, L., Goitein, M., Bucciolini, M., Comiskey, R., Gottschalk, B., Rosenthal, S., Serago, C., and Urie, M. (1996). A pencil beam algorithm for proton dose calculations. *Physics in Medicine and Biology*, 41:1305–1330.

Hu, Z., Li, G., Zhang, X., Ye, K., Lu, J., and Peng, H. (2020). A machine learning framework with anatomical prior for online dose verification using positron emitters and pet in proton therapy. *Physics in Medicine Biology*.

Huang, J. Y., Pulliam, K. B., McKenzie, E. M., Followill, D. S., and Kry, S. F. (2014). Effects of spatial resolution and noise on gamma analysis for imrt qa. *Journal of Applied Clinical Medical Physics*, 15:93–104.

Hudson, H. M. and Larkin, R. S. (1994). Accelerated image reconstruction using ordered subsets of projection data. *IEEE Transactions on Medical Imaging*, 13:601–609.

Hueso-González, F., Rabe, M., Ruggieri, T. A., Bortfeld, T., and Verburg, J. M. (2018). A full-scale clinical prototype for proton range verification using prompt gamma-ray spectroscopy. *Physics in Medicine Biology*, 63:185019.

Hui, Z., Zhang, X., Starkschall, G., Li, Y., Mohan, R., Komaki, R., Cox, J. D., and Chang, J. Y. (2008). Effects of interfractional motion and anatomic changes on proton therapy dose distribution in lung cancer. *International Journal of Radiation Oncology Biology Physics*, 72:1385–1395.

Ibáñez, P., Villa-Abaunza, A., Vidal, M., Guerra, P., Graullera, S., Illana, C., and Udías, J. M. (2021). XIORT-MC: A real-time MC-based dose computation tool for low- energy X-rays intraoperative radiation therapy. *Medical Physics*, 48(12):8089–8106.

Jagtap, S., Chopade, P., Tadepalli, S., Bhalerao, A., and Gosavi, S. (2019). A review on the progress of znse as inorganic scintillator. *Opto-Electronics Review*, 27(1):90–103.

James, F. and Moneta, L. (2020). Review of high-quality random number generators. *Computing and Software for Big Science*, 4:1–12.

Janni, J. F. (1982). Energy loss, range, path length, time-of-flight, straggling, multiple scattering, and nuclear interaction probability: In two parts. part 1. for 63 compounds part 2. for elements 1 z 92. *Atomic Data and Nuclear Data Tables*, 27:147–339.

Kalos, M. H. and Whitlock, P. A. (2008). *Monte Carlo Methods*. Wiley, Germany, Darmstadt, second, re edition.

Kawachi, K. (1975). Calculation of electron dose distribution for radiotherapy treatment planning. *Physics in Medicine Biology*, 20:571.

Kemper, K. W., McKenna, C. M., and Nelson, J. W. (1970). Mass of ca 39. *Physical Review C*, 2:213–214.

Kiener, J., Berheide, M., Achouri, N. L., Boughrara, A., Coc, A., Lefebvre, A., De, F., Santos, O., and Vieu, C. (1998). ray production by inelastic proton scattering on 16 o and 12 c.

Kipergil, E. A., Erkol, H., Kaya, S., Gulsen, G., and Unlu, M. B. (2017). An analysis of beam parameters on proton-acoustic waves through an analytic approach. *Physics in Medicine and Biology*, 62:4694–4710.

Klein, O. and Nishina, T. (1929). ??ber die streuung von strahlung durch freie elektronen nach der neuen relativistischen quantendynamik von dirac. *Zeitschrift f??r Physik*, 52:853–868.

Kneff, D. W., Mann, F. M., and Switkowski, Z. E. (1975). The 100mo(p, n)100tc reaction cross section and its use as a normalization for shuttle-system measurements. *Nuclear Physics A*, 250:285–294.

Knoll, G. F. (2010). *Radiation Detection and Measurement*. John Wiley, 4th edition.

Knoll, G. F. (2011). *Radiation Detection and Measurements*. John Willey & Son, fourth edi edition.

Knopf, A. C. and Lomax, A. (2013). In vivo proton range verification: A review. *Physics in Medicine and Biology*, 58:131–160.

Koning, A. J., Rochman, D., Sublet, J. C., Dzysiuk, N., Fleming, M., and van der Marck, S. (2019). Tendl: Complete nuclear data library for innovative nuclear science and technology. *Nuclear Data Sheets*, 155:1–55.

Kooy, H. M., Clasie, B. M., Lu, H. M., Madden, T. M., Bentefour, H., Depauw, N., Adams, J. A., Trofimov, A. V., Demaret, D., Delaney, T. F., and Flanz, J. B. (2010). A case study in proton pencil-beam scanning delivery. *International Journal of Radiation Oncology*Biology*Physics*, 76:624–630.

Krasnov, N. (1974). Thick target yield. *International Journal of Applied Radiation and Isotopes*, 25:223–227.

Krimmer, J., Dauvergne, D., Létang, J. M., and Testa (2018). Prompt-gamma monitoring in hadrontherapy: A review. *Nuclear Instruments and Methods in Physics Research, Section A: Accelerators, Spectrometers, Detectors and Associated Equipment*, 878:58–73.

Krishnamoorthy, S., Blankemeyer, E., Mollet, P., Surti, S., Holen, R. V., and Karp, J. S. (2018). Performance evaluation of the molecubes β -cube—a high spatial resolution and high sensitivity small animal pet scanner utilizing monolithic lyso scintillation detectors. *Physics in Medicine Biology*, 63:155013.

Lang, F. L., Werntz, C. W., Crannell, C. J., Trombka, J. I., and Chang, C. C. (1987). Cross sections for production of the 15.10-mev and other astrophysically significant gamma-ray lines through excitation and spallation of c12 and o16 with protons. *Physical Review C*, 35:1214–1227.

Langen, K. and Zhu, M. (2018). Concepts of ptv and robustness in passively scattered and pencil beam scanning proton therapy. *Seminars in Radiation Oncology*, 28:248–255.

Lee, H., Shin, J., Verburg, J. M., Bobić, M., Winey, B., Schuemann, J., and Paganetti, H. (2022). Moqui: an open-source gpu-based monte carlo code for proton dose calculation with efficient data structure. *Physics in Medicine Biology*, 67:174001.

Lesko, K. T., Norman, E. B., Larimer, R. M., Kuhn, S., Meekhof, D. M., Crane, S. G., and Bussell, H. G. (1988). Measurements of cross sections relevant to -ray line astronomy. *Physical Review C*, 37:1808–1817.

Li, Z., Wang, Y., Yu, Y., Fan, K., Xing, L., and Peng, H. (2019). Technical note: Machine learning approaches for range and dose verification in proton therapy using proton-induced positron emitters. *Medical Physics*, 46:5748–5757.

Liu, C., Li, Z., Hu, W., Xing, L., and Peng, H. (2019). Range and dose verification in proton therapy using proton-induced positron emitters and recurrent neural networks (rnns). *Physics in Medicine Biology*, 64:175009.

Lomax, A. J. (2008). Intensity modulated proton therapy and its sensitivity to treatment uncertainties 1: The potential effects of calculational uncertainties. *Physics in Medicine and Biology*, 53:1027–1042.

Lopez-Montes, A., Herraiz, J. L., Galve, P., Espana, S., Vicente, E., Cal-Gonzalez, J., and Udias, J. M. (2019). PeneloPET v3.0, an improved multiplatform PET Simulator. In *2019 IEEE Nuclear Science Symposium and Medical Imaging Conference (NSS/MIC)*, pages 1–3. IEEE.

Low, D. A., Harms, W. B., Mutic, S., and Purdy, J. A. (1998). A technique for the quantitative evaluation of dose distributions.

Luo, X., Modamio, V., Nyberg, J., Valiente-Dobón, J., Nishada, Q., de Angelis, G., Agramunt, J., Egea, F., Erduran, M., Ertürk, S., de France, G., Gadea, A., González, V., Goasduff, A., Hüyük, T., Jaworski, G., Moszyński, M., Di Nitto, A., Palacz, M., Söderström, P.-A., Sanchis, E., Triossi, A., and Wadsworth, R. (2018). Pulse pile-up identification and reconstruction for liquid scintillator based neutron detectors. *Nuclear Instruments and Methods in Physics Research Section A: Accelerators, Spectrometers, Detectors and Associated Equipment*, 897:59–65.

Ma, D., Wolf, P., Clough, A. V., and Schmidt, T. G. (2013). The performance of mlem for dynamic imaging from simulated few-view, multi-pinhole spect. *IEEE Transactions on Nuclear Science*, 60:115–123.

Ma, S., Hu, Z., Ye, K., Zhang, X., Wang, Y., and Peng, H. (2020). Feasibility study of patient-specific dose verification in proton therapy utilizing positron emission tomography (pet) and generative adversarial network (gan). *Medical Physics*, 47:5194–5208.

MacKay, R. I. (2018). Image guidance for proton therapy. *Clinical Oncology*, 30:293–298.

Mairani, A., Böhlen, T. T., Schiavi, A., Tessonnier, T., Molinelli, S., Brons, S., Battistoni, G., Parodi, K., and Patera, V. (2013). A monte carlo-based treatment planning tool for proton therapy. *Physics in Medicine and Biology*, 58:2471–2490.

Mann, F. M., Kneff, D. W., Switkowski, Z. E., and Woosley, S. E. (1976). A study of the 23na+p reactions to determine 23mg consumption in stars. *Nuclear Physics A*, 256:163–172.

Masuda, T., Kataoka, J., Arimoto, M., Takabe, M., Nishio, T., Matsushita, K., Miyake, T., Yamamoto, S., Inaniwa, T., and Toshito, T. (2018). Measurement of nuclear reaction cross sections by using cherenkov radiation toward high-precision proton therapy. *Scientific Reports*, 8:1–8.

Masuda, T., Nishio, T., Kataoka, J., Arimoto, M., Sano, A., and Karasawa, K. (2019). Ml-em algorithm for dose estimation using pet in proton therapy. *Physics in Medicine Biology*, 64:175011.

Masuda, T., Nishio, T., Sano, A., and Karasawa, K. (2020). Extension of the ml-em algorithm for dose estimation using pet in proton therapy: Application to an inhomogeneous target. *Physics in Medicine and Biology*, 65.

Maxim, V., Lojacono, X., Hilaire, E., Krimmer, J., Testa, E., Dauvergne, D., Magnin, I., and Prost, R. (2016). Probabilistic models and numerical calculation of system matrix and sensitivity in list-mode mlem 3d reconstruction of compton camera images. *Physics in Medicine and Biology*, 61:243–264.

McGowan, S. E., Burnet, N. G., and Lomax, A. J. (2013). Treatment planning optimisation in proton therapy. *The British journal of radiology*, 86:20120288.

Measday, D. F. (1966). The 12c(p, pn)11c reaction from 50 to 160 mev. *Nuclear Physics*, 78:476–480.

Medrano, M., Liu, R., Zhao, T., Webb, T., Politte, D. G., Whiting, B. R., Liao, R., Ge, T., Porras-Chaverri, M. A., O'Sullivan, J. A., and Williamson, J. F. (2022). Towards subpercentage uncertainty proton stopping-power mapping via dual-energy ct: Direct experimental validation and uncertainty analysis of a statistical iterative image reconstruction method. *Medical Physics*, 49:1599–1618.

Mehta, S. R., Suhag, V., Semwal, M., and Sharma, N. (2010). Radiotherapy: Basic concepts and recent advances. *Medical journal, Armed Forces India*, 66:158–62.

Miften, M., Olch, A., Mihailidis, D., Moran, J., Pawlicki, T., Molineu, A., Li, H., Wijesooriya, K., Shi, J., Xia, P., Papanikolaou, N., and Low, D. A. (2018). Tolerance limits and methodologies for imrt measurement-based verification qa: Recommendations of aapm task group no. 218. *Medical Physics*, 45:e53–e83.

Mizuno, H., Tomitani, T., Kanazawa, M., Kitagawa, A., Pawelke, J., Iseki, Y., Urakabe, E., Suda, M., Kawano, A., Iritani, R., Matsushita, S., Inaniwa, T., Nishio, T., Furukawa, S., Ando, K., Nakamura, Y. K., Kanai, T., and Ishii, K. (2003). Washout measurement of radioisotope implanted by radioactive beams in the rabbit. *Physics in Medicine and Biology*, 48:2269–2281.

Mohan, R. and Grosshans, D. (2017). Proton therapy – present and future. *Advanced Drug Delivery Reviews*, 109:26–44.

REFERENCES

Moreno, A. C., Frank, S. J., Garden, A. S., Rosenthal, D. I., Fuller, C. D., Gunn, G. B., Reddy, J. P., Morrison, W. H., Williamson, T. D., Holliday, E. B., Phan, J., and Blanchard, P. (2019). Intensity modulated proton therapy (impt) - the future of imrt for head and neck cancer. *Oral oncology*, 88:66–74.

Moteabbed, M., España, S., and Paganetti, H. (2011). Monte carlo patient study on the comparison of prompt gamma and pet imaging for range verification in proton therapy. *Physics in Medicine and Biology*, 56:1063–1082.

Motz, J. W. and Missoni, G. (1961). Compton scattering by k-shell electrons. *Physical Review*, 124:1458–1468.

Muñoz, E., Ros, A., Borja-Lloret, M., Barrio, J., Dendooven, P., Oliver, J. F., Ozoemelam, I., Roser, J., and Llosá, G. (2021). Proton range verification with macaco ii compton camera enhanced by a neural network for event selection. *Scientific Reports 2021 11:1*, 11:1–12.

Nedunchezhian, K., Aswath, N., Thiruppathy, M., and Thirugnanamurthy, S. (2016). Boron neutron capture therapy - a literature review. *Journal of clinical and diagnostic research : JCDR*, 10:ZE01–ZE04.

NVIDIA, Vingelmann, P., and Fitzek, F. H. (2020). Cuda, release: 10.2.89.

Onecha, V. V., Galve, P., Ibanez, P., Espinosa, A., Sanchez-Parcerisa, D., Espana, S., Fraile, L. M., and Udias, J. M. (2020). Dictionary based MLEM-algorithm for real-time proton range verification from PET data: the virtue of contrasts. In *2020 IEEE Nuclear Science Symposium and Medical Imaging Conference Proceedings (NSS/MIC)*.

Onecha, V. V., Galve, P., Ibáñez, P., Freijo, C., Arias-Valcayo, F., Sanchez-Parcerisa, D., España, S., Fraile, L. M., and Udías, J. M. (2022). Dictionary-based software for proton dose reconstruction and submilimetric range verification. *Physics in Medicine Biology*, 67:045002.

Otuka, N., Dupont, E., Semkova, V., Pritychenko, B., Blokhin, A. I., Aikawa, M., Babykina, S., Bossant, M., Chen, G., Dunaeva, S., Forrest, R. A., Fukahori, T., Furutachi, N., Ganesan, S., Ge, Z., Gritzay, O. O., Herman, M., Hlavač, S., Kato, K., Lalremruata, B., Lee, Y. O., Makinaga, A., Matsumoto, K., Mikhaylyukova, M., Pikulina, G., Pronyaev, V. G., Saxena, A., Schwerer, O., Simakov, S. P., Soppera, N., Suzuki, R., Takács, S., Tao, X., Taova, S., Tárkányi, F., Varlamov, V. V., Wang, J., Yang, S. C., Zerkin, V., and Zhuang, Y. (2014). Towards a more complete and accurate experimental nuclear reaction data library (exfor): International collaboration between nuclear reaction data centres (nrdc). *Nuclear Data Sheets*, 120:272–276.

Paganetti, H. (2011). *Proton Therapy Physics*, volume 20115763.

Paganetti, H. (2012). Range uncertainties in proton therapy and the role of monte carlo simulations. *Physics in Medicine and Biology*, 57:R99–R117.

Paganetti, H., Botas, P., Sharp, G. C., and Winey, B. (2021). Adaptive proton therapy. *Physics in Medicine Biology*, 66:22TR01.

Paganetti, H. and Fakhri, G. E. (2015). Monitoring proton therapy with pet. *British Journal of Radiology*, 88:20150173.

Paganetti, H., Jiang, H., Lee, S. Y., and Kooy, H. M. (2004). Accurate monte carlo simulations for nozzle design, commissioning and quality assurance for a proton radiation therapy facility. *Medical Physics*, 31:2107–2118.

Parodi, K., Bauer, J., Kurz, C., Unholtz, D., Sommerer, F., Frey, K., Haberer, T., Herfarth, K., Welzel, T., Combs, S., and Debus, J. (2013). We-g-500-06: Offline pet/ct imaging of scanned proton and carbon ion beams: Initial clinical experience for different tumour sites. volume 40, page 504. John Wiley Sons, Ltd.

Parodi, K. and Bortfeld, T. (2006). A filtering approach based on gaussian–powerlaw convolutions for local pet verification of proton radiotherapy. *Physics in Medicine and Biology*, 51:1991–2009.

Parodi, K., Paganetti, H., Shih, H. A., Michaud, S., Loeffler, J. S., DeLaney, T. F., Liebsch, N. J., Munzenrider, J. E., Fischman, A. J., Knopf, A., and Bortfeld, T. (2007). Patient study of in vivo verification of beam delivery and range, using positron emission tomography and computed tomography imaging after proton therapy. *International Journal of Radiation Oncology Biology Physics*, 68:920–934.

Parodi, K. and Polf, J. C. (2018). in vivo range verification in particle therapy. *Medical Physics*, 45:e1036–e1050.

Parodi, K., Ponisch, F., and Enghardt, W. (2005). Experimental study on the feasibility of in-beam pet for accurate monitoring of proton therapy. *IEEE Transactions on Nuclear Science*, 52:778–786.

Perl, J., Shin, J., Schümann, J., Faddegon, B., and Paganetti, H. (2012). Topas: An innovative proton monte carlo platform for research and clinical applications. *Medical Physics*, 39:6818–6837.

Polf, J. C., Panthi, R., Mackin, D. S., McCleskey, M., Saastamoinen, A., Roeder, B. T., and Beddar, S. (2013). Measurement of characteristic prompt gamma rays emitted from oxygen and carbon in tissue-equivalent samples during proton beam irradiation. *Physics in Medicine and Biology*, 58:5821–5831.

Poludniowski, G., Allinson, N. M., and Evans, P. M. (2015). Proton radiography and tomography with application to proton therapy. *The British Journal of Radiology*, 88(1053):20150134. PMID: 26043157.

Pratx, G., Chinn, G., Olcott, P., and Levin, C. (2009). Fast, Accurate and Shift-Varying Line Projections for Iterative Reconstruction Using the GPU. *IEEE Transactions on Medical Imaging*, 28(3):435–445.

Pratx, G. and Xing, L. (2011). GPU computing in medical physics: A review. *Medical Physics*, 38(5):2685–2697.

REFERENCES

Ramavataram, K., Larue, R., Turcotte, V., St-Pierre, C., and Ramavataram, S. (1980). Study of the 11b(p, n)11c reaction below the giant dipole resonance in12c. *Il Nuovo Cimento A Series 11*, 58:342–354.

Reske, S. N. and Kotzerke, J. (2001). Fdg-pet for clinical use. *European Journal of Nuclear Medicine*, 28:1707–1723.

Reynaert, N., der Marck, S. V., Schaart, D., der Zee, W. V., Tomsej, M., Vliet-Vroegindeweij, C. V., Jansen, J., Coghe, M., Wagter, C. D., and Heijmen, B. (2006). Ncs report 16: Monte carlo treatment planning: An introduction.

Richter, C., Pausch, G., Barczyk, S., Priegnitz, M., Keitz, I., Thiele, J., Smeets, J., Stappen, F. V., Bombelli, L., Fiorini, C., Hotoiu, L., Perali, I., Prieels, D., Enghardt, W., and Baumann, M. (2016). First clinical application of a prompt gamma based in vivo proton range verification system. *Radiotherapy and Oncology*, 118:232–237.

Rodriguez, A. E., Onecha, V., Sánchez-Tembleque, V., Gutiérrez-Neira, C., García-Díez, M., Ibáñez, P., España, S., Sánchez-Parcerisa, D., Udías, J., and Fraile, L. (2021). Can iodine be used as a contrast agent for protontherapy range verification? measurement of the 127i(p,n)127mxe (reaction) cross section in the 4.5–10 mev energy range. *Radiation Physics and Chemistry*, 185:109485.

Rutenbar, R. A. (1989). Simulated annealing algorithms: An overview. *IEEE Circuits and Devices Magazine*, 5:19–26.

Ruth, T. J. and Wolf, A. P. (1979). Absolute cross sections for the production of 18f via the 18o(p, n)18f reaction. *Radiochimica Acta*, 26:21–24.

Rutherford, H., Chacon, A., Mohammadi, A., Takyu, S., Tashima, H., Yoshida, E., Nishikido, F., Hofmann, T., Pinto, M., Franklin, D. R., Yamaya, T., Parodi, K., Rosenfeld, A. B., Guatelli, S., and Safavi-Naeini, M. (2020). Dose quantification in carbon ion therapy using in-beam positron emission tomography. *Physics in Medicine Biology*, 65:235052.

Sajjad, M., Lambrecht, R. M., and Wolf, A. P. (1985). Cyclotron isotopes and radiopharmaceuticals: Xxxvi investigation of some excitation functions for the preparation of 15o, 13n and 11c. *Radiochimica Acta*, 38:57–64.

Salvat, F. (2013). A generic algorithm for monte carlo simulation of proton transport. *Nuclear Instruments and Methods in Physics Research Section B: Beam Interactions with Materials and Atoms*, 316:144–159.

Sanchez-Parcerisa, D., Sanz-Garciá, I., Ibánez, P., Espana, S., Espinosa, A., Gutiérrez-Neira, C., López, A., Vera, J. A., Mazal, A., Fraile, L. M., and Udiás, J. M. (2021). Radiochromic film dosimetry for protons up to 10 mev with ebt2, ebt3 and unlaminated ebt3 films. *Physics in Medicine Biology*, 66:115006.

Sanders, J. and Kandrot, E. (2010). *The CUDA Handbook: A Comprehensive Guide to GPU Programming*. Addison-Wesley Professional, 1st edition.

Schneider, W., Bortfeld, T., and Schlegel, W. (2000). Correlation between ct numbers and tissue parameters needed for monte carlo simulations of clinical dose distributions. *Physics in Medicine and Biology*, 45:459–478.

Schuemann, J., Dowdell, S., Grassberger, C., Min, C. H., and Paganetti, H. (2014). Site-specific range uncertainties caused by dose calculation algorithms for proton therapy. *Physics in Medicine and Biology*, 59:4007–4031.

Segel, R. E., Hanna, S. S., and Allas, R. G. (1965). States in c 12 between 16.4 and 19.6 mev. *Physical Review*, 139:B818–B830.

Shepp, L. A. and Vardi, Y. (1982). Maximum likelihood reconstruction for emission tomography. *IEEE Transactions on Medical Imaging*, 1:113–122.

Sonzogni, A. A. (2005). Nudat 2.0: Nuclear structure and decay data on the internet. *AIP Conference Proceedings*, 769:574–577.

Soppera, N., Bossant, M., and Dupont, E. (2014). Janis 4: An improved version of the nea java-based nuclear data information system. *Nuclear Data Sheets*, 120:294–296.

Sterpin, E., Janssens, G., Smeets, J., Stappen, F. V., Prieels, D., Priegnitz, M., Perali, I., and Vynckier, S. (2015). Analytical computation of prompt gamma ray emission and detection for proton range verification. *Physics in Medicine and Biology*, 60:4915–4946.

Strijkers, G. J., Mulder, W. J. M., van Tilborg, G. A. F., and Nicolay, K. (2008). Mri contrast agents: Current status and future perspectives. *Anti-Cancer Agents in Medicinal Chemistry*, 7:291–305.

Sudhakar, A. (2009). History of cancer, ancient and modern treatment methods. *Journal of Cancer Science Therapy*, 01:i–iv.

Takács, S., Tárkányi, F., Hermanne, A., and de Corcuera, R. P. (2003). Validation and upgrading of the recommended cross section data of charged particle reactions used for production of pet radioisotopes. *Nuclear Instruments and Methods in Physics Research, Section B: Beam Interactions with Materials and Atoms*, 211:169–189.

Teoh, S., George, B., Fiorini, F., Vallis, K., and den Heuvel, F. V. (2017). Robustness assessment using probabilistic scenarios of intensity modulated proton therapy and volumetric arc therapy in non-small-cell lung cancer: an in-silico radiotherapy planning study. *The Lancet*, 389:S94.

Tian, L., Landry, G., Dedes, G., Kamp, F., Pinto, M., Niepel, K., Belka, C., and Parodi, K. (2018). Toward a new treatment planning approach accounting for in vivo proton range verification. *Physics in Medicine Biology*, 63:215025.

Tian, X., Liu, K., Hou, Y., Cheng, J., Zhang, J., Hou, Y., Cheng, J., Cheng, J., Zhang, J., and Zhang, J. (2017). The evolution of proton beam therapy: Current and future status (review). *Molecular and Clinical Oncology*, 8:15–21.

Tommasino, F., Rovituso, M., Fabiano, S., Piffer, S., Manea, C., Lorentini, S., Lanzone, S., Wang, Z., Pasini, M., Burger, W. J., Tessa, C. L., Scifoni, E., Schwarz, M., and Durante, M. (2017). Proton beam characterization in the experimental room of the trento proton therapy facility. *Nuclear Instruments and Methods in Physics Research, Section A: Accelerators, Spectrometers, Detectors and Associated Equipment*, 869:15–20.

Toramatsu, C., Mohammadi, A., Wakizaka, H., Seki, C., Nishikido, F., Sato, S., Kanno, I., Takahashi, M., Karasawa, K., Hirano, Y., and Yamaya, T. (2020). Biological washout modelling for in-beam pet: rabbit brain irradiation by 11c and 15o ion beams. *Physics in medicine and biology*, 65.

Toramatsu, C., Yoshida, E., Wakizaka, H., Mohammadi, A., Ikoma, Y., Tashima, H., Nishikido, F., Kitagawa, A., Karasawa, K., Hirano, Y., and Yamaya, T. (2018). Washout effect in rabbit brain: in-beam pet measurements using ¹⁰ c, ¹¹ c and ¹⁵ o ion beams. *Biomedical Physics Engineering Express*, 4:035001.

Tárkányi, F. T., Ignatyuk, A. V., Hermanne, A., Capote, R., Carlson, B. V., Engle, J. W., Kellett, M. A., Kibédi, T., Kim, G. N., Kondev, F. G., Hussain, M., Lebeda, O., Luca, A., Nagai, Y., Naik, H., Nichols, A. L., Nortier, F. M., Suryanarayana, S. V., Takács, S., and Verpelli, M. (2019). Recommended nuclear data for medical radioisotope production: diagnostic positron emitters. *Journal of Radioanalytical and Nuclear Chemistry 2019 319:2*, 319:533–666.

Valentin, L. (1965). Réactions (p, n) et (p, pn) induites à moyenne énergie sur des noyaux légers. *Nuclear Physics*, 62:81–102.

Vedia, V., Mach, H., Fraile, L., Udías, J., and Lalkovski, S. (2015). Enhanced time response of 1-in. labr3(ce) crystals by leading edge and constant fraction techniques. *Nuclear Instruments and Methods in Physics Research Section A: Accelerators, Spectrometers, Detectors and Associated Equipment*, 795:144–150.

Verburg, J. M. and Seco, J. (2014). Proton range verification through prompt gamma-ray spectroscopy. *Physics in Medicine and Biology*, 59:7089–7106.

Verburg, J. M., Shih, H. A., and Seco, J. (2012). Simulation of prompt gamma-ray emission during proton radiotherapy. *Physics in Medicine and Biology*, 57:5459–5472.

Versluis, M., Stride, E., Lajoinie, G., Dollet, B., and Segers, T. (2020). Ultrasound contrast agent modeling: A review. *Ultrasound in Medicine Biology*, 46:2117–2144.

Vítek, P., Kubeš, J., Vondráček, V., Andrlik, M., Navrátíl, M., Zapletal, R., Haas, A., Dědečková, K., Ondrová, B., Grebenyuk, A., and Rosina, J. (2021). Pencil beam scanning (pbs) intensity-modulated proton therapy (impt) chemoradiotherapy for anal canal cancer-single institution experience. *Cancers*, 14.

wa Kitwanga, S., Leleux, P., Lipnik, P., and Vanhorenbeeck, J. (1990). Production of o 1 4 , 1 5 , f 18 , and ne 19 radioactive nuclei from (p , n) reactions up to 30 mev. *Physical Review C*, 42:748–752.

Whitehead, A. B. and Foster, J. S. (1958). Activation cross sections for c ¹² (p , pn)c ¹¹ , o ¹⁶ (p , α)n ¹³ , and f ¹⁹ (p , pn)f ¹⁸. *Canadian Journal of Physics*, 36:1276–1285.

Wieser, H. P., Cisternas, E., Wahl, N., Ulrich, S., Stadler, A., Mescher, H., Muller, L. R., Klinge, T., Gabrys, H., Burigo, L., Mairani, A., Ecker, S., Ackermann, B., Ellerbrock, M., Parodi, K., Jakel, O., and Bangert, M. (2017). Development of the open-source dose calculation and optimization toolkit matrad. *Medical Physics*, 44:2556–2568.

Wilson, R. R. (1946). Radiological use of fast protons. *Radiology*, 47:487–491.

Wohlfahrt, P. and Richter, C. (2020). Status and innovations in pre-treatment ct imaging for proton therapy. *British Journal of Radiology*, 93.

Woodcock, E., Murphy, T., Hemmings, P., and Longworth, S. (1965). Techniques used in the GEM code for Monte Carlo neutronics calculation. *Proc. Conf. Applications of Computing Methods to Reactors, ANL-7050*, (3):557–579.

Yabe, T., Yamaguchi, M., Tsuda, M., Nagao, Y., and Kawachi, N. (2023). Time-of-flight based neutron background reduction in secondary-electron-bremsstrahlung imaging for in-vivo range verification of proton therapy: a monte carlo study. *Journal of Instrumentation*, 18:C02041.

Yang, Z., Li, H., Li, Y., Li, Y., Chang, Y., Li, Q., Yang, K., Wu, G., Sahoo, N., Poenisch, F., Gillin, M., Zhu, X. R., and Zhang, X. (2019). Statistical evaluation of worst-case robust optimization intensity-modulated proton therapy plans using an exhaustive sampling approach. *Radiation Oncology*, 14:1–9.

Yang, Z., Zhang, X., Wang, X., Zhu, X. R., Gunn, B., Frank, S. J., Chang, Y., Li, Q., Yang, K., Wu, G., Liao, L., Li, Y., Chen, M., and Li, H. (2020). Multiple-ct optimization: An adaptive optimization method to account for anatomical changes in intensity-modulated proton therapy for head and neck cancers. *Radiotherapy and Oncology*, 142:124–132.

Ytre-Hauge, K. S., Skjerdal, K., Mattingly, J., and Meric, I. (2019). A monte carlo feasibility study for neutron based real-time range verification in proton therapy. *Scientific Reports*, 9:2011.

Zhang, S., Han, D., Williamson, J. F., Zhao, T., Politte, D. G., Whiting, B. R., and O'Sullivan, J. A. (2019). Experimental implementation of a joint statistical image reconstruction method for proton stopping power mapping from dual-energy ct data. *Medical Physics*, 46:273–285.

Zhengrong Liang, J., Li, T., Schulte, R. W., Satogata, T. J., Williams, D. C., and Sadrozinski, H. F.-W. (2008). 1 - proton computed tomography. In Hayat, M., editor, *Cancer Imaging*, pages 3–16. Academic Press, San Diego.

Zhu, X., España, S., Daartz, J., Liebsch, N., Ouyang, J., Paganetti, H., Bortfeld, T. R., and Fakhri, G. E. (2011). Monitoring proton radiation therapy with in-room pet imaging. *Physics in Medicine and Biology*, 56:4041–4057.

Zhu, X. and Fakhri, G. E. (2013). Proton therapy verification with pet imaging. *Theranostics*, 3:731–740.

Zou, W., Dong, L., and Teo, B. K. K. (2018). Current state of image guidance in radiation oncology: Implications for ptv margin expansion and adaptive therapy. *Seminars in Radiation Oncology*, 28:238–247.